



HAL
open science

Numerical model for the assessment of the seismic vulnerability of traditional masonry structures with seismic bands

Damien Decret

► **To cite this version:**

Damien Decret. Numerical model for the assessment of the seismic vulnerability of traditional masonry structures with seismic bands. Mechanics of materials [physics.class-ph]. Université Grenoble Alpes [2020-..], 2021. English. NNT : 2021GRALI081 . tel-03847763

HAL Id: tel-03847763

<https://theses.hal.science/tel-03847763>

Submitted on 10 Nov 2022

HAL is a multi-disciplinary open access archive for the deposit and dissemination of scientific research documents, whether they are published or not. The documents may come from teaching and research institutions in France or abroad, or from public or private research centers.

L'archive ouverte pluridisciplinaire **HAL**, est destinée au dépôt et à la diffusion de documents scientifiques de niveau recherche, publiés ou non, émanant des établissements d'enseignement et de recherche français ou étrangers, des laboratoires publics ou privés.



THÈSE

Pour obtenir le grade de

DOCTEUR DE L'UNIVERSITÉ GRENOBLE ALPES

Spécialité : 2MGE : Matériaux, Mécanique, Génie civil,
Electrochimie

Arrêté ministériel : 25 mai 2016

Présentée par

Damien DECRET

Thèse dirigée par **Laurent DAUDEVILLE**, Professeur, Université Grenoble Alpes
et codirigée par **Yannick SIEFFERT**, Maître de Conférence, Université Grenoble Alpes
et **Yann MALECOT**, Professeur, Université Grenoble Alpes (UGA)
préparée au sein du **Laboratoire Laboratoire Sols, Solides, Structures et Risques**
dans l'**École Doctorale I-MEP2 - Ingénierie - Matériaux, Mécanique, Environnement, Energétique, Procédés, Production**

Modèle numérique pour la caractérisation de la vulnérabilité sismique des constructions traditionnelles avec bandes sismiques

Numerical model for the characterization of the seismic vulnerability of traditional masonry constructions with seismic bands

Thèse soutenue publiquement le **14 octobre 2021**,
devant le jury composé de :

Monsieur Stéphane GRANGE

PROFESSEUR DES UNIVERSITES, INSA de Lyon, Président

Madame Katrin BEYER

PROFESSEUR ASSOCIE, Ecole Polytechnique Fédérale de Lausanne, Suisse, Rapporteur

Monsieur Emmanuel FERRIER

PROFESSEUR DES UNIVERSITES, Université Claude Bernard - Lyon 1, Rapporteur

Monsieur Sergio LAGOMARSINO

PROFESSEUR, Université de Gènes, Italie, Examineur

Monsieur Laurent DAUDEVILLE

PROFESSEUR DES UNIVERSITES, Université Grenoble Alpes, Directeur de thèse

Monsieur Malecot Yann

PROFESSEUR DES UNIVERSITES, Université Grenoble Alpes, Invité

Monsieur Sieffert Yannick

MAÎTRE DE CONFERENCE, Université Grenoble Alpes, Invité

Monsieur Vieux-Champagne Florent

MAÎTRE DE CONFERENCE, Polytech Grenoble, Invité

Abstract

Masonry structures are particularly vulnerable to seismic hazards. Nevertheless, architectural strategies have been developed by local population in different areas to improve their seismic resistance. One of these methods is the use of horizontal bands also called seismic bands. These bands can be made of different materials such as wood, reinforced concrete or bricks. The contribution of these bands is well known. For this reason, their use is prescribed in the building codes for masonry in several Himalayan countries. However, the prescribed number of bands and their placement in the walls vary from one regulation to another. In addition, the codes do not take into account seismic hazards, but consider the use of bands inappropriate in the most vulnerable areas.

A numerical model is needed to optimize the use of horizontal bands and to tailor designs to the degree of seismic hazard. To achieve this, it is necessary to identify the categories of masonry structures and determine the failure modes that may occur in these structures. The focus is placed on masonry structures with seismic bands, and the different elements that compose them are identified: the masonry portions, the seismic bands, the reinforcements at the openings and the roof. This allows the identification of an appropriate numerical model. Among the models from the literature, only meso-models and macro-models are considered. The Rigid Macro Element Model appeared to be the most interesting model for the modeling masonry buildings with bands, but due to some limitations in correctly capturing the OOP bending of the walls, it was decided to create a new meso-model: the Deformable Frame Model.

The development of the numerical model is presented in Chapters 4 to 6. The Deformable Frame Model consists of a frame made with elastic beams. The kinematics of the frame is such that the beams can be considered as struts for 2D modeling. Within the frame, there is one strut per diagonal to reproduce the inelastic behavior of masonry under cyclic shear loading. The model can capture three modes of failure of masonry under in-plane shear loading. Under out-of-plane loading, the meso-element behaves elastically. The seismic bands are modeled with zero-thickness interfaces to reproduce sliding at their interface with the masonry portions. The reinforcements are modeled as elastic beams since they are not damaged during seismic excitation. The roof is simply modeled as a mass at the top of the wall. The properties of all these elements are defined with the properties of the materials, which can be measured without expensive experimental tests.

Then, the proposed numerical model is tested. First, the modal analysis of several structures is performed. These structures range from the size of a square wall to the size of a five-walled

structure. In this way, the elastic properties of the model can be validated and the limitations of the model for dynamic analysis can be evaluated. Then, the numerical model is used to model three different experimental campaigns. The first campaign consists of the horizontal cyclic test of two walls of different sizes, the second one of the cyclic test of a wide wall with openings and the last one of the cyclic test of adobe walls with and without seismic bands. This can be used to show the efficiency of Deformable Frame Model in predicting the cyclic behavior of masonry walls. Finally, the dynamic analysis of three houses is carried out at a reduced scale. These houses had the same dimensions but were constructed differently. One house was without straps, another with wooden straps and the last one with reinforced concrete straps. The results obtained with the numerical model are compared with those obtained with the shake table tests in order to evaluate the performance of the model.

The study presented in this paper is the first step towards the optimization of masonry structures with straps through the proposal of a reliable numerical model that allows the prediction of the dynamic analysis of these structures. This model aims to allow the study of different structures in a short time without the help of expensive experimental tests.

Résumé en français

Cette thèse a pour but de proposer un modèle numérique simple et rapide pour l'analyse dynamique des structures en maçonnerie avec bandes horizontales appelés aussi bandes sismiques. Ces bandes sont utilisées en tant que dispositif parasismique et leurs apports sont bien connus:

- **Elles réduisent la hauteur effective des murs.** Cela permet de réduire les déplacements hors-plan et limite les risques d'effondrement qui en résultent.
- **Elles permettent le contrôle de la fissuration.** Lorsqu'une fissure se propage dans le mur, elle ne peut pas traverser une bande et se propage le long de celle-ci.
- **Elles divisent le mur en maçonnerie en plusieurs parties.** Ainsi, une fissure ne peut pas se propager que dans la partie dans laquelle elle se trouve ce qui permet de protéger les zones saines du mur.
- **Elles augmentent l'énergie dissipée.** Lorsqu'une fissure se propage le long d'une bande, un déplacement différentiel entre la bande et la maçonnerie a lieu engendrant une dissipation d'énergie par frottements.

Si leur utilité est bien connue, ils restent encore des incertitudes pour l'optimisation de ce procédé technique. La première incertitude concerne le nombre de bandes à utiliser. Suivant le code de construction, ce nombre diffère. En plus de cette inconnue, l'emplacement des bandes n'est pas toujours le même même si certaines typologies reviennent. De plus, les codes de construction ne prennent pas en compte le niveau de l'aléa sismique pour l'emplacement des bandes. Le modèle numérique proposé dans cette thèse a pour but de proposer une réponse à ces incertitudes et manques de connaissance.

Le Chapitre 1 donne les connaissances nécessaires sur les constructions en maçonnerie afin de bien appréhender le sujet. Dans la majorité des cas, ce type de structure est composé de briques séparées par des joints. Les constructions en maçonnerie peuvent être classées en quatre catégories: maçonnerie non renforcée, maçonnerie renforcée, maçonnerie confinée et portiques avec remplissage en maçonnerie. L'identification du type de structure est essentielle car c'est un facteur déterminant dans le choix du modèle numérique. Par exemple, l'Equivalent Strut Model (ESM), modèle représenté sur la figure 2, ne peut être utilisé que pour les portiques avec remplissage. En outre, la maçonnerie n'est pas soumise aux mêmes types de rupture suivant le type de construction. Pour ce qui est des constructions non renforcées, on recense quatre modes de ruptures:

- **La rupture diagonale:** Elle est reconnaissable par une fissuration en escalier au sein du mur. Elle est liée à la rupture en cisaillement des joints et à la flexion du mur. Elle dépend du chargement vertical et de l'élançement du mur. La fissure peut traverser à la fois les joints et les briques.
- **La rupture en cisaillement des joints:** Elle est reconnaissable par une rupture le long d'un joint horizontal. Elle dépend du chargement vertical et des caractéristiques des joints.
- **La rupture en compression:** Elle est reconnaissable par des fissures verticales au bas du mur. Elle est liée à la rupture en compression des joints et/ou des briques.
- **La rupture par basculement:** Elle est reconnaissable par une fissuration proche des coins du mur. Elle est liée au chargement vertical et à l'élançement du mur.

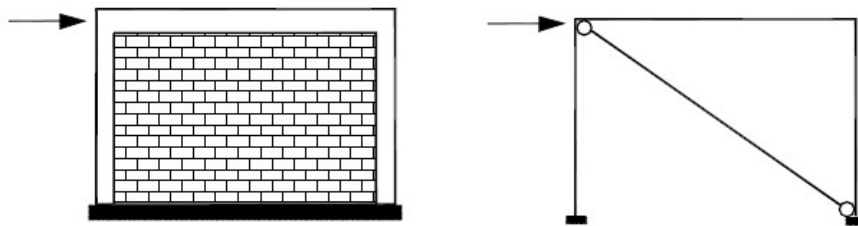


Figure 1: L'Equivalent Strut Model pour modéliser les portiques avec remplissage en maçonnerie [1]

Lorsqu'elle est utilisée pour faire du remplissage, la maçonnerie est soumise à de la compression le long de ses diagonales. Cela donne lieu à des ruptures qui ne sont pas rencontrées dans les autres types de constructions: fissuration au centre du mur ou aux coins due à une compression trop importante dans la diagonale. Afin de reproduire correctement le comportement des constructions en maçonnerie, il est nécessaire que le modèle numérique utilisé puisse capturer les différentes ruptures qui peuvent avoir lieu pour le type de construction considéré. Ceci est d'autant plus important que les murs sollicités dans leur plan gouvernent le comportement global de la structure. Les murs hors-plan, quant à eux, apportent une faible rigidité. Cependant, il est fréquent qu'ils s'effondrent lors des séismes. Il est donc nécessaire de modéliser ses murs et de pouvoir déterminer leur comportement limite.

Pour identifier les constructions qui sont dans les cadre de la thèse, les constructions avec bandes sismiques, le Chapitre 2 fait un état de l'art des constructions avec insertions horizontales. Cette étude montre que ces constructions peuvent être confondues avec les constructions pour lesquelles la maçonnerie est utilisée en remplissage. Les structures dans le cadre de la thèse sont identifiées grâce à certaines spécificités:

- Les bandes horizontales ne sont pas les éléments porteurs de la structure.
- Les bandes horizontales sont placées à des endroits précis: au-dessus et en-dessous des ouvertures, au niveau du toit...

Les bandes peuvent être réalisées en différents matériaux: bois, briques, béton armé ou même bambou. Des essais ont montré que, suivant le matériau utilisé, les apports de la bande ne sont pas les mêmes pour le comportement du mur. Ces essais ont aussi permis d'identifier les différents éléments au sein des constructions avec bandes qu'il est nécessaire de modéliser pour bien reproduire le comportement des constructions avec bandes sismiques. En plus de la maçonnerie, il est nécessaire de modéliser les bandes, les éventuels renforts et le toit. De plus, il en résulte l'identification d'une échelle intermédiaire, l'échelle méso, correspondant à l'échelle d'un bloc de maçonnerie entre deux bandes.

Suite à l'identification des différents éléments, une étude bibliographique des différents modèles numériques pour les constructions en maçonnerie est proposée au Chapitre 3 afin de connaître quel modèle est le plus pertinent pour l'étude. Les modèles peuvent être classés en trois catégories: micro-modèles, méso-modèles et macro-modèles. Cette classification correspond à l'échelle considérée pour modéliser la maçonnerie. Les micro-modèles modélisent tous les éléments au sein du mur, les macro-modèles modélisent la maçonnerie à l'échelle du mur ou à l'échelle de grandes portions et les méso-modèles modélisent la maçonnerie à une échelle intermédiaire. Suite à l'identification des éléments effectuées au Chapitre 2, le choix se porte sur les méso-modèles afin de limiter le nombre de degrés de liberté. Parmi les modèles rencontrés, l'un d'entre eux permet de modéliser tous les éléments identifiés et de modéliser la maçonnerie de manière simple. Le modèle en question est le Rigid Macro Element Model proposé par Calio et al [2], représenté sur la figure ?? . Il consiste en la modélisation de la maçonnerie par un cadre rigide avec une articulation à chaque sommet. Au sein du cadre, en élément diagonal est utilisé pour reproduire le comportement en cisaillement de la maçonnerie. Le cadre est relié aux autres éléments par deux types de ressorts:

1. Des ressorts transversaux pour le comportement en traction/compression de la maçonnerie.
2. Des ressorts longitudinaux pour le comportement en cisaillement des joints.

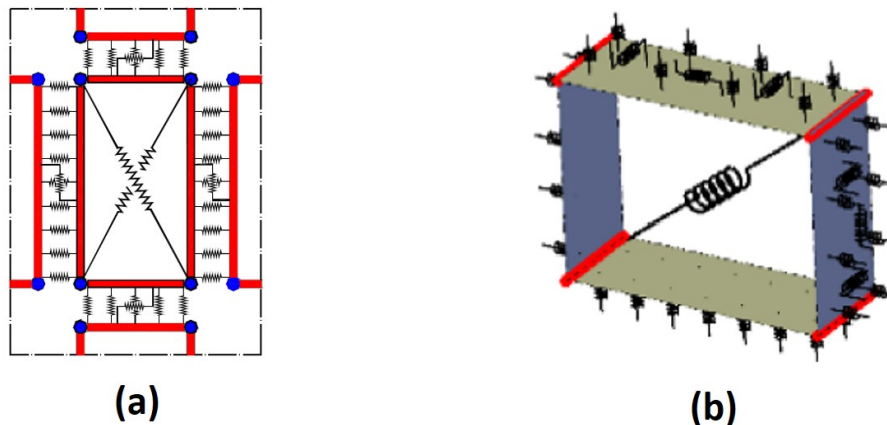


Figure 2: Le RMEM pour modéliser les structures en maçonnerie [1]

Le comportement des trois types d'éléments sont liées aux caractéristiques géométriques et mécaniques de la maçonnerie modélisée. L'identification est simple et nécessite seulement 2

paramètres empiriques pour reproduire le comportement cyclique du matériau. Bien qu'il ait de nombreux avantages, le modèle nécessite un maillage fin pour reproduire correctement la flexion du mur hors-plan. Cela implique une quantité importante de degrés de liberté et, par conséquent, un temps de calcul non négligeable. Afin de ne pas avoir ce problème, un modèle numérique inspiré du RMEM est créé pour les études dans le cadre de la thèse: le Deformable Frame Model (DFM), représenté sur la figure 3.

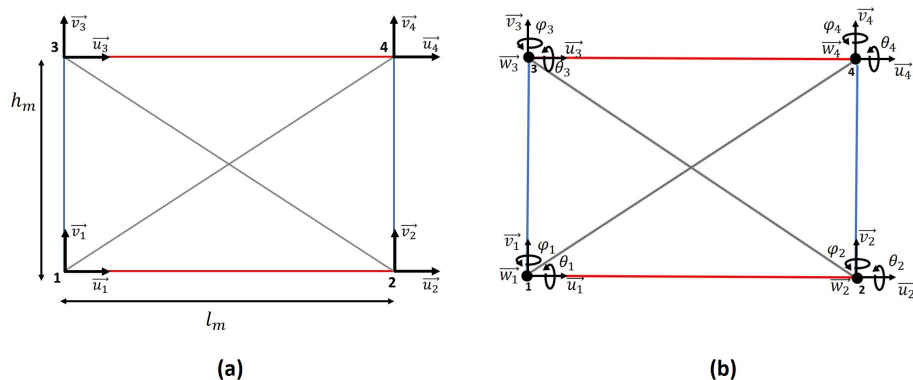


Figure 3: Le DFM pour: (a) étude dans le plan ; (b) étude 3D

Le DFM est présenté pour une modélisation dans le plan dans le Chapitre 4. Ce méso-modèle est composé d'un cadre déformable réalisé avec des éléments barres. Au sein du cadre, une barre relie les sommets diagonalement opposés. Chaque élément est utilisé pour un type de sollicitation précis: les barres verticales (respectivement horizontales) sont utilisées pour le comportement en traction/compression verticale (resp. horizontale) et les éléments diagonaux sont utilisés pour le cisaillement. L'identification des rigidités des éléments se fait simplement avec l'aide du Principe des Puissances Virtuelles (PPV). Le but de ce modèle est de reproduire le comportement de la maçonnerie sous chargement sismique, c'est à dire sous cisaillement cyclique. C'est pour cela que seuls les éléments diagonaux ont un comportement inélastiques. La courbe enveloppe de leur loi de comportement est bi-linéaire, semblable à un comportement élasto-plastique parfait. Le plateau a pour ordonnée F_u qui correspond à l'effort ultime de la maçonnerie. Celui-ci est déterminé à partir de formules issues de la littérature sont utilisés capturer deux modes de ruptures: la rupture diagonale, formule de Turnšek et Čačovič [3], et la rupture des joints horizontaux, critère de Mohr-Coulomb. Pour la modélisation de murs en maçonnerie non renforcée, il est possible de capturer la rupture par basculement. Le comportement hystérétique est inspiré du modèle proposé par Panagiotakos et Fardis [4] pour l'ESM. Ce modèle utilise seulement trois paramètres pour définir la forme de l'hystérèse. Afin d'avoir un comportement prédictif, des formules sont proposées pour ces trois paramètres.

En plus de la maçonnerie, les bandes et les renforts aux ouvertures doivent être modélisés. Lors des essais expérimentaux, les bandes servaient essentiellement d'interface glissante lorsque l'interface maçonnerie/bande fissurait. Pour cette raison, les bandes sont modélisées par des éléments d'interface avec une épaisseur nulle, représenté sur la figure 4. Ces éléments utilisent les mêmes noeuds que le DFM avec le même nombre de degrés de liberté. Les joints ont un comportement élastique en compression, élastique endommageable en traction et elasto-plastique en cisaillement. L'endommagement dû au comportement en traction de l'interface affecte la

cohésion mais l'inverse n'est pas vrai. Une fois que l'interface a rompu en traction, elle n'a plus de rigidité pour les sollicitations perpendiculaires à son plan et la cohésion est nulle. Le comportement au cisaillement de l'interface est défini avec le critère de Mohr-Coulomb. Dans le cas spécifique des constructions en maçonnerie avec bandes, des fissures peuvent se propager de la maçonnerie aux bandes. Afin de modéliser cet endommagement de l'interface, les joints sont couplés avec les DFM auxquels ils sont reliés. Lorsque les éléments diagonaux des DFM concernés plastifient, ils endommagent aussi la cohésion de l'interface. La vitesse de l'endommagement est contrôlée par un paramètre empirique, le seul utilisé pour le modèle. Lors des essais, les renforts n'ont pas été endommagés. Ils sont donc modélisés par des poutres élastiques qui partagent les mêmes noeuds que le DFM. Seuls les linteaux sont un cas particulier suivant s'ils sont réalisés par des bandes horizontales ou des renforts qui se limitent aux ouvertures.

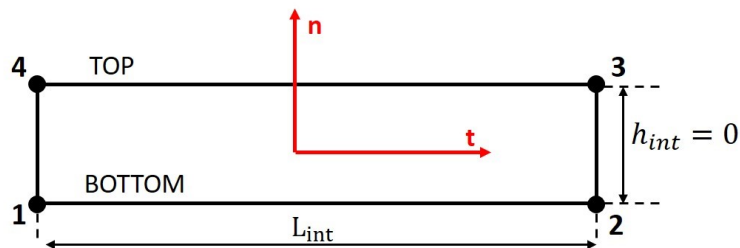


Figure 4: L'élément d'interface pour modéliser les bandes

Afin de permettre l'étude dynamique de structure en maçonnerie complètes, le Chapitre 6 définit le DFM pour une modélisation 3D. Comparé au modèle 2D, ce format a des éléments poutres pour le cadre. Aux noeuds, il y a dorénavant cinq degrés de liberté (seule la rotation autour de l'axe hors-plan est omise). Ces poutres ont un comportement élastique et permettent de reproduire la flexion hors-plan du mur et sa torsion. Cette formulation 3D du DFM n'affecte pas la définition du méso-élément pour une étude 2D. Des spécificités apparaissent pour la modélisation des structures aux intersections des murs. Dans ce cas précis, les éléments verticaux appartiennent à la fois à des murs sollicités hors-plan et des murs sollicités dans le plan. Afin d'éviter une multiplication des cas qui peuvent arriver, le choix a été fait de ne considérer que le comportement en traction/compression et torsion de ces éléments. En plus de la définition du comportement 3D du DFM, le Chapitre 6 propose la définition de la matrice de masse du modèle complet (DFM + interface + renforts). La masse de la maçonnerie est définie aux noeuds en déterminant le volume qui leur est associé. Un point quelconque appartient au volume associé au noeud le plus proche.

Les Chapitres 7 à 9 permettent de tester le DFM. Le Chapitre 7 consiste en une succession d'études modales allant de l'analyse d'un mur simple à l'analyse d'une maison deux pièces. Ces différentes études montrent que le DFM permet de déterminer avec une bonne précision les modes propres d'une structure mis à part les modes verticaux pour lesquels le modèle sous-estime la masse modale, mais donne une bonne approximation de la fréquence associée. En termes de temps de calculs, le modèle est bien plus rapide qu'un modèle 3D FE classique. Le Chapitre 8 consiste en la modélisation de trois campagnes expérimentales afin de tester les capacités du modèle à prédire le comportement cyclique de mur en maçonnerie. La première campagne expérimentale est celle d'Anthoine et al. [5] qui consiste en deux essais de cisaillement cycliques: un essai sur un petit mur et un essai sur un grand mur. Ces deux murs, qui n'ont pas d'ouvertures, diffèrent

l'un de l'autre seulement par leur taille. Ce facteur a une influence sur leur mode de rupture. Le petit mur a une fissuration diagonale alors que le grand mur a une fissuration liée à la flexion. Le DFM arrive à prédire le comportement des deux murs de manière très précise. Le second essai modélisé est l'essai cyclique d'un mur en adobe de Reyes et al. [6]. Ce mur est représentatif des constructions historiques en Colombie. Il a des dimensions supérieures aux deux murs d'Anthoine et al. [5] et a deux ouvertures avec linteaux. La présence d'ouverture joue sur la taille des éléments et, pour cet essai, les méso-éléments n'ont pas tous la même dimension. Le modèle numérique parvient à prédire la courbe enveloppe de l'essai avec une précision satisfaisante. Cependant, il surestime l'énergie dissipée lors des cycles. La troisième campagne expérimentale est celle de Yadav [7]. Elle consiste en deux essais quasi-statiques sur des murs en adobe qui ont les mêmes dimensions. L'un des deux murs a une bande horizontale en son centre alors que le second n'en a pas. Contrairement aux modélisations précédentes de ce chapitre, l'essai sur le mur sans bande est utilisé pour déterminer les caractéristiques des matériaux utilisés pour les essais dynamiques modélisés au Chapitre 9. Afin d'avoir une meilleure approximation de la courbe enveloppe des résultats expérimentaux, une loi tri-linéaire est utilisée pour le comportement des éléments diagonaux. La branche additionnelle correspond au changement de rigidité après l'apparition des premières fissures avant que la résistance maximale de la maçonnerie soit atteinte. Seuls les paramètres de l'hystérèse ne sont pas déterminés sur la courbe expérimentale mais calculés avec les formules proposées au Chapitre 4. Une fois les propriétés mécaniques de l'adobe déterminées, les propriétés de l'interface sont déterminées avec le second essai en considérant que les propriétés de la maçonnerie restent les mêmes. Pour cet essai, l'interface n'a pas fissuré. Il n'est donc pas possible de déterminer le paramètre gérant le couplage entre les éléments d'interface et les méso-éléments ainsi que le coefficient de frottement. De plus, ce mur a une résistance plus grande que le mur précédent qui ne peut pas être reproduite avec le modèle. Il en résulte une différence notable entre les résultats obtenus avec le modèle numérique et expérimentalement. Une analyse de l'influence des différents paramètres de l'interface est aussi effectuée pour identifier ceux qui ont un rôle majeur et ceux qui ont une faible influence sur le comportement du mur.

Le Chapitre 9 présente l'analyse dynamique de trois maisons à l'échelle 1/2 ayant les mêmes dimensions testées sur table vibrante. L'une des maisons est une maison en adobe non renforcée, une autre est en adobe avec des bandes sismiques en bois et la dernière est en adobe avec des bandes sismiques en béton armé. Les briques et le mortier utilisés pour ces maisons sont les mêmes que pour les essais quasi-statiques de Yadav [7]. Cependant, le temps de séchage et les conditions extérieures sont différents. Ainsi, les propriétés mécaniques identifiées au chapitre précédent ne peuvent être utilisées et les valeurs sont ajustées avec l'aide de la littérature. Pour chaque maison, cinq signaux sismiques d'intensité croissante sont utilisés. Lors des essais, des capteurs à fil sont utilisés pour mesurer les déplacements en des points précis des maisons. Deux capteurs placés dans l'axe des murs sollicités dans leur plan et trois capteurs sont utilisés pour mesurer les déplacements hors-plan d'un mur à des hauteurs différentes. Le modèle numérique arrive à bien prédire les déplacements mesurés expérimentalement pour les murs sollicités dans leur plan. Cependant, le modèle n'arrive pas à capturer le déplacement maximal pour les déplacements positifs au second essai sismique. Il en résulte un endommagement moins important qui a un impact sur les essais suivants. Ce phénomène se cumule d'un essai à l'autre réduisant les chances que le modèle capture correctement le déplacement maximal. Cela se vérifie pour les trois essais. Pour ce qui est du déplacement hors-plan, le modèle n'arrive pas à bien le reproduire. Pour les essais avec le signal le plus faible, la différence est de l'ordre de 20% mais pour les essais suivants, le mur est endommagé alors que le modèle a un comportement élastique. Le développement d'un critère limite pour déterminer le déplacement ultime pour l'effondrement hors-plan doit prendre cela en compte.

Contents

I	General presentation	5
1	Knowledge about masonry structures	7
1.1	Basic vocabulary	7
1.2	Categories of masonry constructions	8
1.3	IP behavior of masonry	9
1.3.1	Modes of failure	9
1.3.2	IP cyclic behavior	11
1.4	OOP behavior of masonry	13
1.5	Conclusion	14
2	Masonry structures with bands	15
2.1	Introduction	15
2.2	Typologies	15
2.3	Prescribed positions for the bands	19
2.4	The limitation of the study	21
2.5	Experimental studies on masonry with bands	22
2.5.1	Scale of the wall	22

2.5.2	Scale of the structure	25
2.6	Conclusion	28
3	Modeling of masonry	30
3.1	Models in the literature	31
3.1.1	Micro-models	31
3.1.2	The meso-models	32
3.1.3	Macro-models	36
3.2	Discussion for the context of the thesis	38
3.3	The Rigid Macro-Element Model (RMEM)	40
3.3.1	Area of influence the springs	41
3.3.2	Calibration of the normal spring	42
3.3.3	Calibration of the shear-sliding springs	43
3.3.4	Calibration of the diagonal springs	44
3.3.5	The OOP behavior	45
3.3.6	Connection between elements	46
3.3.7	Mass matrix of the RMEM	47
3.3.8	FE version of the model	48
3.4	Conclusion	49
II	Modeling at the scale of the elements	50
4	Deformable Frame Model for IP loading	52
4.1	Hypothesis for the modeling	52

4.2	Kinematics of the DFM	53
4.3	Definition of the stiffness of the elements	54
4.3.1	Modeling with one macro-element	54
4.4	Inelastic behavior of the DFM	55
4.4.1	Shear strength of the DFM	55
4.4.2	Hysteresis models	58
4.5	Refined mesh	68
4.6	Conclusion	69
5	Modeling of other structural elements	71
5.1	Modeling of bands	71
5.1.1	Overview of interface models	72
5.1.2	Inelastic behavior of the interface	75
5.1.3	The coupling with the DFM	77
5.2	Reinforcements at the openings	78
5.2.1	Frames at the opening	79
5.2.2	Frames at the opening	80
5.2.3	Lintels	80
5.3	Conclusion	81
6	3D modeling	83
6.1	Introduction	83
6.2	DFM for 3D modeling	83
6.2.1	Models from the literature	84

6.2.2	DFM for OOP loading	85
6.3	Mass matrix definition	89
6.4	Conclusion	91
III	Numerical modeling of masonry structures	93
7	Validation of the elastic properties	95
7.1	Modal analysis of walls without openings	97
7.1.1	Square wall	97
7.1.2	Wide wall	101
7.1.3	Study of the influence of the Poisson's ratio	103
7.1.4	Conclusions	104
7.2	Modal analysis of a 4-wall structure	105
7.3	Modal analysis of a 5-wall structure	110
7.3.1	5-wall structure without openings	110
7.3.2	5-wall structure with openings	114
7.4	Conclusions about the modal analysis	118
8	Modeling of static IP cyclic tests on walls	119
8.1	URM piers	119
8.1.1	Modeling of the tests	119
8.1.2	Influence of the size of the mesh	122
8.2	Wide walls with openings	124
8.2.1	Modeling with a bilinear behavior	124

8.2.2	Modeling with a trilinear behavior	126
8.2.3	Influence of the modeling of the lintels	128
8.2.4	Conclusion	129
8.3	Adobe wall with bands	129
8.3.1	Wall without bands	131
8.3.2	Sensitivity analysis for masonry properties	132
8.3.3	Wall with timber band	134
8.3.4	Sensitivity analysis interface	136
8.3.5	Conclusion	138
8.4	Conclusion	139
9	Dynamic analysis	140
9.1	The experimental campaign	141
9.1.1	The shaking table	141
9.1.2	The sample houses	142
9.1.3	The seismic signals	145
9.1.4	The measurements	147
9.2	Dynamic analyses	148
9.2.1	Study of the house without bands	148
9.2.2	Study of the house with wood bands	155
9.3	Study of the house with RC bands	159
9.3.1	Input data	159
9.3.2	Numerical modeling	160

9.4	Analysis of the effects of bands	163
9.4.1	Deformation during seismic excitation	163
9.4.2	Damage after the seismic tests	166
9.5	Conclusion	168
A	Diagonal strut explanations	186
B	Creation of the problem	188
B.1	Inelastic behavior of diagonal struts	188
B.2	Rocking failure	189
C	ATL4S	190
C.1	Numerical dynamic analysis with ATL4S	191
C.2	Modal analysis	191
C.3	Constitutive laws for the elements	192
C.3.1	Already implemented laws	192
C.3.2	Added laws	193
D	Evolution of damage during the experimental tests	194
D.1	House without bands	194
D.1.1	Beginning of the tests	194
D.1.2	After the Guadeloupe 100%	196
D.1.3	After the Guadeloupe 150%	198
D.1.4	After the Guadeloupe 200%	200
D.1.5	After the Guadeloupe 300%	202

D.2	House with timber bands	203
D.2.1	Beginning of the tests	203
D.2.2	After the Guadeloupe 100%	205
D.2.3	After the Guadeloupe 150%	207
D.2.4	After the Guadeloupe 200%	209
D.2.5	After the Guadeloupe 300%	211
D.3	House with RC bands	213
D.3.1	Beginning of the tests	213
D.3.2	After the Guadeloupe 100%	215
D.3.3	After the Guadeloupe 150%	217
D.3.4	After the Guadeloupe 200%	219
D.3.5	After the Guadeloupe 300%	221

List of Figures

1	L'Equivalent Strut Model pour modéliser les portiques avec remplissage en maçonnerie [1]	iv
2	Le RMEM pour modéliser les structures en maçonnerie [1]	v
3	Le DFM pour: (a) étude dans le plan ; (b) étude 3D	vi
4	L'élément d'interface pour modéliser les bandes	vii
5	Masonry structure with seismic bands in Nepal	1
1.1	Common brickworks	8
1.2	Examples of RC FIM and RC CM structures	9
1.3	Modes of failure for URM buildings	10
1.4	Deformation of a masonry infilled RC frame	10
1.5	Modes of failure for masonry infill frames	11
1.6	Shear cyclic behavior of two walls of different height	12
1.7	Cyclic behavior of the high wall under a higher vertical stress	12
1.8	The OOP failures of URM structures	13
2.1	Examples of masonry structures with bands	16
2.2	Possible designs for wooden bands	17

2.3	Proposed designs of masonry houses with bands	20
2.4	Example of structure in the scope of this study	22
2.5	Two tested specimens for cyclic tests	23
2.6	Results of the quasi-static cyclic tests on the UW and the RW specimens	24
2.7	Energy dissipation rate for the UW and the RW specimens	24
2.8	Apparatus used for the OOP test	25
2.9	Force-Deflection behavior of the walls under OOP solicitation	26
2.10	Reduced scale houses tested in Pakistan	26
2.11	Damage of the three reduced scale houses	28
2.12	Identification of the elements for the numerical modeling	29
3.1	Examples of micro-models for masonry	31
3.2	Examples of meso-model for masonry	33
3.3	The first methods of homogenization	34
3.4	Different RVEs for the running bond pattern	35
3.5	Examples of macro-model for masonry	36
3.6	Different versions of the RMEM	41
3.7	Area of influence of the springs of the RMEM	41
3.8	Behavior of the transversal springs of the RMEM	42
3.9	Constitutive law of the shear/sliding spring of the RMEM	43
3.10	RMEM element under shear solicitation	44
3.11	Constitutive law of the diagonal springs of the RMEM	45
3.12	Interface between a RMEM element and a rigid element	46

3.13	Interface between two macro/elements	46
3.14	Shape of the meso-element for the determination of the mass matrix	47
3.15	Finite Element version of the RMEM	48
4.1	The DFM for 2D modeling	53
4.2	Virtual work for the definition of the stiffness of vertical struts of the DFM	54
4.3	Moment distribution in a wall	57
4.4	Four constitutive laws for ESM	59
4.5	Force-Displacement constitutive law of the diagonal struts of the DFM	62
4.6	Force-Displacement behavior of the diagonal struts of the DFM with small cycles	65
4.7	Hysteresis loop of the diagonal struts constitutive law with a negative value of δ	66
4.8	Diagonal crack pattern for masonry walls with different slenderness	67
4.9	Example of a refined mesh with the DFM	68
4.10	Meshing with the DFM with several meso-elements	68
5.1	Zero-thickness interface model	72
5.2	Thin interface model	74
5.3	Example of connection between interface element and DFM elements	75
5.4	Behavior of the band in the normal direction and in the tangential direction	76
5.5	Cyclic behavior of the interface model	77
5.6	Damage of the cohesion by crack propagation by coupling the interface element with the DFM	78
5.7	Kinematics of the nodes part of frame elements	79
5.8	Intersection of vertical beam elements in presence and zero-thickness interface . . .	80

5.9	Modeling of lintel when it is not made by a horizontal band	81
6.1	Models for masonry from the literature able to reproduce OOP deformation	84
6.2	The DFM for 3D modeling with kinematics defined in the global orthonormal coordinate system	85
6.3	Definition of the height and the width of influence of the beams of the DFM	86
6.4	Kinematics of beam elements of the DFM defined in the local orthonormal coordinate system	87
6.5	Intersection of two walls	88
6.6	Examples of area of influence for nodes	90
6.7	Examples of area of influence of nodes in presence of an interface	91
7.1	Examples of mesh for the square wall	97
7.2	The first modal frequencies of the square wall	98
7.3	Modal masses of the square wall	98
7.4	Modal shapes for the important modes of the square wall	99
7.5	Evolution of the accuracy in determining the important modes of the square wall with the mesh size	100
7.6	Evolution of the value of mode 4 with the mesh size	100
7.7	Examples of mesh for the wide wall	101
7.8	The first modal frequencies of the wide wall	102
7.9	Modal masses for the wide wall	102
7.10	Modal shapes for the important modes of the wide wall	103
7.11	Evolution of the accuracy in determining the important modes of the wide wall with the mesh size	104
7.12	Modal masses for the wide wall with Poisson's ratio of zero	104

7.13	Evaluation of the accuracy in the determination of the important modal frequencies with Poisson's ratio of zero	105
7.14	Examples of mesh for the 4-wall structure	105
7.15	The first modal frequencies of the 4-wall structure	106
7.16	The modal masses of the 4-wall structure	106
7.17	The modal masses of the 4-wall structure determined with the DFM for each direction	107
7.18	Modal shapes of the 4-wall structure	108
7.19	Evolution of the accuracy in determining the frequencies of the important of the 4-wall structure with the mesh size	109
7.20	Schemes of the 5-wall structure for the modal analysis	110
7.21	Meshes for the 5-wall structure without openings	111
7.22	The first modal frequencies of the 5-wall structure without openings	111
7.23	Modal masses for the 5-wall structure without openings	112
7.24	Modal shapes of the 5-wall structure without openings	113
7.25	Evolution of the accuracy in determining the important frequencies of the 5-wall structure without openings with the mesh size	114
7.26	Meshes for the 5-wall structure with openings	114
7.27	The first modal frequencies for the 5-wall structure with openings	115
7.28	Modal analysis of the 5-wall structure with the DFM	115
7.29	Modal shapes of the 5-wall structure with openings	117
8.1	Experimental setup for the test of the two walls by Anthoine et al.	120
8.2	Force-displacement curves obtained experimentally by Anthoine et al.	122
8.3	Force-displacement curves obtained with the DFM	122

8.4	Influence of the mesh for the Force-Displacement curve of the small wall tested by Anthoine et al.	123
8.5	Influence of the mesh for the Force-Displacement curve of the high wall tested by Anthoine et al.	123
8.6	Wall with openings tested by Reyes et al.	125
8.7	Cyclic response of the adobe wall and result of the modeling with the DFM with bilinear behavior	126
8.8	Force-displacement curves of Reyes et al.'s test with trilinear behavior of the diagonal strut	127
8.9	Modeling of the adobe walls with different lengths of the lintels	128
8.10	Push-over curves for the cases with different lengths of the lintels	128
8.11	Apparatus for the quasi-static test of Yadav	129
8.12	Cyclic horizontal displacement loading used by Yadav	130
8.13	Experimental results for the wall without bands	131
8.14	Curve obtained with the DFM and experimental curve for the URM wall	132
8.15	Sensitivity analysis for masonry properties	133
8.16	Experimental results for the wall with timber bands	134
8.17	Cyclic behavior of the RM wall	135
8.18	Sensitivity analysis of interface properties for Yadav's experiment	137
8.19	Sensitivity of the coupling between the DFM and the interface	138
9.1	The shaking table of Institut Technologique FCBA	141
9.2	The three houses for the shaking table tests	142
9.3	Schemes of the reduced scale houses	144
9.4	Installation of the samples on the shaking table	144

9.5	Ground displacement, ground velocity and ground acceleration of the Guadeloupe seismic signal	146
9.6	Positions of the cable sensors on the North wall of the reduced scale houses	147
9.7	Modeling of the house without bands	148
9.8	Experimental and numerical displacements histories of the house without bands with the properties of adobe determined in Section 8.3	150
9.9	Experimental and numerical displacements histories of the house without bands .	153
9.10	Crack pattern before the tests of the house without bands	155
9.11	Mesh of the numerical modeling of houses with bands	156
9.12	Experimental and numerical displacements histories of the house with wood bands	157
9.13	Experimental and numerical displacements histories of the house with RC bands	161
9.14	Deformed shapes of the house without bands according to the numerical model at maximum displacements for every test	164
9.15	Top view of the deformed shapes of the house without bands according to the numerical model	164
9.16	Deformed shapes of the house with wood bands according to the numerical model at maximum displacements for every test	165
9.17	Deformed shapes of the houses according to the numerical model at the end every test	166
9.18	Evolution of the damage owing to the numerical model	167
9.19	Damage in the specimens at the end of the experimental campaign	168
A.1	The first design for the DFM	186
A.2	Kinematics of the DFM with horizontal diagonal strut	187
B.1	Procedure to define the plastic behavior of the diagonal struts	188
B.2	Procedure to determine the rocking failure	189

D.1	Drawing of crack pattern of the house without band at the beginning of the tests	194
D.2	Cracks in the house without bands at the beginning of the tests: (a-b) West wall; (c) East wall; (d) Middle wall	195
D.3	Drawing of crack pattern of the house without band after the Guadeloupe 100%	196
D.4	Cracks in the house without band after the Guadeloupe 100%: (a-c) West wall; (d-e) East wall	197
D.5	Drawing of crack pattern of the house without band after the Guadeloupe 150%	198
D.6	Cracks in the house without band after the Guadeloupe 150%: (a) West wall; (b) North Wall; (c-d) East wall; (e) Middle Wall	199
D.7	Drawing of crack pattern of the house without band after the Guadeloupe 200%	200
D.8	Cracks in the house without band after the Guadeloupe 200%: (a) East wall; (b) South Wall; (c) West wall; (d) North Wall	201
D.9	House without band after the Guadeloupe 300%	202
D.10	Drawing of crack pattern of the house with wood bands at the beginning of the tests	203
D.11	Cracks in the house with wood bands at the beginning of the tests: (a-b) West wall; (c-d) East wall	204
D.12	Drawing of crack pattern of the house with wood bands after the 100% Guadeloupe test	205
D.13	Cracks in the house with wood bands after the 100% Guadeloupe test: (a-b) West wall	206
D.14	Drawing of crack pattern of the house with wood bands after the 150% Guadeloupe test	207
D.15	Cracks in the house with wood bands after the 150% Guadeloupe test: (a-c) West wall; (d) East Wall; (e) Middle Wall	208
D.16	Drawing of crack pattern of the house with wood bands after the 200% Guadeloupe test	209
D.17	Cracks in the house with wood bands after the 200% Guadeloupe test: (a-c) West wall; (d) North Wall; (e) Middle Wall; (f) East Wall	210

D.18 Drawing of crack pattern of the house with wood bands after the 300% Guadeloupe test	211
D.19 Cracks in the house with wood bands after the 300% Guadeloupe test: (a-c) West wall; (d) North Wall; (e-f) East Wall; (g) South Wall	212
D.20 Drawing of crack pattern of the house with RC bands at the beginning of the tests	213
D.21 Cracks in the house with RC bands at the beginning of the tests: (a) East wall; (b) West wall	214
D.22 Drawing of crack pattern of the house with RC bands after the 100% Guadeloupe test	215
D.23 Cracks in the house with RC bands after the 100% Guadeloupe test: (a) West wall; (b) South Wall	216
D.24 Drawing of crack pattern of the house with RC bands after the 150% Guadeloupe test	217
D.25 Cracks in the house with RC bands after the 150% Guadeloupe test: (a-b) East wall	218
D.26 Drawing of crack pattern of the house with RC bands after the 200% Guadeloupe test	219
D.27 Cracks in the house with RC bands after the 200% Guadeloupe test: (a) West wall; (b) Earth Wall	220
D.28 Drawing of crack pattern of the house with RC bands after the 300% Guadeloupe test	221
D.29 Cracks in the house with RC bands after the 300% Guadeloupe test: (a-b) East wall; (c) South Wall; (d-f) West Wall	222

List of Tables

2.1	Determination of the type of masonry construction for the cases in Figure 2.1 . . .	19
3.1	Performances of the model regarding the objectives of the thesis	39
3.2	Properties of the normal springs of the RMEM	42
3.3	Properties of the shear/sliding springs	43
4.1	Characteristics of the hysteresis models	61
4.2	Parameters for the definition of the DFM	69
5.1	Parameters for the definition of the interface and reinforcement elements	82
6.1	Definition of the inertia terms of the beam elements of the DFM	88
7.1	Masonry mechanical properties for modal analyzes	96
7.2	Dimensions of the 4-wall structure	106
8.1	Properties of the URM piers	121
8.2	Parameters of the hysteresis for the DFM	121
8.3	Proprieties of the adobe wall	125
8.4	Average values of the parameters of the hysteresis	126

8.5	Proprieties of the adobe wall for the second study	127
8.6	Properties of the adobe walls for the quasi-static tests	130
8.7	Material properties of adobe for Yadav's experiment	132
8.8	Mechanical properties of the interface for Yadav's experiment	136
9.1	Cauchy similitude law	143
9.2	Maximum values of the Guadeloupe signal	146
9.3	Material properties of adobe determined in Section 8.3	149
9.4	Maximum displacements measured experimentally and determined with the DFM with the properties of adobe determined in Section 8.3 for the house without bands	151
9.5	Modified properties for the adobe	152
9.6	Comparison of displacements determined with the DFM and measured experimen- tally for the house without bands	154
9.7	Mechanical properties of the wood bands specimen	156
9.8	Comparison of displacements determined with the DFM and measured experimen- tally for the house with wood bands	158
9.9	Material properties for the RC bands specimen	160
9.10	Comparison of displacements determined with the DFM and measured experimen- tally for the house with RC bands	162

Symbols

A_0	Effective contact area of shear-sliding springs of the RMEM
A_n	Area of influence of node n
A_t	Cross section of a masonry portion
b	Parameter taking into account the slenderness of the element
B	Width of the considered side of the RMEM element
c	Cohesion of masonry
\bar{c}	New definition of the cohesion of masonry proposed by Mann and Muller [8]
d	Suggested distance between the springs of the RMEM to capture the out-of-plane behavior of masonry wall
D	Pier width
d_{cr}	Displacement at the occurrence of cracks
D_{int}	Damage parameter for interface models taking into account all the damage in the structure
D_{meso}	Damage parameter for interface models linked to cracks in masonry
D_{param}	Damage parameter for interface models linked to solicitations
d_u	Displacement at the ultimate strength of the diagonal strut of masonry
$E_{h,eff}$	Effective energy dissipated in one symmetrical loading loop
E_j	Joint Young modulus
E_m	Masonry Young modulus
E_r	Reinforcement Young modulus
E_u	Unit Young modulus
F_0	Yielding force with no confinement
f_c	Masonry strength in compression
F_{cr}	Force that triggers the cracking in masonry portions
F_{cy}	Yielding force of masonry in compression for the RMEM
F_{diag}	Force in the diagonal element
f_t	Masonry tensile strength
f_{tb}	Brick tensile strength
f_{tm}	Joints tensile strength
F_{ty}	Yielding force of masonry in tension for the RMEM
F_u	Ultimate strength of a diagonal strut of the DFM
F_v	Vertical effort applied on the DFM

$f_{v,1}$	Shear strength of masonry for the diagonal cracking failure by Turnšek and Čačovič [3]
$f_{v,2}$	Shear strength of masonry for the diagonal cracking failure by Turnšek and Sheppard [9]
$f_{v,3}$	Shear strength of masonry for the rocking failure
$f_{v,4}$	Shear strength of masonry with Mohr-Coulomb criterion
$f_{v,5}$	Shear strength of masonry for the shear/sliding failure
F_y	Yielding effort of the diagonal element of the RMEM
$f_{y,f}$	Yielding strength of frame
G_0	Strain-energy release rate at damage initiation
G_c	Shear modulus of concrete
G_{IT}	Fracture energy for mode I
G_{ft}	Fracture energy in tension of the masonry
G_{fc}	Fracture energy in compression of the masonry
G_m	Shear modulus of the masonry
g_{sl}	Fracture energy of the masonry under shear
G_{TC}	Critical mixed-mode energy dissipation
H	Height of the element in the RMEM
h_b	Height of the brick used for the masonry
h_{elem}	Height of vertical beam/strut of the DFM
h_i	Height of macro-element i
h_j	Height of bed joint
h_{inf}	Height of the area of influence of beam elements of the DFM
h_m	Height of the considered masonry portion
h_u	Height of the unit
$\underline{\mathbf{K}}$	Elastic stiffness matrix
K_d	Initial rigidity of a diagonal strut of the macro-element
$K_{d,i}$	Initial rigidity of the diagonal strut i
K_h	In-plane rigidity of a horizontal strut of the macro-element
$K_{h,i}$	In-plane rigidity of a horizontal strut of the macro-element i before the merging of the elements
k_n	Rigidity of interface element in the normal direction
k_t	Rigidity of interface element in the tangential direction
K_v	In-plane rigidity of a vertical strut of the macro-element
$K_{v,i}$	In-plane rigidity of a vertical strut of the macro-element i before the merging of the elements
l_b	Length of bricks
l_{elem}	Length of the considered horizontal beam of the macro-element
l_i	Width of the macro-element i
l_{inf}	Width of the area of influence of a beam element of the macro-element
l_m	Width of masonry portion
M_y	Value of the yielding moment leading to a rocking failure of a masonry pier
N	Axial force
t_m	Thickness of a masonry portion
u_0	Displacement of crack ignition for the interface
u_{cu}	Masonry ultimate displacement under compression
u_{tu}	Masonry ultimate displacement under tension
V	Shear force applied on masonry
V_y	Masonry pier yielding shear force
x_i	Coordinate of the node i owing to the x axis
y_i	Coordinate of the node i owing to the y axis
z_i	Coordinate of the node i owing to the z axis

α	Parameter to take into account the cyclic damage in the DFM
α_0	Zero moment coefficient
α_{diag}	Angle of the diagonal element in the RMEM
α_V	Shear ratio for a masonry pier
β	Parameter used for the macro-element to reproduce the cyclic shear behavior of masonry
$\beta_{c,t,d}$	Parameter to control the shape of the unloading/reloading behavior of the elements of the RMEM
γ	Parameter to account for plasticity in the hysteretic behavior of the DFM
γ_1	Reduction coefficient of vertical axial compression
δ	Masonry displacement under shear solicitation
δ_{eff}	Effective separation at the interface at failure
δ_i	Displacement at the interface in the direction i
δ_{int}	Displacement at the interface
Δu_n	Differential displacement at the interface in the normal direction
Δu_t	Differential displacement at the interface in the tangential direction
λ	Width of the area of influence of the spring for the RMEM
λ_t	Thickness of the area of influence of the spring for the RMEM
θ_i	Angle of the diagonal strut of the DFM element i with the horizontal axis
σ_m	Compressive stress acting on a surface of the RMEM
σ_n	Stress at the interface in the normal direction
σ_v	Vertical stress applied on the macro-element
η_a	Coefficient for allocating the vertical compression
η_j	Strength ratio of head joint compared to bed-joint
ν_j	Poisson's ratio of joint/mortar
ν_m	Poisson's ratio of masonry
ν_r	Poisson's ratio of reinforcement
μ	Friction coefficient of the masonry
$\bar{\mu}$	New definition of the friction coefficient of the masonry proposed by Mann and Muller [8]
φ_{int}	Empirical parameter to capture crack propagation from masonry to bands
Ψ_k^i	Shape function at the node i for the k^{th} degree of freedom of the RMEM
ρ_m	Masonry density
ρ_r	Reinforcement density
τ	Shear stress
τ_b	Pier strength in relation to the failure of a brick
τ_{cs}	Pier strength in relation to the failure of a bed joint
τ_{ws}	Pier strength in relation to the diagonal cracking failure

Abbreviations

CM	Confined Masonry
DEM	Discrete Element Method
DFM	Deformable Frame Model (model introduced in this thesis)
EFM	Equivalent Frame Model (model used in the Tremuri software [10])
F.E.	Finite Element
FIM	Frames Infilled with Masonry
IP	In-Plane
MFE	Macro Frame Element
NLDA	Non Linear Dynamic Analysis
NSA	Non Linear Static Analysis
or	
NLSA	
OOP	Out-of-plane
RM	Reinforced Masonry
RMEM	Rigid Macro-Element Model (model initially proposed by Calìo et al. [2])
RVE	Representative Volume Equivalent
SAM	Simplified Analysis of Masonry building
UCM	Unconfined Masonry
URM	Unreinforced Masonry
XFEM	Extended Finite Element Method

Introduction

Context

Masonry constructions represent a majority of existing structures. They can be very old buildings, such as castles, churches or temples, or recent constructions. This longevity of the use of masonry can be explained by several reasons. The principal ones are the low cost of masonry construction and the ease to get the materials. Moreover, masonry has the advantage to be a simple way of construction compared to other materials such as steel or concrete.



Figure 5: Masonry structure with seismic bands in Nepal

Masonry has a weak tensile strength that leads to a crack propagation even under low solicitation. This proneness to cracking is responsible of the collapse of several masonry buildings during earthquake events in both developing countries and developed countries [11, 12]. Subsequently to these dramatic events, in people’s belief, masonry structures cannot undergo seismic solicitations. This belief is not totally justified since for centuries people living in regions with a high seismic hazard found solutions to improve the anti-seismic capacities of masonry constructions and to limit the risk of collapse. One of these solutions consists in adding horizontal bands, generally made in wood or reinforced concrete, in the structure. These bands can be encountered in the literature with different designations such as ring beams, seismic bands, bond or collar beams [13]. An example of a construction made with horizontal bands is shown in Figure 5.

Motivations of the research

The aseismic capacities of horizontal bands are well known. Therefore, several design catalogs and guidelines for masonry structures propose to use them (Nepal [14], India [15], UNESCO [16]). The benefits of the bands are numerous:

- They confine the masonry.
- They improve the connection of two perpendicular walls and give a box behavior to the structure.
- They divide masonry in independent parts. Thus, safe masonry parts are separated from damaged parts.
- They limit the crack propagation. When a crack spreads in a wall, it cannot go further than the band.
- They increase energy dissipation. Once the crack reaches a band, it spreads along it, causing sliding at the band/masonry interface and energy dissipation.

After the earthquakes that occurred in Nepal in 1988, the Nepalese government decided to add some specificity for aseismic constructions in the building codes [17]. These codes ¹ have been released during the year 1994 [19] and are inspired by the ones in India [17]. These codes propose the insertion of horizontal bands in masonry structures to improve their seismic resistance. Yet, there is not any mention of the limits of this technique. There is not any consideration of the level of the seismic hazard, of the importance of the buildings or about the soil characteristics. Thus, the rules for the use of this architectural strategy are blur.

The last guidelines and designs catalogs proposing the use of horizontal bands were released after the earthquakes that occurred in the region of Kathmandu on the 25th of April 2015 and on the 12th of May 2015 [14, 20]. These catalogs contain several explanations to make useful horizontal bands and where to place them in the structure. Compared to the previous Nepalese building code [19], the new one proposes to use more horizontal bands. A limitation of these

¹They are called code but they do not have any legal status making their use not compulsory [18]

guidelines and codes is the lack of consideration of the level of seismic hazard and an expected working life of the structure for the prescribed designs. That statement is not true for the Pakistani building code [21] on which there are some additional recommendation for important structures but it is limited to the use of vertical reinforcements at the corners.

Objectives of the thesis

A numerical model is proposed in this thesis for the validation and the optimization of the design of masonry structures with horizontal bands regarding the last regulations and codes. That double objective can be achieved if the numerical model meets some requirements:

- To make a differentiation of all the elements in the masonry structure. Every element has to modeled separately from the others to correctly reproduce their localization in the construction.
- To have a short computational time so that it is possible to study different designs in a reasonable time.
- To be simple of use so that the model can be used by any person willing to model masonry structures with bands.
- To predict the behavior of masonry structures.

The objective related to computation time can be fulfilled only with macro-elements and meso-elements. In order to have a better control on the modeling and the creation of the numerical model, a new meso-element to model masonry, the Deformable Frame Model (DFM), is proposed. This meso-element is defined for finite elements (FE) resolution and can reproduce cyclic shear behavior and OOP bending of unreinforced masonry portions. Since masonry is not the only element modeled, the DFM is defined to allow a straightforward connection with additional elements.

Outline of the thesis

The process to achieve the objectives of this research is divided into three parts. **Part I** deals with the literature review. **Chapter 1** defines the basic vocabulary related to masonry construction. The different types of masonry structures are identified and the typical modes of failures are explained. **Chapter 2** focuses on masonry structures with horizontal bands. Different typologies of structures are described, as well as the different forms of horizontal bands. The aim is to learn about the structures within the scope of this thesis and to know what has been experimentally observed in masonry structures with bands. It allows the identification of the different elements that have been modeled and the definition of a meso-scale specific to this type of structures.

Chapter 3 introduces the categories of numerical models and explains why the meso-models are the most pertinent modeling strategy to achieve the objectives of this thesis. The meso-model considered the most relevant to the context of this thesis is examined in detail for modeling masonry at the identified scale. The advantages and disadvantages of the model are highlighted and an explanation is given as to why the decision was made to create a new numerical model.

Part II focuses on the development of the numerical model for masonry structures. A new meso-model, the Deformable Frame Model (DFM), is presented in **Chapter 4** for 2D modeling. It is inspired by the model analyzed in the previous chapter. Since the DFM is only used to model masonry, **Chapter 5** deals with the modeling of the bands with an innovative interface model and the modeling of reinforcements. **Chapter 6** extends the application of the DFM to 3D modeling and dynamic analysis. It explains how the OOP behavior is reproduced by the DFM and how the model's mass matrix of is created.

Part III focuses on the validation of the proposed numerical model. The model is implemented in ATL4S, a FE toolbox on Matlab designed by Grange [22] for all the numerical analysis in this thesis. **Chapter 7** shows the modal analysis of several structures using the DFM. A comparison is made between the results of the DFM and the results of FE models on the Castem software [23]. That study is used to check the elastic properties of the model as well as the definition of the mass matrix. The following step is to validate the inelastic constitutive laws. That verification is done in **Chapter 8** where the proposed model is used to model experimental tests at the scale of the wall. **Chapter 9** shows the results with the proposed model for the modeling of shaking table tests on three reduced scale houses. Some of the samples were made with horizontal bands.

A final part summarizes the work presented in this manuscript. It concludes about the proposed numerical modeling in relation to the set objectives and discusses avenues of research with the DFM.

Part I

General presentation

This first part of the thesis aims to set the context of the study of masonry constructions with bands and the numerical models that can be used.

Chapter 1 gives knowledge about masonry. It tackles the basic vocabulary, the principal type of structures and the modes of failure for in-plane (IP) and OOP loading.

Chapter 2 focuses on masonry structures with bands. It presents different typologies that can be encountered around the world and the prescribed dispositions in building codes. It aims to set the limits of the study.

Chapter 3 tackles numerical modeling of masonry structures. It gives an overview of the different commonly used methods and enables to select a relevant model regarding the objectives of the thesis. This modeled is analyzed in details to know how well it can perform for modeling masonry structures with bands.

Chapter 1

Knowledge about masonry structures

1.1 Basic vocabulary

The word **masonry** covers a large sample group of building methods. It denotes constructions made of bricks and joints, but it can also designate construction made of stones alone. Therefore, the common name for the largest element is not brick but **block** or **unit** since it can be attributed to any type of constituent. In addition to blocks, it is common to have **joints**. A masonry structure made without joints is called dry masonry. The layout of the blocks in a wall, often called **brickwork**, is very important not only for the visual aspect but for the mechanical aspect as well (more details in Section 3.1.2.3). The common brickworks are shown in Figure 1.1.

Masonry can be made of concrete, terra cotta, adobe, stone, and so on... These constituents have mechanical properties that can widely vary and exhibit a nonlinear behavior under low solicitations. This results in a global behavior that can be difficult to predict. Zucchini and Lourenço [24] and Casolo [25], among others, brought that the ratio of Young modulus of the units and the joints plays a role in the global behavior of a wall to light. Therefore, in order to correctly model masonry, it is necessary not only to determine the mechanical properties of blocks and joints but also to study the differential deformations between them. As an example, under vertical compression, for two units separated by a horizontal joint, tensile failure may occur due to the difference of deformations of the two blocks and the joints [26].

Joints behave differently depending on their orientation because of the confinement to which they are subjected and their role in the transmission of forces. Therefore, it is possible to find the designation **bed-joint** for horizontal joints and **head-joint** for vertical joints. Some articles, like the ones of Zucchini and Lourenço [24, 27, 26], make a deeper distinction by considering **cross-joints** at the junction of the bed-joints and the head-joints.

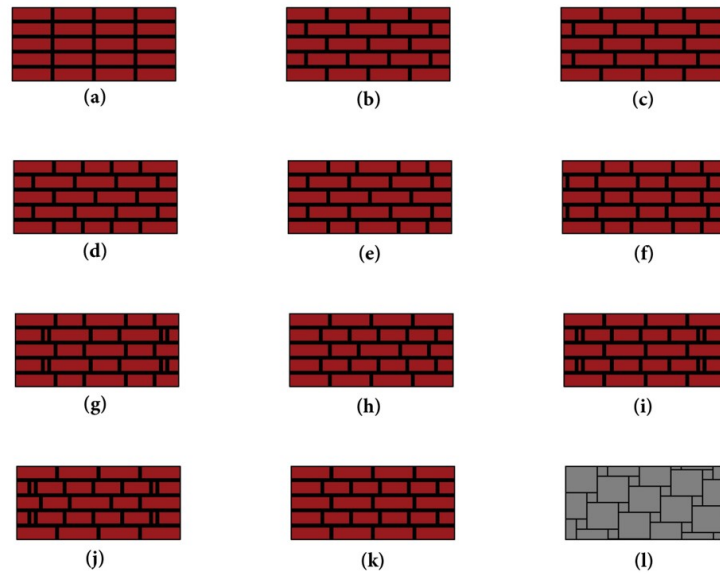


Figure 1.1: Common brickworks: (a) Stack bond ; (b) Running bond; (c) Running bond 1/3; (d) Common bond (course headers); (e) Common bond (Flemish header); (f) Flemish bond (Dutch corner); (g) Flemish bond (English corner); (h) English bond (Dutch corner); (i) English bond (English corner); (j) English cross or Dutch bond (English corner); (k) English cross or Dutch bond (Dutch bond); (l) Interlocking masonry

1.2 Categories of masonry constructions

As mentioned earlier, masonry constructions represent a large amount of constructions. The most common type of construction is when masonry is the only used material. This kind of construction is commonly called **UnReinforced Masonry (URM)** structure. Through the years, the methods of construction have evolved and have been adapted to meet with environmental and societal situations. That is why it is common in several countries to find masonry constructions with some reinforcements. We talk then about **Reinforced Masonry (RM)** structures. This reinforcement can affect the strength of the structure as well as their ductility, the energy dissipation, etc... The use of horizontal band is a reinforcing method. An other strategy to improve the performance of masonry is to confine it with frames, most commonly RC frames or steel frames. We then talk about **Confined Masonry (CM)** structure. (See Chapter 2 for the discussion related to the category of structure for constructions with bands)

The CM structures can be mistaken for **Frames Infilled with Masonry (FIM)** for which masonry is not the load bearing material. The frames for FIM structures can be made of wood [28], steel [29] or reinforced concrete (RC) [30]. Reinforced masonry building and frames infilled with masonry can look alike when RC is used (see Figure 1.2). Yet, it is possible to distinct them by knowing their specific features. First of all, RC elements for CM are smaller than RC elements for FIM. Moreover, for CM structures, the RC frames do not follow a pattern in the

structure unlike for FIM (see Figure 1.2). Another way to identify CM structures is the use of beams and columns around the openings.

The way of construction is different as well. Masonry walls are built first and the frames are built later on for CM structures. For FIM structures, the process is reversed. The frames are built first and masonry infill afterwards.



Figure 1.2: Examples of: (a) RC FIM structure (from [31]; (b) RC CM structure (from taxonomy.openquake.org)

The consideration of the type of structure is very important for the use of a numerical model. Indeed, some models are specially created for a given type a structure, the Equivalent Strut Model (ESM) for FIM for example.

1.3 IP behavior of masonry

1.3.1 Modes of failure

Figure 1.3, taken from Pantó et al. [32], shows the different modes of failure that can occur in masonry under IP loading. These modes of failure are:

- a) **The rocking failure** is the consequence of the bending behavior of the wall. Bending leads to the failure of joint in tension at the top and the bottom of the wall. It is more likely to occur for slender walls.
- b) **The toe crushing failure** occurs when the vertical compression is too high in the masonry wall and damage both the bricks and the joints. It can happen when the wall is bending as well. Its occurrence depends on the boundary conditions of the wall since the rocking failure can happen before. Depending on the characteristics of the material, bricks can break in compression or tension.

- c) **The diagonal crack failure** is the failure of joints under shear. The cracks propagate not only along the bed joints but through the head joint as well.
- d) **The shear/sliding failure** is the failure of the bed joints under shear. In this case, only the bed joint is affected. The occurrence of shear/sliding failure or of diagonal crack failure depends on the vertical stress and the shape ratio of the wall.

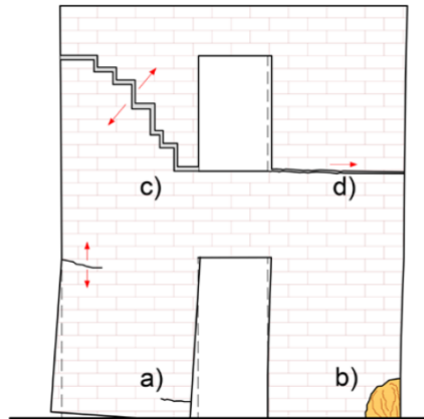


Figure 1.3: Modes of failure for URM buildings: (a) Cracks due to rocking; (b) Cracks due to toe crushing; (c) Diagonal cracks; (d) Crack due to shear-sliding failure

These four failure modes cannot occur in any type of masonry structure. Indeed, some configurations are prone to certain failures and limit the occurrence of others. For example, in FIM structures, the deformation of the frame leads to a compression strut in the diagonal of the infill (see Figure 1.4, taken from Combesure [33]). That particular loading can cause cracks at the corners or at the center of the masonry panel due to a too high compression (see Figure 1.5). However, because of the geometry of the panel and the load applied on the masonry, it is unlikely to have a rocking failure or a toe crushing failure for FIM structures.

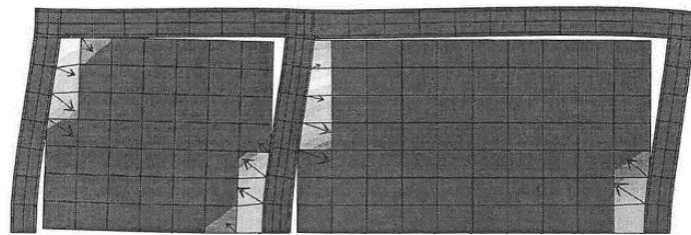


Figure 1.4: Modeling of the deformation of a RC FIM [33]

In the case of structures with bands, the effective height of the wall is reduced. It decreases the risk of rocking failure of the masonry since, if the structure is well designed, the connection between the masonry and the band breaks before the masonry is damaged. For these structures, another type of failure can occur: the failure of the interface between masonry and bands. That

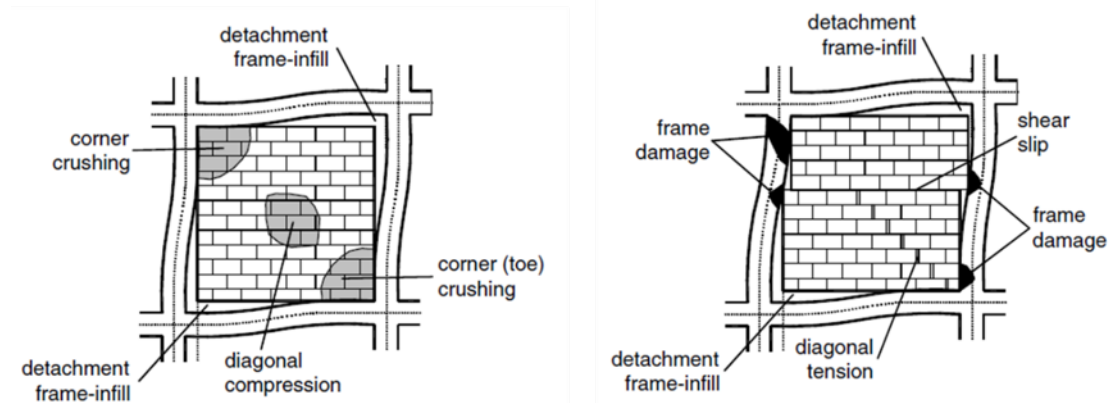


Figure 1.5: Modes of failure for masonry infill frames [34]

failure is complex. It can occur because the joint at this spot breaks because of the shear solicitation but it can occur because of cracks propagation as well.

1.3.2 IP cyclic behavior

The behavior of the walls loaded in their plane during an earthquake defines the behavior of the complete structure. Thus, the numerical model has to be able to reproduce their behavior. The experimental tests by Anthoine et al. [5] are used to analyze how the cyclic behavior of masonry looks like. These experimental tests consist in quasi-static cyclic tests on two different walls. The "small" wall is $100 \times 135 \times 25 \text{ cm}^3$ ($L \times H \times T$) big and the "high" wall is $100 \times 200 \times 25 \text{ cm}^3$ big. The boundary conditions and the vertical loading are the same for both wall. More details on the experimental tests are given in Section 8.1.1.

Figure 1.6 taken from the article by Anthoine et al. [5] shows the results of the experimental campaign. It can be seen on the sketches of the walls that they have different patterns of failure. The small wall has a diagonal shear failure while the high wall exhibits the start of a rocking failure. The envelope curves are quite different as well. The small wall has a brittle behavior with a cyclic damage while the high wall has a softening behavior. It can be concluded that the pre-peak behavior depends on the geometrical characteristics of the wall and on the vertical loading. As for the post-peak behavior, it seems to depend on the failure mode.

In order to lead the high wall to failure, a higher vertical stress is applied on the wall and another cyclic test is performed. The results of this second test are shown in Figure 1.7. The increase of the vertical stress leads to a different type of failure. While the first test resulted in a rocking failure, the second one ended with a diagonal shear failure. This test shows that a higher wall needs a higher compression stress to have a diagonal failure and that the vertical stress limits the effect of rocking. Like for the small wall, the high wall has a brittle post-peak behavior. It can be considered that this pattern for the cyclic curve of the wall is related to the

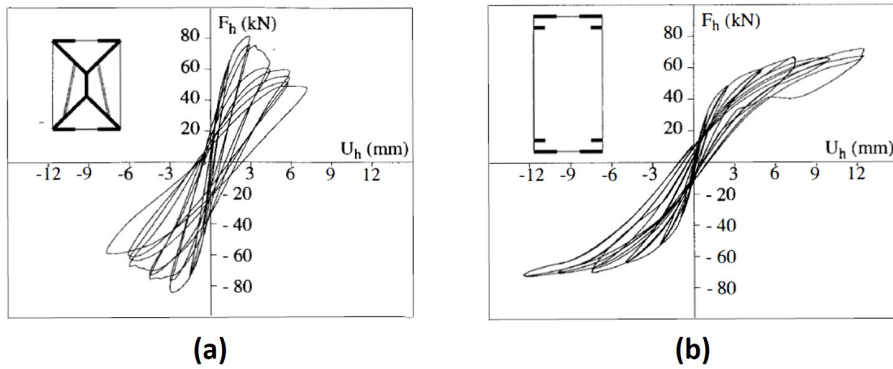


Figure 1.6: Shear cyclic behavior: (a) Small wall; (b) High wall

diagonal failure.

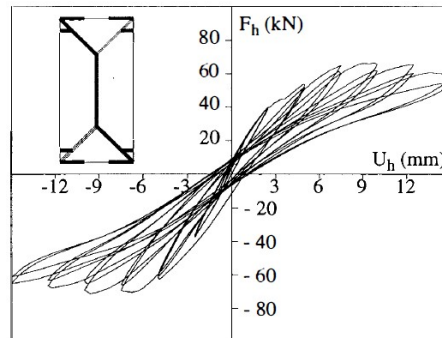


Figure 1.7: Cyclic behavior of the high wall under a higher vertical stress

The high wall exhibits an unloading/reloading behavior in three steps. The unloading starts with a quick loss of strength. Afterwards, the wall has low rigidity on a range of displacements that depends on the historic of loading. When one approaches the maximal displacement reached historically in the other direction of solicitation, the wall regains rigidity. This behavior can be explained by what is happening in the wall during this unloading/reloading. When the unloading of the wall starts, the change of direction leads to a fast rearrangement of the elements and the opened cracks close. Once the wall starts being loaded in the other direction, cracks that opened because of a solicitation in this direction before get reopen. Since it is already existing cracks, the wall does not exhibit a high resistance. At some point, the imposed displacement is high enough to have in the same time the reopening of the existing cracks and the solicitation of the still undamaged parts. These parts can get damaged before that the maximal reached displacement is reached again. That is why the experimental curves exhibits a stair shape: additional cracks have been created for the same imposed displacement.

1.4 OOP behavior of masonry

For a uni-axial loading, it is usually considered that the contribution of the OOP loaded walls to the global strength of structures is negligible and that the global building response is mainly governed by IP damage. Therefore, these walls do not have an important impact on the seismic behavior of the structures aside from inertial forces related to their mass. Yet, these walls collapse because of bending (Figures 1.8.(a-b)) for URM constructions. That bending is directly related to the geometry of the wall. Higher the wall is, higher the chance of toppling.

The length of the wall influences the cracking pattern and the resulting failure. For long walls, a horizontal crack appears at a certain height in the wall coupled with vertical cracks. These cracks result in the collapse of the upper part of the wall but they seldom result to the collapse of the entire wall (Figure 1.8.(a)). For small walls, diagonal cracks appear and the connection with the perpendicular walls are damaged. If the connection of perpendicular walls is not correctly made or too damaged, the walls untie and the OOP solicited wall collapses (Figure 1.8.(b)). The failure of small wall is more critical for the sake of the construction compared to the failure of long walls. However, under a same OOP solicitation, the bending is less important for a small wall than for a long wall. Thus, the small wall is more likely to remain safe.

It is possible, as well, that the OOP failure occurs at the corner of the wall (Figure 1.8.(c)). This type of failure is less common than the one related to bending. They are more likely to occur when the house is affected by torsion and for multi-story constructions.

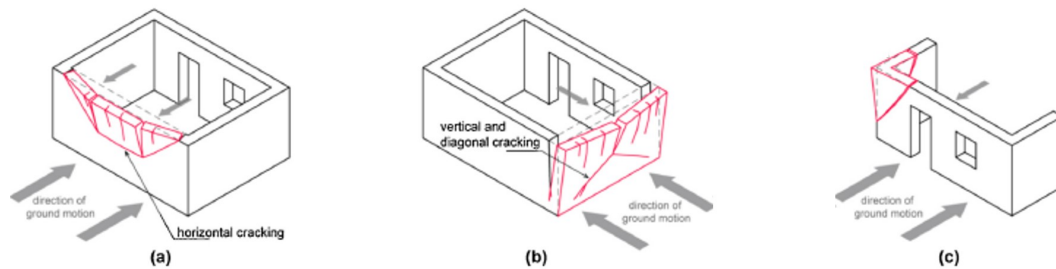


Figure 1.8: The OOP failures of URM structures: (a) for long walls; (b) for short walls; (c) at the corners (taken from Ortega et al. [13])

The risk of failure under OOP loading can be reduced by paying attention to the geometry of the wall and the connection between the walls. The use of bands has an influence on both aspects. It divides the walls in several parts and, therefore, it reduces their effective heights and the OOP deformation accordingly. Moreover, the bands can improve the connection between two perpendicular walls. These aspects will be shown in the following chapter.

1.5 Conclusion

This chapter gave some elementary knowledge about masonry. It is generally made of two constituents: bricks and joints. Both constituents have a weak tensile strength and can have elastic properties quite different. This leads to a non-linear behavior that is difficult to predict.

For IP loading, four different modes of failure have been identified: diagonal cracking, shear-sliding failure, rocking failure and crushing toe failure. Usually, cracks first occur in joints and propagate along them. Since there are several possible layouts, the crack pattern can differ from a construction to another. The failure of the wall is governed by the vertical loading, the geometry of the wall and the mechanical properties of masonry. Under cyclic IP loading, masonry has a hysteretic behavior. The shape of the hysteresis depends on the failure that occurs. These features related IP loading have to be reproduced as best as possible by the numerical model since they affect the global behavior of the structure for seismic solicitations.

OOP loaded walls are not of first importance for the behavior of the complete structure during an earthquake. Their contribution to the global strength of the structure is negligible. So is their contribution to the energy dissipation. However, these walls can collapse and this can affect the viability of the structure. Thus, if the taking into consideration of the cyclic behavior of masonry under OOP loading does not appear as essential, the numerical model has to reproduce, at least, the bending behavior of the wall in that direction.

In conclusion, the characteristics of masonry that the model has to take into account have been identified. Next chapter focuses on masonry constructions made with horizontal bands. It tackles the different typologies that can be encountered and experimental studies made for masonry with bands. That chapter sets the limits regarding the type of structures in the scope of the thesis and aims to give information for the modeling of a complete structures by identifying all the elements and their behavior.

Chapter 2

Masonry structures with bands

2.1 Introduction

The use of horizontal bands in masonry structures is an ancient aseismic method. The oldest known structures using this type of architectural strategy are from the region of Turkey and Anatolia. They were built about 9000 years ago [35]. The use of wooden horizontal bands was noted in the Palace of Knossos (1450 BC), in the Small Temple of Aton in Egypt (1350 BC) and also in Mohenro Daro in Pakistan [36]. Since then, the use of wood in masonry construction spread to surrounding areas and was developed in Mediterranean and Himalayan countries. The aim of this chapter is to list the different typologies and to highlight their architectural principles, especially in relation to the localization of the bands and the way they are made. The aim is to clearly identify the type of structures that fall within the scope of the thesis and the ones that do not.

In Chapter 1, it was announced that confusion is possible between CM structures with RC beams and columns and RC FIM structures. In fact, this is not the only possible confusion. Indeed, confusion can be made between masonry structures with horizontal bands and wood FIM structures. In the second category, the wood frame is the load bearing element of the structure. Therefore, in this case, the attention is more on the modeling of the frame than on the masonry itself [28]. A way to identify wooden FIM is the use of timber elements to enhance the shear strength of walls (braces, St Andrew's cross, ...). Moreover, timber frame in FIM can be self-sufficient. Figure 2.1.(e) shows an example of house where the first story is a RM construction while the second story is a wooden FIM structure.

2.2 Typologies

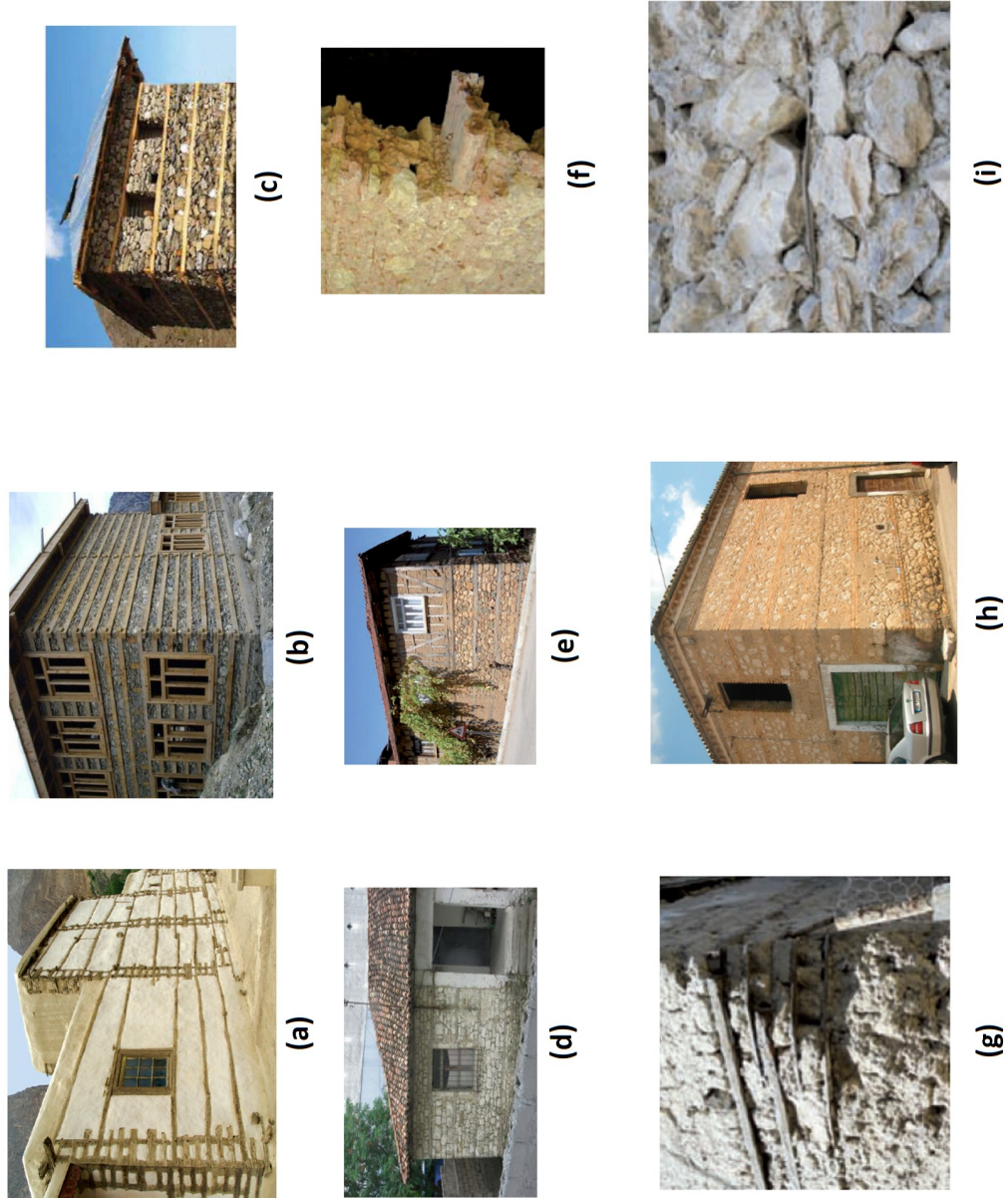


Figure 2.1: Examples of masonry structures with bands: (a) *Cator and cribbage* constructions [37]; (b) typical houses of the Nuristan region in Afghanistan (from wordpress website); (c) *Baithar* type construction in Pakistan [38]; (d) *Hatil* type of house in Albania [39]; (e) *Narilica* type construction [36]; (f) wood logs in *Casbah* type construction [40]; (g) wood planks as corner reinforcement [36]; (h) brick band in Italian construction [41]; (i) thin wood band [36]

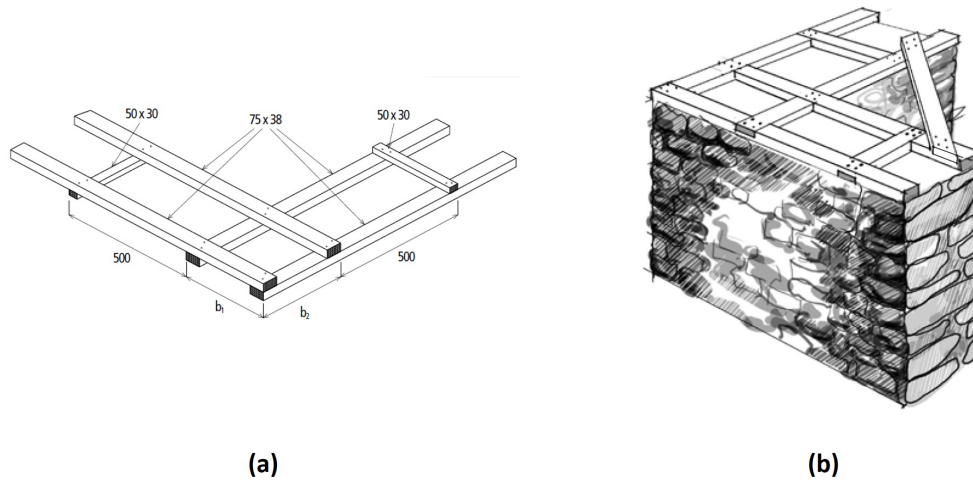


Figure 2.2: Possible designs for wooden bands

There are several options for positioning the bands, as shown in Figure 2.1. Typologies may vary from country to country but some similarities can be identified. The main factors affecting the choice of a typology are the materials available in the region and the environmental hazards to which the region is affected. However, it is possible to find architectures in some places where bands only have an aesthetic function.

Wooden bands can be made in a number of ways. The most common wood band in masonry structures consists in two wooden brackets placed along the wall. They are connected together by small wood ties. These ties are used to reinforce the bands and improve the connection between two perpendicular walls (see Figure 2.2). This type of bands can be encountered in Pakistan, Turkey, Greece, India, Macedonia and Nepal. This type of bands can be used in a limited part of the house (see Fig. 2.1.(e)), commonly for the foundations and the ground level, or for the totality of the structure (see Fig. 2.1.(b)). Generally, these bands are separated by a distance of 50 cm to 90 cm in the height of the wall (see Fig. 2.1.(c-e)). This type of bands can be encountered in masonry structures made of any type of material.

It is possible to find structures where the bands are wooden planks. The thickness of these planks can vary from 2 mm (Fig. 2.1.(g)) to 5 cm (Fig. 2.1.(i)). These bands have the advantage to make a complete separation of two masonry portions, while the bands presented earlier may have units between the two brackets. It ensures that cracks do not spread from one part to another. The role and the localization in the structure of the planks are related to their thickness. Compared to the typology seen earlier for the bands, the positioning of the plank bands can be more random. For example, wooden planks can be used at the junctions of walls as local reinforcement or at specific locations. There can be only one plank or several planks closely spaced as shown in Figure 2.1.(d)). In Algeria and Syria, wooden bands may be found made with logs (see Fig. 2.1.(f)) [42]. Their positioning in the structure is similar to that of plank bands.

As shown in Figure 2.1.(b), in some countries of the Himalayan Belt, wood bands can be set alternatively with stones in a structure. In this type of structure, the bands of two perpendicular walls are superposed. A layer of stone is added above the upper band before a new band is added. This typology can be found in *kath-khuni/koti-banal* construction type [36].

In addition to the bands, it is possible to have vertical reinforcements at the corners like shown in Figure 2.1.(a). The *Cator and cribbage* constructions in Pakistan are the most known examples for this kind of structure. In Figure 2.1.(a), some wood bands are all along the walls and are separated by approximately the same distance. At the corners, wood vertical reinforcements with small wood horizontal inclusions to make the corner even stiffer are used. These small wooden inclusions are placed on top of each other. This type of structure is a mix of wood frames structures and masonry structures. Similar constructions can be found in Nepal, Tibet and Syria.

Wood is not the only possible material for the bands. Bands can be made of brick as shown in Figure 2.1.(h). These bands are inserted into masonry at regular intervals and can play the role of lintels and chaining. The spacing between two bands is the same for a given construction but it may vary from one building to another, as in the case of wood bands. In recent masonry constructions, RC is used for the bands. The typology of constructions with these bands is described further.

Table 2.1 indicates what type of constructions the cases in Figure 2.1 are with some explanations. This helps to understand better these categories. The cases d, f and h in Figure 2.1 can be actually in two categories. In this figure, there are not visible vertical reinforcements and the type of structures indicated in Table 2.1 consequently. If there are actually vertical reinforcements, all these cases can be considered as CM structures.

Table 2.1: Determination of the type of masonry construction for the cases in Figure 2.1

Case	Elements other than masonry	Category
(a)	Vertical reinforcements at the corners, horizontal bands spaced by tens of centimeters, reinforcements at the openings	CM
(b)	Horizontal bands spaced by some centimeters, reinforcements at the openings	CM
(c-d)	Horizontal bands spaced by tens of centimeters	RM
Bottom of (e)	Horizontal bands spaced by tens of centimeters	RM
Top of (e)	Wood frame with masonry infill	FIM
(f)	Horizontal bands spaced by tens of centimeters	RM
(g)	Local reinforcements at the corners	RM
(h)	Horizontal bands spaced by tens of centimeters	RM
(i)	Small reinforcements	RM

2.3 Prescribed positions for the bands

The last recommendations and guidelines masonry structures with bands were released in Nepal after the earthquakes of 2015 [14]. They are an improvement of the former guidelines and are inspired of guidelines in India [15]. These guidelines were accompanied by a design catalog followed two years later by a second volume [43, 44]. All the designs in the first catalog are masonry constructions with horizontal bands. These bands are whether wooden bands or RC bands. Masonry in this first design catalog are stone masonry with cement mortar, brick masonry with cement mortar, stone masonry with mud mortar and brick masonry with mud mortar. For each type of masonry, the catalog gives basic designs for one-story and two-story constructions with wooden bands or RC bands. The designs for masonry construction in the second catalog have RC bands only. The bamboo bands that are proposed in the building code 203 [20] are not proposed in any design of the catalogs.

Two designs of the first catalog [43] are used to show suggested arrangements of bands for one-story stone masonry houses in Figure 2.3. Similar arrangement is proposed for brick masonry. In the catalog, the choice of the material for the bands depends on the mortar. The RC bands are for cement mortar and the wooden bands are for mud mortar.

The two designs in Figure 2.3 have some similarities:

1. A band along the walls at the level of the floor
2. A band along the walls below the windows
3. A band along the walls above the windows and the doors

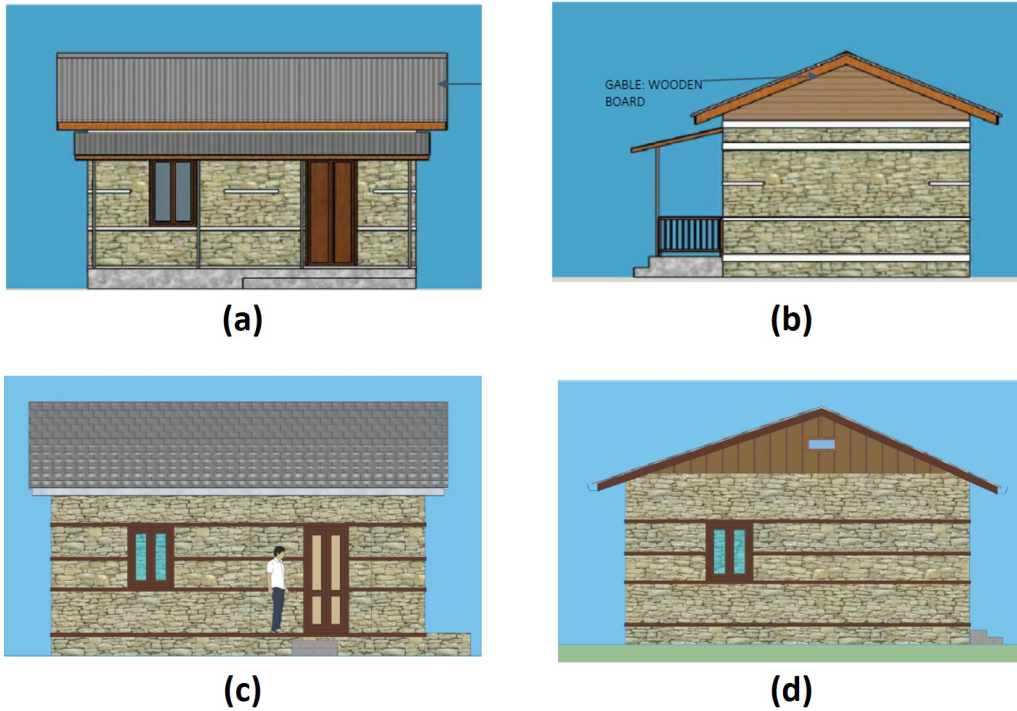


Figure 2.3: Proposed designs of masonry houses with bands: (a) front side of a house with RC bands; (b) right side of a house with RC bands; (c) front side of a house with wood bands; (d) right side of a house with wood bands

Despite these similarities, the two designs have some differences besides the mortar used for the construction:

1. The RC band does not run all along the walls when it is at the middle level of the opening, unlike the wooden bands. It is outside the scope of the study, but two-story structures with RC bands do not have this feature.
2. The thickness of RC bands depends on its position in the wall, unlike the wooden bands.
3. The design with RC bands has a roof band while the design with wooden bands does not have one.

It can be concluded with these two designs that the dimensions of the bands and their position depend on the material they are made of. Moreover, some spots for the bands are always the

same but some locations are related to the material of the bands. There is not any explanation of these differences of dispositions in the design catalog.

In the recommendations of UNESCO [16], it is recommended to use RC bands as plinth band, lintel band, roof band and gable band for masonry structures made of fired bricks, solid concrete blocks, hollow concrete or mortar blocks. It is also recommended to have RC vertical reinforcements at the corners. For masonry structures made of stone, it is possible to use wooden bands instead of RC bands but this solution remains the most recommended. For earthen structures, it is recommended to use a wooden band as lintel and at the level of the roof. Depending on the seismic risk of the area, UNESCO [16] recommends to add vertical reinforcements made of bamboo or cane.

In the building code of Pakistan [21], RC bands are recommended as lintel bands and roof bands. It is also recommended to have vertical reinforcements at the corners and reinforcements at the openings. The code allows the use of brick bands as well but it is not what is the most recommended.

2.4 The limitation of the study

The structures in the scope of the thesis are similar to the ones shown in Figures 2.3.(c) and 2.3.(d). They are either CM or RM structures. These structures have horizontal bands at specific locations in the wall. These bands are all along the walls. Thus, constructions such as the houses from the Nuristan region in Figure 2.1.(b) are out of the scope of the study. Structures such as the model with RC bands in Figures 2.3.(a) and 2.3.(b) that have bands that not extend along the entire length of the wall, are also outside the scope of this study.

Figure 2.4 taken from the first Nepalese design catalog [43] is an example of structure in the scope of the thesis. It represents all the elements that the numerical model has to take into account. These elements are the masonry, the bands, the wood frames at the openings and vertical reinforcement at the corners. The foundations are shown in Figure 2.4 but they will not be modeled. Walls are considered perfectly embedded into foundations. In the technical details of the Nepalese catalog [43], it is suggested that the roof is tied to the roof band. It enables the complete construction to act as one unit and to maintain the vertical load due to the roof uniformly distributed during a seismic solicitation. Moreover, roofs like the one in Figure 2.4 are very rigid. Thus, it is unlikely that the roofs undergo any damage during earthquakes and that they have a differential displacement compared to the masonry structure.

The masonry structure shown in Figure 2.4 is CM structure. The same house without vertical reinforcements at the corners, which is a RM structure, is also in the scope of the thesis. It allows to analyze the importance of the reinforcements and to know to what extent their properties play a role in the behavior of the structure.

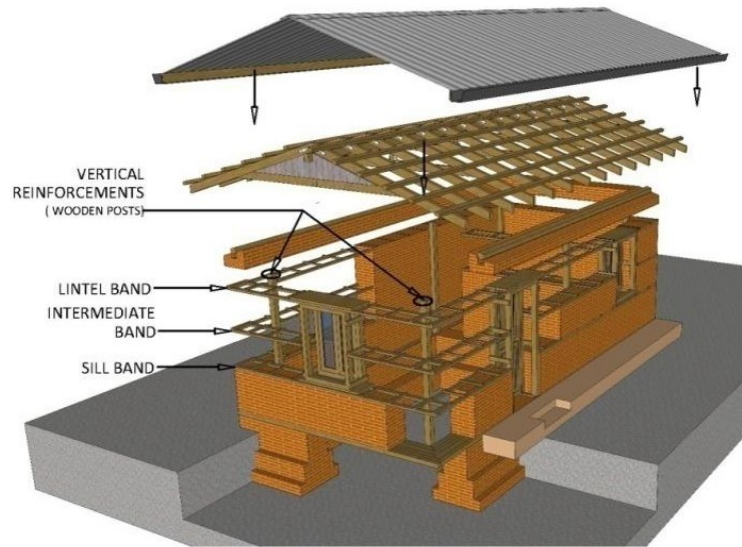


Figure 2.4: Example of structure in the scope of this study

2.5 Experimental studies on masonry with bands

The observations made during experimental tests are used to guide the modeling of the elements identified in Figure 2.4. Two different scales are identified for the study of masonry structures with bands: scale of the element and scale of the structure. The scale of the element ranges from the size of a few courses to the size of a complete wall. The discussion about the scale is the conclusion section of this chapter and in the following chapter.

2.5.1 Scale of the wall

Aranguren et al. [45] conducted an experimental study on two masonry walls: one URM wall (UW) and one wall with horizontal band (RW) (see Fig. 2.5.(a) and Fig. 2.5.(b)). Both walls have the same dimensions and are made with earth bricks and mud mortar. The aim of the campaign was to show the benefits of timber bands for the cyclic IP behavior of the wall. To achieve this, both walls were loaded with the same quasi-static cyclic displacement at their head. A vertical stress $\sigma_v = 0.2MPa$ was applied to the walls during all the experiment using hydraulic cylinders. The URM wall exhibited diagonal shear failure during the test (see Fig. 2.5.(c)). The wall with wooden band had the same failure initiation in the lower part of the wall. However, once the crack reached the timber band, it propagated along the timber band, instead of spreading to the upper part of the wall, which allowed sliding at the masonry/band interface. Therefore, the upper part of the wall remained undamaged in the second specimen, unlike for the URM which was completely damaged. The band does not undergo any damage during the cyclic test.

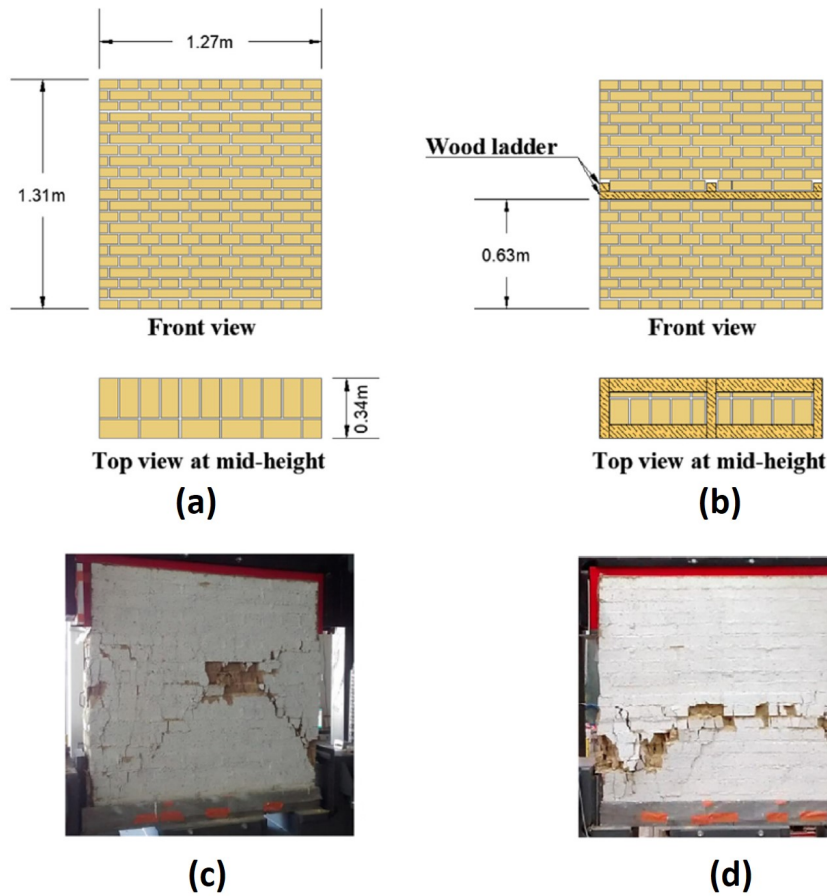


Figure 2.5: The two specimens for the cyclic tests [45]: (a) design of the URM wall; (b) design of the wall with wooden band; (c) failure pattern of the UW; (d) failure pattern of the RW

The benefits of the wood band for the strength of masonry are not obvious at the view of the envelope curve (see Fig. 2.6). In fact, the ultimate strength of the RW is approximately equal to that of the UW and it is difficult to say whether the difference in the values comes from the wood band or from the variability associated with the experimental process like the mechanical properties of the material. The initial stiffness of the walls is also the same. The post-peak behavior of the walls is the same in the pulling direction (negative displacement) but the UW specimen has a more brittle behavior than the RW specimen where the envelope curve has a plateau. The differences between the two samples is more significant for their hysteretic behavior. The loops of the RW specimen are wider than those of the UW specimen meaning that this wall dissipates more energy. This is confirmed by comparing the dissipated energy per cycle between the two walls (see Fig. 2.7). The dissipated energy E_{dis} is the area of the loops for each cycle and E_{inp} is the energy transferred to the wall to reach the imposed displacement. The rate of energy dissipation is more significant at the initial state for the RW wall and remains constant throughout the experiment. This shows the aseismic benefits of the band.

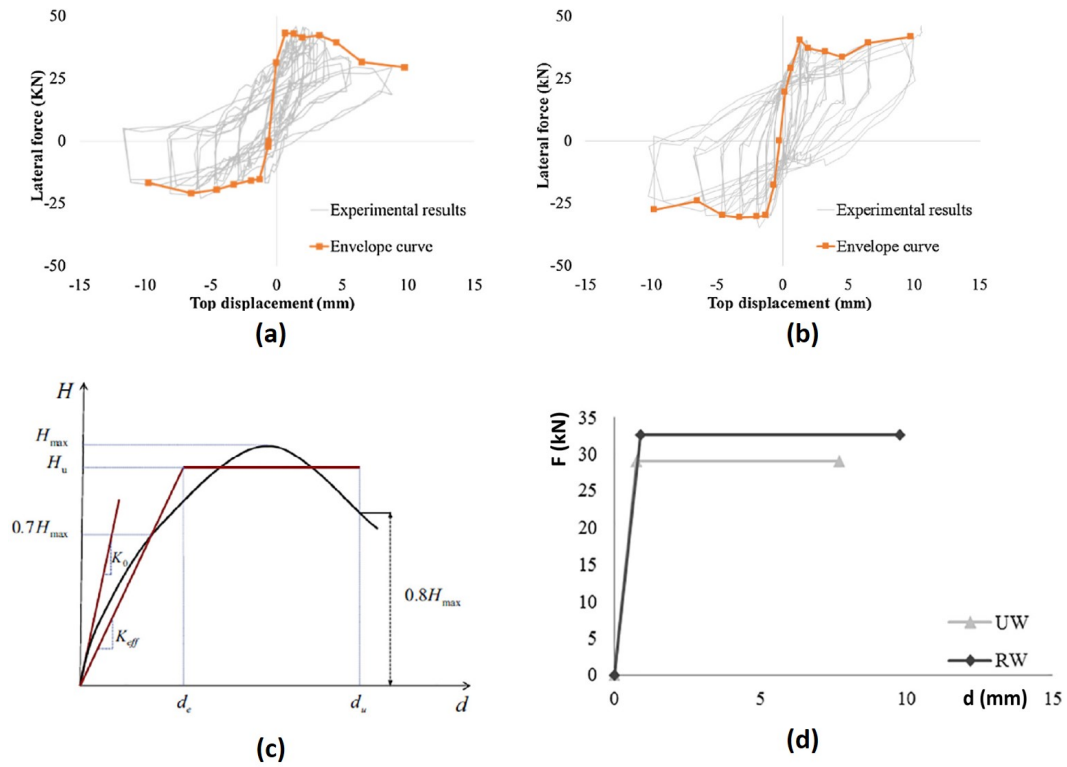


Figure 2.6: Results of the cyclic test: (a) cyclic behavior of UW (Envelope curve in orange); (b) cyclic behavior of RW (Envelope curve in orange); (c) bilinear idealization method for the envelope curve; (d) simplified envelope curves

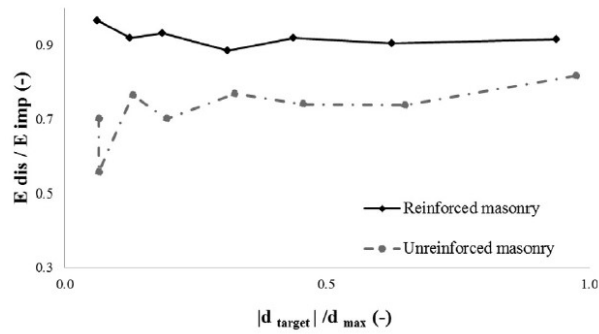


Figure 2.7: Energy dissipation rate for the UW and the RW specimens

First conclusions can be deduced from these tests: (i) the band limits the propagation of cracks into masonry parts and (ii) the dissipated energy under alternate loading is higher with a band due to friction between the band and the masonry.

To determine the benefits of bands for the OOP behavior, Spence and Coburn [46] tested four different walls with the apparatus shown in Figure 2.8. The four tested walls have the following configurations:

- Wall 1: Standard random-rubble stone wall with mud mortar. It is representative of constructions in villages in eastern Turkey.
- Wall 2: Standard random-rubble stone wall with mud mortar and a horizontal timber band.
- Wall 3: Random-rubble stone wall with cement mortar and RC band. This wall respects the Turkish Standards and are representative of schools and government institutions buildings.
- Wall 4: Cut and dressed stonework with cement mortar. It is representative of mosques and community buildings.

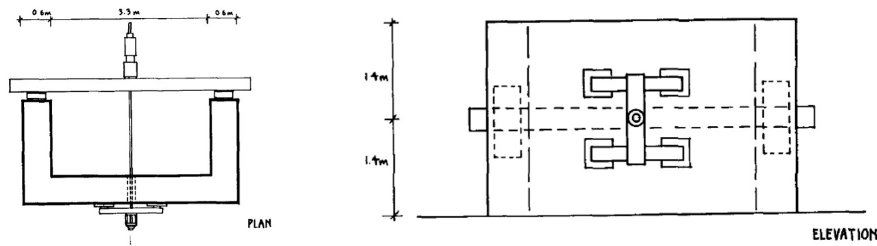


Figure 2.8: Apparatus used for the OOP test

Figure 2.9 shows that the use of bands gives important strength to the wall for an OOP loading. For Wall 1 and Wall 2, the ultimate displacement of the hydraulic cylinder was the limit of the test. For Wall 3, the hydraulic jack reached its maximum force in terms of effort (100 kN) without damaging the wall. It can be seen that the RC band gives a higher stiffness to the wall in the OOP direction than the wooden band. This increase in the stiffness of the wall was not measured during the IP test by Araguren et al. [45] leading to the assumption that this additional stiffness is related to the direction of the loading of the wall. The maximal strength of the wall is also greatly increased. It is five times higher with the wooden band and even higher with the RC band.

It can be concluded from these tests that the bands improve, as expected, the strength of masonry walls in the OOP direction. The stiffness of the wall is also enhanced. The benefits related to the band depends on the material it is made of.

2.5.2 Scale of the structure

Ali et al. [47] conducted an experimental campaign consisting of shake table tests of three reduced-scale rumbled stones houses named SM1, SM2 and SM3 (see Fig. 2.10). The first model, SM1, is representative of the typical public buildings in the northern areas of Pakistan. This house has only one roof band and no vertical reinforcement. The roof was made of RC and the walls are

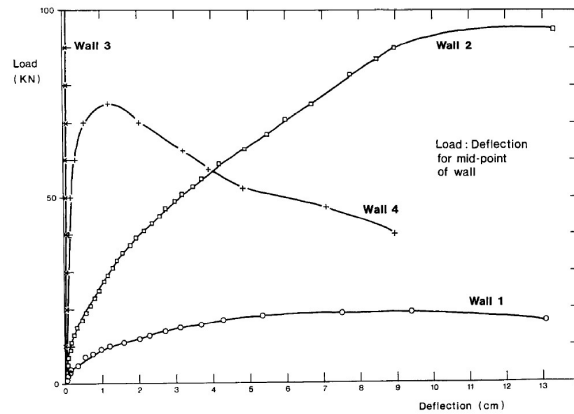


Figure 2.9: Force-Deflection behavior of the walls under OOP solicitation

150 mm thick. Model SM2 is representative of residential buildings of the same region. It has RC reinforcement at the corners and a wooden lintel band. Unlike the SM1 model, the roof is made of wood and the walls are 125 mm thick. The third model is an improvement of the SM2 model. This model has a RC band above and below the openings and at the roof level. There is also a RC frame at the door and wooden frames at the windows.

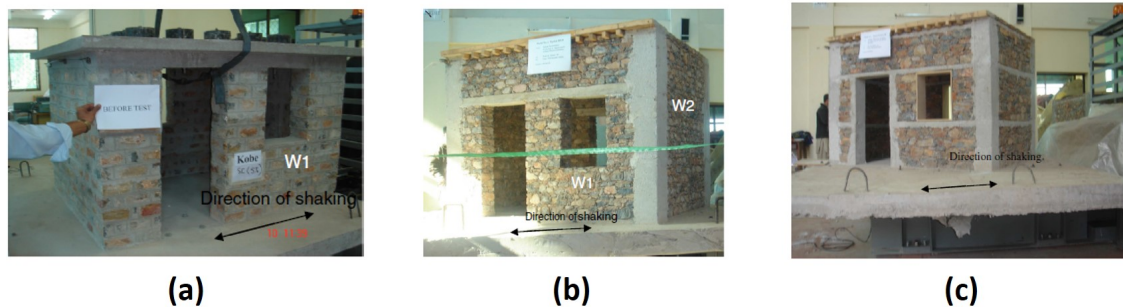


Figure 2.10: The three reduced scale houses [47]: (a) SM1; (b) SM2; (c) SM3

The three houses were tested with signals of increasing amplitudes of the Kobe and El-Centro earthquakes. Model SM1 is tested along its longitudinal axis while models SM2 and SM3 are tested along their diagonal. During the tests, the SM1 model collapsed completely due to the OOP bending combined with the weight of the roof, which was too large for the deformed walls. For the SM2 model, the walls without bands (W2 and W4) collapsed because of the OOP loading. Moreover, cracks spread in the masonry from the corners of the openings. These cracks lead to the collapse of the window wall W3. These various failures lead to complete failure of the structure. In the SM3 model, for the wall with the door (wall W1), the masonry part between the wooden band and the roof band collapsed. However, the walls that exhibited OOP failure for the SM2 specimen did not collapse. On the opposite side of the door wall, a crack developed in the masonry part above the window. This crack propagated along the bands and causes sliding. The crack patterns for the specimen are shown in Figure 2.11.

That study leads to the following conclusions:

- Vertical reinforcements are not enough to prevent the collapse of the structure.
- The use of horizontal bands limit the collapse of the walls subjected to OOP solicitations. It is consistent with the conclusions of the test by Spence and Coburn [46].
- The use of frames at the openings limits the propagation of cracks at the corners of the openings. It preserves the integrity of the walls.
- Bands preserve safe masonry parts from those which are damaged. Cracks propagate along the masonry/band interface and sliding occurs.

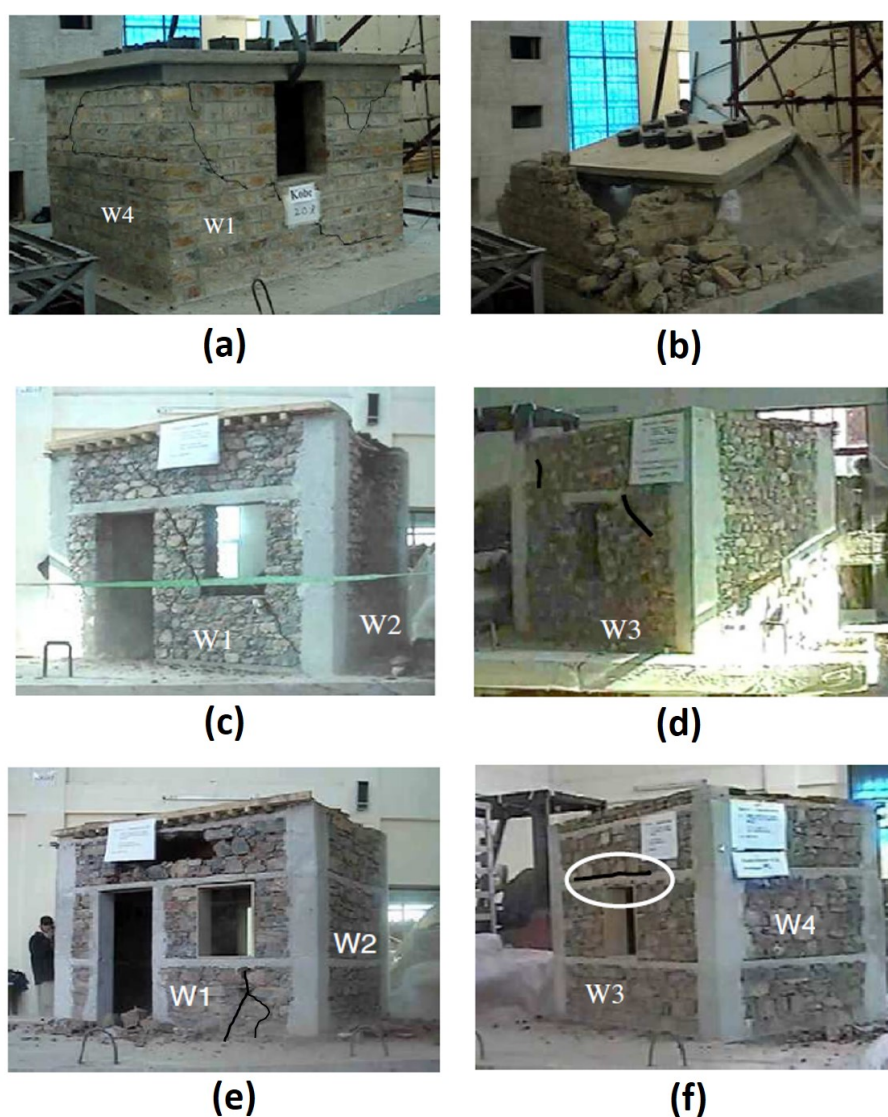


Figure 2.11: Damage of the three samples [47]: (a) crack pattern for SM1 specimen; (b) collapse of SM1 specimen; (c) diagonal cracks of Wall W1 and collapse of the upper part of the W2 wall of SM2; (d) cracks in the Walls W3 and W4 of SM2 specimen that spread and lead to the collapse of the house; (e) walls W1 and W2 of SM3 at the end of the test; (f) walls W3 and W4 of SM3 at the end of the test. The masonry/RC band interface for the upper band failed.

2.6 Conclusion

This chapter imparted some knowledge about masonry construction with bands. The aim was first to identify the type of architecture within the scope of the thesis. These are structures with bands placed at specific locations in the wall (roof band, lintel band and so on). These bands

are along the whole perimeter of the structure. Different materials can be used for the bands: wood, reinforced concrete, bricks or even bamboo.

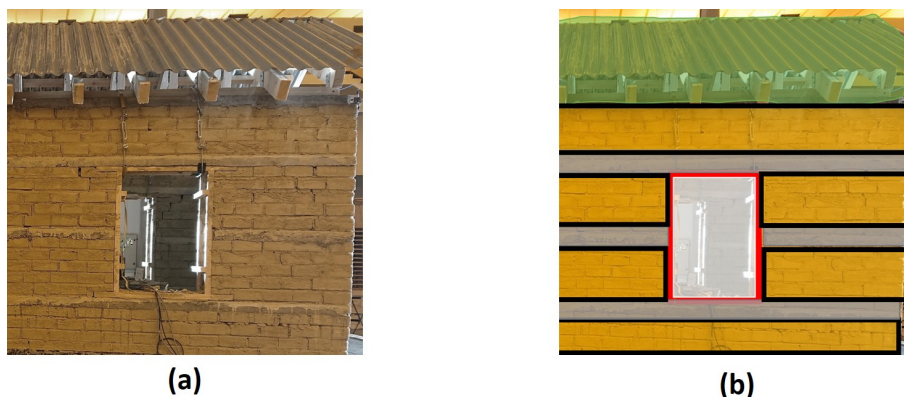


Figure 2.12: (a) Typical masonry wall that will be studied in this thesis and (b) its constitutive elements for the modeling [Masonry in yellow, opening in white, frames in red, bands in gray, roof in green]

Figure 2.12 shows the part of a house that will be studied in this thesis. The different elements to be modeled are marked with different colors. Masonry portions are colored yellow. These yellow parts are delimited by the sides of the walls, the openings (colored white in Figure 2.12.(b)) and the bands (colored gray). The red elements are the frames at the openings and the green element is the roof.

Thanks to the observations made during experimental test and to the guidelines, it is possible to choose how to model the different elements:

- Masonry (= yellow elements) modeled with an inelastic behavior for IP solicitations and elastic behavior of for OOP solicitations.
- Bands (= gray elements) modeled by interface elements reproducing sliding since that phenomenon was observed during experimental tests and because the bands have not been damaged.
- Frames (= red elements) at the opening, and potential vertical reinforcements at the corners, modeled by beams with an elastic behavior because the frames have not been damaged during the tests conducted by Ali et al. [47].
- Roof (= green element) modeled either by dead load at the head of the wall or by elastic beams.

Then, the most difficult element to model will be the masonry. Frames and roof will have a simple modeling. The interface models will depend on how the masonry is modeled. Therefore, the next chapter focuses on the possibilities for modeling the masonry.

Chapter 3

Modeling of masonry

The numerical model must allow the determination of the seismic behavior of masonry structures with or without horizontal bands. For this purpose, it has to **allow the modeling of all the components of these structures**. These different elements must interact with each other and be connected in a simple way. Therefore, the aim is to **avoid as much as possible the use of different modeling strategies**. The model should also have a **relatively short computation time**. For example, the target computation time for the dynamic analysis of a two-room house is a few hours (at most half a day) for a regular computer without any parallel computation.

In the context of the thesis, the models are classified in three categories: **micro-models, meso-models and macro-models**. This classification is related to the scale of the masonry block identified in the previous section (scale of the yellow parts in Figure 2.12). Micro-models aim to model the units and the joints composing the masonry. Meso-models aim to model masonry at the scale of a Representative Volume Equivalent (RVE) or even a bigger part of the masonry wall. For example, one can imagine a rectangular element the size of the yellow block to model the masonry. Macro-models aim to model the masonry at a higher scale like the size of a whole wall. These latter are inappropriate in the context of the thesis because they do not allow the modeling of other elements.

The first section of this chapter briefly introduces the different categories of models. It allows to present the most common models in each category in the literature and to explain why the Rigid Macro-Element Model is the most interesting model from the literature for modeling masonry structures with bands. The last section of the chapter describes the Rigid Macro-Element Model and aims to highlight the advantages and disadvantages of the model in the context of the thesis.

3.1 Models in the literature

3.1.1 Micro-models

Micro-models involve modeling at the scale of the bricks and the joints. There are two principal methods: modeling all constituents (see Fig. 3.1.(a-b)) or modeling of expanded bricks separated by zero-thickness interfaces (see Fig. 3.1.(c)). The second category of models is usually referred to as simplified micro-models.

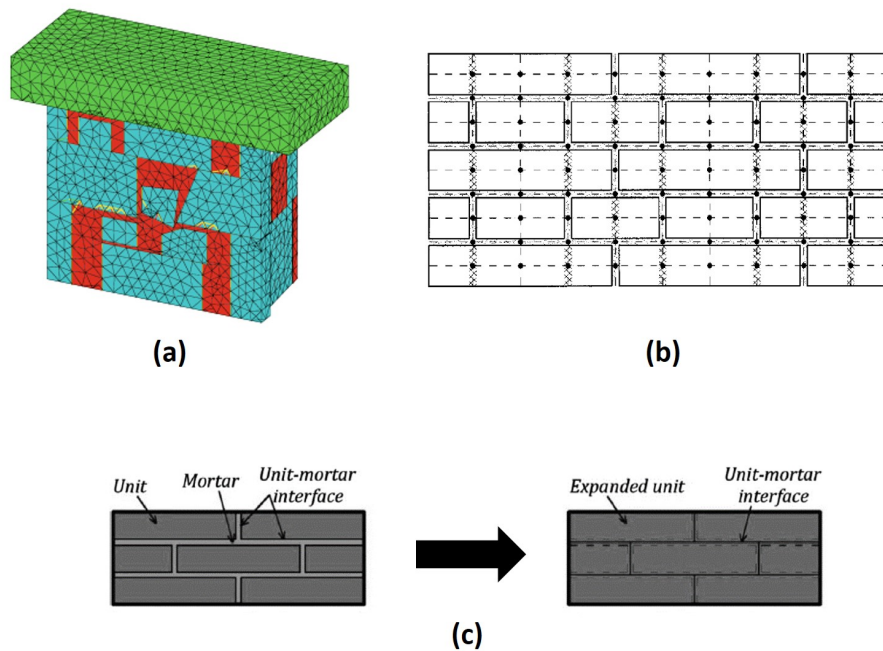


Figure 3.1: Micro-models for masonry: (a) Costa et al.'s [48]; (b) Gambarotta and Lagomarsino's [49]; (c) Simplified micro-model [50]

3.1.1.1 Modeling of all the constituents

Two different approaches can be cited for this kind of model. The first is to try to reproduce the geometry of the masonry specimen as realistically as possible and to use simple constitutive laws to reproduce its behavior. This is the strategy followed by Costa et al. [48]. The first step is to create a computer assisted drawing of the masonry block under study (see Figure 3.1.(a)). This drawing is then exported to Castem software [23] for numerical modeling. Costa et al. [48] use this method to reproduce numerically the cyclic shear test and modal analysis of stone masonry block.

The second approach was followed by Gambarotta and Lagomarsino [49] (see Figure 3.1.(b)). A wall is modeled with 2D four-node elements. If the edge of an element is the interface between two bricks, it is considered as a brick-mortar interface. If the edge is inside a brick element but is vertically aligned with a brick-mortar interface, it is considered a brick interface. If the edge is not one of these cases, it is considered an ordinary part of the brick. The joint elements have a constitutive law that takes into account the damage of the bricks and the decohesion of the brick-mortar interface. The bricks have an inelastic behavior that takes into account the tensile failure and the failure under compression.

3.1.1.2 The simplified micro-model

The simplified micro-model is the most common modeling method for masonry among all models. It is possible to find this method using different modeling strategies: extended finite elements (XFEM) [50], discrete elements (DEM) [51], FE [52]. By and large, it is always the same method: extended bricks with a simple mechanical behavior, often elastic, separated by zero-thickness interface elements aims to reproduce the overall inelasticity in the masonry (see Fig. 3.1.(c)).

3.1.2 The meso-models

The most common meso-models in the literature are shown in Figure 3.2. The Rigid Macro-Element Model (RMEM), the Rigid Body Spring Model (RBSM) and the Rigid Element Model (REM) can be found in the literature with the designation macro-model. Such a designation is valid with a definition of macro-models different from that of this thesis

3.1.2.1 The Rigid Macro-Element Model

An example of modeling of a wall with the RMEM is shown in Figure 3.5.(a). This model was first described by Calió et al. [2] for the study of URM walls under IP loading. It is used only for modeling masonry parts. It consists in a rigid quadrilateral with articulated corners that has 4 degrees of freedom for IP modeling: two translations, one rotation, and the shear deformation. The diagonally opposite hinges are connected by a spring, which is used to model the diagonal shear failure of the masonry. The quadrilaterals, also referred to as “panels” in the literature, interact with each other through zero-thickness springs at their edges. There are two different types of interface springs: normal springs and longitudinal springs (also called shear-sliding springs). The normal springs are used to capture the flexural failure of masonry due to different deformations. The longitudinal springs allow the model to capture the sliding failure of masonry. Ultimately, the model can capture through its various springs: the tension/compression in the vertical and horizontal directions, the sliding between two elements, and the diagonal failure. Since its first appearance, the model has been improved to allow the modeling of reinforced masonry walls, the modeling of 3D structures and the modal analysis of structures. An inconvenient with this method is that there is not any element related to bending. Therefore, the bending of a wall can be correctly reproduced only with a fine mesh.

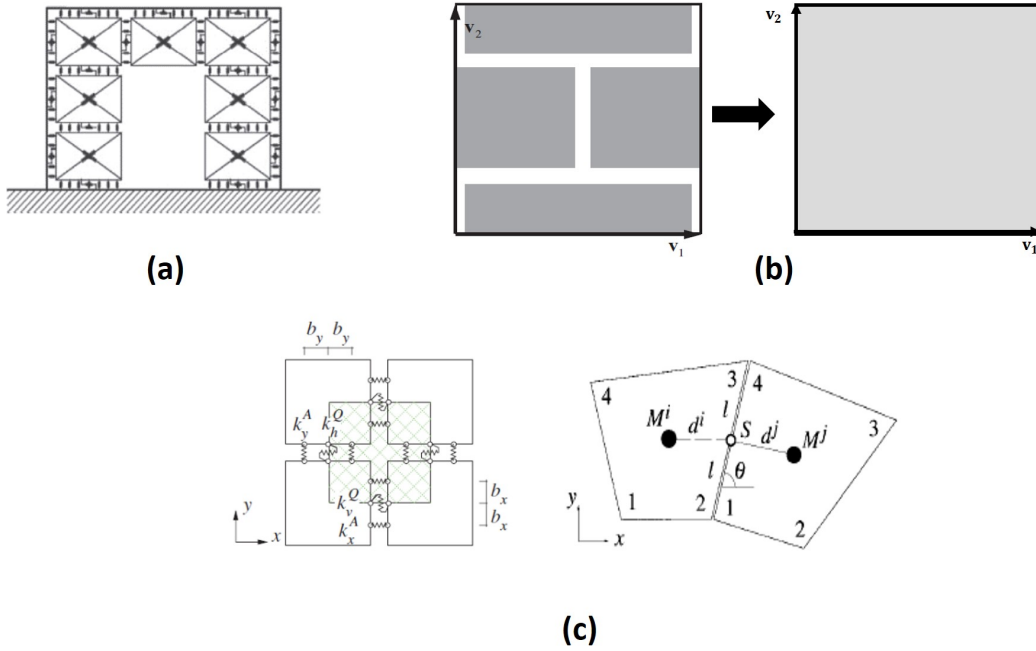


Figure 3.2: Examples of meso-model: (a) Rigid Macro-Element Model [2]; (b) Homogenization method [53]; (c) Rigid Body Spring Model [54] and Rigid Element Model [55]

3.1.2.2 The Rigid Body Spring Model and the Rigid Element Model

The REM was first proposed by Casolo to reproduce the OOP behavior of masonry [55]. It is the example on the right in Figure 3.5.(c). A few years later, the version of the model for IP solicitation, named RBSM, was proposed by Casolo and Pena [56] (example on the left in Figure 3.5.(c)). In both variants, the masonry is modeled by connected rigid blocks. For OOP modeling, the connections are moment/curvature hinges, and for IP modeling, the connections are force/displacement springs. The springs/hinges are calibrated by establishing an energy equivalence between the microscale and the scale of the rigid body. In general, a RVE is considered as a reference for the behavior of the masonry and the springs are adjusted to reproduce the behavior of the RVE.

Another version of the RBSM, the Homogenized Rigid Body Spring Model (HRBSM) proposed by Bertolesi et al. [57], captures the OOP behavior strain/stress springs. The determination of the characteristics of the springs in the model is made by an energy equivalence between an homogenized medium and the macro-element. The methods of homogenization of next section can be used.

3.1.2.3 Homogenization methods

The first articles that proposed the homogenization method considered masonry as a sequence of layers. Since the structure of masonry is complex, vertical and horizontal layers must be considered simultaneously. Therefore, to obtain a homogenized medium, it is necessary to perform two successive homogenizations. Pande et al. [58] considered vertical layers for the first homogenization and then horizontal layers. Later, Papa [59] considered vertical layers first and then the horizontal ones. Figure 3.3 illustrates these two methods. If it seems that both methods would lead to the same result, this is actually not the case. More details on the methods of layer homogenization and the results obtained can be found in Lourenço [60]. A continuum whose properties are based on considering the masonry as different layers is also proposed by Gambarotta and Lagomarsino [49]. This continuum is defined in both elastic and inelastic domains.

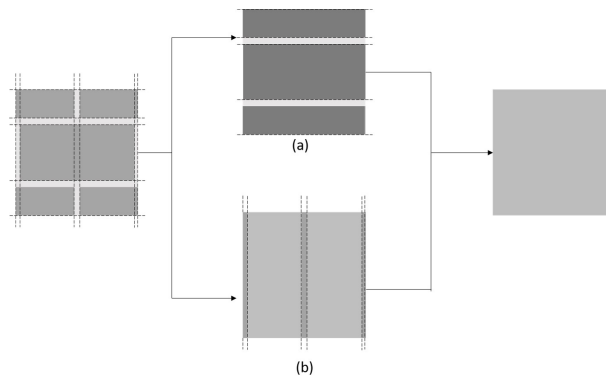


Figure 3.3: The first methods of homogenization: (a) Pande et al. [58] method; (b) Papa [59] method

More recent articles on the homogenization method consider a RVE. It is a more accurate method because it takes better into account the brickwork and can distinguish the different types of joints. Another difference with the first homogenization methods is that it is suggested that the RVE is periodically reproduced throughout the masonry portion. Therefore, the proposed model is limited to a specific brickwork. Interestingly, the representative shell considered may be different from one article to another for the same brickwork. As an example, three different RVEs for the running bond pattern are shown in Figure 3.4.

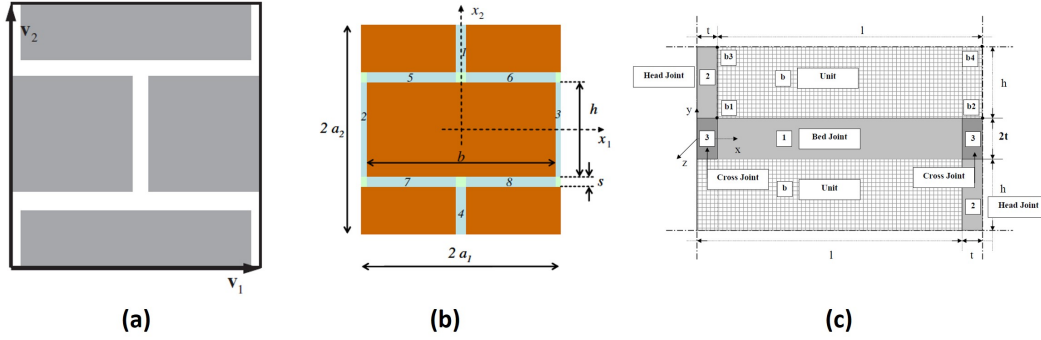


Figure 3.4: Different RVEs for the running bond pattern: (a) RVE used by Bacigalupo and Gambarotta [53]; (b) RVE used by Addessi and Sacco [61]; (c) RVE used by Zucchini and Lourenço [27]

Once the RVE is selected, there are several ways to define the behavior of the shell. Some of the methods are listed below with some of the articles that use them. This list represents the methods the author has come across and does not claim to be exhaustive.

- **Two-scale analysis: Cosserat¹ for macro-scale and Cauchy for micro-scale**

This method can be encountered in the articles by Forest and Sab [62] and later by Addessi et al. [61, 63] and De Bellis with Addessi [64]. The wall is considered as a homogenized Cosserat medium and is coarsely meshed. At the beginning of the time step, the displacements at the nodes are determined. Knowing the displacements at the nodes, it is possible to determine the displacements on a finer scale, the scale of the RVE. At this scale, all the elements are defined like for a micro-model with their specific constitutive law. This is possible because the RVE is defined as a Cauchy medium. With the constitutive laws, it is possible to determine the stress at the scale of the RVE, and knowing it, it is possible to go back to the stress for the Cosserat medium. This process is possible by determining the path to transition from one scale to another. That is the purpose of the articles cited above.

- **Second gradient of the displacement**

This method is proposed by Bacigalupo and Gambarotta [65, 66]. It consists in enriching the kinematics by considering the second order of displacement. The displacement is divided into two parts: one considers the heterogeneity of the material and the other is a continuous displacement defined periodically. The second order of displacement is used because the first order is not rich enough in information to represent well the complex kinematics of the masonry.

- **Analysis of a RVE by consideration of specific deformations**

This method is proposed by Zucchini and Lourenço [24, 27, 26]. It consists in studying the equilibrium of the RVE shown in Figure 3.4.(c) in terms of strain and stress. To make it more efficient, specific deformations are considered, such as the dilation of the joint under compression. The authors have also proposed a way to account for damage in the model so that it can be used in both the elastic and inelastic domains. If there are definitions that

¹This is a medium whose kinematics are defined differently from the kinematics of a Cauchy medium. In a Cosserat medium, internal rotations are added compared to a Cauchy medium.

link the behavior of the RVE to the properties of the elements, a study of the RVE under simple solicitations must be performed numerically to determine all the properties of the medium.

- **Study of a RVE with minimal kinematic and static parameters**

This method can be found in Mistler et al. [67], Mercatoris and Massart [68]. The aim is to define the kinematics of the RVE with only a few parameters. For this purpose, the method links the kinematics of the RVE with the applied force. By applying the equivalence of energy with force/displacement and stress/strain, it is possible to determine equivalent Young's moduli for the RVE with the displacements and geometry of the element. It has the advantage of minimizing the degrees of freedom of the model, thus reducing the computation time. The main disadvantage of this method is that it can only be applied in the elastic domain if used alone. Uva and Salerno [69] proposed to couple the method with the Eshelby method to account for the cracks and their orientation as well as the shape of the considered element and its orientation.

3.1.3 Macro-models

The most common macro-models in the literature are shown in Figure 3.2. These models aim to model masonry at the scale of elements bigger than meso-model like the size of a wall.

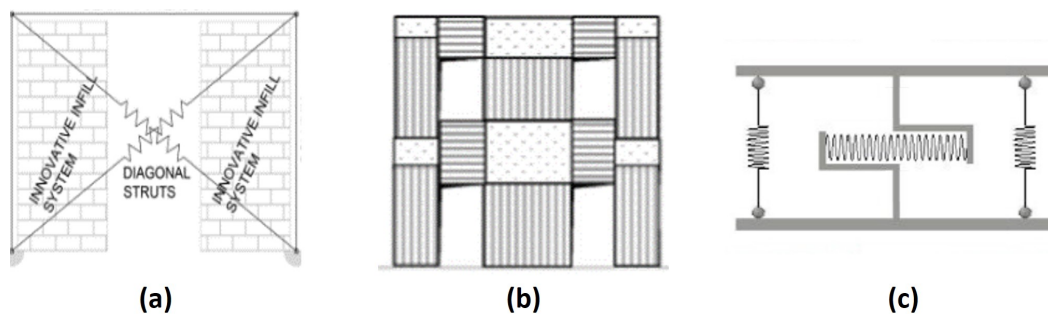


Figure 3.5: Examples of macro-model: (a) Diagonal Strut Model [70]; (b) Equivalent Frame Model [10]; (c) Xu et al.'s model [71]

3.1.3.1 The Equivalent Strut Model

An example of modeling of a wall with the Equivalent Strut Model (ESM) is shown in Figure 3.5.(a). This modeling strategy consists in representing masonry with diagonal struts only, as proposed by Polyakov [72]. This idea is based on the occurrence of diagonal compression struts in masonry infill as seen in Section 1.3.1. Therefore, this model is only valid for FIM structures. The most common version of the model uses only one strut in its diagonal. However, there are version with two struts [73], three struts [74], five struts [75] or even nine struts [76].

The cyclic behavior of the masonry is reproduced by the diagonal struts. There are several proposals for the hysteresis law. Some aim to be as accurate as possible, while others accept more deviation from experimental results but require a simpler calibration. If the calibration of the hysteresis law can be difficult, the definition of the elastic properties of the element can also be hazardous since the model takes into account the presence of openings directly in the definition of the struts (see Figure 3.5.(a)).

3.1.3.2 The Equivalent Frame model (and assimilated)

It is the most commonly used macro model [77]. Its use is proposed in some international standards such as Eurocode 8 [78] or FEMA 356 [79]. This type of model is used in both research and engineering, especially with the Tremuri software [10] (3Muri for the commercial version).

These models consist in the modeling of the wall by identifying the piers, the spandrels and the rigid parts. Piers are the parts with vertical lines in Figure 3.5.(b) while the spandrels are the elements with horizontal lines and the rigid parts are filled with dots. There are different ways to model the behavior of the elements:

- Beam with elastic-plastic behavior. It is the modeling used for the (Simplified Analysis of Masonry) SAM method. This kind of modeling is found in the articles by Magenes and Della Fontana [80] or Magenes [81] for example. Once the elastic limit is reached at a node, a plastic hinge forms there.
- Elastic beam with plastic hinges. This method can be found in the articles by Pasticier et al. [82] and Salonikios et al. [83]. For these models, the plastic hinges are pre-located and plasticity can only happen at these spots.
- Rectangular elements defined with 8 nodes. It is the modeling used in the Macro Frame Element (MFE) method. It can be encountered in the articles proposed by Gambarotta and Lagomarsino [84, 85] and by Brencich et al. [86].
- Changing shape panel. This method is proposed by D'Asdia and Viskovic [87]. The piers and the spandrels are modeled by specific panels that change of shape depending on the applied stress and the damage.
- Rigid struts and plastic hinges. This method is proposed by Mobarake et al. [88]. The piers and the spandrels are represented by four plastic hinges (one at each corner of the panel) connected by rigid struts. The rigid pannels are modeled with rigid struts only.

3.1.3.3 Xu et al.'s model

This model was found only in the article by Xu et al. [71]. It consists in modeling a URM wall or a CM wall by a frame with a horizontal spring (see Fig. 3.5.(c)). The frame has an elastic

behavior under vertical loading, but is not deformable under horizontal tension/compression. The horizontal spring in the frame is used to capture the shear behavior of the masonry. Since this element models a complete URM or CM wall, its properties must account for the presence of openings and the presence of frames as in the ESM.

3.2 Discussion for the context of the thesis

In the previous section, an overview of the main masonry models in the literature was proposed. In order to know which model can be interesting for modeling structures with bands, their performances are evaluated in relation to the objectives of the thesis (see Table 3.1). These performances are assumed after intensive bibliographic studies. The evaluation of the performances ranges from “++” for very good to “-” for not suitable.

The models that do not meet the requirements for computation time and modeling of structures with bands are disregarded, since these are the two main goals for the model. Some models could be modified to allow modeling of masonry structures with bands, but it is not conceivable to claim that the model’s performance can be improved to get rid of the important computation time. Among all the models, the RMEM exhibits all the desired properties. Therefore, the next section explains how it is defined and identifies its advantages and disadvantages. The ultimate objective with this in-depth study is to determine what is the best conceivable method for modeling masonry structures with bands in the framework of this thesis and if the RMEM is that method.

Table 3.1: Performances of the model regarding the objectives of the thesis

	URM/CM/RM	Structure with bands	Computation time	Definition of the model	Allow IP and OOP
Micro-model	++	++	-	+	++
Simplified micro-model	++	++	-	+	++
(H)RBSM-REM	-	-	+	+	+
RMEM	++	+	++	+	++
Homogenization	++	++	-	-+	-+
EFM	-	-	++	++	+
ESM	-	++	++	+	+-
Xu et al.'s	+	-	++	+	-

- RBSM-REM-HRBSM: the first versions of the model do not allow the simultaneous study of the IP and OOP behavior of a structure. The HRBSM does not have this problem. However, its properties are determined by the study of a RVE and its use is therefore limited to running bond brickwork. For modeling structures with bands, the REM is not suitable for a connection with additional elements. For the RBSM and the HRBSM, the connection with other elements does not seem to be straightforward as well.
- EFM: the method with identification of piers, spandrels and rigid parts is not suitable for RM and CM structures. One possibility is to assume that all elements are piers, but this assumption may not be appropriate. Also, modeling reinforcement at the opening is not possible with any version of the model.
- Strut: the ESM theory lies on the occurrence of diagonal compression struts. If it is possible to model masonry parts between two bands and vertical reinforcements with such a model, it is impossible if the masonry is not surrounded by frames or confined. There are versions of the model for IP and OOP loading, but there are not many for OOP behavior.
- Xu et al's: the model is designed to reproduce the behavior of a complete wall. It is reasonable to think that the model can be adapted to model masonry at the meso-scale. However, it is difficult to know to what extent the properties of the model are suitable for such modifications.
- Homogenization: it includes several models. Therefore, the data in Table 3.1 may not be appropriate in some specific cases. Homogenization methods are rarely defined for OOP loading. The mesh is coarsened compared to other meso-models.

3.3 The Rigid Macro-Element Model (RMEM)

The model, in its usual definition, is defined for Discrete Elements oriented software. The 2D version of the model is shown in Figure 3.6.(a). It is defined by four degrees of freedom (two IP translations, one rotation and shear deformability). While the number of springs in the diagonal is fixed at one, the number of normal springs is chosen by the user, knowing that two normal springs per edge are sufficient to capture the normal and flexural behaviour of the masonry. For shear-sliding springs, it is common to take only one per side. The springs are evenly distributed on the side of the rigid body to have a discrete determination of the behaviour of the interfaces. The deformations of the springs at the interfaces are defined with the degrees of freedom of the panels. The number of springs affects the accuracy of the model and allow to better capture some phenomena like bending.

The model has been improved over the years so that it can be used for both IP and OOP solicitations. The first proposal for 3D modeling is shown in Figure 3.6.(b). This element has additional lines for normal springs and new longitudinal springs normal to the plane of the macro-element. The number of lines for the normal springs is chosen by the user. It would affect to accuracy to capture the OOP bending and the arching. The new shear-sliding springs are used to capture the sliding and shear failure of the masonry in the OOP direction and to determine the OOP bending behavior in the same manner as the normal springs for IP bending. To capture

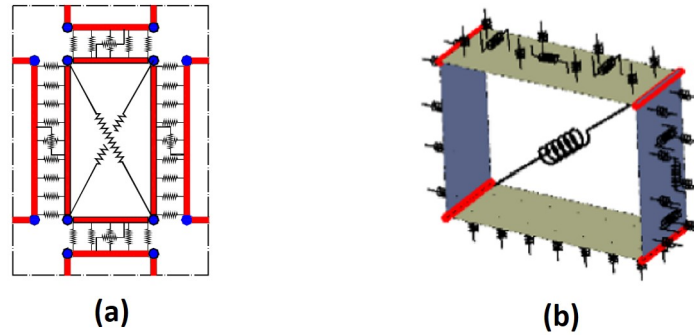


Figure 3.6: Different versions of the RMEM: (a) 2D model; (b) 3D model

torsion with the OOP shear-sliding springs, at least two of them are required on each side of the rigid quadrilateral. For the IP longitudinal springs, one per edge is still sufficient. The rigid 3D element has seven degrees of freedom (Displacement in the three directions, rotation around each space axis and the IP shear deformability).

There are other forms for the RMEM, but their use is beyond the scope of this thesis since they concern constructions with arches and domes.

3.3.1 Area of influence the springs

The area of influence is used to link the properties of the springs to the properties of the masonry. For the springs on the sides of the rigid frame, it is determined as for a fibre discretization (see Figure 3.7).

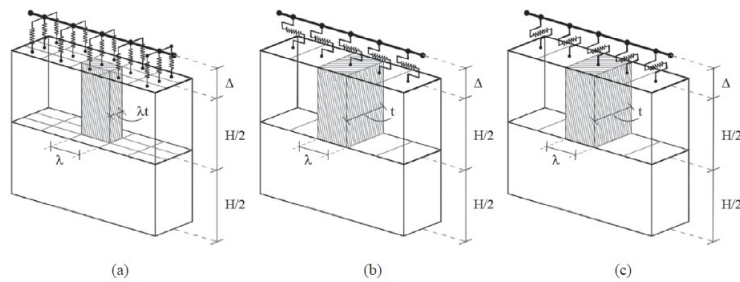


Figure 3.7: Area of influence of the springs of the RMEM: (a) Transversal springs; (b) IP shear/sliding springs; (c) OOP shear/sliding springs [89]

The area of influence of the diagonal spring is determined in a different way. Since this element is used to capture the shear behavior of the masonry, the cross-section of the wall A_t is taken as the value for its area of influence.

3.3.2 Calibration of the normal spring

The nonlinear behavior of the transverse springs is determined using a fracture energy-based approach. The tensile behavior is modeled with a parabolic curve and the compressive behavior with an exponential curve, as shown in Figure 3.8. The yield forces F_{ty} and F_{cy} are determined using the properties of the homogenized masonry represented by the macro-element. The final displacement is estimated using the fracture energies G_{ft} and G_{fc} considering the crack bandwidth as a discretization of the macro-element mesh size. When a normal spring fails in compression, it is removed. However, if a normal spring fails in tension, it can still work in compression.

For the hysteretic behavior, the model proposed by Takeda et al. [90] for RC is used. This model has an unloading curve controlled by a fixed parameter β , which can be different in compression β_c and in tension β_t . The hysteresis behavior is shown in Figure 3.8 for different values of β .

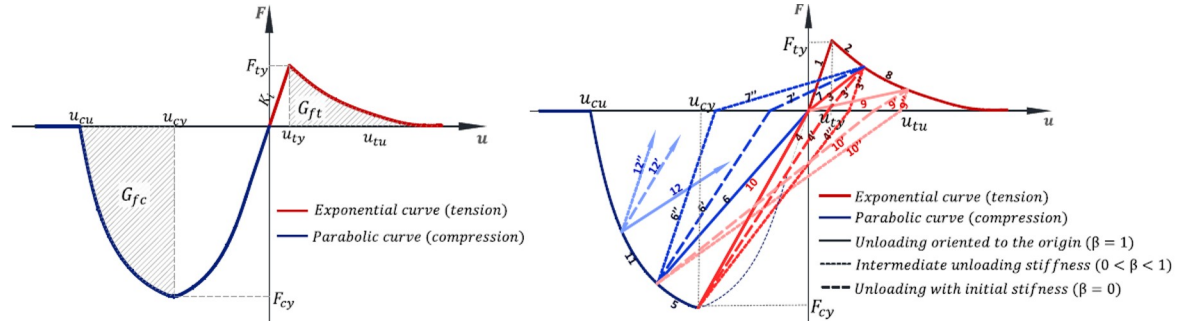


Figure 3.8: Behavior of the transversal springs of the RMEM [91]

The parameters defining the envelope curve of the constitutive laws are given in Table 3.2. In this table, E_m is the masonry Young's modulus in the direction of the considered normal spring determined, for example, by homogenization, u_{tu} and u_{cu} are the limit displacement in tension and in compression, f_t and f_c are the strength in tension and in compression, g_t and g_c are the fracture energies in tension and in compression. The different parameters λ are related to the area of the member (see Figure 3.7). H is the height of the macro-element.

Table 3.2: Properties of the normal springs of the RMEM [89]

$K = 2 \frac{E_m \lambda \lambda_t}{H}$	$F_{yc} = f_c \lambda \lambda_t$	$F_{yt} = f_t \lambda \lambda_t$	$u_{tu} = \frac{2g_t}{f_t}$	$u_{cu} = \frac{2g_c}{f_c}$
-----------------------------------------	----------------------------------	----------------------------------	-----------------------------	-----------------------------

3.3.3 Calibration of the shear-sliding springs

Whether for IP or OOP sliding, the constitutive law of the shear/sliding spring is the same: an elastic perfectly plastic behavior. The yield force is determined with the Mohr-Coulomb criterion (see Equation (3.1)). The parameter c in the criterion is the cohesion of the mortar, μ is the coefficient of friction at the mortar/unit interface, σ_m is the mean compressive stress acting on the edge of the rigid body, and A_0 is the effective contact area of the spring. Figure 3.9 shows the behavior of the spring for a fixed value of N . If N varies, the yield force changes.

$$F_y = (c + \mu\sigma_m)A_0 \quad (3.1)$$

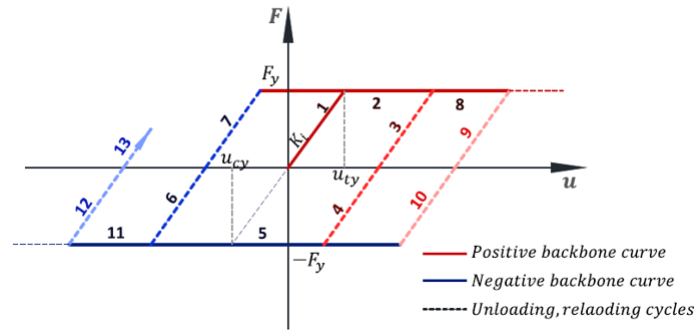


Figure 3.9: Constitutive law of the shear/sliding spring of the RMEM [91]

If the constitutive law of the shear-sliding spring is the same for the OOP and the IP directions, the parameters for the two directions may still be different. The values of the mechanical properties of the longitudinal springs are given in Table 3.3, where g_{sl} is the fracture sliding energy and G_m is the shear modulus of the masonry.

Table 3.3: Properties of the shear/sliding springs [89]

$K = 2 \frac{G\lambda t}{H}$	$u_{tu} = \frac{2g_{sl}}{c}$
------------------------------	------------------------------

3.3.4 Calibration of the diagonal springs

Figure 3.10 shows a masonry portion under shear solicitation. The meso-element under the same solicitation is sketched on the right. All the data required to define the area of influence are given in this figure.

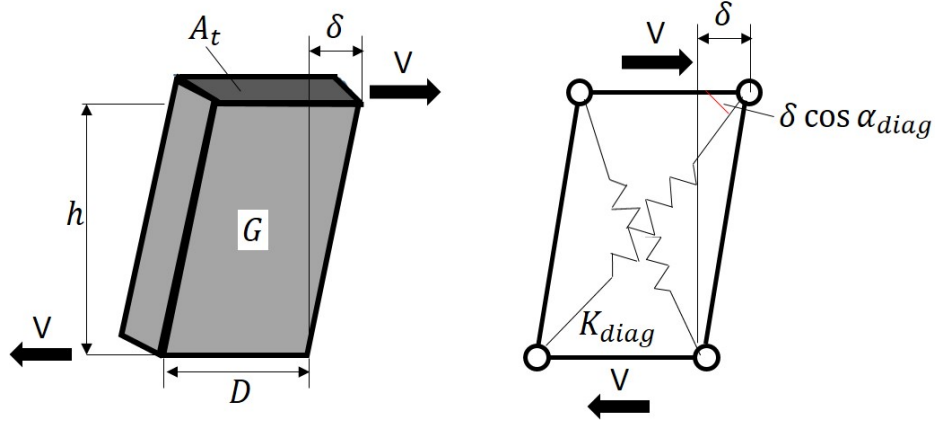


Figure 3.10: RMEM element under shear solicitation [92]

Since the assumption of a homogenized medium is made, it is possible to write the transverse displacement δ under the shear force V as:

$$\delta = \frac{V}{G_m A_t} h_m \quad (3.2)$$

Determining the equilibrium at one corner of the meso-element leads to the relation:

$$F_{diag} = \frac{V}{2 \cos \alpha_{diag}} = K_{diag} \times \cos(\alpha_{diag}) \delta \quad (3.3)$$

By rearranging Equation (3.3) and substituting δ by means of Equation (3.2) it is possible to know the value of the stiffness of the diagonal springs given by Equation (3.4), where D is the width of the rigid quadrilateral.

$$K_{diag} = \frac{GA_t}{2H \cos^2 \alpha} = \frac{GDt}{2H \cos^2 \alpha} \quad (3.4)$$

For these springs, there are two possible yielding criteria. The first is the Mohr-Coulomb criterion and is expressed by Equation (3.5). The second criterion is the one of Turnšek and Čačovič [3] (see Equation (3.6)). Here F_y is the yielding force and F_0 is the yielding force with no confinement.

$$F_y = F_0 + \mu \cdot N \quad (3.5)$$

$$F_y = F_0 \sqrt{\frac{N}{1.5F_0} + 1} \quad (3.6)$$

As in the case of shear/sliding springs, the normal force N varies and is equal to the value of the vertical force acting on the rigid body. The hysteretic behavior of the diagonal spring is like that of the transversal spring, but unlike these springs, there are not two different coefficients depending on the type of solicitation. Thus, there is another empirical parameter β_d in the model. Figure 3.11 represents the behavior curve for the diagonal springs.

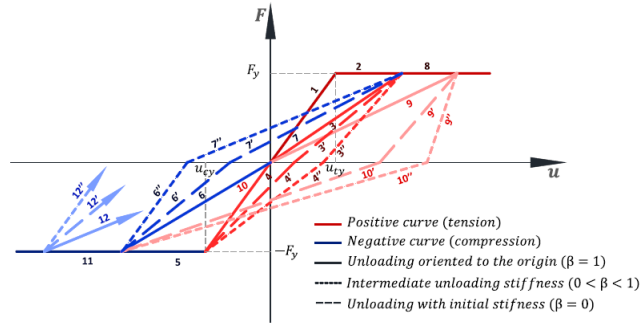


Figure 3.11: Constitutive law of the diagonal springs of the RMEM [91]

3.3.5 The OOP behavior

For OOP springs, the determination of their properties has already been explained. However, one detail is still missing. Indeed, Caddemi et al. [93] proposes a distance d between the two springs (see Equation (3.7)). This distance d allows a better capture of the OOP bending behavior and depends on the thickness t_m and the length B of the considered side of the rigid body. The same type of formula can be applied to the normal IP springs if one chooses to take only two springs. Note that for the OOP behavior of a wall, if the mesh size is not small enough, the meso-model will not be able to reproduce the mechanism of the wall accurately.

$$d = 2t_m \sqrt{\frac{1}{3} - 0.21 \frac{t_m}{B} \left(1 - \frac{t_m^4}{12B^4} \right)} \quad (3.7)$$

3.3.6 Connection between elements

3.3.6.1 Interface between RMEM element and frame

If this chapter has already dealt with the modeling of the masonry for this type of model, the modeling of the frames has not yet been presented. The frames, or any additional reinforcement, are modeled by beam elements. These elements have common constitutive laws used in FE models.

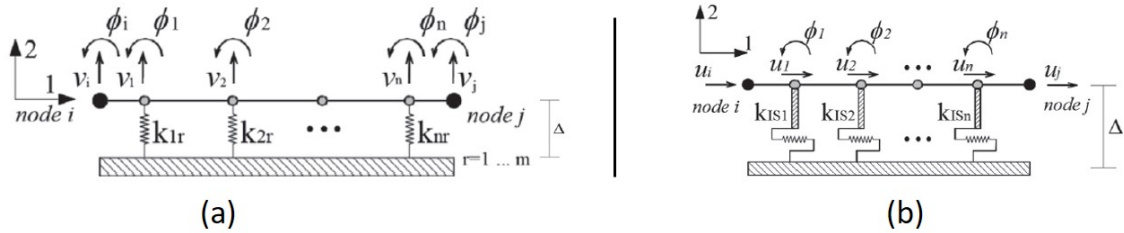


Figure 3.12: Interface between a RMEM element and a rigid element (in plane-view): (a) normal springs; (b) shear/sliding springs

Figure 3.12 taken from Pantó et al. [94] shows the interface between a meso-element and a beam. Figure 3.7 also shows this type of interface, but with a perspective view in 3D modeling. The springs of the meso-element are connected to internal nodes of the beam. The peculiarity in this type of interface comes from the distance Δ , which is shown in Figure 3.12. Assuming that the beam element is the neutral axis of the frame, Δ is the distance between the neutral axis and the edge of the frame. Usually, its value is half the width of the frame in the direction under consideration.

3.3.6.2 Interface between two RMEM elements

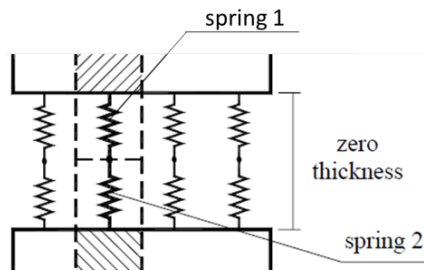


Figure 3.13: Interface between two macro/elements [2]

Figure 3.13 shows the interface between two meso-elements. As it is explicitly stated, it is a zero thickness interface. This interface is formed by springs consisting of two springs connected

in series: Spring 1 and Spring 2. This means that two meso-elements facing each other have the same number of springs on their side. Springs 1 and 2 do not necessarily have the same properties. Therefore, two aligned meso-elements do not necessarily have the same size.

3.3.7 Mass matrix of the RMEM

In order to perform a modal analysis of the structure, it is necessary to determine the mass matrix of the meso-element. Its determination is described by Chácara et al. [95]. In that paper, the determination of the mass matrix for an element with a random shape is explained. Since only rectangular shapes will be used to model structures in the context of the thesis, only the details for the rectangular shapes are given in this section.

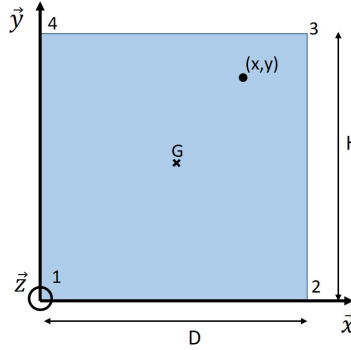


Figure 3.14: Shape of the meso-element for the determination of the mass matrix

One considers a meso-element as sketched in Figure 3.14. Its height is noted H , its width D and its thickness t_m . The density of the masonry is denoted by ρ_m . For a 3D modeling, the element has seven degrees of freedom. Degrees of freedom 1 to 3 are for the translation owing to the space axis (1 for x axis, 2 for y axis and 3 for z axis). Degrees of freedom 4 to 6 are for the rotation around these axis (4 for rotation around x axis, 5 for y axis and 6 for z axis). The degree of freedom 7 is the shear deformability. To each of them, one attributes a matrix operator Ψ_k^i , where k is the degree of freedom and i is the node under consideration. The centroid of the meso-element is denoted by G . Its coordinates are (x_G, y_G, z_G) . The matrix operators for rectangular meso-elements are given by Equations (3.8a), (3.8b) and (3.8c).

$$\Psi_1^{n=1\dots 4} = \begin{Bmatrix} 1 \\ 0 \\ 0 \end{Bmatrix}, \Psi_2^{n=1\dots 4} = \begin{Bmatrix} 0 \\ 1 \\ 0 \end{Bmatrix}, \Psi_3^{n=1\dots 4} = \begin{Bmatrix} 0 \\ 0 \\ 1 \end{Bmatrix} \quad (3.8a)$$

$$\Psi_4^{n=1,\dots,4} = \begin{Bmatrix} 0 \\ z_G - z_n \\ y_n - y_G \end{Bmatrix}, \Psi_5^{n=1\dots 4} = \begin{Bmatrix} z_n - z_G \\ 0 \\ x_G - x_n \end{Bmatrix}, \Psi_6^{n=1\dots 4} = \begin{Bmatrix} y_G - y_n \\ y_n - y_G \\ 0 \end{Bmatrix} \quad (3.8b)$$

$$\Psi_7^{n=1,2} = \begin{Bmatrix} 0 \\ 0 \\ 0 \end{Bmatrix}, \Psi_7^{n=3,4} = \begin{Bmatrix} -H \\ 0 \\ 0 \end{Bmatrix} \quad (3.8c)$$

Using these matrix operators, it is possible to determine the mass matrix at each node, taking into account all degrees of freedom of the meso-element. The component for the mass matrix at node n is simply defined by Equation (3.9), where i and j denote the directions.

$$m_{i,j}^n = \int_V \rho_m \Psi_i^n(x, y, z) \Psi_j^n(x, y, z) dV \quad (3.9)$$

3.3.8 FE version of the model

The RMEM is defined for discrete element oriented software. One of the problems with this kind of numerical method, as announced by Pantó and Rossi [96], is the connection with other elements such as beams to model the frames. This indeed leads to a computation burden and requires specific strategies, since these additional elements are defined for the finite element strategy. To solve this problem, Pantó and Rossi [96] have recently proposed a modification of RMEM that allows the use of finite element oriented software (see Figure 3.15).

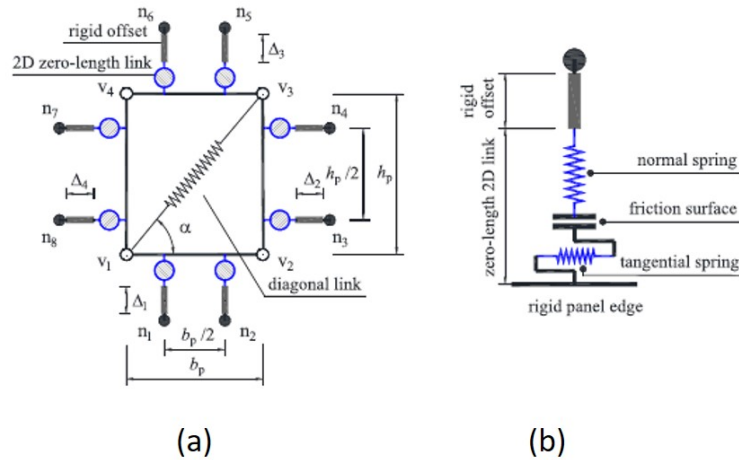


Figure 3.15: Finite Element version of the RMEM: (a) The macro-element; (b) Details on the 2D zero-length link

The proposed meso-element can be considered as a combination of the RMEM and the RBSM proposed by Casolo [55]. The base of the RMEM is kept as it can be seen in Figure 3.15. The modifications concern the elements modeling the interfaces and the use of only one diagonal

spring. The discretization of the bonds between the rigid quadrilaterals had to be changed to adapt the model to finite element oriented software. The new meso-element has two 2D zero-length links on each side, separated by a distance equal to half the length of the edge to which they are attached. Each link is composed of a tangential spring, a friction spring, and a normal spring. In addition to the 2D zero length links, there is a rigid offset that is used when the macro element is connected to the frames. This offset corresponds to half the thickness of the frame.

The calibration of the springs is similar to that described above. The differences in the mechanical parameters of the links between the model of Pantó and Rossi [96] and the values given in Section 3.3.2 result from the use of constitutive laws already implemented in the software Opensees [97].

3.4 Conclusion

In the first part of the chapter, a brief overview of numerical models for masonry was given. The aim was to present the most common models and to determine which model seems to be the most suitable for modeling masonry structures with bands. The model under consideration is the RMEM, since it satisfies several objectives. It allows an easy modeling of masonry at the meso-scale and has a small computation time (Chacara et al. [91] got a computation time for a push-over analysis 96 % smaller than with a FE micro-model). Moreover, the RMEM is defined for both IP and OOP behaviors. Yet, defining the behavior of the elements is not straightforward due to the use of zero-thickness elements. Apart from this drawback, most of the input parameters are the material properties of the masonry, only four parameters are empirical parameters.

The RMEM in its original definition does not allow a simple modeling of masonry structure with bands since it would mix discrete elements and finite elements. This problem is overcome with the last form of the model proposed by Pantó and Rossi [96], which is defined for finite element-oriented software. Even though Pantó and Rossi [96] only propose a definition of the model for IP solicitations, it does not seem very complex to extend the use of the model to 3D modeling, thanks to the work already done on the classical RMEM for 3D modeling. However, there is a drawback regarding this hypothetical 3D modeling with the FE version of RMEM. Indeed, the OOP bending behavior of the wall requires at least two lines of normal springs to be captured. This implies a significant increase in the degrees of freedom for the model, which are already 28 in 2D FE modeling. Therefore, the computation time for a complete structure can be significant particularly if the mesh must be fine enough to well capture the OOP bending behavior.

Due to the advantages and the few drawbacks of the RMEM, it was decided to use it as the basis for a new meso-model: the Deformable Frame Model (DFM). This model aims at exploiting the advantages of the RMEM and eliminating its disadvantages. The DFM is defined for a FE oriented software to allow a simple modeling of a complete masonry structure with horizontal bands. Its features are described in detail in Chapter 4 for IP loading and in Chapter 6 for 3D modeling.

Part II

Modeling at the scale of the elements

The numerical study of masonry structures with horizontal bands requires the modeling of multiple elements: masonry, frames and bands. The connection between every element has to be as simple as possible to allow a straightforward modeling. Therefore, every **element of the model is defined for FE oriented software**.

Chapter 4 presents a new meso-element for the modeling of URM: the Deformable Frame Model (DFM). In this chapter, all the features for the modeling of URM for IP loading are presented.

Chapter 5 presents the modeling of horizontal bands and reinforcements at the openings. The set hypothesis for the modeling are based on the experimental results seen in Chapter 2.

Chapter 6 presents the modification of the DFM to enable a 3D modeling. In addition to the enriched kinematics, the chapter gives additional details for the determination of the mass matrix in order to make a dynamic analysis.

Chapter 4

Deformable Frame Model for IP loading

In the last chapter, it was found that the meso-models and macro-models from the literature do not fully satisfy the desired requirements for modeling masonry structures with horizontal bands. The model that seemed most appropriate has drawbacks that make it unattractive for the context of this thesis. Nevertheless, it has very interesting aspects that can serve as a basis for a new meso-model. This new meso-model is the Deformable Frame Model (DFM).

4.1 Hypothesis for the modeling

The DFM models the masonry at the meso-scale (see Figure 4.1). Although the brickwork plays a role in the behavior of a masonry wall, as shown in Section 3.1.2.3, the study of its influence on the behavior of masonry portions is beyond the scope of the thesis. Therefore, the brickwork is not taken as input data to the model and no importance is given to it in the overall numerical modeling. As it is possible to link the properties of the brickwork to the properties of an equivalent homogenized medium, it may be possible to link the properties of the DFM to the brickwork.

It is assumed that all **damage in masonry under seismic loading** is a consequence of its shear behavior. Therefore, only the elements that reflect the shear behavior of masonry in the model have inelastic behavior, as in the model of Xu et al. [71]. All other elements of the meso-model have an elastic behavior.

Masonry is an anisotropic material. Therefore, the Young's modulus is different in each direction. However, for the definition of the DFM, it is assumed that the **Young's modulus is the same in all the directions**.

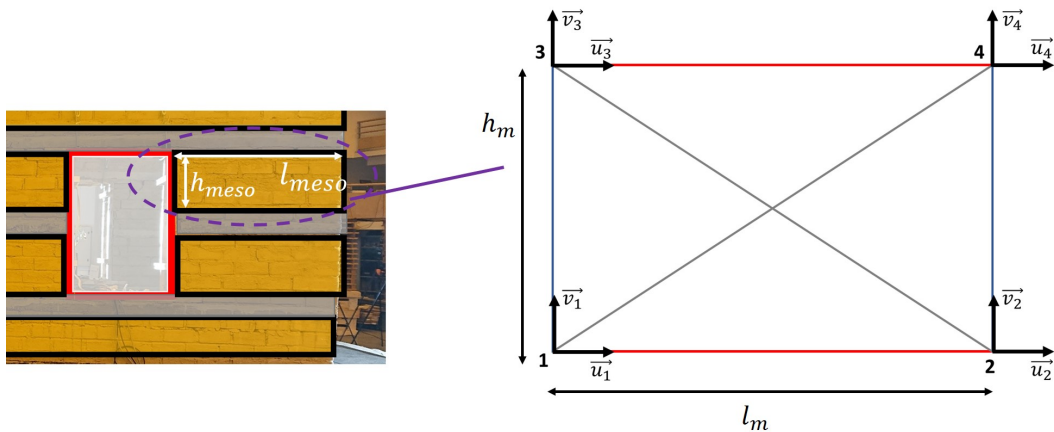


Figure 4.1: The DFM for 2D modeling

4.2 Kinematics of the DFM

The DFM for an IP solicitation is shown in Figure 4.1. The form of the DFM is clearly inspired by that of the RMEM. The intent is to keep the same philosophy as the RMEM, where each link is used for a specific solicitation. The problem of the RMEM was the use of zero-length springs at the interfaces, which were a constraint to capture the OOP bending with a reasonable number of degrees of freedom¹. To get rid of this, the choice is made to transform the rigid frame into a deformable frame (hence the name of the model), as in the model proposed by Xu et al. [71]. However, unlike the macro-model, the DFM does not have any rigid element in order to reproduce the behavior of masonry under any type of loading.

In Figure 4.1 it can be seen that the diagonal strut inside the rectangular body is adopted from the RMEM. These elements allow the DFM to rock under horizontal loading. Horizontal struts like in the model of Xu et al. [71] do not enable this. The DFM is defined with four nodes, there is no node at the intersection of the diagonals. The representation of the macro element in Figure 4.1 is chosen for the sake of clarity. Similarly, there is only one diagonal strut in each diagonal and not two. Each node is connected to three struts: one horizontal strut, one vertical strut, and one diagonal strut respectively in red, in blue, and in grey in Figure 4.1. Since they are strut elements, they only act on tension-compression with respect to their axis, which facilitates the definition of their properties. The kinematics of the meso-element for IP analysis is thus defined with only eight degrees of freedom.

¹With the considered change in the FE definition of the model inspired by the 3D shape of the model for 3D modeling

4.3 Definition of the stiffness of the elements

4.3.1 Modeling with one macro-element

The stiffness of each strut can be identified from the virtual work value by establishing an equivalence between an isotropic 2D medium and the macro-element. An example is shown in Figure 4.2 for a vertical strut. The masonry element of height h_m , width l_m and thickness t_m is under a uniformly distributed vertical force F_v . The 2D isotropic medium has a Young's modulus E_m and a shear modulus G_m . It is initially modeled with only one meso-element whose vertical struts have stiffness K_v , horizontal struts have stiffness K_h , and diagonal struts have stiffness K_d . For the example of Figure 4.2, the virtual work leads to:

Cohesive media (Fig. 4.2.(a)):

$$\underline{F}_v \cdot \underline{u}_v = \iiint \underline{\sigma} : \underline{\varepsilon} dV = E \cdot l_m \cdot t_m \frac{u_v^2}{h_m} \quad (4.1)$$

Meso-element (Fig. 4.2.(b)):

$$\underline{F}_v \cdot \underline{u}_v = 2 \cdot (K_v \cdot \vec{u}_v \cdot \vec{u}_v + K_d \cdot \vec{u}_d \cdot \vec{u}_v) = 2 (K_v u_v^2 + K_d \cos^2(\theta) \cdot u_v^2) \quad (4.2)$$

The equality between the two cases, leads to Equation (4.3) which defines the rigidity of vertical struts.

$$K_v = E_m \cdot \frac{l_m \cdot t_m}{2 \cdot h_m} - K_d \cdot \cos^2(\theta) \quad (4.3)$$

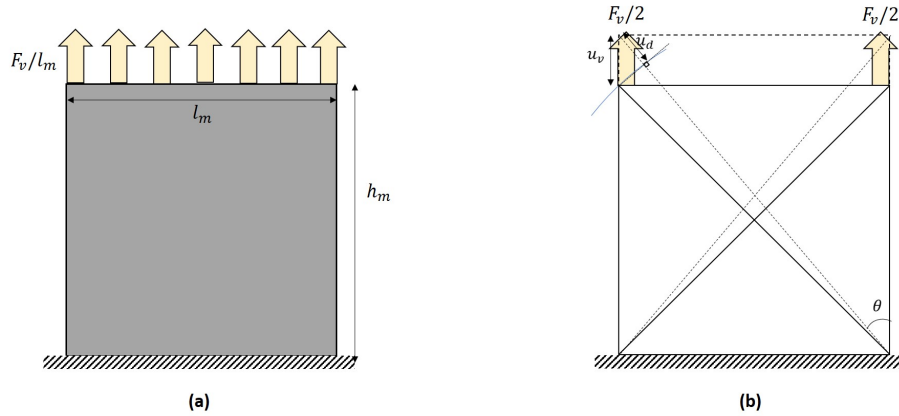


Figure 4.2: Masonry element under vertical loading modeled with: (a) an isotropic medium; (b) the DFM (the deformed configuration is dashed)

Equation (4.4), which defines the stiffness of horizontal struts, and Equation (4.5), which defines the stiffness of diagonal struts, can be obtained by the same reasoning.

$$K_h = E_m \cdot \frac{h_m \cdot t_m}{2 \cdot l_m} - K_d \cdot \sin^2(\theta) \quad (4.4)$$

$$K_d = G_m \cdot \frac{l_m \cdot t_m}{2 \cdot h_m \cdot \sin^2(\theta)} \quad (4.5)$$

In the DFM, the stiffness of the vertical struts and the stiffness of the horizontal struts are linked to the stiffness of the diagonal struts (see Equations (4.4) and (4.3)). This can lead to negative values if the properties of the meso-element do not satisfy some conditions. These conditions are deduced by imposing a positive value for both K_v and K_h . Using the relationship between the shear modulus and the elastic modulus $G_m = E_m / (2(1 + \nu_m))$, with ν_m the Poisson's ratio of the masonry, the conditions for the slenderness of the meso-element are:

$$\frac{1}{\sqrt{2(1 + \nu_m)}} \leq h_m / l_m \leq \sqrt{2(1 + \nu_m)} \quad (4.6)$$

4.4 Inelastic behavior of the DFM

The diagonal struts are the elements used to model the inelastic behavior under a cyclic shear solicitation. A force-displacement constitutive law is determined by two components: the envelope curve defining the push-over behavior, and the hysteresis loop. Each of these components will be described in specific sections below. The first part will deal with the hysteretic behavior of the diagonal element. The second part will deal with the envelope curve.

4.4.1 Shear strength of the DFM

There are four main modes of failure in masonry walls: rocking, diagonal cracking, shear-sliding and toe crushing (see Chapter 1). These modes of failures depend on the mechanical properties of the masonry as well as the boundary conditions. It is possible to find a definition of ultimate strength for each of them in the literature.

Toe crushing occurs due to excessive vertical stress and is not directly related to shear behavior. Therefore, it is not considered in this section.

4.4.1.1 Diagonal shear failure

There are two formulae for defining the diagonal shear failure of a masonry pier. The first was proposed by Turnšek and Čačovič [3] (see Equation (4.7)) and takes into account the aspect ratio of the pier, the vertical stress σ_v , and the tensile strength of the masonry f_t . The second definition for diagonal shear failure is a modification of the definition of Turnšek and Čačovič by Turnšek and Sheppard [9] (see Equation (4.8)).

$$f_{v,1} = \frac{f_t}{b} \sqrt{\frac{\sigma_v}{f_t} + 1} \quad (4.7)$$

$$f_{v,2} = \frac{1.5f_t}{b} \sqrt{\frac{\sigma_v}{1.5f_t} + 1} \quad (4.8)$$

In these equations, b is the shear stress distribution factor [98]. It is used to account for the dependency of the stress distribution on the slenderness of the wall. It is defined by Equation (4.9).

$$b = 1 \leq h_m/l_m \leq 1.5 \quad (4.9)$$

4.4.1.2 Rocking failure

Usually, rocking is defined by a maximum bending moment. However, since the diagonal strut element is defined by a force-displacement constitutive law, it is not possible to use this type of criterion. Yet, Petrovčič and Kilar [99] propose a definition for the maximum stress associated with the rocking failure (see Equation (4.10)).

$$f_{v,3} = \frac{\sigma_v}{2\alpha_V} \left(1 - \frac{\sigma_v}{0.85f_c} \right) \quad (4.10)$$

The value 0.85 in this equation is used to account for the nonlinear distribution of axial strain in the masonry pier. The coefficient α_V is the pier shear ratio (4.12). It depends on the zero moment coefficient α_0 whose value varies with the location of the zero moment axis in the masonry and naturally depends on the boundary condition of the wall. The definition of α_0 is obtained from Equation (4.11), where all parameters are defined in Figure 4.3 from the article by Petrovčič and Kilar [99]. The moment M in Equation (4.11) is the moment with the highest absolute value applied to the pier.

$$\alpha_0 = \text{sign}(M) \times \begin{cases} \frac{H_0}{H} & \text{if } H_0 > H/2 \\ 1 - \frac{H_0}{H} & \text{otherwise} \end{cases} \quad (4.11)$$

$$\alpha_V = |\alpha_0|H/D \quad (4.12)$$

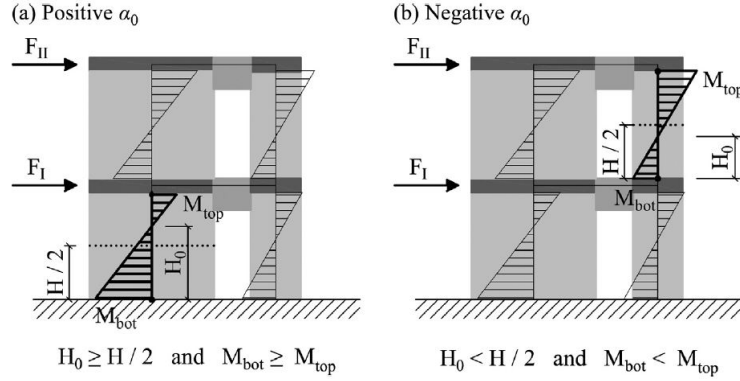


Figure 4.3: Moment distribution in a wall

4.4.1.3 Shear-sliding failure

There are two definitions in the literature for the shear-sliding failure of a masonry pier. The most common definition is the Mohr-Coulomb criterion (see Equation (4.13)). The other definition of shear-sliding failure considers the bending of the masonry in the pier and can predict the ultimate strength if the crack induced by sliding along the bed joint propagates along the head joints. To make it possible, this definition relies on the pier shear ratio as the definition of rocking (see Equation (4.14)).

$$f_{v,4} = \bar{c} + \bar{\mu}\sigma_v \quad (4.13)$$

$$f_{v,5} = \frac{1.5\bar{c} + \bar{\mu}\sigma_v}{1 + 3\alpha_V \cdot \frac{\bar{c}}{\sigma_v}} \quad (4.14)$$

Terms \bar{c} and $\bar{\mu}$ in Equation (5.11) and Equation (4.14) are adjustments of the value of the cohesion more accurate proposed by Mann and Muller [8] to make the results closer to the values determined experimentally. They consider the effects of vertical joints on these two parameters. Their definitions for cohesion and friction coefficient are:

$$\bar{c} = \frac{c}{1 + 2 \cdot \mu \frac{H_b}{L_b}} \quad (4.15)$$

$$\bar{\mu} = \frac{\mu}{1 + 2 \cdot \mu \frac{H_b}{L_b}} \quad (4.16)$$

4.4.1.4 Shear strength of the DFM

Equations (4.10) and (4.14) depend on the pier shear ratio α_V , which depends on the boundary conditions of the wall. Thus, the determination of such a parameter depends on the whole structure and does not make sense at the scale of the meso-element. For this reason, these two equations are not considered in the definition of the shear strength of the DFM.

Regarding the diagonal shear failure, among the above two definitions, the one proposed by Turnšek and Čačovič [3] is used, since it gives a better approximation to the ultimate force measured in experimental tests². Therefore, only Equations (4.7) and (5.11) are used to define the shear strength of the DFM F_u with the mechanical properties of the masonry (see Equation (4.17)).

$$F_u = l_m \cdot t_m \min(f_{v,1}, f_{v,4}) \cos(\theta_m) \quad (4.17)$$

4.4.2 Hysteresis models

The non-linear behavior of the diagonal elements allows to capture the hysteric behavior of the masonry under lateral cyclic IP solicitation. The ESM, which models masonry only by diagonal struts has the same feature. Therefore, it was decided to investigate in more detail the definition of the proposed hysteresis model in the literature and not to only consider those proposed for the RMEM. Four of the models studied are selected and are briefly presented below. They are chosen because they have some specificities compared to other models. The hysteresis behavior of these four models is shown in Figure 4.4.

4.4.2.1 Panagiotakos and Fardis's model

The model was proposed by Panagiotakos and Fardis [4]. It is inspired by the hysteretic model proposed by Tassios [102]. It is shown in Figure 4.4.(a). The hysteretic behavior is controlled

²Result of comparisons of the values with the two definitions of the diagonal failure for several experimental tests

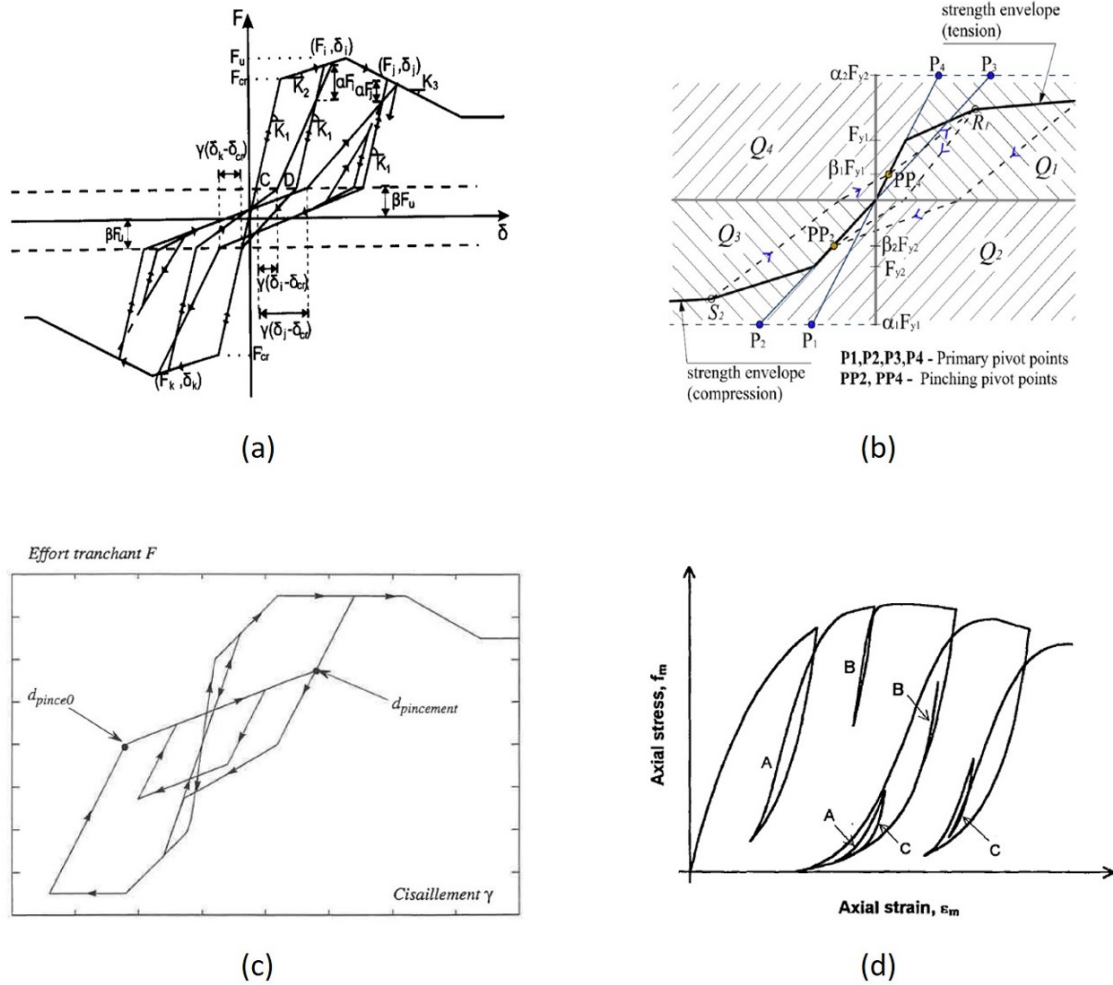


Figure 4.4: Four constitutive laws for ESM: (a) Panagiotakos and Fardis [4]; (b) Pivot Model [100]; (c) Combescure [33]; (d) Crisafulli [101]

by three empirical parameters: α , which accounts for a decrease in strength after a complete cycle, β , which defines the threshold for the change in stiffness during unloading-reloading when cracks close and reopen, and γ , which controls the width of the hysteresis loop. With only this limited set of empirical parameters, it is possible to obtain a reasonable approximation of the cyclic behavior of masonry described in Section 1.3.2. This model has a specific definition of the envelope curve which is composed of four different branches: Initial behavior, behavior after the first crack, softening behavior and the residual behavior. Different elastic definitions for these branches can be found in the literature.

4.4.2.2 Pivot model

It was presented and well detailed by Dowell et al. [103]. The envelope curve and hysteresis behavior of this model are shown in Figure 4.4.(b). Historically, it was not a model for masonry structures, but some researchers have used it because it is a very simple model. The unloading-reloading behavior is defined with only two parameters: α and β . These parameters can be different in tension and in compression, so the total number of empirical parameters is four. Unlike the first model, there is no cyclic damage in this model and the options for the shape of the hysteresis are limited. Ultimately, the small number of parameters makes the model easy to calibrate, but at the same time leads to lower accuracy compared to more sophisticated models, especially for the shape of the hysteresis.

4.4.2.3 Combescure's model

The unloading-reloading behavior proposed by Combescure is well described in his doctoral thesis [33]. The envelope curve and hysteresis behavior of this model are shown in Figure 4.4.(c). This model is not common in the literature, but it has some interesting aspects. Namely, it considers a degradation of the envelope as a function of the number of cycles, which causes the unloading stiffness to decrease. The damage parameter, D_{param} , is different in tension and compression. The model has fewer parameters than the model proposed by Crisafulli [101] (see below) and can provide a good approximation to the experimental results. Nevertheless, it needs a longer calibration than the above two models because there are more parameters.

The model has a specific envelope curve. Unlike the model proposed by Panagiotakos and Fardis, there are five branches and not four. The additional branch is located before the softening branch. The model considers that the masonry has a plateau at the maximum strength of the masonry.

4.4.2.4 Crisafulli's model

The unloading-reloading behavior is well described in the thesis of Crisafulli [101]. It takes into account several events: the complete unloading-reloading process, but also the cycles not completed, either for reloading or unloading; the influence of cracking; and the influence of the number of cycles in the damage process. This model tends to be as close as possible to reality and can therefore reproduce experimental curves with very good accuracy. This is at the same time the main strength of the model, but also its drawback. Indeed, in order to calibrate the model, several empirical parameters are used. Crisafulli [101] gives a set of values for each of them, but the calibration is still burdensome. This model has a specific envelope curve and, unlike all other models, it is defined in the stress-strain domain.

4.4.2.5 Choice of hysteresis model

The diagonal struts have to reproduce the cyclic behavior of masonry seen in Section 1.3.2. In this section, the following conclusions were drawn regarding the cyclic shear behavior of masonry:

- There is cyclic damage. After a complete cycle, the wall exhibits lower resistance at the maximum displacement reached.
- Masonry has different phases during an unloading-reloading process. This means that the secant stiffness of the masonry changes during a cycle. This change in secant stiffness can occur during both unloading and reloading processes.

Table 4.1 shows the peculiarities of the models presented earlier. In some models, cyclic damage is not taken into account. This is not a real problem, but it means that the model has to be modified. Some models offer the possibility to define a tripartite unloading-reloading process, but they are too strict in defining the unloading branch in the sense that it is always defined until the force changes sign. Panagiotakos and Fardis [4] and Crisafulli [101] are the only two models among those proposed that have a two-step unloading process.

The choice of the hysteresis behavior of the diagonal strut lies on the desire to have a model that is easy to calibrate. This implies that the hysteresis behavior has a limited number of parameters. This may affect the accuracy of the model in reproducing cyclic test curves, but this aspect is beyond the objectives of the model. In fact, the goal is to obtain a prediction of the behavior of the masonry structure. This prediction involves a global behavior of several masonry portions and since the behavior is not 100 % reproducible, the author believes that it is better to have a model that is easy to calibrate to approximate the experimental curve than a model that requires a long time of calibration to be accurate for an experimental curve that would be different if the test is reproduced several times.

For these reasons, the model proposed by Panagiotakos and Fardis [4] was chosen for the unloading-reloading behavior of the diagonal struts.

Table 4.1: Characteristics of the hysteresis models

	Unloading part	Reloading part	Cyclic damage	Empirical parameters
Xu et al. [71]	1 branch	2 branches	X	3
Combesure [33]	1 branch	2 branches	X	6
Crisafulli [101]	2 branches	2 branches	X	11
RMEM [2]	1 branch	1 branch		1
Panagiotakos and Fardis [4]	2 parts	2 parts	X	3
Pivot [103]	1 branch	2 branches		2

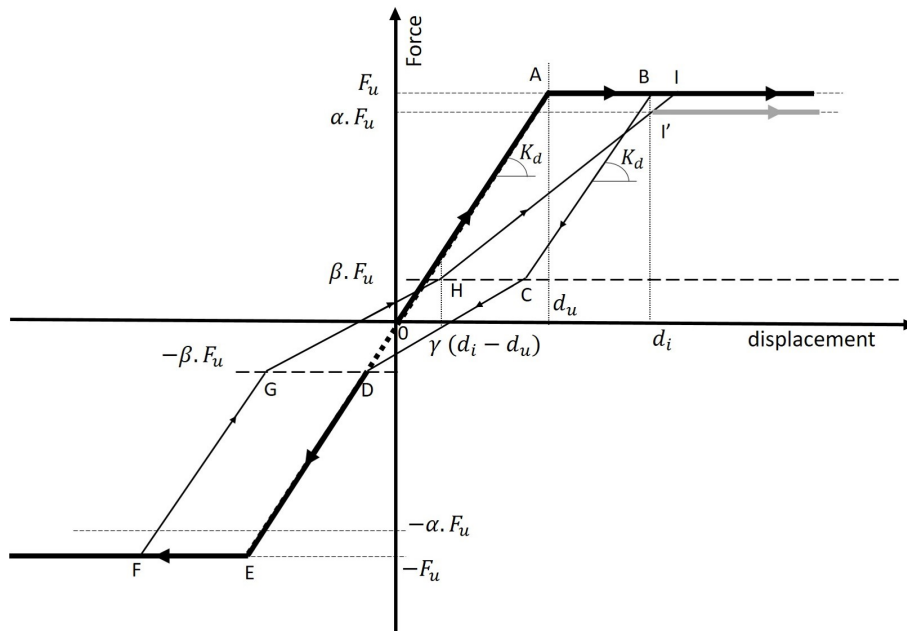


Figure 4.5: Force-Displacement constitutive law of the diagonal struts of the DFM

4.4.2.6 Envelope curve

The objective is to define the envelope curve only with parameters that have a fixed definition. As shown above, there are almost as many definitions for the envelope as there are hysteresis models. One parameter almost always has the same definition: the maximum strength. The other parameters (strength for the occurrence of the first crack F_{cr} , stiffness for the softening part, residual strength, etc.) do not have fixed definitions and vary from one article to another. Therefore, the envelope curve of the DFM is bilinear and is defined by only two parameters: the maximum strength and the initial stiffness of the diagonal strut. However, the envelope curve can be adjusted (trilinear curve) to model experimental tests if information on the ignition force of cracks is available (see Section 8.2).

4.4.2.7 Cyclic behavior of the DFM

The behavior of the DFM under cyclic shear loading with important displacements is shown in Figure 4.5. Since the unloading-loading path is the one proposed by Panagiotakos and Fardis [4], the only empirical parameters are α, β, γ . They are all initially defined with positive values. The black bold line represents the envelope curve, dashed lines represent parts of the curve that exist but that are not taken in the path of the considered loading. The first complete unloading-reloading is represented by the path BC-CD and the second complete unloading-reloading by the path FG-GH-HI (FG-GH-HI' with cyclic damage). The latter consists of a complete cycle when the wall has been damaged in both direction of solicitation. The difference between the

grey bold line and black bold line is the type of failure that occurs. The arrows in Figure 4.5 help to understand the different steps in the unloading-reloading behavior and do not represent the possible reversibilities on the different branches. In order to better understand the loading-reloading behavior, the two different paths are explained.

Wall damaged in one direction:

In the path represented by branches BC-CD (Figure 4.5) the ultimate force (resp. ultimate displacement) of the wall F_u (resp. d_u) has been reached in only one direction. That does not necessarily mean that the wall has been loaded in only one direction. The unloading path in this case is as follows:

1. From point B, the unloading occurs with initial stiffness K_d . This behavior occurs until the force $\beta.F_u$ is reached. This branch represents the beginning of the unloading of the wall when the cracks are closed. The change in the behavior of the wall occurs once the force $\beta.F_u$ is reached. It is the point C in Figure 4.5.
2. Arriving at point C, the stiffness decreases. It allows to reproduce the opening of the cracks produced by the solicitation in this direction. Since the wall has not been damaged in the other excitation direction, the point targeted by the constitutive law is the point of ordinate $\beta.F_u$ on the envelope on the opposite side, point D in Figure 4.5. After this point the DFM follows the behavior of the envelope curve.

Wall damaged in both direction:

It is represented by the path FG -GH- HI (or FG -GH- HI'). In this case, the maximal force of the wall F_u is reached in both directions. The maximum displacement reached in the opposite direction is denoted as d_{max} . For the path described in Figure 4.5, $d_{max}=d_B$. The unloading path in this case is as follows:

1. From point F, the unloading takes place with the initial stiffness K_d as from point B. The branch FG is described exactly as the branch BC.
2. After reaching the point G, the following branch is not defined like the branch CD. Since the wall has already been damaged in the opposite direction, some cracks remain open due to the reloading. Thus, two phenomena occur on the branch GH: closing of cracks in one direction and reopening of cracks in the other direction. To describe the path, one notes $d_{\beta F_u} = \gamma.(d_{max} - d_u)$ the displacement at force $\beta.F_u$ in the other direction.
3. Depending on the mode of failure that occurs, the last part of the curve is defined differently.
 - At point H, the wall exhibits damaged stiffness until the maximal force F_u is recovered. To account for cyclic damage, one considers that the force reached at displacement d_{max} is no longer F_u , but αF_u with $\alpha < 1$. Therefore, point I in Figure 4.5 is different from point B. After the point I, one follows the envelope curve again. This type of behavior occurs when the failure occurs along a bed joint.

- If the failure is along the wall diagonal, the wall has a brittle behavior. Therefore, the envelope curve is degraded. To capture this degradation, the value $\alpha F(d_{max})$ is chosen as the new maximum of the envelope curve as shown in Figure 4.5 with the branch HI' . After the point I' , the new definition of the envelope curve is followed.

Small cycles may occur during seismic excitations. If the first step of the unloading part is reversible, the second step is not. Figure 4.6 shows the behavior of the diagonal strut when there is a small cycle. If there is a change in the load direction during the cycle, the force-displacement curve targets the coordinate point $(d_i, \alpha F_u)$ and continues until it reaches the envelope curve again. If the load changes direction again before reaching the envelope curve, at a point Y , there are two possibilities:

1. $|F_y| > |\beta \cdot F_u|$: In this case, a branch similar to the branch BC is followed until the point X at the force $\beta \cdot F_u$ is reached. After this point the behavior follows the path XD (see Fig. 4.6.(a)).
2. $|F_y| < |\beta \cdot F_u|$: In this case the branch has a slope K_d , but the point X is not on the ordinate $\beta \cdot F_u$. The point X is the intersection of the unloading branch from the point Y and the branch CD . Once the point X is reached, the path XD is followed (see Fig. 4.6.(b)).

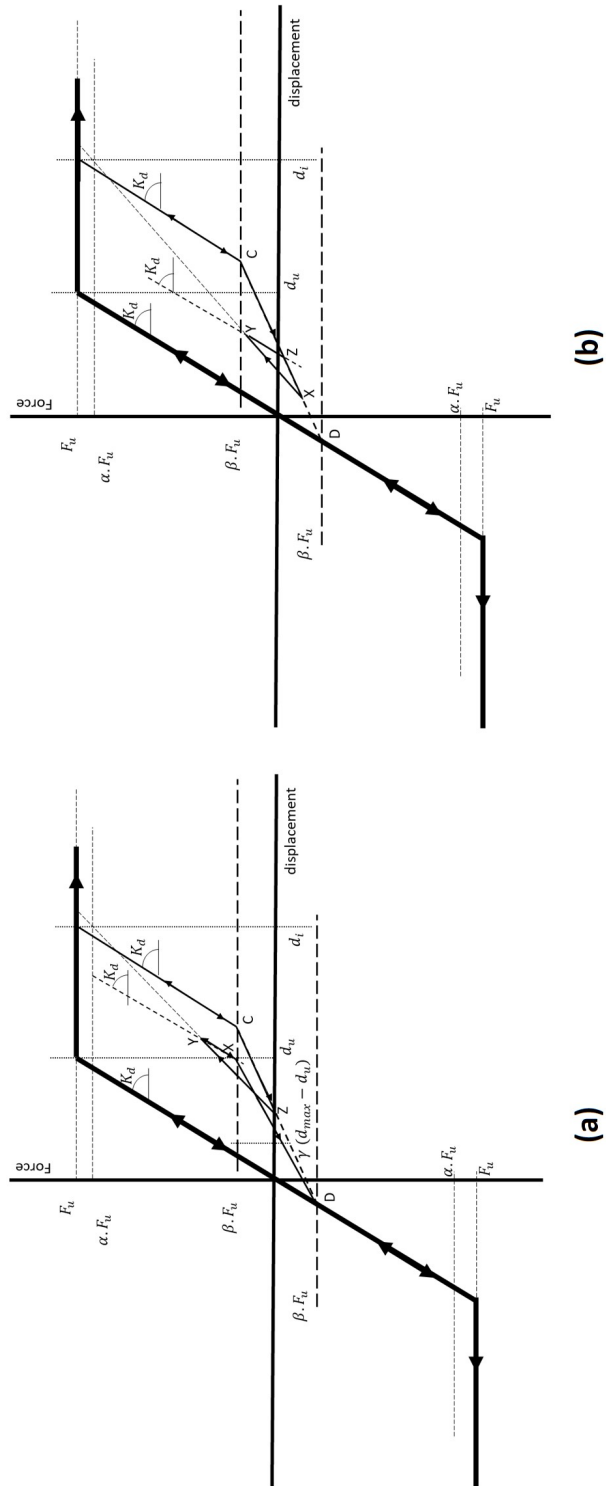


Figure 4.6: Force-Displacement behavior of the diagonal struts of the DFM with small cycles

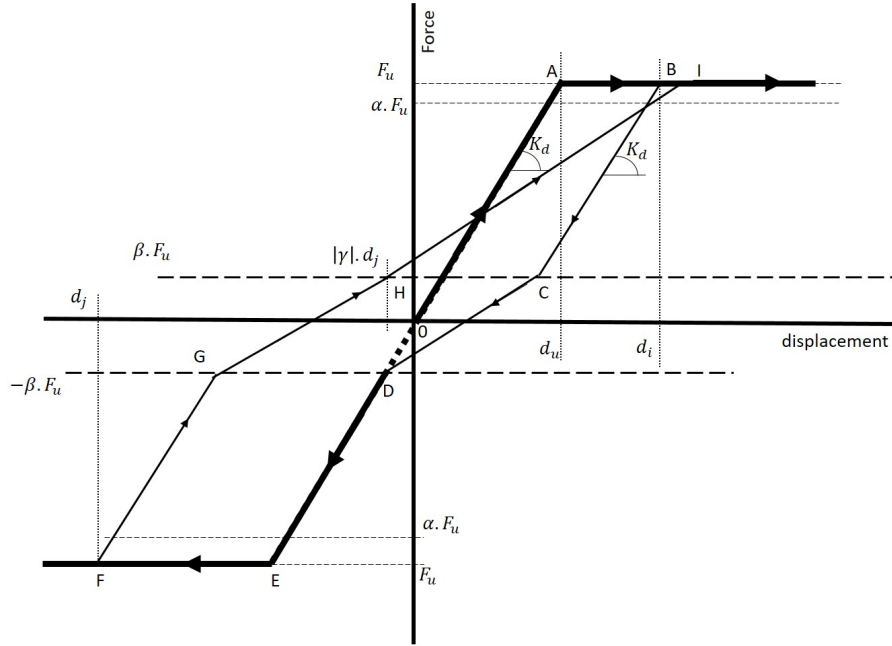


Figure 4.7: Hysteresis loop of the diagonal struts constitutive law with a negative value of δ

To extend the capabilities of the model proposed by Panagiotakos and Fardis [4], the DFM unloading-reloading behavior can be defined with a negative value of the parameter γ . In this case, the path BC-CD remains unchanged. However, the location of the point H changes. Its new definition is given by Equation (4.18), where the displacement d_j is the displacement when the unloading occurs. The path described above does not change. This new definition of the branch enables to have wider hysteresis loops. Figure 4.7 shows the shape of the curve with this new definition. This new definition of d_h is inspired by the Humbert hysteresis model originally developed for timber connections [104].

$$d_h = \text{sign}(d_j) \cdot \min \left(|\gamma| \cdot d_j, \text{abs} \left(d_j - (1 + \text{sign}(d_j)\beta) \frac{F_u}{K_0} \right) \right) \quad (4.18)$$

4.4.2.8 Parameters of the hysteresis

Panagiotakos and Fardis [4] did not give any formula for the parameters defining the hysteresis. In order to predict the cyclic behavior of masonry structures without the help of experimental cyclic tests, formulas for α , β and γ are proposed. These empiric formulas are defined to approximate values determined by fitting experimental curves on walls without openings. It is supposed that the value of the parameters is the same in the two directions of loading.

The parameter α is used to reproduce the softening behavior of masonry associated with

cyclic loading. The deterioration of the properties of the wall depends on its slenderness and the vertical load. Since the strength of masonry associated with diagonal failure increases with the vertical loading, it is assumed that the cyclic damage is inversely proportional to the vertical loading. Finally, the parameter α is defined as follows:

$$\alpha = 0.9 + \frac{b_{diag} - 1}{1 + \sigma_v/f_t} \quad (4.19)$$

The parameter b_{diag} in Equation 4.19 is similar to the parameter b used to define the maximum strength of the diagonal element. However, its definition is slightly different, as shown by Equations (4.20) and (4.21). This parameter b_{diag} is inspired by the crack pattern for diagonal cracks, which depends on the slenderness of the wall as shown in Figure 4.8, and the definition of the parameter b in the literature that differs for masonry piers and spandrels. The crack pattern affects the cyclic behavior of the wall. Even though the shear-sliding failure does not have such a pattern, it appeared that this formula can approximate the experimental results for this failure.

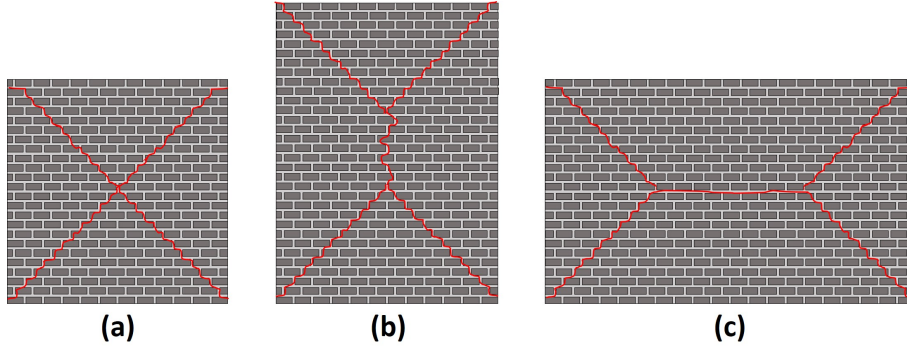


Figure 4.8: Diagonal crack pattern for masonry walls with different slenderness

- if $h_m > l_m$

$$b_{diag} = 1 \leq h_m/l_m \leq 1.5 \quad (4.20)$$

- if $h_m < l_m$

$$b_{diag} = 1 \leq l_m/h_m \leq 1.5 \quad (4.21)$$

The parameters β and δ define the change of stiffness of the wall during the unloading-reloading of masonry and the global shape of the hysteresis loop. It is considered that they only depend on the slenderness of the wall. They are defined by Equations (4.22) and (4.23).

$$\beta = 0.2b_{diag}^2 + (1 - b_{diag})^2 \quad (4.22)$$

$$\gamma = -0.4 + 2(1 - b_{diag}) \quad (4.23)$$

4.5 Refined mesh

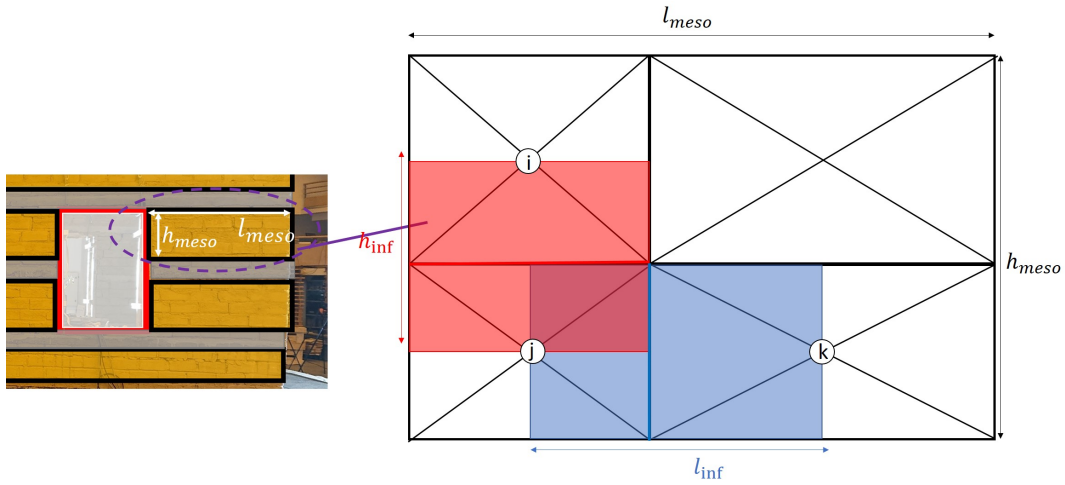


Figure 4.9: Example of a refined mesh with the DFM

The yellow part in Figure 4.1 can be modeled by more than one meso-element. An example of a finer mesh is shown in Figure 4.9. This example provides several pieces of information. First, for modeling purposes, the meso-elements are not necessarily equal in size. However, horizontally aligned meso-elements have the same height and vertically aligned meso-elements have the same width. Moreover, adjacent DFM elements share nodes. This reduces the number of elements and degrees of freedom. Namely, if one models two adjacent meso-elements, one has eight nodes to define the RMEM, while the proposed model has only six nodes. This reduction in the number of elements and degrees of freedom aims to reduce the computation time of the DFM. However, this modeling strategy does not have only advantages. Since the elements share struts, it is not possible to capture the splitting of masonry parts.

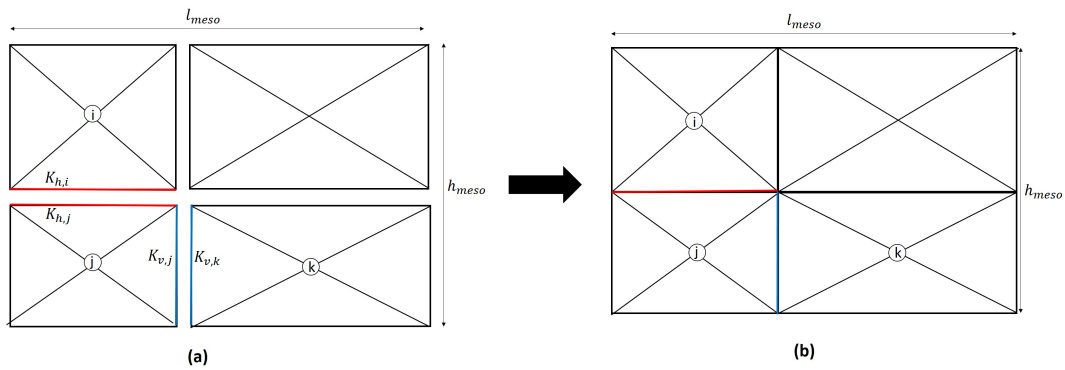


Figure 4.10: Meshing with the DFM with several meso-elements: (a) exploded view of the 2x2 meshing and (b) merging of the elements to create the mesh

Figure 4.10 shows the four meso-elements of the 2x2 mesh to explain the creation of the mesh. The red and blue struts in Figure 4.10.(b) are equivalent to two springs connected in parallel, the two blue in Figure 4.10.(a) (one strut from meso-element i with stiffness $K_{h,i}$ and one strut from meso-element j with stiffness $K_{h,j}$ for the red strut, and one strut from meso-element j with stiffness $K_{v,j}$ and one from meso-element k with stiffness $K_{v,k}$ for the blue strut). The stiffness of the red struts and the blue struts are defined by Equation (4.24) and Equation (4.25), respectively. In these equations h_{elem} (resp. l_{elem}) is the length of the strut under consideration and θ_i is the angle of the diagonal strut with the horizontal in meso-element i and $K_{d,i}$ is the stiffness of the diagonal strut of meso-element i . In Equation (4.24), $h_{inf} = 0.5(h_i + h_j)$ is the height of the influence area of the horizontal strut. Similarly, $l_{inf} = 0.5(l_j + l_k)$ is the width of the area of influence of the vertical strut.

$$K_h = E_m \cdot \frac{h_{inf} \cdot t_m}{2 \cdot l_{elem}} - K_{d,i} \sin^2(\theta_i) - K_{d,j} \sin^2(\theta_j) \quad (4.24)$$

$$K_v = E_m \cdot \frac{l_{inf} \cdot t_m}{2 \cdot h_{elem}} - K_{d,j} \sin^2(\theta_j) - K_{d,k} \sin^2(\theta_k) \quad (4.25)$$

4.6 Conclusion

Table 4.2: Parameters for the definition of the DFM

Material properties for the stiffness of the DFM	
Young's modulus [E_m]	Shear modulus [G_m]
Material properties for the shear strength of the DFM	
Tensile strength [f_t]	Cohesion [c]
Coefficient of friction [μ]	Density of masonry [ρ_m]
Length of the bricks [L_b]	Height of the bricks [H_b]
Parameters for the hysteresis of the DFM	
Cyclic damage [α]	Force for change of stiffness [β]
Plasticity [γ]	

A new meso-model, the Deformable Frame Model, has been introduced for FE oriented software. It is strongly inspired by the RMEM and somewhat by the model proposed by Xu et al. [71] and the ESM. With only four nodes and eight degrees of freedom, the DFM aims to reproduce the behavior of masonry under seismic loading. The meso-element consists of three different elements: vertical and horizontal struts forming the sides of the frame, and diagonal struts inside the frame. Only the last elements have an inelastic behavior. This inelastic behavior is defined by a bi-linear constitutive law. The change of branch in the envelope curve occurs when the shear strength of the masonry is reached. This maximum strength is determined by considering diagonal failure and shear-sliding failure. The cyclic shear behavior of masonry is defined by a modified version of the law proposed by Panagiotakos and Fardis [4]. The aim is to obtain an acceptable approximation of the experimentally measured hysteresis loops with few parameters.

The properties of the DFM are determined using the parameters in Table 4.2. All of these properties are necessary to model the cyclic behavior of masonry.

The DFM models only masonry portions. For the modeling of masonry structures with bands, it must be connected with interface elements and beams. These additional elements are the topic of the next chapter.

Chapter 5

Modeling of other structural elements

The DFM was introduced for modeling masonry in the previous chapter. Since it can only model masonry, additional elements are required to model structures with horizontal bands. This new chapter describes the way to model the other structural elements: horizontal bands, frames at the opening and lintels.

The bands are modeled by interfaces because sliding occurs at the masonry/band interface. The first section focuses on the modeling strategies for interface elements. This allows explaining the model of interface chosen for this work. This model is presented in the second section. Lastly, the modeling of the reinforcements at the openings and the lintels is tackled.

5.1 Modeling of bands

During the experimental tests shown in Section 2.5, the same phenomena were often observed at the bands. First of all, the bands did not suffer any damage during the tests, regardless of the material they were made of. However, when the band did not suffer damage, the masonry/band interface is damaged, resulting in sliding. The damage at the interfaces is either due to their own failure or to the propagation of cracks from the masonry to the bands. Since only sliding has to be reproduced, horizontal bands are modeled by interface elements separating two DFM elements.

With the RMEM, the interface between two meso-elements is modeled by sliding springs (see Section 3.3.6.2). These springs were defined by the Mohr-Coulomb criterion. In the context of the thesis, with the DFM, the use of springs is not considered. This modeling is possible for FE, but it is desired to have a continuous model for the interface and not just a local behavior defined between two nodes. To obtain an adequate model for the interfaces, models from the bibliography are considered. Besides discrete modeling of interfaces, there are two main types

of modeling: zero-thickness interfaces and thin interfaces. These two types of interface modeling are examined below. The advantages and disadvantages of each are addressed in order to make a choice for the context of masonry structures with bands.

5.1.1 Overview of interface models

5.1.1.1 Zero-thickness interface

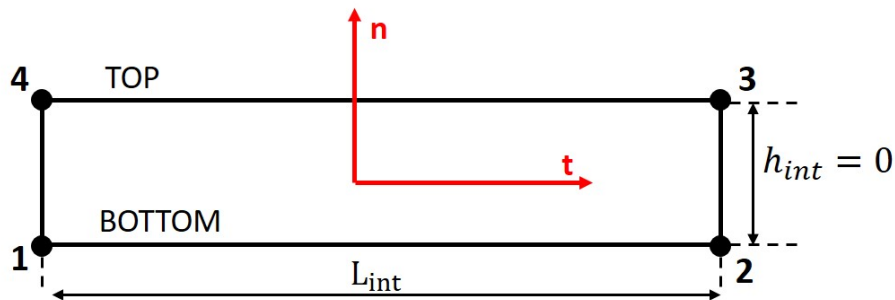


Figure 5.1: Zero-thickness interface model

This type of model can be found under the names "zero-thickness interface" or "joint elements". The zero-thickness interface model is the oldest and the most commonly used interface model. This interface type is used for simplified micro-models. It is based on the rock joint modeling element created by Goodman et al. [105].

As the name implies, the interface is modeled with zero-thickness elements. To do this, four nodes are used to define the interface, as shown in Figure 5.1. In this figure, points 1 and 4 (resp. points 2 and 3) are initially at the same coordinates. The constitutive law of the element is defined by the differential displacement of the points that have the same position at the beginning. Therefore, the zero-thickness interface is in some sense similar to a discrete interface. The elastic behavior of the interface is given by Equation (5.1), where σ_n is the stress with respect to the axis \vec{n} , τ is the shear stress with respect to the axis \vec{t} , k_n and Δu_n (respectively k_t and Δu_t) are the stiffness and the differential displacement in normal direction (respectively tangential direction). Depending on the unit of stiffness, Equation (5.1) can be encountered with the force vector t_{int} in place of σ_{int} .

$$\{\sigma_{int}\} = \underline{K}_{int} u_{int} = \begin{Bmatrix} \sigma_n \\ \tau \end{Bmatrix} = \begin{bmatrix} k_n & 0 \\ 0 & k_t \end{bmatrix} \cdot \begin{Bmatrix} \Delta u_n \\ \Delta u_t \end{Bmatrix} \quad (5.1)$$

This way of modeling interfaces has a major drawback: to avoid interpenetration of elements, the stiffness k_n in compression must be high. It consists in a penalization method and a well-known aspect of this method is that the choice of the value of the penalization rigidity has an

impact on the final result. When interpenetration is accepted, it is common to define the stiffness of the interface using the mechanical properties of the bed joint of height h_j , Young's modulus E_j and Poisson's ratio ν_j (see Equations (5.2) and (5.3)). In its original formulation (Goodman et al. [105]), the zero-thickness element does not have any rigidity if the bottom and top surfaces are not in contact. The model has since been improved to allow tensile behavior, as shown in the next section.

$$k_n = \frac{E_j}{h_j} \quad (5.2)$$

$$k_t = \frac{k_n}{2(1 + \nu_j)} \quad (5.3)$$

The differential displacement, whose coordinates are Δu_n and Δu_t in Equation (5.1), can be determined by calculating the difference between the global displacement of the top surface u_{top} and the bottom surface u_{bot} . These two displacements u_{top} and u_{bot} are determined using isoparametric shape functions (N_1 and N_2 in Equation (5.4)). The displacements $u_{n,i}$ and $u_{t,i}$ are the normal and tangential displacements at node i .

$$\begin{Bmatrix} \Delta u_n \\ \Delta u_t \end{Bmatrix} = \begin{Bmatrix} u_{n,top} - u_{n,bot} \\ u_{t,top} - u_{t,bot} \end{Bmatrix} = \begin{Bmatrix} N_1 \cdot (u_{n,4} - u_{n,1}) + N_2 \cdot (u_{n,3} - u_{n,2}) \\ N_1 \cdot (u_{t,4} - u_{t,1}) + N_2 \cdot (u_{t,3} - u_{t,2}) \end{Bmatrix} \quad (5.4)$$

Equation (5.1) and Equation (5.4) are defined for 2D modeling, but it is possible to extend them to 3D modeling by considering the second tangential displacement, as proposed by Beer [106]. Equation (5.1) thus becomes Equation (5.5).

$$\{\sigma_{int}\} = \underline{K}_{int} u_{int} = \begin{Bmatrix} \sigma_n \\ \tau_t \\ \tau_s \end{Bmatrix} = \begin{bmatrix} k_n & 0 & 0 \\ 0 & k_t & 0 \\ 0 & 0 & k_t \end{bmatrix} \cdot \begin{Bmatrix} \Delta u_n \\ \Delta u_t \\ \Delta u_s \end{Bmatrix} \quad (5.5)$$

5.1.1.2 Thin interface

Thin interface elements were introduced to get rid of the zero-thickness interface problems associated with the rigidity of the elements. In such models, the interface is modeled by a continuum that has non-zero thickness to avoid interpenetration (see Figure 5.2). This idea of modeling was first proposed by Desai et al. [107] for soil/structure interaction. In this type of study, the properties of the interface are not straightforward since it does not model either the soil or the structure. However, in the case of masonry, the thin interface can be interpreted as the mortar between blocks or between units and bands. Thus, the interface element has the mechanical properties of the mortar.

This type of model has the advantage of allowing the user to link the strain and the stress directly to measurable parameters such as the elastic modulus and Poisson's ratio, as shown by

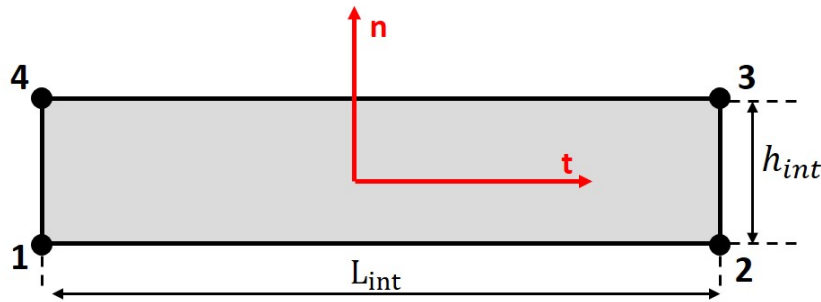


Figure 5.2: Thin interface model

Equation (5.6), which defines the elastic behavior. Gaussian integration points are normally used to determine the strain and stress at each node of the element. The use of Gaussian integration points requires a certain distance between them to avoid convergence problems.

$$\{\sigma_{int}\} = \underline{D}_{int}\varepsilon_{int} = \begin{Bmatrix} \sigma_n \\ \tau \end{Bmatrix} = \begin{bmatrix} E_j & 0 \\ 0 & \frac{E_j}{2(1+\nu_j)} \end{bmatrix} \cdot \begin{Bmatrix} \varepsilon_n \\ \varepsilon_t \end{Bmatrix} \quad (5.6)$$

To obtain good results, the dimensions of the thin interface, h_{int} and L_{int} , must respect the inequality (5.7) proposed by Desai et al. [107].

$$0.01 \leq h_{int}/L_{int} \leq 0.1 \quad (5.7)$$

5.1.1.3 Choice of interface model

Both types of models have their advantages and disadvantages. The choice between them depends on what one can accept for modeling masonry with horizontal bands. In order to make a choice, one considers the connection of the interface model with the DFM. Figure 5.3 shows an example of the connection between the interface element and the DFM. Since both zero-thickness elements and thin-interface use four nodes, the connection with the DFM would be the same regardless of the model chosen. As expected, the connection between the interface element and the DFM is simple. The interface element shares two nodes with the DFM element at the bottom and two nodes with the DFM element at the top. This simple connection allows the number of degrees of freedom to be limited since the element uses pre-existing nodes.

Since the interface elements use the same nodes as the DFM, the conditions on the dimensions of the thin interface affect the dimensions of the DFM. Using Equation (5.7), it is possible to set bounds that the width of the DFM l_m must respect in order to obtain trustworthy results with thin interfaces. The bounds are the following:

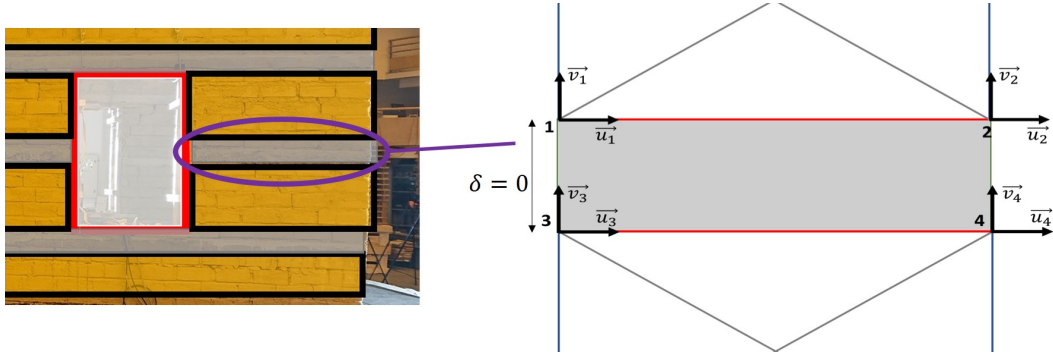


Figure 5.3: Example of connection between interface element and DFM elements

$$0.01l_m \leq h_{int} \leq 0.1l_m \quad (5.8)$$

This inequality would be another constraint on the size of the meso-elements after the constraint in Section 4.3.1 associated with the coupling of the stiffness of the different struts of the DFM. In order to avoid another constraint to be considered when modeling masonry structures with bands, the choice was made to use zero-thickness elements for the interface. The elastic behavior of the interface is defined by Equation (5.1) and the displacement by Equation (5.4).

5.1.2 Inelastic behavior of the interface

The inelastic behavior of the interface is based on the models used for the simplified micro-models. The interface used in the context of the thesis has a brittle behavior in tension and a plastic behavior in shear, as shown in Figure 5.4. The behavior in pure compression remains elastic with the same stiffness than in tension. Thus, interpenetration of the elements is allowed. The constitutive law chosen is a mixture of the law used by D'Altri et al. [52] and the law used by Abdulla et al. [50].

The interface has a brittle behavior after the tensile strength f_{tm} is reached. This tensile behavior is described by a damage parameter D_{param} . The evolution law of this parameter is linear and is the same as that used by Abdulla et al. [50]. Equation (5.9) defines D_{param} with the parameters shown in Figure 5.4.(a). These parameters are the displacement limiting the elastic behavior of the interface in tension u_{0n} , the maximal reached normal displacement $u_{max,n}$ and the ultimate displacement u_{fn} . The definition of u_{0n} is straightforward. The ultimate displacement u_{fn} is determined by an energy criterion. The blue area in Figure 5.4 is actually the energy release rate for the mode I failure G_I . Since the constitutive law has a linear behavior in the softening part, it is possible to simply relate the value of the blue area to the displacement u_{fn} (see Equation (5.10)). The interface has an elastic behavior under compression. Therefore, it is not shown in Figure 5.4.

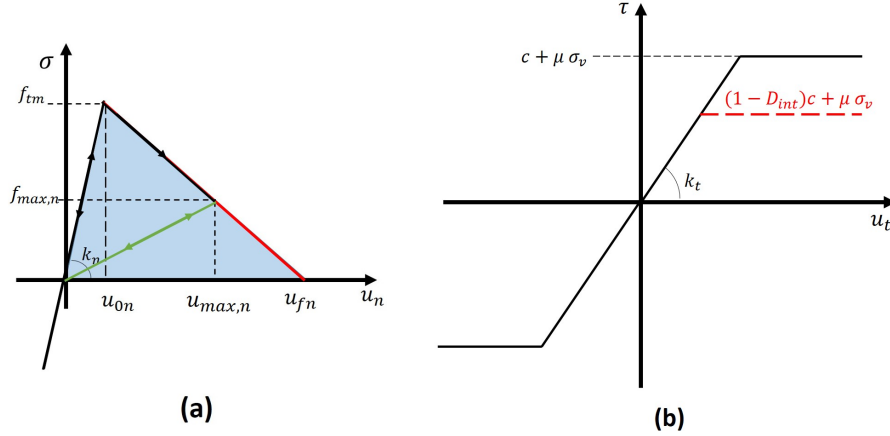


Figure 5.4: Behavior of the interface: (a) tensile behavior; (b) shear behavior. The red line is the part of the envelope curve that has not been reached by the loading.

$$D_{param} = \frac{u_{fn}(u_{max,n} - u_{0n})}{u_{max,n}(u_{fn} - u_{0n})} \quad (5.9)$$

$$u_{fn} = \frac{2G_I}{f_{tm}} \quad (5.10)$$

The shear behavior differs from the proposals of Abdulla et al. [50] and D'Altri et al. [52]. In order to avoid convergence problems due to a complex definition of the damage parameter D_{param} , it was decided to consider only the damage due to mode I failure, which is considered to be the main factor responsible for the interface damage. Therefore, in Figure 5.4.(b), after reaching the ultimate shear strength defined by the Mohr Coulomb criterion (Equation (5.11)), sliding without damage can be seen. However, the cohesion of the interface may be affected by the damage due to mode I failure. Therefore, the maximum strength in shear is defined by Equation (5.15).

Not damaged interface:

$$\tau_{im} = c + \mu \langle -\sigma_v \rangle \quad (5.11)$$

Damaged interface:

$$\tau_{im} = (1 - D_{param})c + \mu \langle -\sigma_v \rangle \quad (5.12)$$

The cyclic behavior is different in the normal direction and in the tangential direction. The interface has a damaged elastic behavior in tension. This means that the unloading process is performed with a damaged stiffness defined by Equation (5.13) and the interface returns to its initial state. In compression, the interface has always the initial stiffness k_n . However, when

the interface is loaded in tension again, the path follows the unloading branch aiming the point $(u_{max,n}; u_{fmax,n})$ (green path in Fig 5.5).

$$\hat{k}_{u,n} = (1 - D_{param})\hat{k}_n \quad (5.13)$$

Under cyclic shear excitation, the interface exhibits plastic behavior. The unloading occurs with the initial tangential stiffness k_t . This behavior with the initial tangential stiffness occurs until the maximal shear stress $\pm\tau_{lim}$ is reached again (see Figure 5.5). In Figure 5.5 the damage parameter is not called D_{param} . The reason for this is given in the next section.

The interface model does not consider dilatation because it is considered a phenomenon of minor importance [60]. The angle of dilatation was determined by Van der Pluijm [108] for bed joints under shear excitation equal to 10° and is therefore neglected in several studies. The coefficient of friction is considered constant regardless of what happens to the interface.

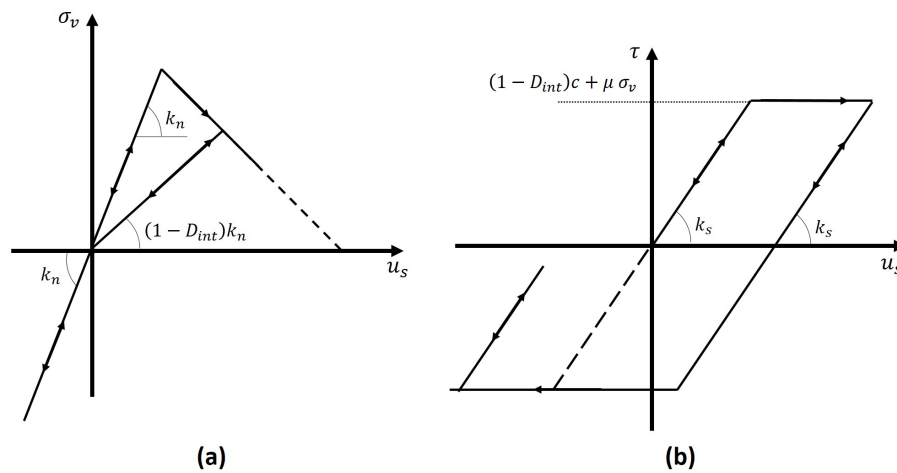


Figure 5.5: Cyclic behavior of the interface model: (a) tensile behavior; (b) shear behavior

5.1.3 The coupling with the DFM

In chapter 2, with the experiments of Aranguren et al. [45], it was seen that it is possible for a crack to propagate from the masonry to the band. This crack can damage the interface between the masonry and the band and initiate sliding. The interface model as currently defined cannot capture this phenomenon. To capture it, a coupling is set between the interface element and the DFM.

Since the DFM elements and the interface elements use the same nodes, it is easy to identify the diagonal elements connected to the interface. The determination of the damage of the interface due to crack propagation is related to the behavior of these diagonal elements. For this

purpose, a new parameter, φ_{int} , is used. This parameter helps to define the displacement for which the cohesion of the interface becomes zero, as shown in Figure 5.6. In this figure, the curve on the left is the envelope curve of the diagonal element of the DFM. To keep the same reasoning for the damage of the interface as described in the previous section, the damage associated with the behavior of the meso-element is denoted by D_{meso} . It is zero if the meso-element does not have any damage and is equal to 1 if the cracks in the masonry completely damaged the interface. This parameter D_{meso} has a linear behavior as a function of the maximum deformation of the diagonal elements, as shown in Figure 5.6. It is defined as:

$$D_{meso} = \begin{cases} 0 & \text{if } d < d_u \\ \frac{d - d_u}{\varphi_{int} \cdot d_u - d_u} & \text{if } d_u < d < \varphi_{int} \cdot d_u \\ 1 & \text{if } \varphi_{int} \cdot d_u < d \end{cases} \quad (5.14)$$

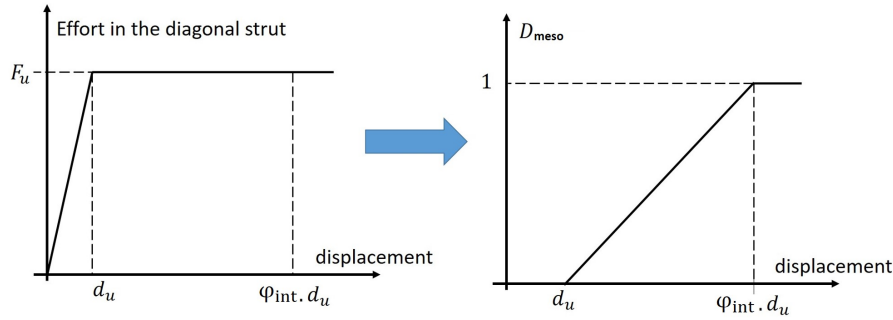


Figure 5.6: Damage of the cohesion by crack propagation by coupling the interface element with the DFM

The damage due to the behavior of the meso-element D_{meso} is not cumulative to the damage due to the behavior of the interface itself D_{param} . The total damage parameter of the interface D_{int} is the maximum of the two parameters, as shown in Equation (5.15). The parameter D_{meso} is used in Section 8.3.

$$D_{int} = \max(D_{param}; D_{meso}) \quad (5.15)$$

5.2 Reinforcements at the openings

In the context of the thesis, only two kinds of reinforcement are encountered: frames at the openings and lintels. Vertical reinforcements at the corners are not addressed in any of the proposed modeling, but they would follow the same modeling methodology.

During the experimental tests shown in Chapter 2, only one test was performed on structures with frames at the openings and/or lintels. This experimental test by Ali et al. [47] showed that these elements did not suffer any damage during seismic loading, although the structure was considered to be destroyed. Therefore, the choice is made in this thesis to model them as beams with an elastic behavior. Since they are beam elements, the use of an inelastic constitutive law, if necessary, will be straightforward.

The modeling of the lintels and the frames at the opening is similar, but there are some peculiarities in each case. Therefore, each type of reinforcement has its own section.

5.2.1 Frames at the opening

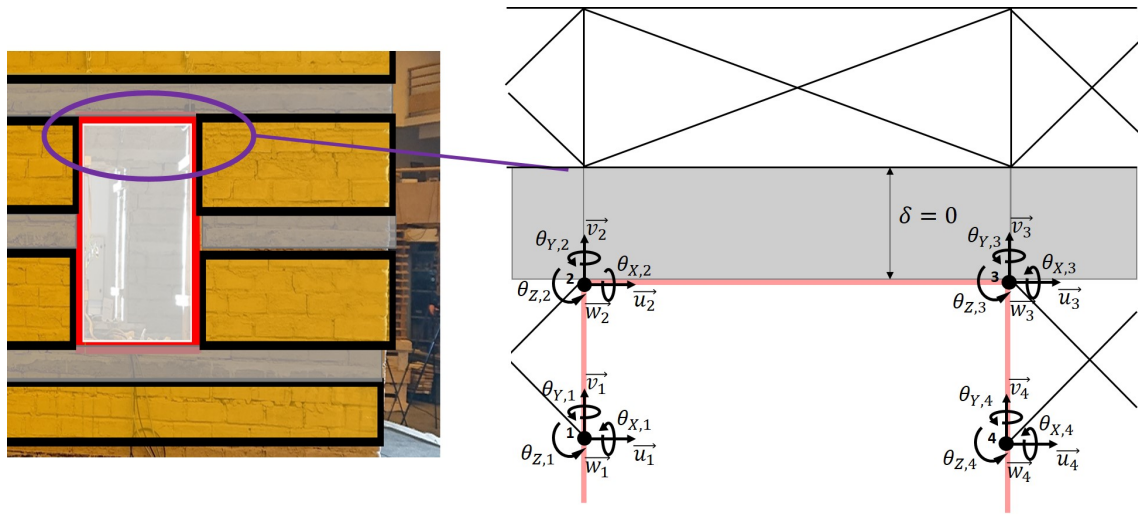


Figure 5.7: Kinematics of the nodes part of frame elements

An example of modeling the frame at the opening is shown in Figure 5.7. The beam elements representing the frame are shown in red in the figure. The nodes are shared with the other elements. Therefore, the beam of the frames are set in parallel to the struts of the DFM. In Figure 5.7, nodes 1 and 4 are part of the beam element that models the frame and the DFM elements, and nodes 2 and 3 are part of the beam element that represents the frame, the DFM element, and the interface. These nodes have four additional degrees of freedom to represent the beam (the OOP displacement w + the rotations around every axis θ_i for \vec{i} axis), while they have only two degrees of freedom in the case of the DFM for IP modeling and in the case of the interface.

Note that it is not possible to model a loss of contact between the different elements (beam and DFM elements with nodes 1-2 and nodes 3-4). The definition of the beam elements in this case is straightforward.

5.2.2 Frames at the opening

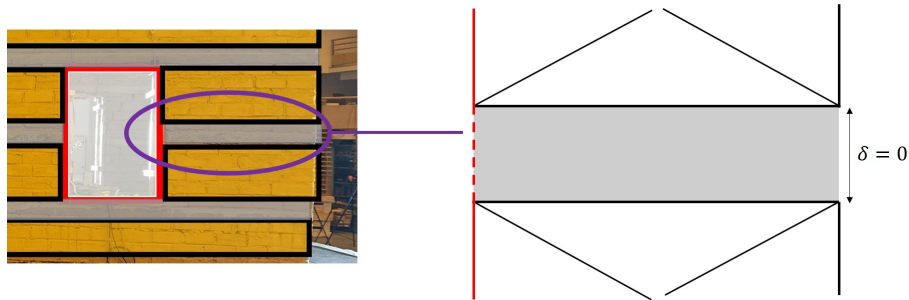


Figure 5.8: Intersection of vertical beam elements in presence and zero-thickness interface

A special case occurs at the intersection of vertical beam elements in presence and zero-thickness interface. An example of this situation can be seen in Figure 5.8, where the frame in question is represented by a dashed line. At this location, there are in fact two meso-elements separated by a zero-thickness interface. For the frame modeling, the two nodes located at the same coordinate in the interface are connected by a beam element with small length to avoid problems with zero-length elements. It ensures a non-sick definition of the element and provides a force transmission and a kinematic continuity between the two nodes to obtain a relevant beam behavior.

5.2.3 Lintels

Some constructions, such as the SM2 model tested by Ali et al. [47] in Section 2.5.2, have lintels above the opening and no additional reinforcements. In this context, there are two possible cases: there is a lintel above an opening, but this lintel has a limited length, or there is a lintel band along the entire wall.

If the lintel has a limited size, either the DFM element mesh has to be adapted to the size of the lintel or the lintel is not be fully modeled. This choice is a consequence of the connection between the different elements. Since the beam elements and the DFM share the same nodes, the dimensions of the lintel could have an important influence on the meshing. To avoid this important constraint, the mesh is created with the DFM without considering the dimensions of the lintel. Once the mesh is created with the DFM, the lintel is modeled by a beam element whose size is limited to the nodes included in the real dimensions of the lintel, as shown in Figure 5.9. This means that the lintel in the model is either as long as the lintel in reality, or it is smaller. Section 8.2 presents a study case with a wall that has lintels with a limited size over the openings. This study case shows the effects of this choice of the lintel modeling on the results.

In the case where the shear band is used as a lintel, the beam elements representing the lintels are modeled only above the opening so as not to interfere with the proposed modeling of the bands. This modeling above the opening allows the structural benefits of the lintel to be

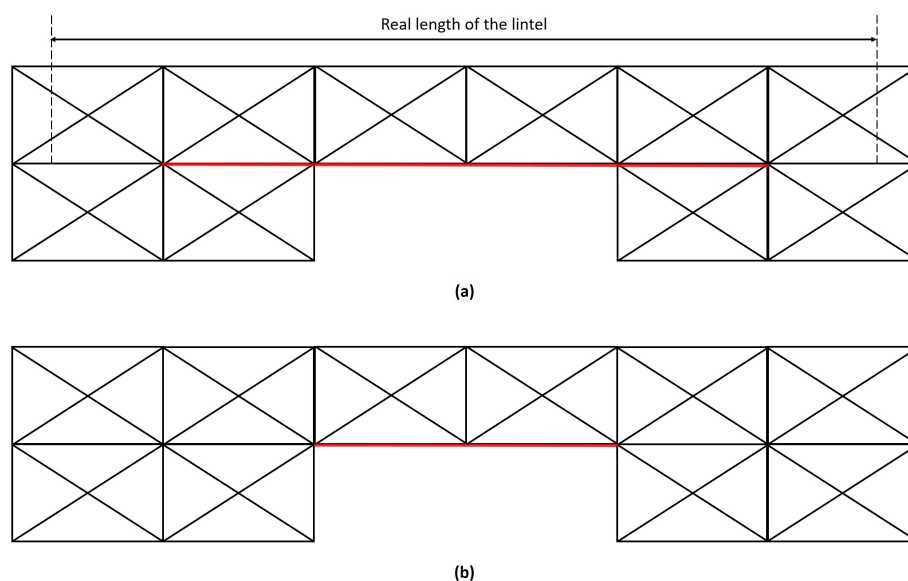


Figure 5.9: Modeling of lintel when it is not made by a horizontal band

preserved and interface elements to be modeled along the entire wall. However, this beam element adds an important stiffness in the horizontal direction and the behavior of the two masonry parts connected by the element obtains a composite behavior that does not exist in reality.

5.3 Conclusion

This chapter presented the modeling of structural elements other than masonry. The bands were not damaged in the experimental tests found in the literature. However, crack propagation and sliding occurred at the interface between the bands and the masonry. For this reason, horizontal bands are modeled by a zero-thickness interface with a brittle behavior in tension and a damaging cohesive behavior in shear. These elements allow to model the sliding at the masonry/band interface. To capture the damage at the interface due to crack propagation from the masonry to the bands, the interface elements are coupled to the DFM. A damage parameter D_{meso} is defined as a function of the deformation of the diagonal struts of the DFM. Thus, the damage of the interface is induced either by its brittle behavior or by the propagation of cracks. The interface elements are defined by their the parameters in Table 5.1.

Like the horizontal bands, the frames at the opening did not suffer any damage during the tests carried out. Therefore, they are modeled by beam elements with elastic behavior. These beam elements come parallel to the strut elements of the DFM or to interface surfaces. In the case of lintels, the modeling depends on how they are designed. If they consist of a horizontal band along the entire wall, they are modeled by interface elements and a beam element above the opening. If the lintel is only above the openings, it is modeled by a beam that can be extended

Table 5.1: Parameters for the definition of the interface and reinforcement elements

Elastic properties of the interface elements	
Stiffness in normal direction [k_n]	Stiffness in tangential direction [k_t]
Inelastic properties of the interface elements	
Tensile strength [f_{tm}]	Cohesion [c]
Coefficient of friction [μ]	Energy release rate for mode I [G_I]
Coupling parameter [φ_{int}]	
Elastic properties of the reinforcements	
Young's modulus [E_r]	Density [ρ_r]
Poisson's ratio ν_r	Height of the cross section [h_r]
Width of the cross section [l_r]	

parallel to DFM elements. These beam elements do not have the actual length of the lintels so as not to have a significant constraint on the size of the mesh and not to interfere with the proposed modeling of bands. The beam elements are defined by the parameters in Table 5.1.

The proposed modeling enables all the set objectives for IP analysis. It allows a simple modeling of masonry structures with bands. The definition of the elements is simple and does not require any special knowledge in numerical modeling. Moreover, all the reinforcement elements can be easily linked with the DFM elements. The sharing of nodes reduces computation time, although the use of beam elements increases the number of degrees of freedom for some nodes. The next step in modeling a masonry structure with bands is the definition of the DFM element for 3D modeling and the definition of the mass matrix for dynamic analysis.

Chapter 6

3D modeling

6.1 Introduction

The previous two chapters focused on defining the DFM for 2D analysis and on modeling elements other than masonry. The model as presented does not allow the OOP analysis of a structure, nor the analysis of a 3D structure. In the previous chapters, it was found that horizontal bands reduce the OOP deformation of masonry walls and the probability of collapse related to this direction of loading. In addition, OOP loaded walls do not have much effect on the stiffness of the structure compared to IP loaded walls. The same remark can be drawn for energy dissipation during an earthquake. Nevertheless, the OOP loading is responsible for the collapse of several structures. Therefore, the choice is made to reproduce the behavior of a wall under OOP loading without attempting to reproduce the non-linearities under cyclic loading in this direction. For the study of a complete structure, it is necessary that the model allows in the same time the modeling of the IP and the OOP behaviors of masonry.

In addition to the OOP behavior of masonry, it is necessary to define the mass matrix of the model to allow the analysis of the dynamic behavior of masonry structures with bands. The last section of this chapter deals with its definition for a complete structure.

6.2 DFM for 3D modeling

The OOP behavior is often not considered in numerical models for the reasons given above. Among the meso-models and macro-models presented in Section 3.1.3, some of them have features to reproduce the OOP behaviour of masonry. These models are the RMEM [94, 89, 109], the Rigid Element Model [55, 110], the SAM model [77] and the ESM [111, 112, 113]. These models can be used as inspiration for modifications to the DFM to reproduce the OOP behaviour of masonry.

6.2.1 Models from the literature

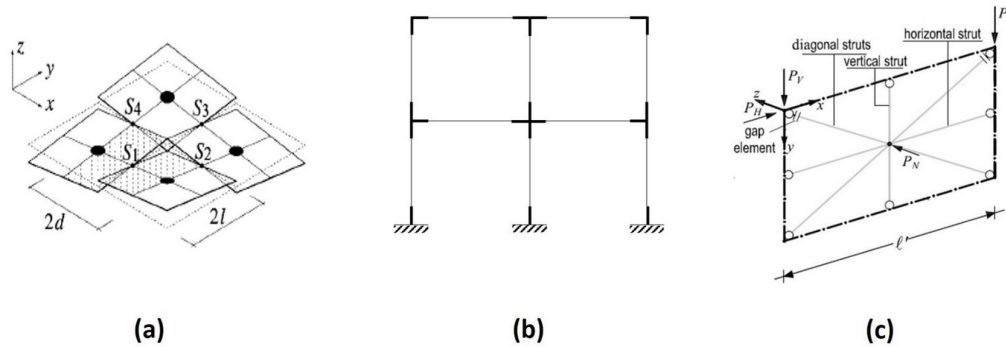


Figure 6.1: Models for masonry from the literature able to reproduce OOP deformation: (a) Rigid Element Model [55]; (b) SAM [77]; (c) ESM proposed by Di Trapani et al. [114]

Three examples of meso-models/macro-models from the literature able to take into account the OOP behavior of masonry are shown in Figure 6.1. The RMEM is not shown in this figure because its way of reproducing the OOP behavior of masonry was one of the reasons why the DFM was developed. The model shown in Figure 6.1.(a) is the Rigid Element Model. It has hinges in the middle of each side of the rigid bodies to reproduce the OOP deformations. This type of strategy is not suitable for the DFM because it does not allow the analysis of the IP behavior of the structure at the same time.

The SAM method is the model shown in Figure 6.1.(b). It is a method of the family of the EFM in which the elements are modeled with elastic-plastic beams. The definition of the elements in the IP direction is adapted for the OOP direction. The yield force of the beams is defined using the formulas for rocking by assuming a different effective height. This type of strategy can be adopted for the DFM.

Figure 6.1.(c) is one of the models in the family of the ESM that aims to reproduce the OOP deformation of masonry used as infill. That is why it has diagonal struts. The method to reproduce the OOP behavior of masonry is to add a node in the middle of the panel. All ESM-like models used to capture OOP behavior (Asteris et al. [115]; Mazza [113]) have at least one additional node at this location. This node has only one degree of freedom corresponding to the OOP displacement. This location is related to the arching mechanism that appears under OOP loading due to the boundary conditions. Di Trapani et al. [114] added the vertical strut in the middle of the slab width and the horizontal strut in the middle of the height, visible in Figure 6.1.(c), to reproduce the damage caused by this mechanism. In the context of the thesis, this type of modeling is not appropriate because it only accounts for one type of OOP mechanism that is defined for specific boundary conditions.

6.2.2 DFM for OOP loading

The goal for the DFM is to accommodate the OOP behavior of masonry without changing the philosophy of the meso-element. Therefore, in order not to significantly increase the number of elements that compose the DFM, the model retains a 2D shape even for 3D modeling.

In order to reproduce the OOP behavior of the masonry, the strut elements composing the frame of the DFM are converted into beam elements. It is the same philosophy as in the SAM. These elements are only used to reproduce the OOP bending behavior, the torsional behavior of masonry and the usual behavior of the strut elements used for 2D modeling. Thus, they do not have the full kinematics of a beam element. These frame elements have no bending and no shear in the plane of the DFM. The diagonal elements retain their usual definition (strut with a pure tension/compression behavior). Figure 6.2 shows the kinematics of the DFM for a 3D modeling. For the use of the beam elements, there are three new DOF per node for a total of 20 DOF for an element of the DFM (5 DOF at each node).

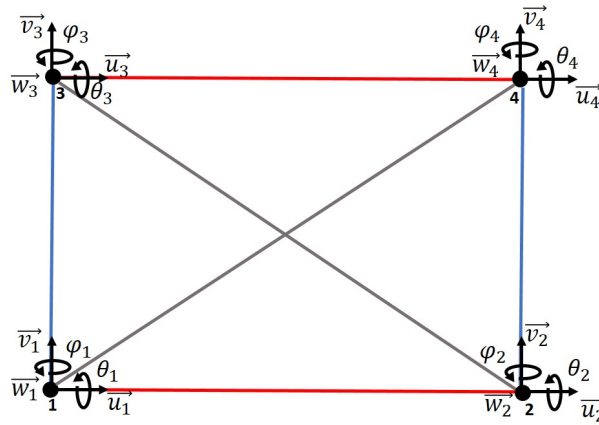


Figure 6.2: The DFM for 3D modeling with kinematics defined in the global orthonormal coordinate system

The beam elements that make up the frame have the same stiffness as the struts when loaded axially. As reminder, this stiffness is not directly linked to the Young modulus of the masonry E_m because of the presence of the diagonal elements (see Equations (4.3) and (4.4)). Therefore, the axial elastic modulus of the beams does not correspond to the Young's modulus of the masonry E_m , but to a new modulus of elasticity denoted E_x . This new modulus of elasticity is defined by Equation 6.1 for horizontal beams and by Equation 6.2 for vertical beams. The stiffness K_h (resp. K_v) in these equations is defined by Equation (4.24) (resp. Equation (4.25)). The length l_m is the width of the meso-element and h_m its height. The height h_{inf} and the width l_{inf} have the same definition as in Chapter 4 and are reminded in Figure 6.3. The Young's modulus E_x is used only for the axial deformation.

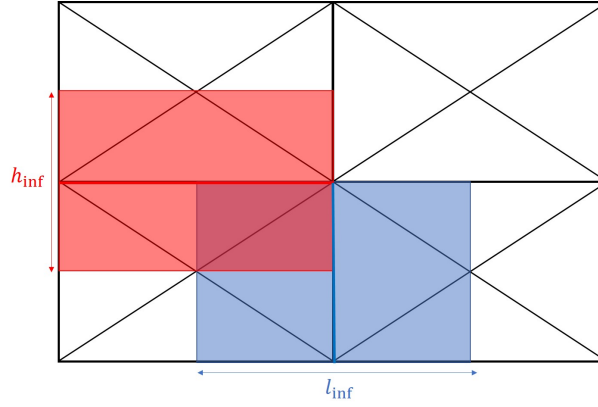


Figure 6.3: Definition of the height and the width of influence of the beams of the DFM

$$E_{x,h} = K_h \frac{l_{elem}}{t_m h_{inf}} \quad (6.1)$$

$$E_{x,v} = K_v \frac{h_{elem}}{t_m l_{inf}} \quad (6.2)$$

The diagonal elements bring additional rigidity for vertical and horizontal IP tension/compression loading. However, they do not have any rigidity for OOP loading. Therefore, the bending behavior of the beams is defined with the Young's modulus of the masonry E_m and not with the elastic modulus E_x .

A beam element of the DFM frame is shown in Figure 6.4 with its local coordinate system. It is defined with nodes i and j , where u_i (resp. u_j) is the axial displacement, v_i (resp. v_j) is the vertical displacement, w_i (resp. w_j) is the OOP displacement, θ_i (resp. θ_j) is the angle related to the bending around the vertical local axis and φ_i (resp. φ_j) is the torsion angle.

The displacement vector of the beam is noted $\underline{U} = \{u_i; v_i; w_i; \varphi_i; \theta_i; u_j; v_j; w_j; \varphi_j; \theta_j\}^T$. The internal force vector of the beam is noted $\underline{F} = \{N_i; T_{y,i}; T_{z,i}; M_{x,i}; M_{y,i}; N_j; T_{y,j}; T_{z,j}; M_{x,j}; M_{y,j}\}^T$. The equilibrium equation (Equation (6.3)) defines the relationship between these two vectors.

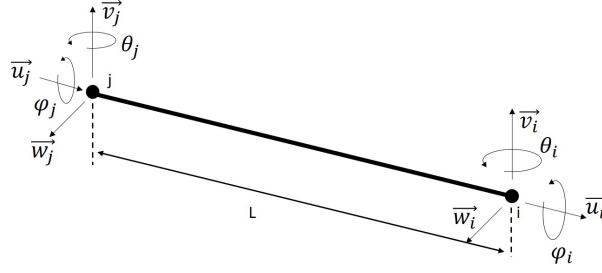


Figure 6.4: Kinematics of beam elements of the DFM defined in the local orthonormal coordinate system

The stiffness matrix $\underline{\underline{K}}$ used for equilibrium with Euler-Bernoulli's beam theory is defined by Equation (6.4).

$$\underline{\underline{F}} = \underline{\underline{K}} \cdot \underline{\underline{U}} \quad (6.3)$$

$$\underline{\underline{K}} = \begin{bmatrix} \frac{SE_x}{2L} & 0 & 0 & 0 & 0 & -\frac{SE_x}{2L} & 0 & 0 & 0 & 0 \\ \frac{3E_m I_z}{2L^3} & 0 & 0 & 0 & 0 & 0 & -\frac{3E_m I_z}{2L^3} & 0 & 0 & 0 \\ \frac{3E_m I_y}{2L^3} & 0 & -\frac{3E_m I_y}{2L^2} & 0 & 0 & 0 & 0 & -\frac{3E_m I_y}{2L^3} & 0 & -\frac{3E_m I_y}{2L^2} \\ \frac{G_m J}{2L} & 0 & 0 & 0 & 0 & 0 & 0 & 0 & -\frac{G_m J}{2L} & 0 \\ \frac{2E_m I_y}{L} & 0 & 0 & 0 & 0 & 0 & \frac{3E_m I_y}{2L^2} & 0 & 0 & \frac{E_m I_y}{L} \\ \frac{SE_x}{2L} & 0 & 0 & 0 & 0 & \frac{SE_x}{2L} & 0 & 0 & 0 & 0 \\ \frac{3E_m I_z}{2L^3} & 0 & 0 & 0 & 0 & 0 & \frac{3E_m I_z}{2L^3} & 0 & 0 & 0 \\ \text{sym} & & & & & & & \frac{3E_m I_y}{2L^3} & 0 & \frac{3E_m I_y}{2L^2} \\ & & & & & & & \frac{G_m J}{2L} & 0 & 0 \\ & & & & & & & & \frac{2E_m I_y}{L} & \frac{E_m I_y}{L} \end{bmatrix} \quad (6.4)$$

The inertia terms in Equation (6.4) I_z , I_y and J are determined with the dimensions of the surrounding meso-elements of the DFM. They are defined for the vertical beams and the horizontal beams in Table 6.1.

There is a special definition for vertical beams of the DFM at corners where two or more walls are connected. In this situation, the IP solicitation of one wall corresponds to the OOP solicitation of perpendicular walls. It is a tricky situation where it is difficult to define the

Table 6.1: Definition of the inertia terms of the beam elements of the DFM

	I_y	I_z	J
Vertical beam	$\frac{t_m^3 \cdot l_{inf}}{12}$	$\frac{t_m \cdot l_{inf}^3}{12}$	$I_z + I_y$
Horizontal beam	$\frac{t_m^3 \cdot h_{inf}}{12}$	$\frac{t_m \cdot h_{inf}^3}{12}$	$I_z + I_y$

properties of the beam correctly. For example, the definition of the properties changes depending on the size of the mesh. In this situation, it is assumed that the definition of the bending behavior of the beam would lead to an overestimation of the stiffness of the structure at the corners, regardless of the size of the mesh. Therefore, the moments of inertia I_y and I_z are set to zero for the vertical beams at the corner.

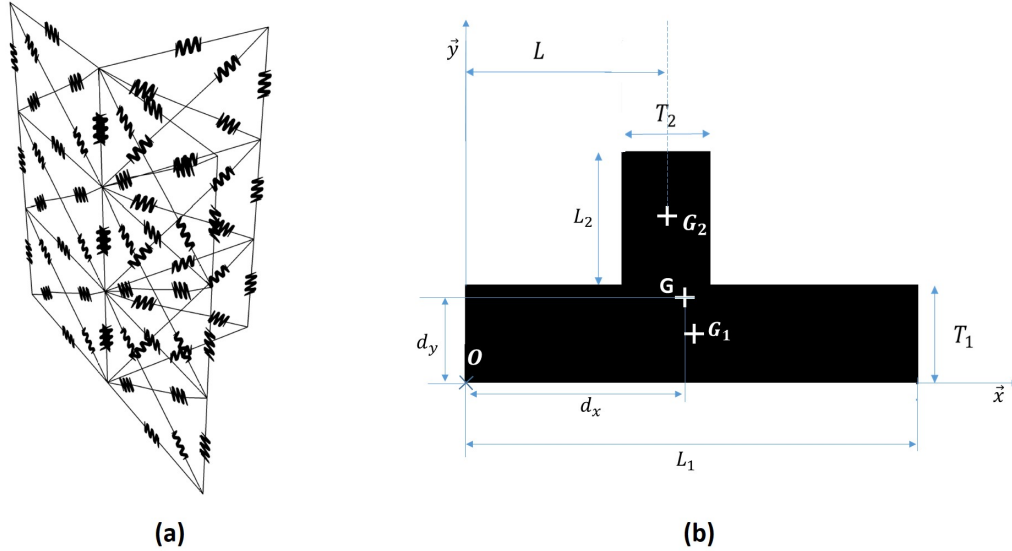


Figure 6.5: Intersection of two walls: (a) modeled with DFM; (b) cross section seen from above

In order to capture well the torsional behavior of the structure, the polar moment of inertia J is kept non-zero (the formula $J = I_z + I_y$ in Table 6.1 is not adequate in this situation). The intersection between two walls is shown in Figure 6.5. In this figure, L_1 (resp. L_2) is the total length of the vertical strut in the x-direction (resp. y-direction). L is the length of influence of the element on the left in direction 1. The thickness of the wall oriented in direction 1 is denoted by T_1 (resp. T_2 in direction 2). With these notations, the polar moment of inertia of the vertical beam at the corner J_{corner} is defined by:

$$\begin{aligned}
 J_{corner} &= \frac{1}{12} (T_1 L_1^3 + L_1 T_1^3 + T_2 L_2^3 + L_2 T_2^3) \\
 &+ L_1 T_1 \left((d_x - 0.5L_1)^2 + (d_y - 0.5T_1)^2 \right) + T_2 L_2 \left((d_x - (L_1 + 0.5T_2))^2 + (d_y - (T_1 + 0.5L_2))^2 \right)
 \end{aligned} \tag{6.5}$$

The distances d_x and d_y are the coordinates of the center of gravity G of the entire domain of influence of the beam in respect to the reference point O in Figure 6.5. These two coordinates are defined by Equations (6.6) and (6.7).

$$d_x = \frac{(L_1 \cdot T_1 \cdot L_1 / 2 + L \cdot L_2 \cdot T_2)}{L_1 \cdot T_1 + L_2 \cdot T_2} \tag{6.6}$$

$$d_y = \frac{(L_1 \cdot T_1^2 + L_2 \cdot T_2 \cdot (T_1 + L_2 / 2))}{L_1 \cdot T_1 + L_2 \cdot T_2} \tag{6.7}$$

The beams of the frame of the DFM do not have inelastic behavior. The OOP definition of yield force used by the SAM model is not appropriate for the DFM. In fact, as announced in the chapter on the IP behavior of the DFM, the definition of the rocking failure in the literature does not make sense at the scale of the macro-element. It is possible to find simple definitions of the OOP behavior of masonry walls, with bi-linear or tri-linear curves (Abbati and Lagomarsino [116]; Doherty et al. [117]; Godio and Beyer [118]), but these curves depend on the boundary conditions of the wall. Therefore, it is not possible to use them as well. The failure of the wall could be defined with a maximum allowable displacement. In the context of the thesis, OOP failure is not considered. Therefore, there is no proposed definition for this maximum displacement.

6.3 Mass matrix definition

In order to perform dynamic and modal analysis, the mass matrix must be defined. For the DFM, the **mass is located at the nodes**. It is calculated by determining their volume of influence. This volume is defined by half the distance of the node to the other vertices of the meso-elements to which it belongs. Two examples of the area of influence are colored yellow and purple in Figure 6.6(a). The yellow region represents the case when the node is surrounded only by DFM elements. The purple region is representative of the case when the node is located at the edge of an opening. In this situation, the area is not rectangular. It is bounded by the edges of the opening.

Equation (6.8) gives the relation between the mass at node n M_n and the associated area of influence A_n . This mass is the same in the three directions defining the space. The other parameters in Equation (6.8) are the masonry density ρ_m and the wall thickness t_m .

$$M_n = \rho_m A_n t_m \tag{6.8}$$

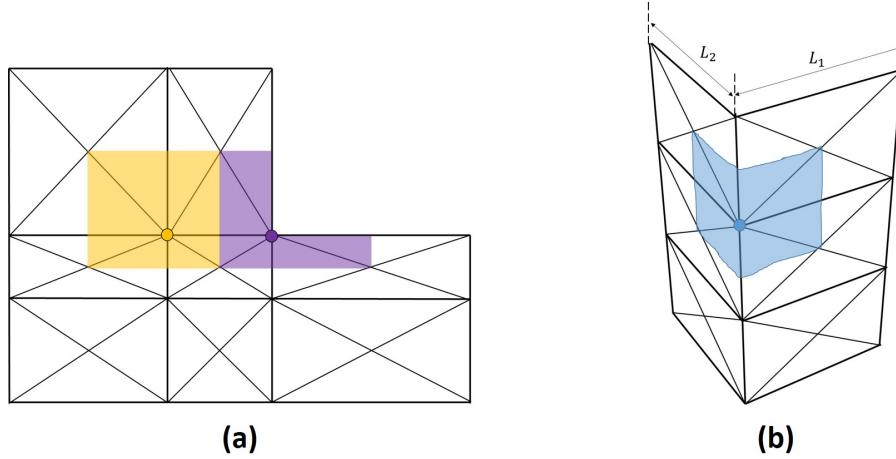


Figure 6.6: Examples of area of influence for nodes: (a) case with adjacent meso-elements; (b) case at a corner

Equation (6.8) is the definition of the mass for the majority of the nodes. However, as with the vertical beam elements, there is a special situation at the intersection of walls. Indeed, the regions shown in Figure 6.6.(a) are rectangles when viewed from above, while the blue region in Figure 6.6.(b) has an L-shape. Depending on the number of walls connected at the corner, U-shaped areas, T-shaped areas, and cross-shaped areas are also possible. For each of these cases, the mass at the node is not defined by Equation (6.8), as this would lead to an overestimation. For the example in Figure 6.6.(b), the length of the area of influence in direction 1 (resp. 2) is noted as L_1 (resp. L_2) and the thickness of the corresponding wall t_1 (resp. t_2). In this configuration, the area of influence associated to the node n represented by a blue circle Figure 6.6.(b) is defined by Equation (6.9). This equation can be adapted to any type of intersection of walls.

$$A_{corner} = \begin{cases} (L_1 + 0.5t_2)t_1 + (L_2 + 0.5t_1)t_2 & \text{if } L_1 > t_1 \text{ and } L_2 > t_2 \\ L_1t_1 + L_2L_1 + (L_2 - 0.5t_1)t_2 & \text{if } L_1 < t_1 \text{ and } L_2 > t_2 \\ L_2t_2 + L_2L_1 + (L_1 - 0.5t_2)t_1 & \text{if } L_1 > t_1 \text{ and } L_2 < t_2 \\ L_1L_2 & \text{if } L_1 < t_1 \text{ and } L_2 < t_2 \end{cases} \quad (6.9)$$

The mass assigned to the nodes is defined by Equation (6.10). In this equation h_{inf} is the height of influence as defined for horizontal struts in Chapter 4. The mass for the rotational degrees of freedom is not considered in the definition of the mass matrix.

$$M_{n,i} = \rho_m A_{corner} h_{inf} \quad (6.10)$$

An interface has a similar influence on the area of influence as an opening (see Figure (6.7)).

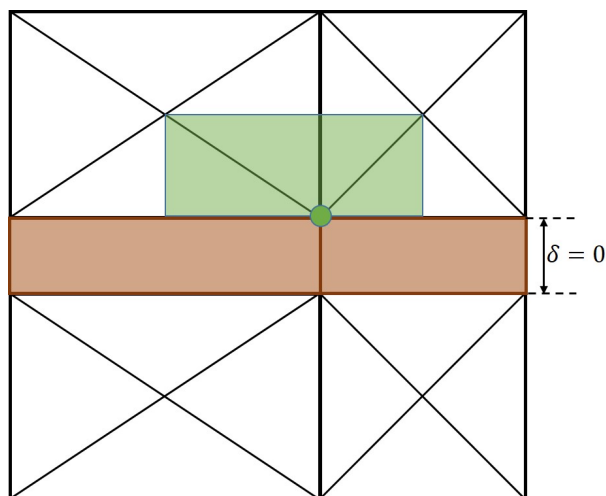


Figure 6.7: Examples of area of influence of nodes in presence of an interface

However, the mass at the node is not defined by Equation (6.8). If the node is part of an interface element, the density of the band ρ_{band} and the height of the band h_{band} are taken into account when determining the mass (see Equation (6.11)).

$$M_{n,int,i} = (\rho_m h_{inf} - 0.5(\rho_m - \rho_{band})h_{band}) A_n \quad (6.11)$$

The beam elements do not interfere with the determination of the mass at the nodes. Their contribution in the mass of the structure is determined by the usual definition of the mass matrix of beam elements. As announced in Chapter 2, the roof is considered as dead load. Its mass is uniformly distributed and added to the mass of the nodes at the top of the structure.

6.4 Conclusion

This chapter aimed to extend the application of the DFM to 3D modeling. In order to reproduce the OOP deformation of the masonry, the strut elements are modified by beam elements with special kinematics. In order not to unmake the definition of DFM proposed in Chapter 4, the beam elements have no stiffness for IP loading except for the axial loading. Moreover, these elements have a specific elastic modulus E_x for the axial deformation, which is obtained by coupling the stiffness of the elements seen in Chapter 4. For 2D modeling, this new version of the DFM is identical to the 2D version introduced in Chapter 4.

The mass matrix for a masonry structure with horizontal bands was also defined. For the DFM, the mass at the nodes is defined by determining the volume of masonry associated to the node. If the nodes are part of an interface (i.e. model part of a horizontal band), the mass is

adjusted to account for the properties of the bands. Only the beam elements used to model the frames at the openings or the lintels have their own mass.

A certain peculiarity arose from the extension to 3D, especially at the corner. At these locations, it is necessary to know the number of connected walls in order to correctly define the properties of the elements. Moreover, the vertical beams of the DFM at the corners have a particular kinematics, since they model simultaneously the OOP and the IP behavior of perpendicular walls. The definition of the mass matrix is also different at the corner.

The intersection of walls requires special attention in the definition of the model, but apart from that, modeling a structure for a dynamic analysis is straightforward. Moreover, no additional parameters are required for the extension to 3D modeling. The proposed model meets all the set objectives in terms of simplicity in modeling masonry structures with bands. In the next part, the model is tested to evaluate its efficiency in reproducing the dynamic behavior of these structures.

Part III

Numerical modeling of masonry structures

The numerical model for modeling masonry buildings with bands was defined in the previous section. This third part aims to validate this numerical model and determine the extent to which it is efficient and meets the objectives set. The model has been implemented in ATLAS, a FE toolbox on Matlab developed by Grange [22]. Information about this toolbox can be found in Appendix A.

Chapter 7 focuses on the modal analysis of structures using the DFM. The study begins with the scale of a wall and proceeds to the scale of a two-room structure. At each step, the DFM results are compared with those obtained with 2D shell elements and 3D cubic finite elements. The modal analysis is used to verify the elastic properties of the DFM and the definition of the mass matrix.

Numerical modeling of three experimental campaigns is presented in **Chapter 8**. They consist of IP cyclic tests. The first study was carried out on URM masonry piers, the second study on an adobe wall with openings and the last study on walls with and without horizontal bands.

Shaking table experiments on three houses in reduced scale are presented in **Chapter 9**. The proposed meso-element is used for numerical modeling and its efficiency is evaluated. Since two of the scaled-down houses have horizontal bands, conclusions can be drawn with respect to the objectives of the thesis.

Chapter 7

Validation of the elastic properties

A modal analysis of several URM structures is proposed as a first step to validate the elastic properties of the DFM and the definition of the mass matrix. Every analyzed structure is considered perfectly embedded in foundations. The analyzed structures are:

- A square wall without openings. It is a basic structure that can be modeled with one meso-element.
- A rectangular wall without openings. This analysis allows to study the influence of the slenderness of the structure on the performances of the DFM.
- A 4-wall structure without openings. This analysis allows to validate the definition of the DFM at the corners.
- A 5-wall structure. Without openings in a first time and with openings afterwards. It allows to see the performances of the DFM for the most complex structure that is studied in the thesis and to see the influence of openings on the results.

The masonry mechanical properties for every modal analysis are shown in Table 7.1. They are the mechanical properties identified with the quasi-static tests of Yadav [7] presented in Section 8.3. They have been chosen because they will also be used for the dynamic analysis of three houses in Chapter 9.

The modal analyzes are performed with several models: (i) the DFM; (ii) a 2D shell FE (2D FE model); (iii) a 3D cubic elements model (3D FE model). Castem software [23] is used for these two additional models. The 3D FE model is used as reference to assess the accuracy of the 2D models. The accuracy of the models for the parameter a is defined as the difference between the results of the considered model with the result of the reference model ($\text{diff} = \text{abs}(a_{ref} - a_{mod})/a_{ref}$).

Table 7.1: Masonry mechanical properties for modal analyzes

Material properties for the stiffness of the DFM	
Young's modulus [E_m]	61.3 MPa
Shear modulus [G_m]	25.5 MPa
Material properties for the mass matrix	
Density of masonry [ρ_m]	2000 kg.m ⁻³

The following process is followed for every modal analysis to evaluate the capacities of the DFM:

1. The n first frequencies determined with all models are exposed. It gives an overview of the performance of the DFM in the determination of the frequencies. The number n of analyzed frequencies correspond to the last important mode for the studied structure. There are not other modes with an important modal mass after the n^{th} mode.
2. The modal masses for all the modes are exposed. Therefore, the important modes are determined. The accuracy in the determination of their modal mass is assessed.
3. (Optional step) If there is a great difference between the modal mass determined with the DFM and the modal mass determined with the reference model, the modal mass in the three directions is computed to know what kind of deformation is not well captured with the DFM.
4. The evolution of the accuracy in the determination of the frequency of the important modes with the discretization of the mesh is exposed. It allows to see how the model performs with a coarse mesh and how accurate it can be.

The computation time is indicated for every study. It is not a criterion of comparison between the models since Castem and Matlab do not have the same process to solve the problem. The computation time is used to see if the use of the DFM with Matlab is relevant or if it would lead to a too important computation time. An evaluation of the influence of the discretization on the accuracy of the results is performed as well.

There are two different notations for the mesh of the DFM. When only one wall is modeled, the mesh is referred to as " $n \times m$ ". The number n is the number of meso-elements in the width of the wall and m is the number of meso-elements in the height of the wall. Therefore, a wall that is modeled with only one meso-element is referred to as "1x1" with this notation. When multiple walls are modeled, a different naming convention is used. In this case, the mesh is named with a number "n". This number n is the refinement of the coarser possible mesh. For example, the 4-wall structure modeled in Figure 7.14 is named as *Mesh_4* because its small wall is modeled

with 4×4 elements and its long wall is modeled with 8×4 elements, while the coarser mesh is created with 1 meso-element for the small wall and 2×1 meso-elements for the long wall.

All the analyzes presented in this chapter are performed with the same computer. This computer has an Intel(R) Core(TM) i5-8250U @ 1.6-1.8 GHz processor and 8.0 Gb of RAM. More information for the modal analysis and for the determination of the modal mass are given in Appendix A.

7.1 Modal analysis of walls without openings

7.1.1 Square wall

The width of the analyzed square wall is 2.5 m and its thickness is 0.3 m. The mesh of each model is shown in Figure 7.1.

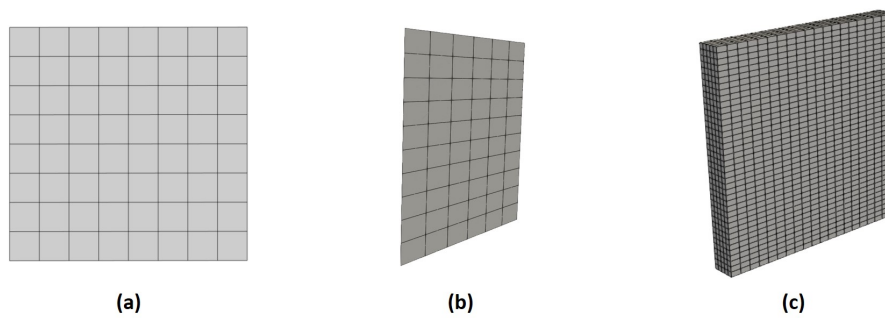


Figure 7.1: Examples of mesh for the square wall: (a) 8×8 mesh with the DFM; (b) 6×10 mesh with 2D FE; (c) $20 \times 30 \times 5$ mesh with 3D FE

The modal frequencies computed with the different models and the computation time are shown in Figure 7.2. The DFM has a computation time in the same range as the 2D FE model and is considerably faster than the 3D FE model.

The results in Figure 7.2 show that the DFM generally gives a good approximation of the modal frequencies obtained with the 3D FE model, although, sometimes, the difference between the two models is not negligible (modes 6 and 8). The 2D FE model gives a good approximation of every mode.

The modal mass is not an output of the Castem software and is determined using a Matlab program that is different from the one used for the DFM. The data is imported from the Castem software and due to a limit on the size of the data that can be loaded into Matlab, the modal mass can only be calculated for problems with a limited number of degrees of freedom.

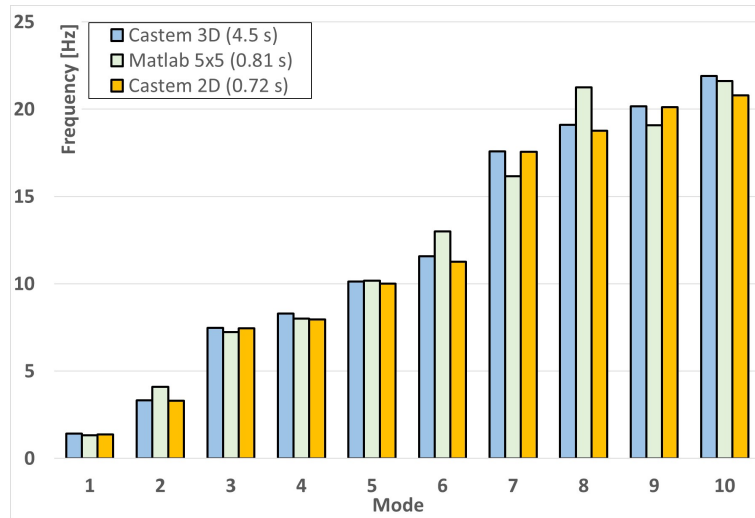


Figure 7.2: The ten first modal frequencies of the square wall

The results for the determination of the modal mass for the ten first modes are shown in Figure 7.3. The models give approximately the same results for the important modes (modes 1, 3, 4, 7 and 9 in Figure 7.3). Unlike for the modal frequencies, the DFM gives better results for the modal masses compared to the shell elements. It has a maximum error of approximately 9%. The modes 6 and 8 mentioned above because of the lack of accuracy of the DFM in their determination do not have a high modal mass.

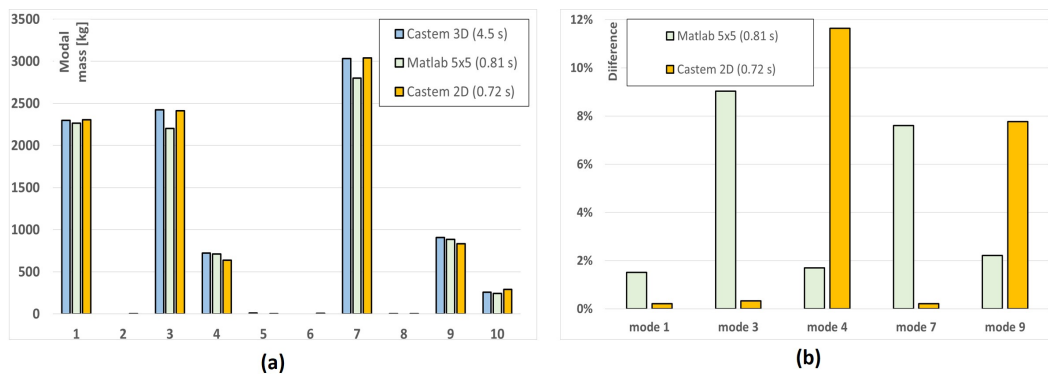


Figure 7.3: Modal masses of the square wall: (a) Modal mass for the first modes; (b) Error in the determination of the modal masses

The modal shapes of modes 1, 3, 4, 7 and 9 are shown in Figure 7.4 for the three models. The shapes for the FE models of the Castem software are drawn using the Paraview [119] software. The colormap used for coloring is the preset colormap *jet* available in Paraview and Matlab. It allows to see the amplitude of displacements. Aside from some minor differences, the deformed shapes are identical. The visible differences are for the second transversal mode and the first vertical mode where the amplitude of the displacements is not the same for all the models. For

the second transversal mode, the amplitude of the displacement with the DFM is the same at a fixed height in the wall but this is not the case for the FE models of Castem. In contrast, for the 1st vertical mode, the displacement is constant at a certain height for FE models in Castem while this is not the case for the meso-model.

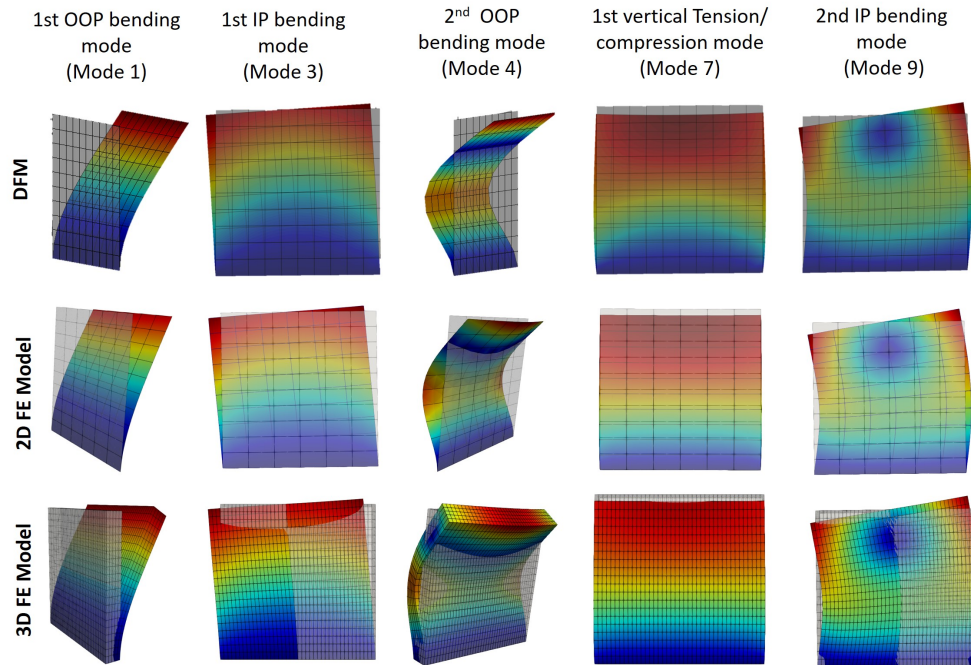


Figure 7.4: Modal shapes of modes 1, 3, 4, 7 and 9 with the three models

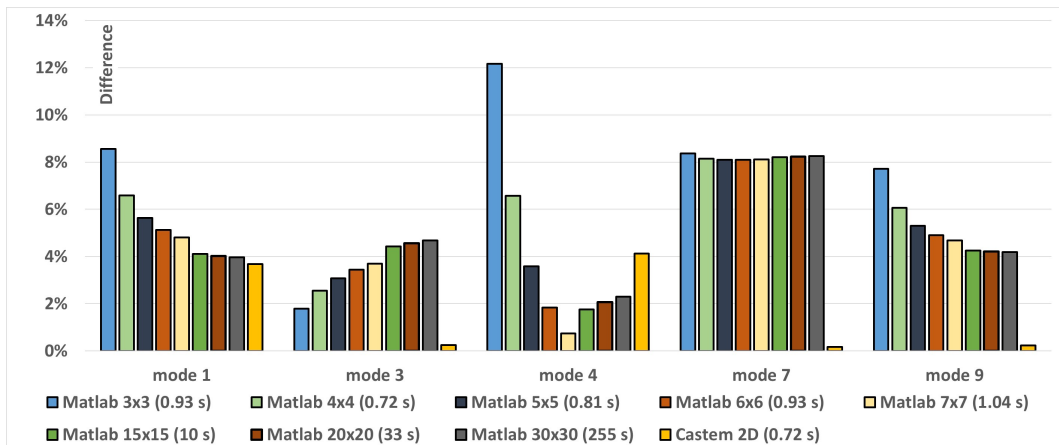


Figure 7.5: Evolution of the accuracy in determining modes shown in Figure 7.4 with the mesh size

Figure 7.5 shows the evolution of the accuracy in determining the frequency of the modes shown in Figure 7.4 with discretization. Very fine meshes are used to see the results to which the model converges. It can be seen that a coarse mesh with the DFM can give results with an error of about 12% in a short time. The accuracy can be improved with a finer mesh, but it is not affected for the mode 7, the 1st vertical tension/compression mode. Therefore, the DFM always has a maximum error of 8% for this mode, while it can be less than 5% for all other modes. It can also be seen that the DFM captures the modes 4 and 9 (2nd OOP bending mode and 2nd IP bending mode in Fig. 7.4) better than the shell element.

The evolution of the values of the mode 4 is shown in Figure 7.6 to explain why the error in determining this mode is not smaller for fine meshes. It can be seen that coarse meshes underestimate the value of this frequency, while fine meshes overestimate it. For this reason, the 7x7 mesh approximates this frequency better than finer meshes.

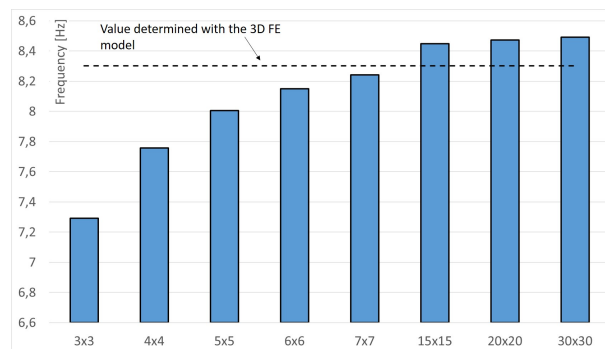


Figure 7.6: Evolution of the value of mode 4 with the mesh size

It can be concluded from this first study that the DFM performs well in the modal analysis of a square wall. It has a computation time close to the one of the shell elements model on the Castem software, and it has a good accuracy for the determination of the important modes and

their modal shape.

7.1.2 Wide wall

This second study allows to know the variability in the accuracy of the DFM with the slenderness of the wall. The analyzed wall has a height of 2.5 m, a width of 8.5 m and a thickness of 0.3 m. A different number of meso-elements in the height and in the width are used to model this wall. Examples of meshes with the three models are shown in Figure 7.7.

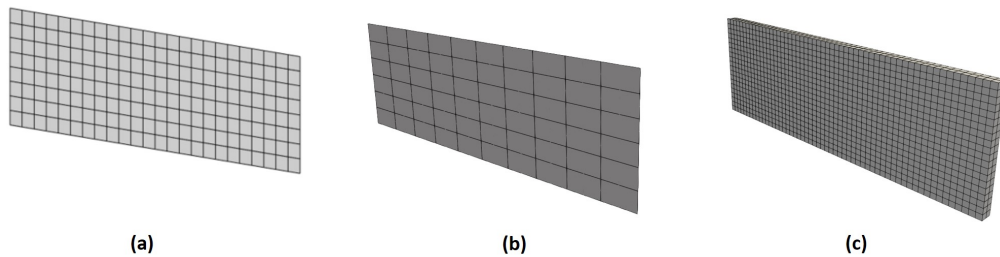


Figure 7.7: Examples of mesh for the wide wall: (a) 24x8 mesh with the DFM; (b) 10x6 mesh with 2D FE; (c) Reference 3D model

The results in determining the seventeen first frequencies are shown in Figure 7.8. The DFM has a better global accuracy for this study since there are not modes where the model exhibits an important difference with the reference model.

Unlike for the square wall, the DFM has a computation time which is not in the same range as the computation time of the shell elements. However, as with the previous example, the DFM performs better than the 3D FE model. Therefore, the computation time with the meso-model remains satisfactory.

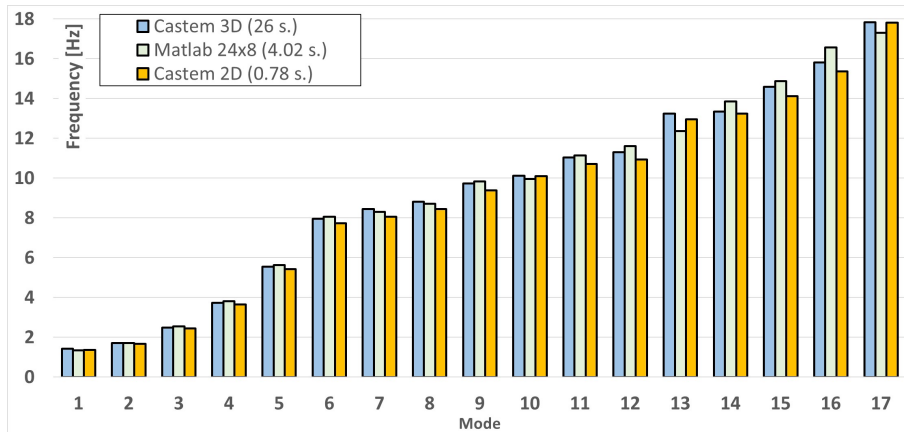


Figure 7.8: The seventeen first modal frequencies of the wide wall

The modal masses of the wide wall are shown in Figure 7.9. For this wall, the important modes have their modal mass much higher than the others. There are three major modes (modes 1, 10 and 17) and another one that can be considered as important (mode 7) (Figure 7.9). The DFM approximates the modal mass well with an error of at most 5% for the important modes aside from mode 17. For this last mode, the difference is considerable. The modal shape in Figure 7.10 shows that this mode is the first vertical tension/compression mode of the wall. For a dynamic analysis, there is not any solicitation along the vertical axis. Therefore, the lack of accuracy for this mode would not have an impact on the results. Since the sum of all the modal masses of a structure is equal to its mass, the difference of mass for this mode has a repercussion on the modal mass of other modes. That is why mode 13 has a modal mass more important with the DFM compared to the other models.

There are two hypothesis for the lack of accuracy of the DFM for the determination of the modal mass of the vertical tension/compression mode: (i) a poor definition of the model linked to the Poisson's ratio and an inability to correctly take it into account; (ii) the IP kinematic of the meso-model that is not defined with rotations at the nodes.

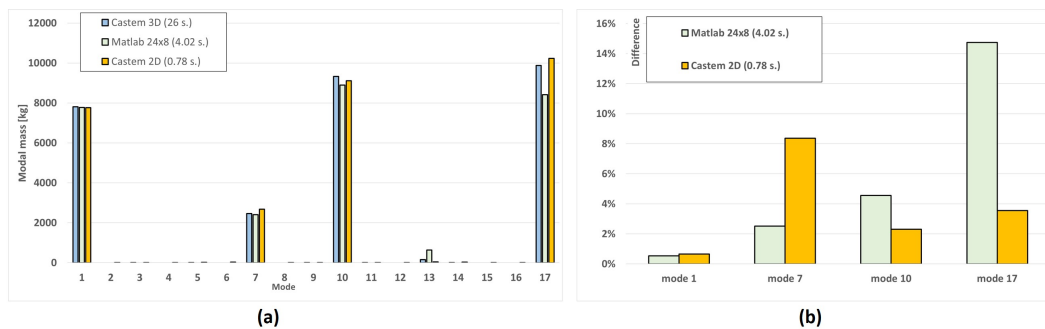


Figure 7.9: Modal masses for the wide wall: (a) The first modal masses; (b) Error in the determination of the important modal masses

There are not obvious differences between the modal shapes obtained with the models (see Fig. 7.10). The only noticeable difference is for the vertical mode where the amplitude of displacement is lower for the DFM at the left and right sides of the wall. This difference may be related to the difference of modal mass for this mode.

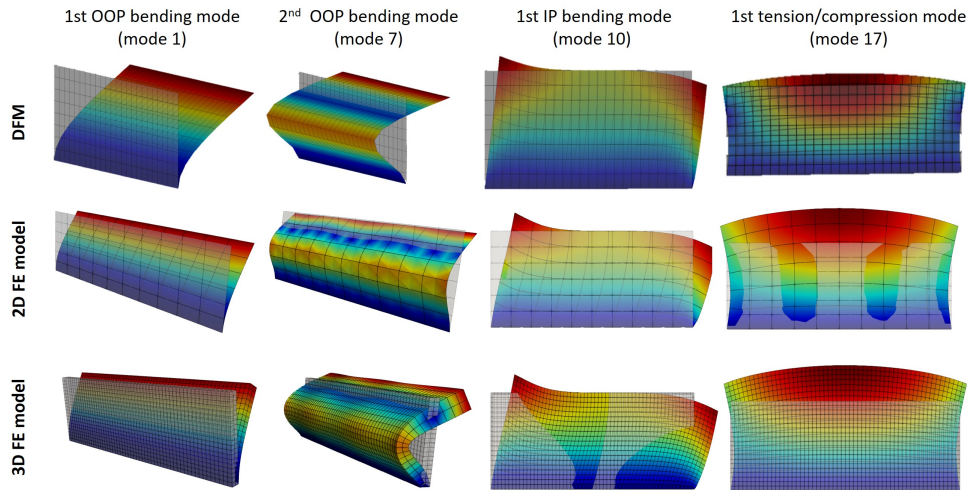


Figure 7.10: Modal shapes for the important modes of the wide wall

The accuracy in determining the frequencies of the modes shown in Fig. 7.10 and the computation time are given in Figure 7.11 for different mesh sizes. The coarser mesh with a maximum error lower than 8% (15x5 mesh) is finer than the mesh with the same accuracy for the square wall (4x4 mesh). The computation time for this mesh is similar to the one of the shell elements. However, the accuracy with the DFM is not as good as for the 2D FE model. With a finer mesh it is possible to obtain a very good approximation of the reference values. Still, like for the square wall, the approximation of the modal frequencies of some modes is not affected by the mesh size. The concerned walls are the 1st IP bending mode and the 1st vertical tension/compression mode. It can be noticed that, even if the modal mass of mode 17 is not well determined with the DFM, its frequency is well approximated with the meso-model.

7.1.3 Study of the influence of the Poisson's ratio

The wide wall is studied again, but with a Poisson's ratio of zero, to see how changing the value of this parameter affects the ability of the DFM to accurately determine the modes. This will also allow us to determine if this parameter is the reason why the DFM is not good at calculating the modal mass of the vertical tension/compression mode. For this purpose, only the modal mass and the influence of the mesh on the determination of the important modes are analyzed to avoid repeating this study.

Figure 7.12 shows the determination of the modal masses with the new elastic properties. It can be seen that the 2D FE model has a higher error in determining the modal mass of Mode 7 in this context (about 15% higher). The same observation can be made for the determination

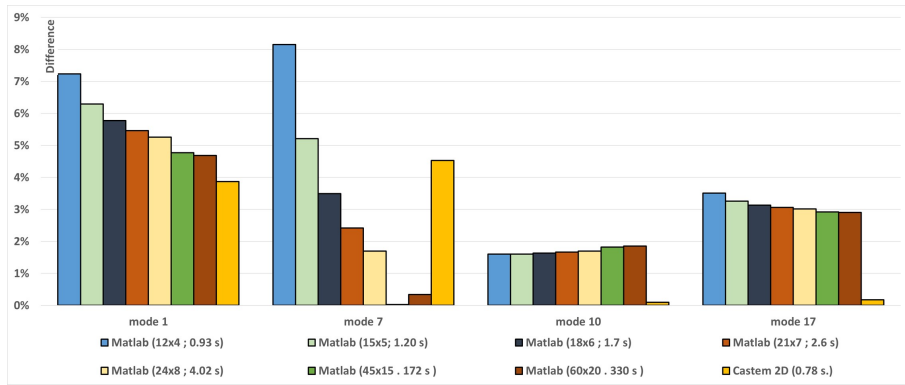


Figure 7.11: Evolution of the accuracy in determining the modes shown in Figure 7.10 of the wide wall with the mesh size

of the 1st vertical tension/compression mode with the DFM, although the evolution of the error for this mode is less consistent (5% higher).

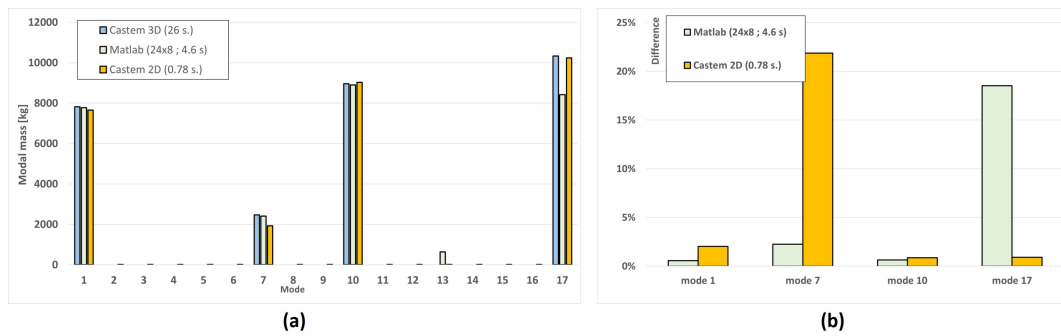


Figure 7.12: Modal masses for the wide wall with Poisson’s ratio of zero: (a) The first modal masses; (b) Error in the determination of the important modal masses

Figure 7.13 shows the evolution of the error with mesh size. The same conclusions can be drawn as in the previous study. The accuracy in determining the frequencies of the modes 10 and 17 is not affected by the mesh size. In general, the DFM performs well in determining the modal frequencies, and the Poisson’s ratio has a small effect on the performances of the model. It can be concluded as well that the lack of accuracy of the DFM to determine the modal mass of the vertical tension/compression mode is not related to the Poisson’s ratio.

7.1.4 Conclusions

These two first studies allow to make some conclusions about the efficiency of the DFM for the modal analysis of URM walls:

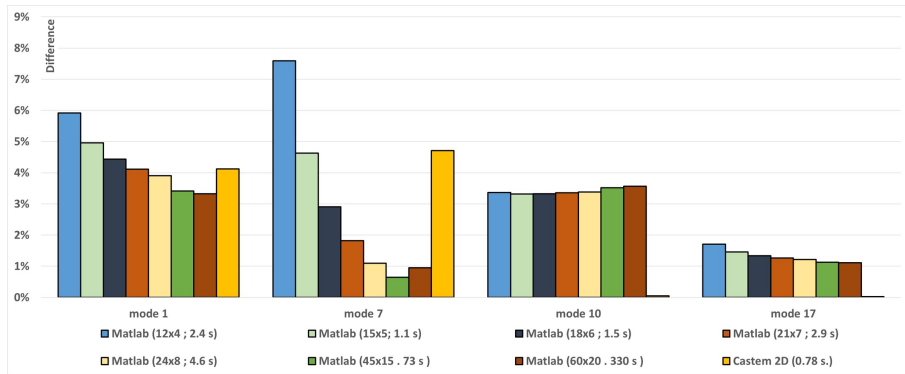


Figure 7.13: Evaluation of the accuracy in the determination of the important modal frequencies with Poisson's ratio of zero

- The computation time of the DFM is satisfying. It is faster than the 3D FE model and is not considerably slower than the 2D FE model even though Castem performs better than Matlab for this type of computation.
- The DFM can determine the frequency of important modes of a wall well and reproduces well the modal shapes.
- The accuracy in determining the frequencies of some modes is not affected by the mesh size.
- The slenderness of the wall does not influence the accuracy of the DFM for the determination of the frequencies. However, it affects the accuracy for the determination of the modal mass. The modal mass of the vertical mode is greatly underestimated with the DFM and this affects the modal mass of the other modes (mode 13 in Figure 7.11).

7.2 Modal analysis of a 4-wall structure

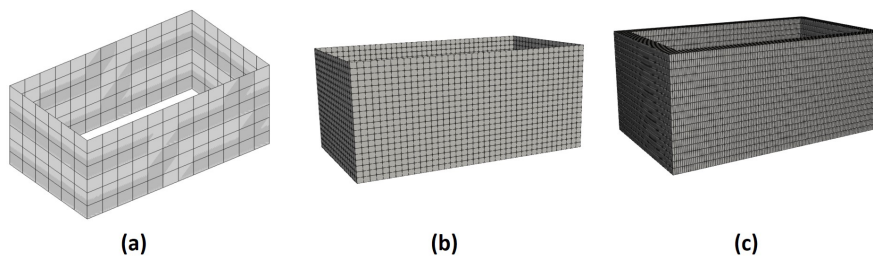


Figure 7.14: Examples of mesh for the 4-wall structure: (a) Mesh_4 for the DFM (or Matlab_4); (b) mesh 2D FE model; (c) mesh with 3D FE model

The modeling of the structure with the different models is shown in Figure 7.14. Small sides of the 4-wall structure are almost squared walls and the long sides are walls with a slenderness lower than 1/2 (see Table 7.2). For the 2D models, the middle plane of the wall is considered. Therefore, the lengths of the walls are taken as $L_{1,2D} = 5.4$ m and $L_{2,2D} = 3.0$ m for these models.

Table 7.2: Dimensions of the 4-wall structure

Characteristic	Value		Characteristic	Value
Height H	2.5 m		Thickness t_m	0.3 m
Width_1 L_1	5.7 m		Width_2 L_2	3.3 m

The twenty eight first modal frequencies obtained with the models are shown in Figure 7.15. The 2D models have a good accuracy for these modes and the computation time of both models is very satisfactory.

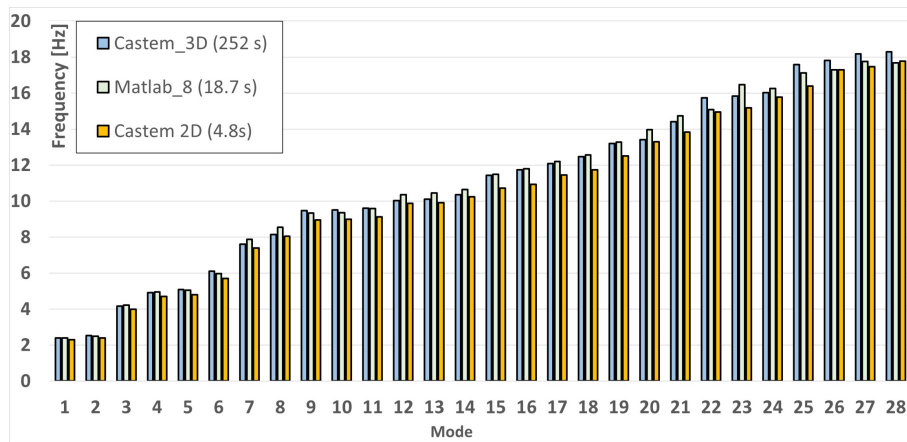


Figure 7.15: The twenty eight first modal frequencies of the 4-wall structure

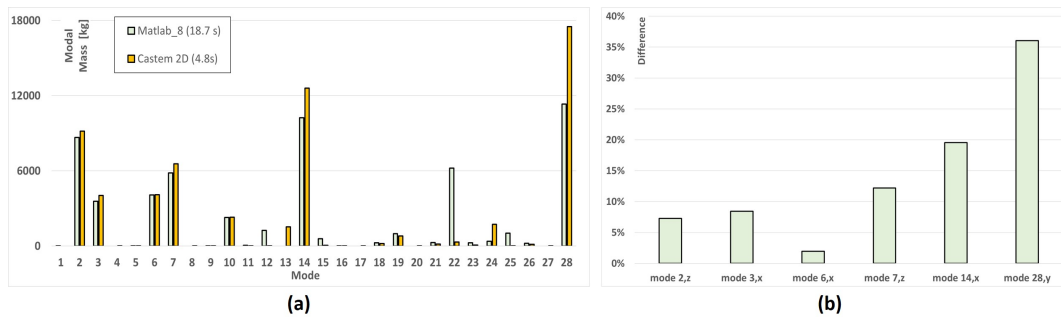


Figure 7.16: The modal masses of the 4-wall structure

For a reason of limitation of the size of the data that can be imported in Matlab, the modal mass of the Castem 3D model is not considered anymore. Therefore, the 2D shell model is considered as reference. In Figure 7.16, the difference of modal mass is determined for the main direction of deformation of the modes. Most of the important modes have their modal mass well approximated by the DFM. However, for the mode 28, the difference is higher than 20%. The difference for this mode is not surprising since it is the first vertical mode (see Fig ??) and it is the same problem as raised above. That difference of modal mass for this mode implies the difference of mass for mode 22 (see Figures 7.17 and ??). In Figures 7.17.(b) and ??, the x direction is the IP direction of the long walls, the y direction is the vertical direction and the z direction is the IP direction of the small walls.

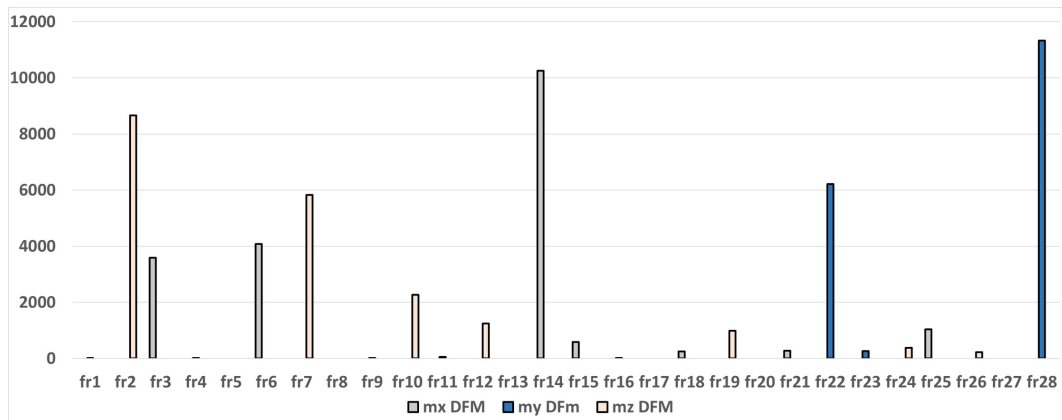


Figure 7.17: The modal masses of the 4-wall structure determined with the DFM for each direction

Mode 14 is the first IP bending mode for the long walls of the 4-wall structure. As it can be seen in Figure ??, the 2D FE model underestimates the global amplitude of the displacement for that mode while the DFM better approximates it. Moreover, the DFM better approximates the frequency of this mode (see Fig. 7.15). Therefore, the DFM may be closer to the 3D reference model than the 2D FE model for the modal mass.

The first modal shapes are similar for all the models (see Figure ??). The noticeable differences are for the longitudinal mode and the vertical modes. These differences were already noticeable with the modal mass of these modes.

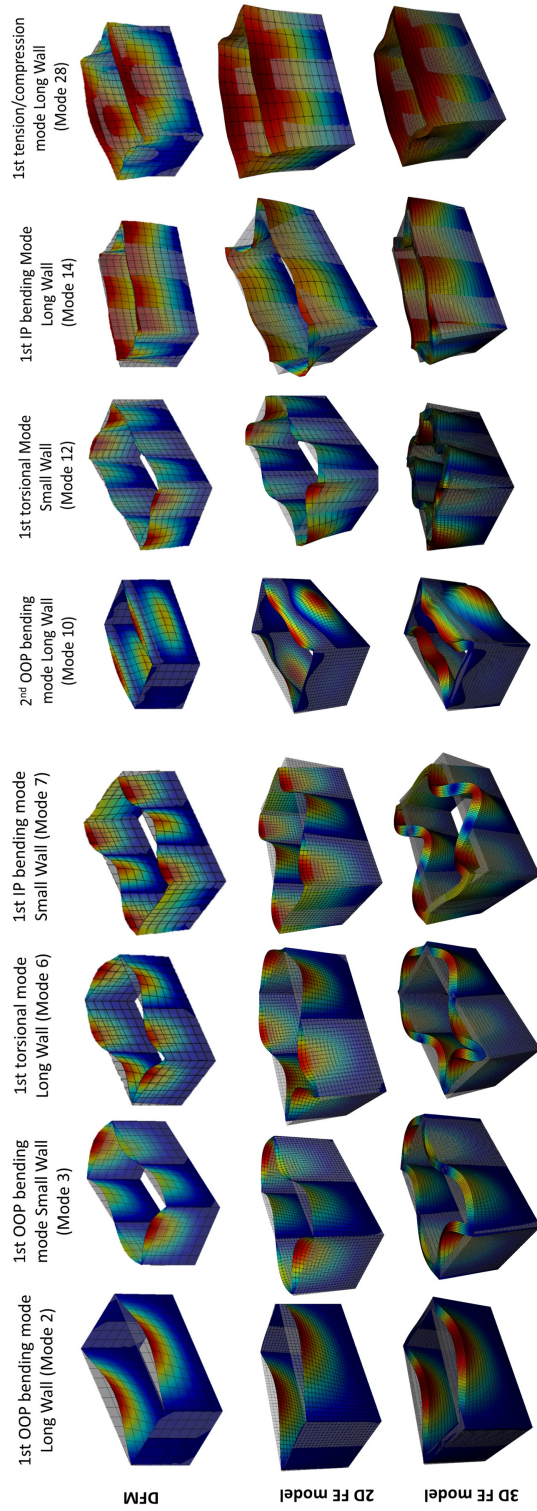


Figure 7.18: Modal shapes of the 4-wall structure

The evolution of the error in the determination of the modal frequencies is shown in Figure 7.19. It can be seen that the DFM has a good accuracy with only 6 elements (maximum error of 8%). Interestingly, the discretization of the mesh is not beneficial for the accuracy of all the modes and it even tends to decrease the performance of the model. This may be related to the definition of the elements at the corner and the limitation related to the computation of the inertia parameters of the beam elements of the DFM. The mesh size has a little influence on the accuracy for the frequencies of mode 28 in Figure 7.15. It can be noticed that, even if the 2D FE model still approximates well the modal frequencies, it tends to perform less better than for the study of walls.

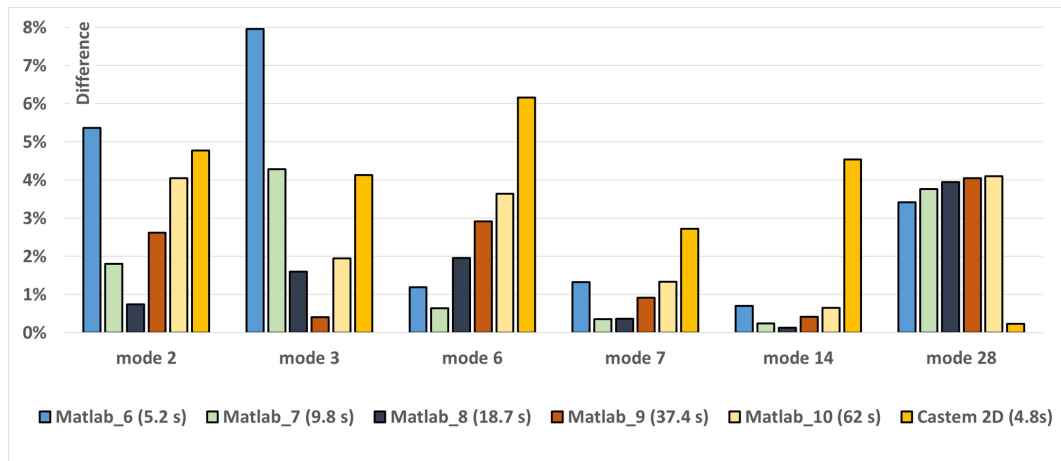


Figure 7.19: Evolution of the accuracy in determining the frequencies of the modes shown in Figure ?? with the mesh size

The modal analysis of the 4-wall structure allows to make additional conclusions about the performance of the DFM:

- The DFM can determine with a satisfactory accuracy (maximal error 4% in this example) the modal frequencies of a 4-wall structure without openings.
- The DFM can determine an additional vertical important mode (mode 22 in this study) because of its inability to correctly capture the first vertical mode.
- The discretization of the mesh is not necessarily beneficial to the performance of the DFM. Still, it does not lead to irrelevant results.

7.3 Modal analysis of a 5-wall structure

The dimensions of the structure are shown in Figure 7.20. This structure has almost the same dimensions as the one of the experimental campaign in Chapter 9. The differences come from the will to easily model the structure in Castem. To make this possible, the nodes at the boundary of two different parts have to be at exactly the same position so that the merging is done correctly. Figure 7.21 and Figure 7.26 show respectively the modeling of the structure without and with openings.

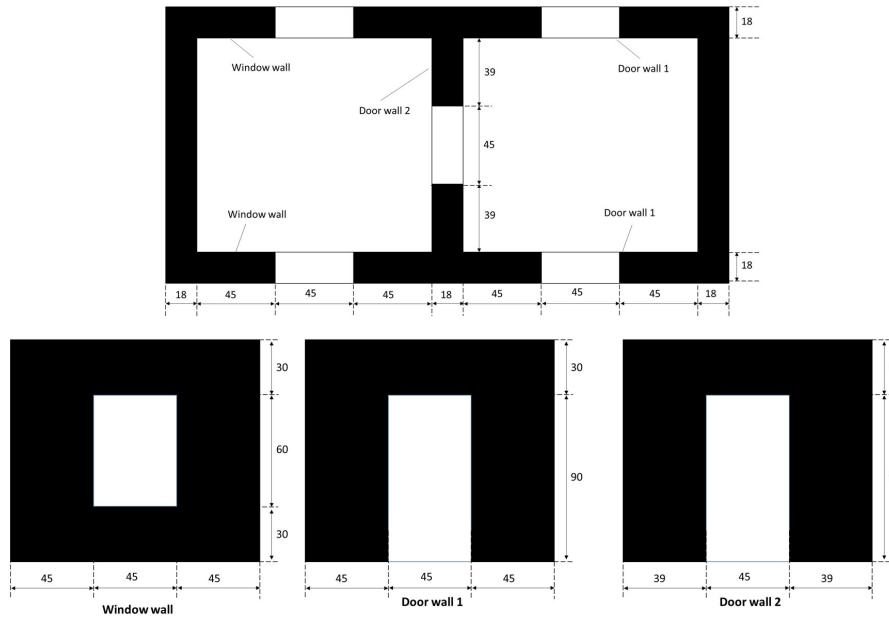


Figure 7.20: Schemes of the 5-wall structure for the modal analysis

7.3.1 5-wall structure without openings

The modal frequencies obtained with the three models are shown in Figure 7.22. The two 2D models exhibit differences in the determination of the frequencies with the reference model. Both of them underestimate the stiffness of the structure. The computation time of the DFM is satisfactory compared to the 3D reference model.

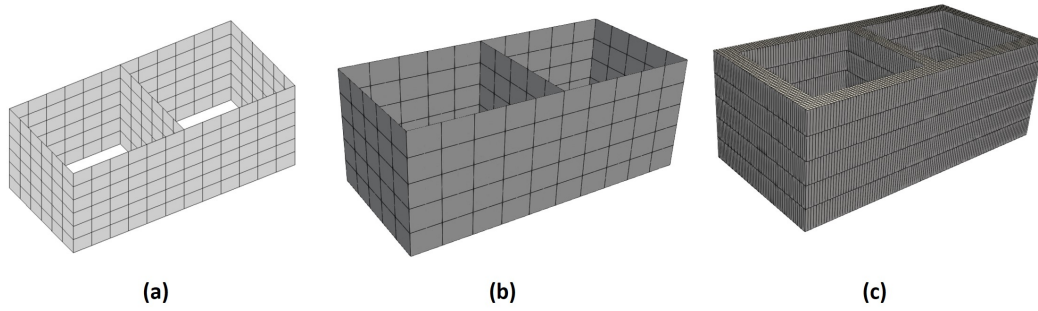


Figure 7.21: Meshes for the 5-wall structure without openings: (a) Mesh_5 for the DFM; (b) mesh 2D FE model; (c) mesh with 3D FE model

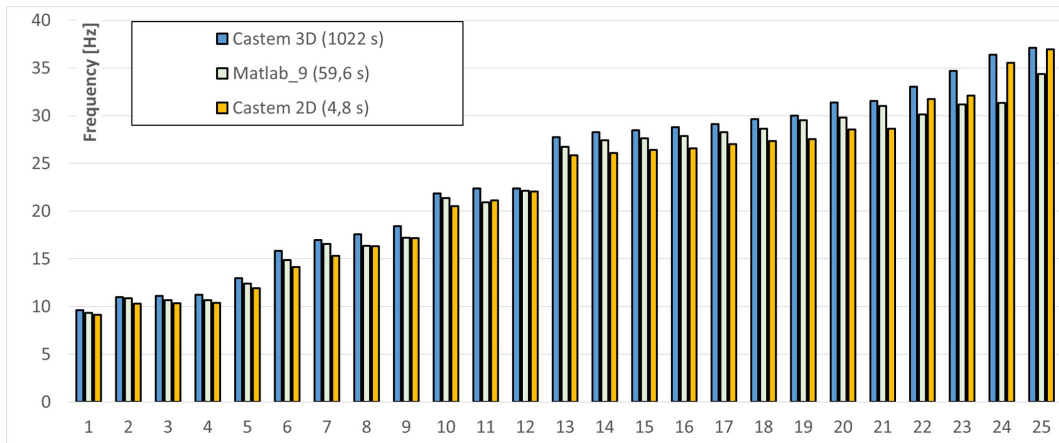


Figure 7.22: The first modal frequencies of the 5-wall structure without openings

The result of the modal mass with the DFM and the shell elements are shown in Figure 7.25.(a). There are five major modes (modes 4, 5, 11, 12 and 25). The two models have quite different results. The reasons of these differences are the same as for the 4-wall structure. Mode 25 is the first vertical tension/compression mode and modes 11 and 12 are the torsional modes of the small and long walls respectively.

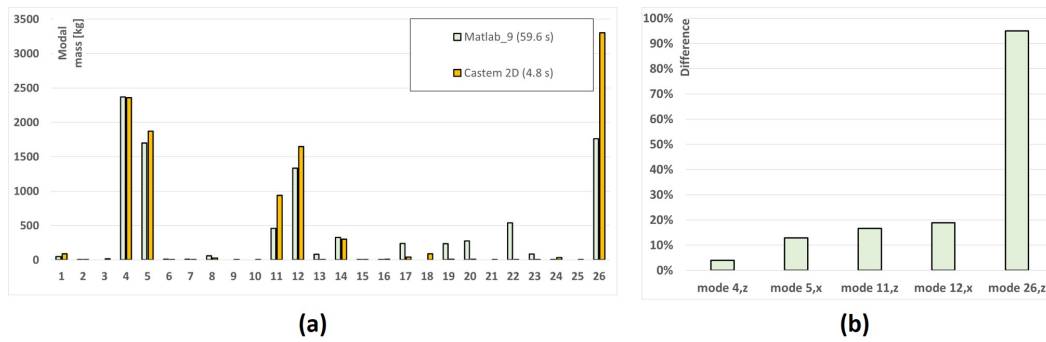


Figure 7.23: Modal masses for the 5-wall structure without openings: (a). Results for the DFM and shell elements; (b) Error in the determination of the modes with high modal mass

Figure 7.24 shows the modal shapes for the important modes of the 5-wall structure without openings. The results of the models are quite similar. The only noticeable difference is for the 1st vertical mode where the DFM tends to underestimate the displacement compared to the reference model. All the other shapes do not exhibit any obvious difference.

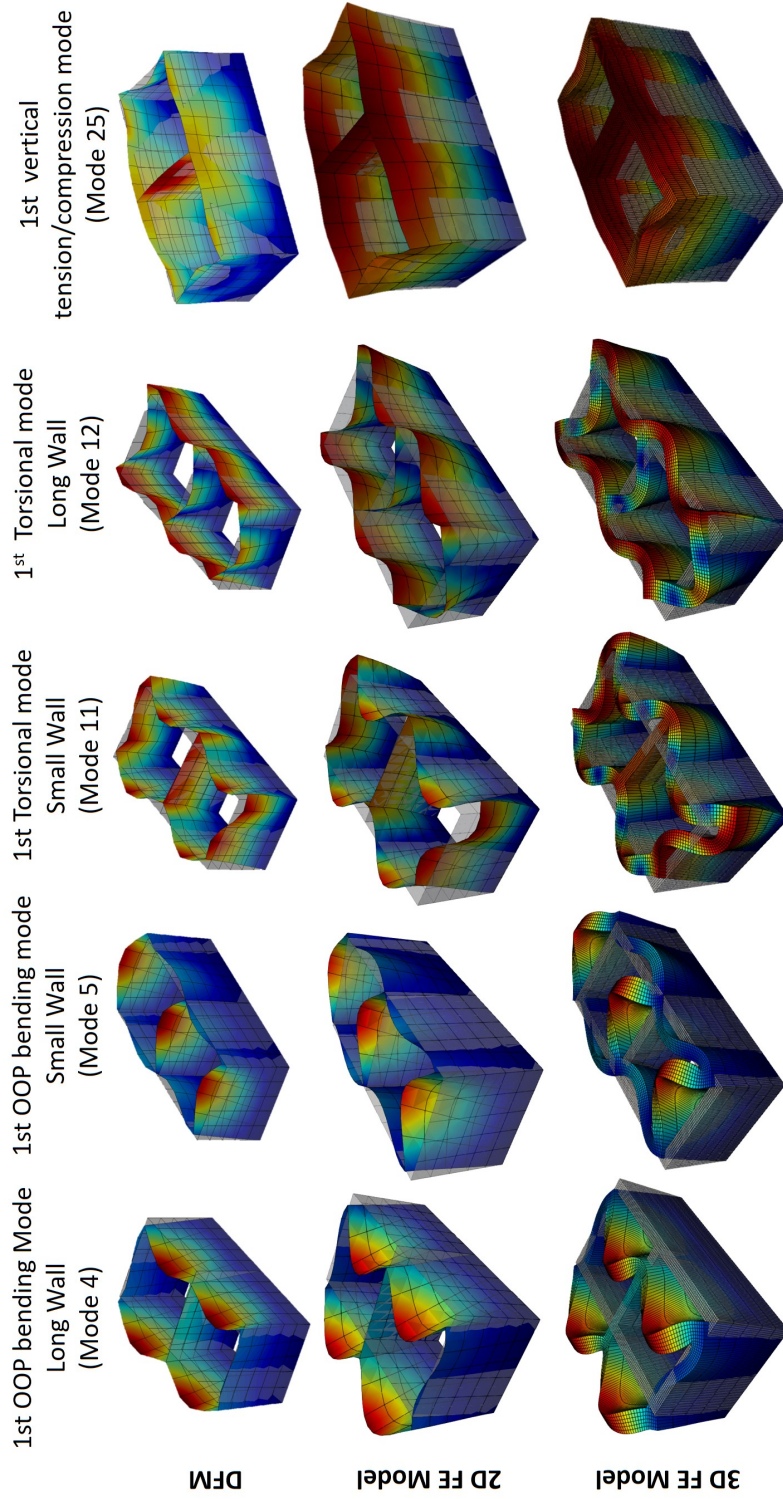


Figure 7.24: Modal shapes of the 5-wall structure without openings

The modes shown in Figure 7.24 are well approximated with the DFM despite the differences of modal mass. The DFM is even more accurate than the shell elements for the modes 4 and 5. Unexpectedly, the DFM performs better with the coarser proposed mesh in Figure 7.22. Still, the model performs well with a more discretized mesh.

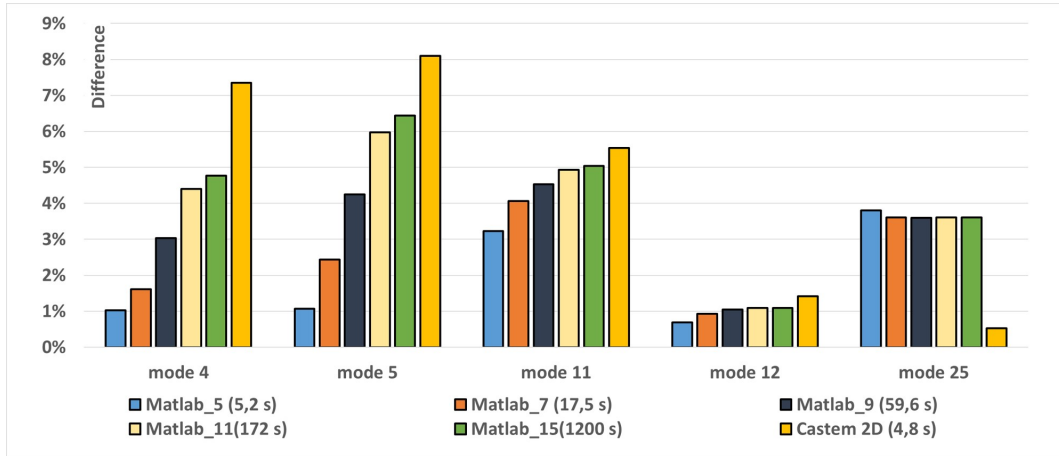


Figure 7.25: Evolution of the accuracy in determining the frequencies of the modes in Figure 7.24 with the mesh size

This study of the 5-wall structure without openings shows that the DFM still performs well despite the increase of the number of modeled walls. Moreover, the DFM tends to perform better than the 2D FE model for a similar computation time.

7.3.2 5-wall structure with openings

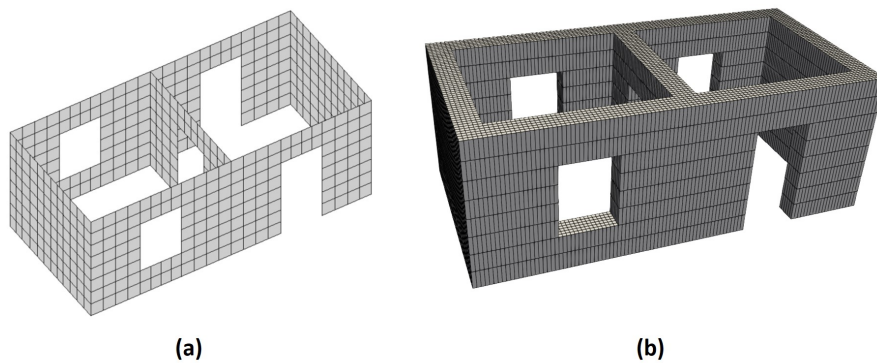


Figure 7.26: Mesh for the 5-wall structure with openings: (a) Mesh_2 with the DFM; (b) reference 3D FE model

Because of the openings, the thickness of the wall is not significantly smaller than the width of

the piers. Therefore, the 5-wall structure with openings cannot be modeled with shell elements. Thus, for this study, only the 3D FE model is used for the comparison with the DFM. The mesh of the 5-wall structure with openings with the DFM is different than the one of the previous study because the presence of the openings imposes some restrictions for the size of the elements (see Fig. 7.26).

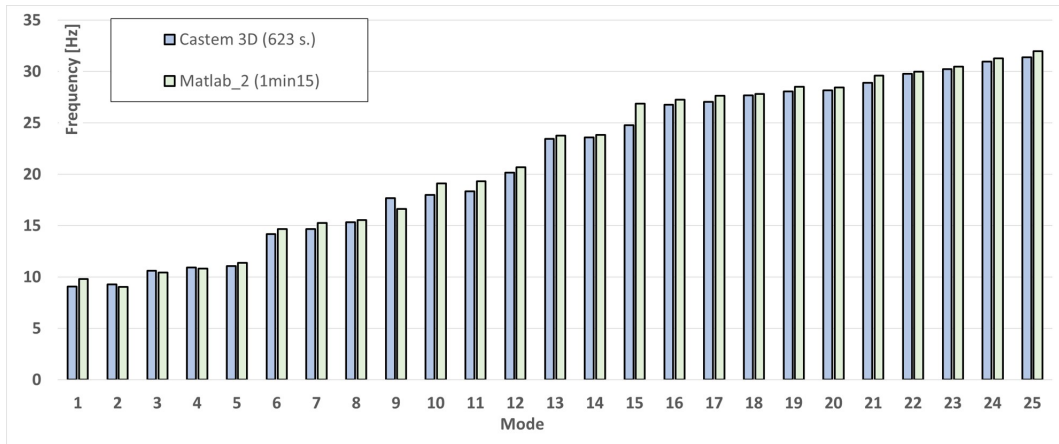


Figure 7.27: The first modal frequencies for the 5-wall structure with openings

Figure 7.27 shows the results for the 25th first modal frequencies of the 5-wall structure with openings. The DFM tends to underestimate the values of the frequencies for the last modes but the frequencies determined with it remain close to the ones of the reference model. Because of the limitations linked to the size of the elements, the coarser mesh is not really coarse, as shown in Figure 7.26. That is why the Mesh_2 gives good results. For this study, the DFM has a very interesting computation time with only one minute to determine the modes of the structure (see Fig. 7.27).

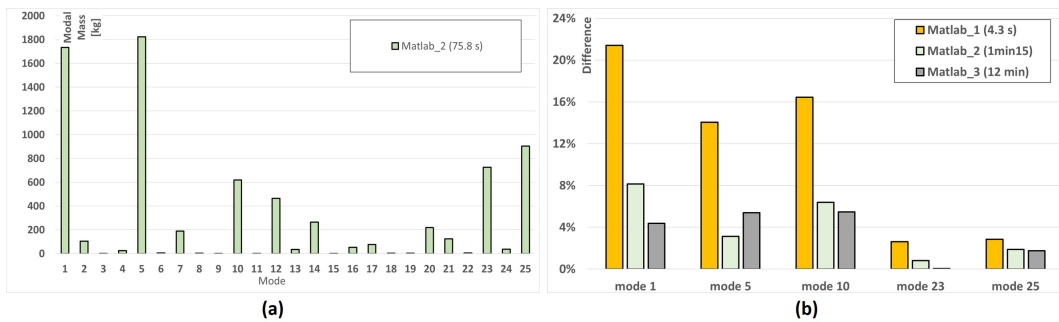


Figure 7.28: Modal analysis of the 5-wall structure with the DFM: (a) the 25th first modal masses; (b) accuracy for the determination of the important modes

Unlike for the previous study, the modal masses shown in Figure 7.28.(a) are not determined with the models on Castem. Therefore, the determination of the modal masses is only used to know the important modes. There are two main modes (modes 1 and 5) and three modes

that have an important mass too (modes 10, 23 and 25). In terms of accuracy of the model, Figure 7.28.(b) shows that the DFM approximates well the results obtained with the reference model. The coarser mesh does not give satisfactory results for the first mode (22% of error) but the second mesh has a maximum error of 8% which is quite satisfactory.

The modal shapes (see Fig. 7.29) are similar with the DFM and with the 3D elements model. There are some differences in the amplitude of displacements that are related to the difference of representation of the models and the complexity of the modeled structure. Therefore, the DFM gives very satisfying results in a short time making its use quite relevant for the study of a complete structure.

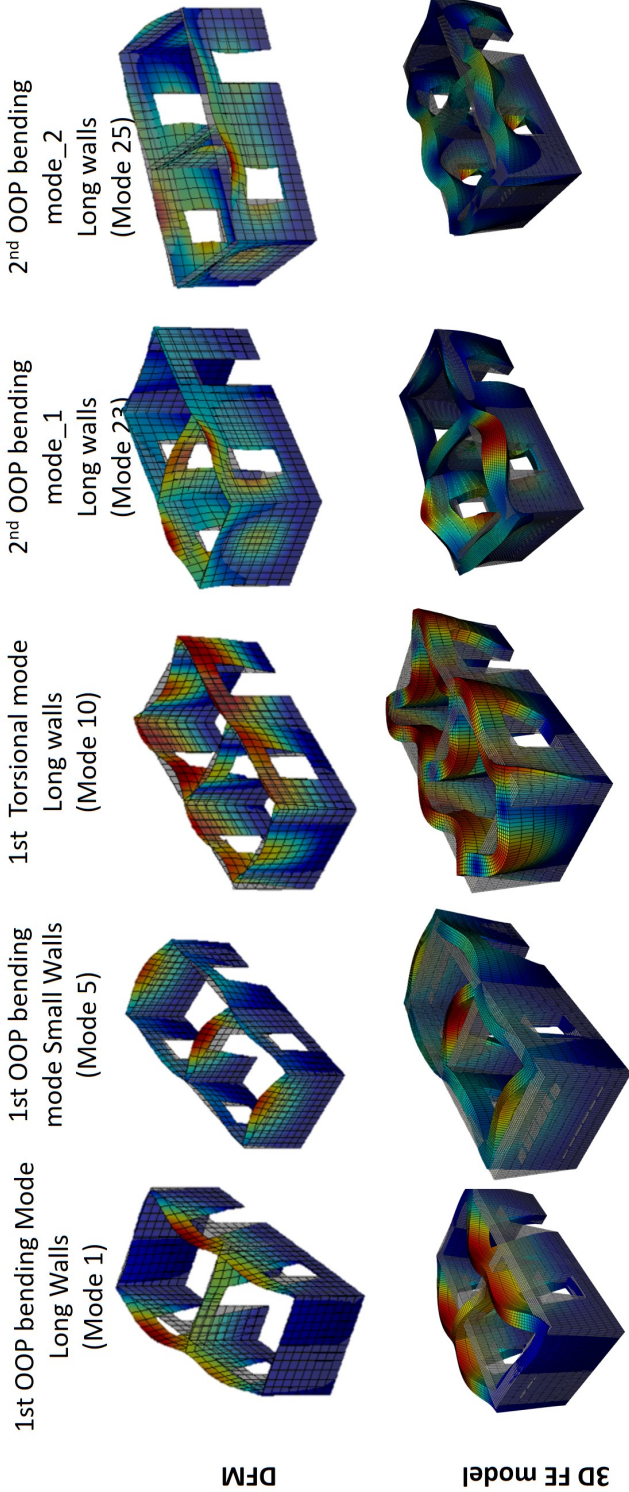


Figure 7.29: Modal shapes of the 5-wall structure with openings

7.4 Conclusions about the modal analysis

In this chapter, the elastic properties of the DFM and the definition of the mass matrix were tested with several modal analyzes. To verify the results and the performances of the model, two FE models were used: a 3D model for reference and a 2D model for computation time and accuracy. Based on these studies, the following conclusions were drawn:

1. The DFM approximates well the modal frequencies of all the tested structures with a very interesting computation time (1 minute for a 5-wall structure).
2. The DFM does not well capture the main vertical mode well. This means that the model sometimes detects an additional main vertical mode (as in the case of the 4-wall structure). This could be related to the definition of the IP kinematics of the DFM, where rotations at the nodes are not taken into account. However, for the dynamic analysis of structures, this is not really a disadvantage, since there will be no vertical excitations.
3. The modal shapes with the DFM are similar to those of the FE models, except for some minor differences.

Since the model is well suited for determining the modal behavior of a structure, its elastic behavior is correctly defined for both IP and OOP directions. Therefore, it is conceivable to use it for dynamic analysis of structures. The second step before processing to this type of analysis is to verify the definition of the inelastic behavior of the DFM. This is the topic of the next chapter.

Chapter 8

Modeling of static IP cyclic tests on walls

In this chapter, three experimental campaigns are used to validate the numerical model. The first experimental test is the benchmark test of Anthoine et al. [5], which was briefly presented in Section 1.3.2. The second experimental test is the one presented by Reyes et al. [6, 120]. It consists of cyclic tests on two wide walls: one wall is made of rammed earth and the other of adobe. Unlike the walls of the tests of Anthoine et al. [5], the walls of this second experiment have two openings and lintels. Only the adobe wall is analyzed. The last experimental test is that of Yadav [7]. It consists of two quasi-static tests on square adobe walls. One of them is without bands and the second has a wooden band in the middle of the height.

The objectives of these modeling tests are to validate the definition of the inelastic behavior of the diagonals of the DFM and the proposed modeling for the bands and the lintels.

All the analyzes presented in this chapter are performed with the same computer. This computer has an Intel(R) Core(TM) i5-8250U @ 1.6-1.8 GHz processor and 8.0 Gb of RAM.

8.1 URM piers

8.1.1 Modeling of the tests

The benchmark test of Anthoine et al. [5] is often used as an example of comparison between experimental and numerical results to validate models [54, 49, 92]. It consists in studying the IP behavior of two different pier walls with the same width and thickness but different heights. The small wall has dimensions $100 \times 135 \times 25 \text{ cm}^3$ (L×H×T) and the second wall has dimensions $100 \times 200 \times 25 \text{ cm}^3$ (L×H×T). The size of the two walls is chosen so that they do not have the

same failure pattern: a bending/rocking failure for the tall wall and a diagonal shear failure for the small wall. Bricks of size $5.5 \times 12 \times 25 \text{ cm}^3$ are used for both walls, arranged in English bond.

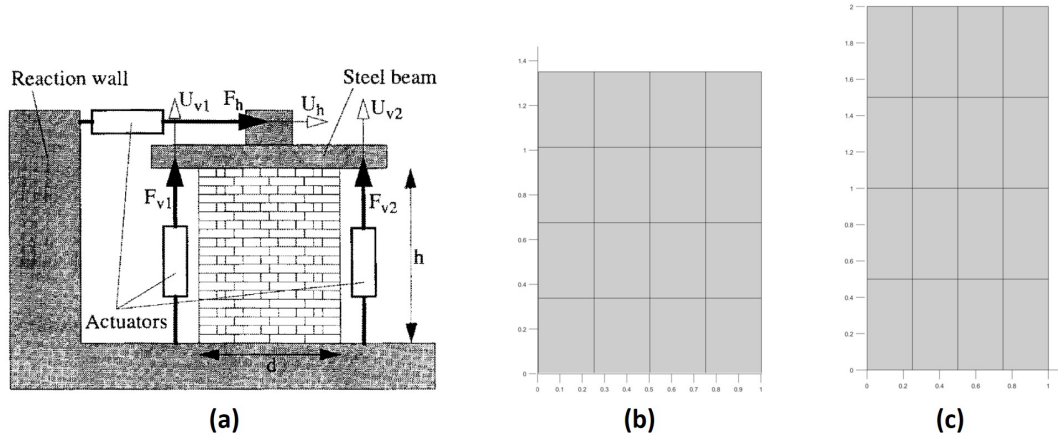


Figure 8.1: (a) Experimental setup for the test of the two walls [5] and modeling of (b) the small wall and (c) the high wall

The experimental setup prevents rotation of the wall (see Fig. 8.1.(a)), so that the experiment reproduces as closely as possible the conditions of pure shear. For this reason, the assumption of a doubly restrained wall is made for the modeling. The shear excitation is applied by an imposed cyclic horizontal displacement at the top of the wall. Two cycles of the same amplitude are performed. If a noticeable loss of strength is observed, three cycles are performed instead of two. In addition to the cyclic displacement, a constant vertical compressive stress $\sigma_{v1} = 0.6 \text{ MPa}$ is applied to the walls.

Parameters of Table 8.1 for the definition of the bi-linear behavior of the DFM as reported by Caliò et al. [92] (superscript “a”), by Gambarota and Lagomarsino [49] (superscript “b”) and by Magenes and Calvi [121] (superscript “c”) are shown in blue Table 8.1.

The computed hysteresis parameters for both walls are shown in Table 8.2. They are determined with the Equations (4.19), (4.22) and (4.23). The values of parameters α show that the small wall has either a shear/sliding failure or a diagonal cracking failure and that the high wall has rocking failure. The output of the model shows that diagonal failure is captured for the small wall. The parameters β and δ are different since the walls have different slenderness.

The experimental results for both walls are shown in Figure 8.2. The high wall has a rocking failure. It does not have a significant loss of strength and has a limited energy dissipation. The small pier has diagonal shear failure. It has a large strength loss after failure and a higher energy dissipation. These two modes of failure correspond to the ones predicted by the DFM.

The curves obtained with the DFM are shown in Figure 8.3. They have been obtained with

¹Obtained with the formula of Mann and Muller [8]

Table 8.1: Properties of the URM piers [49]

Material properties for the stiffness of the DFM	
Young's modulus [E_m] ^(a,b)	2.1 GPa
Shear modulus [G_m] ^(b)	420 MPa
Material properties for the shear strength of the DFM	
Tensile strength [f_t] ^(a)	0.1 MPa
Cohesion [c] ^{1 (c)}	0.17 MPa
Coefficient of friction [μ] ^{1 (c)}	0.43
Density of masonry [ρ_m] ^(b)	1750

Table 8.2: Parameters of the hysteresis for the DFM

	Small wall	High wall
Cyclic damage [α]	0.938	0.99
Force for change of stiffness [β]	0.487	0.7
Plasticity [δ]	0.3	0.6

the mesh shown in Figure 8.1.(b-c). This mesh is the coarser mesh leading to the final result of the DFM. For both the small wall and the high wall, the DFM succeeds in approximating the envelope curve (initial stiffness and maximum strength) before and after failure very well. For the inelastic behavior, the DFM also approximates the loops well with only three parameters. However, for the high wall, with large displacements, the loops shape cannot be reproduced with the chosen cyclic law.

It can be concluded with this first study that: (i) the DFM can predict the initial behavior of an URM pier and its maximal strength and (ii) it can well approximate the hysteretic behavior of masonry under cyclic shear loading.

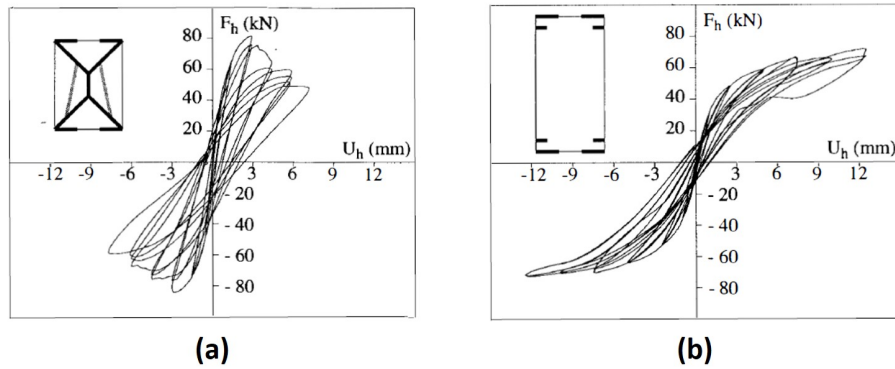


Figure 8.2: Force-displacement curves obtained experimentally by Anthoine et al. [5]: (a) small wall; (b) high wall

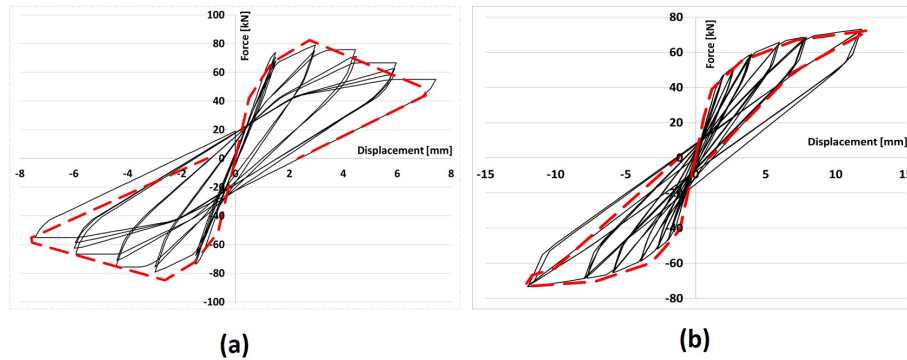


Figure 8.3: Force-displacement curves obtained with the DFM: (a) small wall; (b) high wall. The dashed lines are the envelope curves of the experimental tests and the limits of the last hysteresis loops.

8.1.2 Influence of the size of the mesh

This part aims to study the influence of the mesh on the computation time and the accuracy of the results. The material properties are still those given in Table 8.1. The influence of the mesh is shown in Figure 8.4 for the small wall and in Figure 8.5 for the high wall. It can be seen that the mesh size affects the envelope curve but not the hysteresis. Moreover, it does not have the same influence for both walls. For the high wall, Mesh_2 has a difference of 20% in determining the maximum force compared to Mesh_6, while the difference in maximum force for these two meshes is only 2.5% for the small wall. For both walls, the results do not change when the meshes are finer than Mesh_4, hence its use in the previous section.

The computation time to obtain the final results using the DFM is 20 minutes for the small wall and 15 minutes for the high wall. These computation times are quite satisfactory for

modeling a cyclic test. If an error of about 10% is accepted, a coarser mesh can be used (Mesh_3) and the results can be obtained in less than 10 minutes.

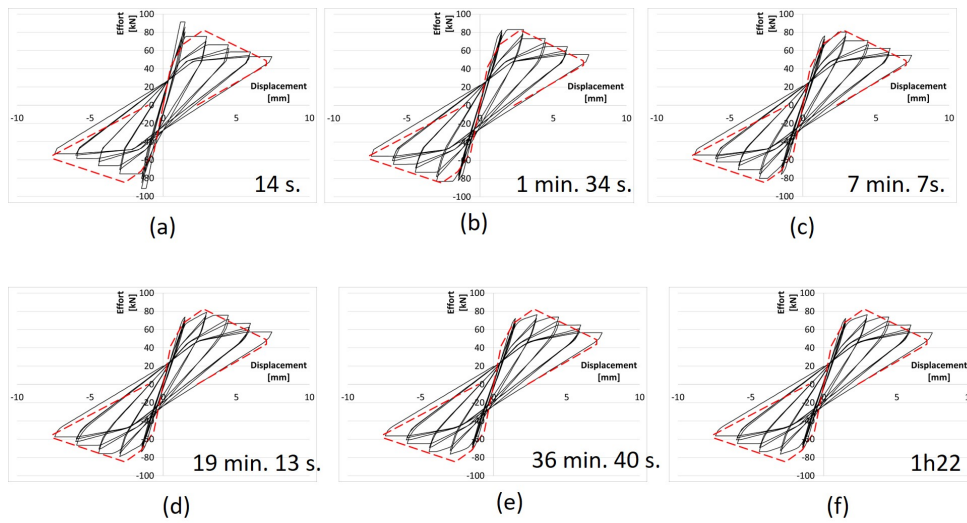


Figure 8.4: Influence of the mesh for the Force-Displacement curve of the small wall tested by Antoine et al. [5]: (1) Mesh 1x1; (b) Mesh 2x2; (c) Mesh 3x3; (d) Mesh 4x4; (e) Mesh 5x5 ; (f) Mesh 6x6

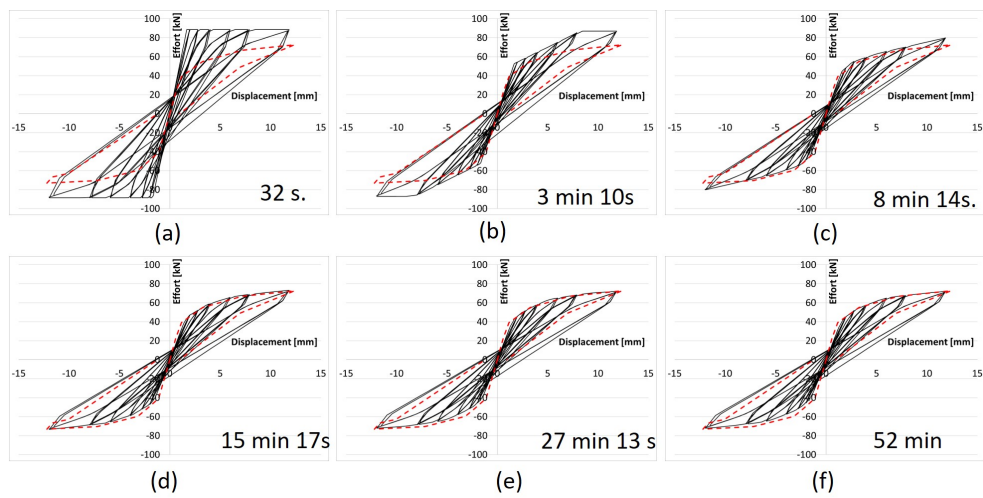


Figure 8.5: Influence of the mesh for the Force-Displacement curve of the high wall tested by Antoine et al. [5]: (1) Mesh 1x1; (b) Mesh 2x2; (c) Mesh 3x3; (d) Mesh 4x4; (e) Mesh 5x5 ; (f) Mesh 6x6

8.2 Wide walls with openings

8.2.1 Modeling with a bilinear behavior

The walls tested by Reyes et al. [120, 6] are used to see how the DFM performs for predicting the behavior of a wide wall with openings. In this section, only the adobe wall is examined. Its design is shown in Figure 8.6.(a). It is inspired by the typical architecture of historic adobe buildings in Columbia. There is a short buttress on each side of the wall to account for the influence of the perpendicular walls. These are not visible in Figure 8.6.(a). Concrete blocks are placed on the wall for a total vertical force $F_v=51.86$ kN. The foundation of the walls is made with a reinforced concrete beam connected to the reaction floor of the laboratory. It is fixed with prestressing anchors. Since nothing blocks the top of the wall vertically, it is modeled as a cantilever wall.

The displacement is imposed by a hydraulic jack on one side of the wall, which is connected to a system that allows the wall to be pulled. The displacement protocol is based on FEMA461 [122]. The first displacement has an amplitude of 0.2 mm. Every other cycle, the amplitude is increased by a factor of 1.4 until the displacement of 15.8 mm amplitude is reached.

Table 8.3 shows the mechanical properties of the adobe wall. The parameters with superscript “a” are given by Reyes et al. [120]. They were obtained by specific experimental tests on adobe prisms and the mortar. The parameters with superscript “b” have been determined using the data from Reyes et al. [120, 6]. The elastic properties of the adobe wall are not reported in these articles. However, the elastic properties of the rammed earth wall are reported. The cyclic tests of the two walls show that both walls have similar initial stiffness. Therefore, the elastic modulus and Poisson’s ratio of the rammed earth wall in Reyes et al. [120] are assumed to be the elastic properties of the adobe wall. The cross section of the lintels is determined based on the figures in the two articles. The parameters with the superscript “c” are given by Sandoval et al. [123], who worked on this experimental campaign.

The mesh shown in Figure 8.6.(b) is the coarsest mesh leading to the final results with the DFM. It is made of 89 nodes for a total of 543 degrees of freedom. The red elements in Figure 8.6.(b) are the lintels above the openings. They are not centered on the opening because of the modeling choice stated in Section 5.2. Since the meso-elements on both sides of the openings are not the same size, the lintel may be extended on one side of the opening but not on the other. The nodes of the lintels have three degrees of freedom except those at the extremities whose rotation is blocked.

The experimental curve of the adobe wall is shown in Figure 8.7.(a) and the force-displacement curve obtained with DFM is shown in Figure 8.7.(b). The red dashed line is the envelope of the experimental results (curve in Figure 8.7.(a)). The model has a slightly lower initial stiffness than the real adobe wall in the pulling direction but the difference remains small. The maximum strength of the wall is overestimated by 20% in the pushing direction but it is well estimated in

Table 8.3: Proprieties of the adobe wall

Stiffness of the DFM	
Young's modulus of masonry $[E_m]^{(b)}$	200 MPa
Poisson's ratio $[\nu]^{(b)}$	0.15
Shear strength of the DFM	
Density $[\rho]^{(a)}$	1850 kg.m ⁻³
Strength in tension $[f_t]^{(a)}$	27.5 kPa
Coefficient of friction $[\mu]^{(a)}$	0.86
Cohesion $[c]^{(a)}$	15 kPa
Elastic properties of the lintels	
Young modulus lintels $[E_l]^{(c)}$	9 GPa
Poisson's ratio lintels $[\nu_l]^{(c)}$	0.2
Section lintels $[A_l]^{(b)}$	15x15 cm ²
Density lintels $[\rho_l]^{(c)}$	700 kg.m ⁻³

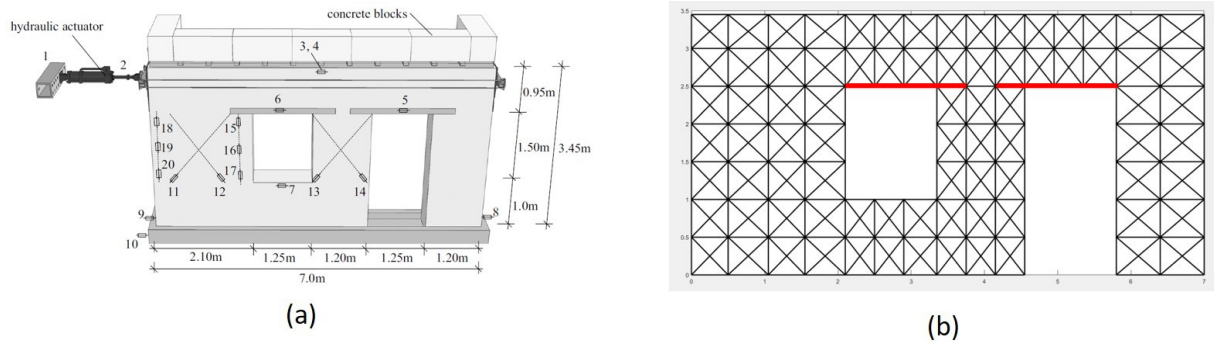


Figure 8.6: Wall with openings tested by Reyes et al. [120]: (a) specimens tested by Reyes [120]; (b) mesh with the DFM

the pulling direction. The reason for this significant overestimation of the maximum strength of the wall in the pushing direction is related to the choice of a bilinear curve for the shear behavior of the DFM. This results in a too high stiffness for small displacements and, thus, in a too high strength of the adobe wall. The computation time is indicated in Figure 8.7.(b) for information. For a shear cyclic test of a wall of this size, this computation time is very satisfying.

The values of the parameters defining the hysteresis loop differ from one meso-element to another. Table 8.4 contains the average values for the three parameters. The DFM with the proposed definitions of the hysteresis parameters overestimates the size of the loops. The average value of the parameter β , which defines the force at which the diagonal element changes its stiffness, is too low. It leads to an important energy dissipation compared to the experimental test.

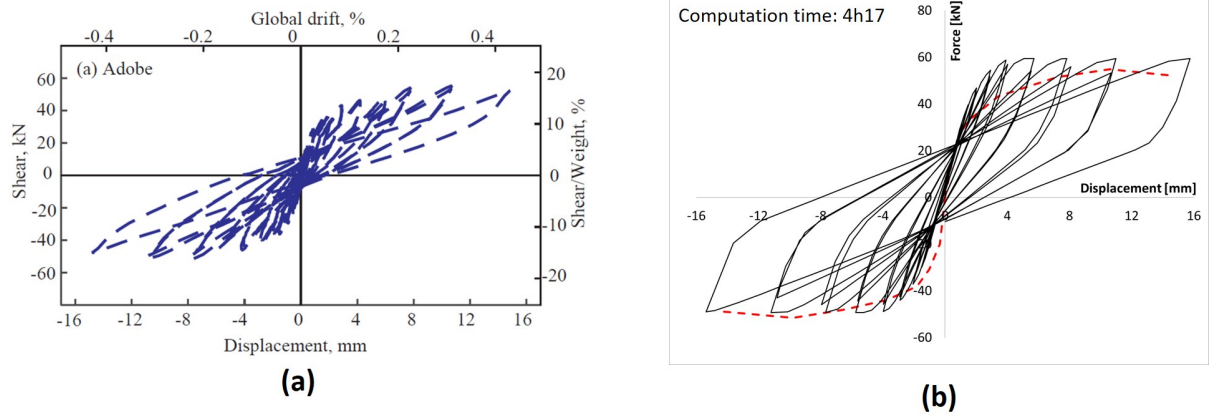


Figure 8.7: (a) Experimental cyclic response of the adobe wall [120]; (b) cyclic response with bilinear behavior. The red dashed line is the envelope of the experimental curve. The continuous line is the results obtained with the DFM.

Table 8.4: Average values of the parameters of the hysteresis

	Adobe wall
Cyclic damage [α]	0.89
Force for change of stiffness [β]	0.2
Plasticity [δ]	0.02

8.2.2 Modeling with a trilinear behavior

In this section, the aim is not to predict the behavior of the adobe wall but to well approximate the experimental curve. To improve the results obtained with the DFM, it is possible to use a trilinear behavior for the diagonal struts. The displacement and the force at the appearance of the cracks and when the maximal strength is reached are given by Reyes et al. [6]. The new parameters are defined in Table 8.5. The stiffness of the elements and the definition of the maximal strength are still defined with the parameters in Table 8.3. The new constitutive law for the diagonal elements is shown in Figure 8.8.(a) with the values used for the new parameters. With this type of envelope, the hysteretic unloading/reloading behavior presented in Section 4.4.2.6 begins as soon as the force F_{cr} in Figure 8.8.(a) is reached. The displacement d_{cr} is the displacement for the occurrence of cracks.

Figure 8.8.(b) shows the result of the model with the changes. As expected, the envelope curve is better reproduced by taking a trilinear curve for the diagonal elements. The maximum error is now about 15 %, which is satisfactory knowing that there are uncertainties related to the material properties. However, the behavior in the pulling direction is less accurate with the trilinear behavior. This is due to the fact that the model does not have the same initial stiffness in this direction as in the experimental test.

Table 8.5: Proprieties of the adobe wall for the second study

Trilinear behavior of the DFM	
Appearance of cracks F_{cr}/F_u	0.73
Displacement when the maximal strength is reached d_u/d_{cr}	7.5
Hysteresis parameters	
Cyclic damage $[\alpha]$	0.85
Force for change of stiffness $[\beta]$	0.67
Plasticity $[\delta]$	0.5

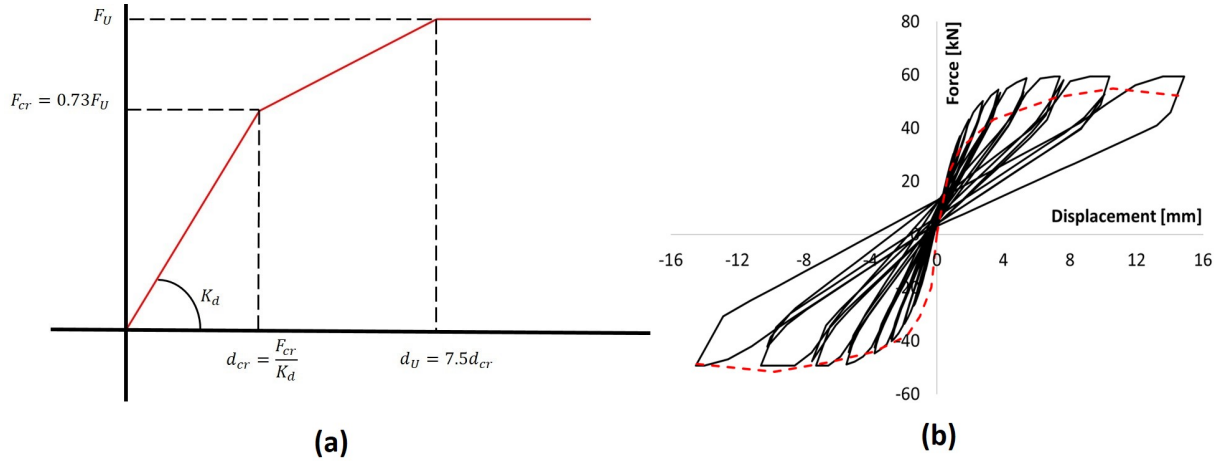


Figure 8.8: Results with trilinear behavior: (a) trilinear force-displacement law for the diagonal struts (data from Reyes et al. [6]); (b) results with the trilinear model. The dashed line is the envelope of the experimental curve. The continuous line is the result obtained with the meso-model.

The hysteresis loop in the experimental results would lead to two different values for the parameter β depending on the loading direction. It was decided to approximate the two behaviors as closely as possible by taking an in-between value: $\beta = 0.67$. The parameter α was adjusted so that the cyclic damage was the same for the model and for the experimental results. The parameter δ was taken equal to 0.5 to obtain the same size for the hysteresis loop for the experimental curve and the DFM curve. With these values, the hysteresis is better approximated than with the proposed definitions. Nevertheless, the reloading part of the hysteresis loop cannot be well reproduced with the definition of the third branch of the hysteresis loop of the DFM. The model reaches the envelope curve too early compared to the experimental curve (positive loading direction in Figure 8.8. (b)). This can be changed by setting a different parameter β for the unloading and reloading branches, but this would add a new parameter.

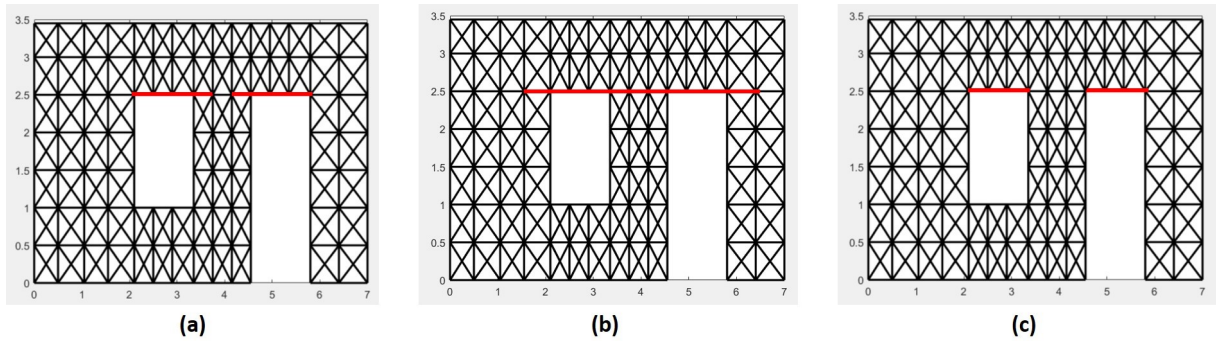


Figure 8.9: Modeling of the adobe walls with different lengths of the lintels: (a) current modeling in this section; (b) modeling with longer lintels; (c) modeling with lintels only above the openings

8.2.3 Influence of the modeling of the lintels

The lintels in the model do not have the same length as those in reality, for reasons of mesh size. Since the mesh is coarse, the lintels in the model can be much smaller compared to the real ones. To evaluate the impact of this simplification on the results, three different meshes are compared (Figure 8.9). Case (a) is the one studied in this chapter, case (b) is the one where the length of the lintel is extended to the nearest node and case (c) is the modeling of the lintel only above the opening and not in the masonry.

The push-over curves of the three cases are shown in Figure 8.10. It can be seen that the modeling of the lintels has a small effect on the push-over behavior of the walls, except for the behavior after the appearance of cracks, where the lintels add more rigidity. To reproduce the experimental results as well as possible, the choice was made to model the lintel in the masonry as well. Since it has an elastic behavior, it does not cause any significant extra computational time.

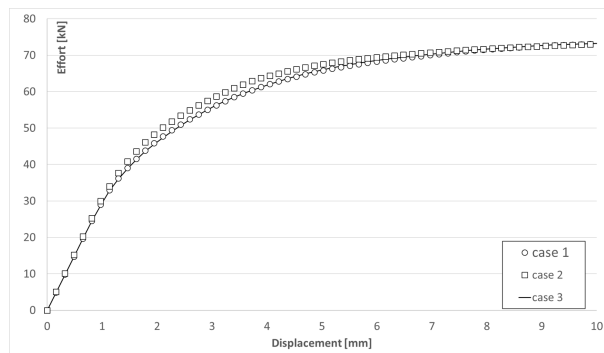


Figure 8.10: Push-over curves of the cases in Figure 8.9

8.2.4 Conclusion

The analysis of the adobe walls with openings allows to make some conclusions about the capacities of the DFM:

- The DFM is able to predict the maximal strength of a wide wall with openings with a good accuracy.
- The bilinear behavior for the diagonal elements gives a stiffness for small displacements that can lead to an overestimation of the strength of the wall of around 20 %
- The trilinear behavior for the diagonal elements gives good approximation of the envelope curve.
- The definition of the hysteresis parameters give a good approximation of the experimental curves.

8.3 Adobe wall with bands

The final modeling is the modeling of Yadav's experimental test [7] performed at the 3SR laboratory. This experimental test consists in a quasi-static shear test of two adobe walls: one with timber band (RM) and one without any band (URM). Both walls have the same dimensions. They are made of extruded adobe bricks produced by a French company (Brique de Nagen) and mud mortar (50% soil and 50% sand). The walls were tested 3 months after they were made.

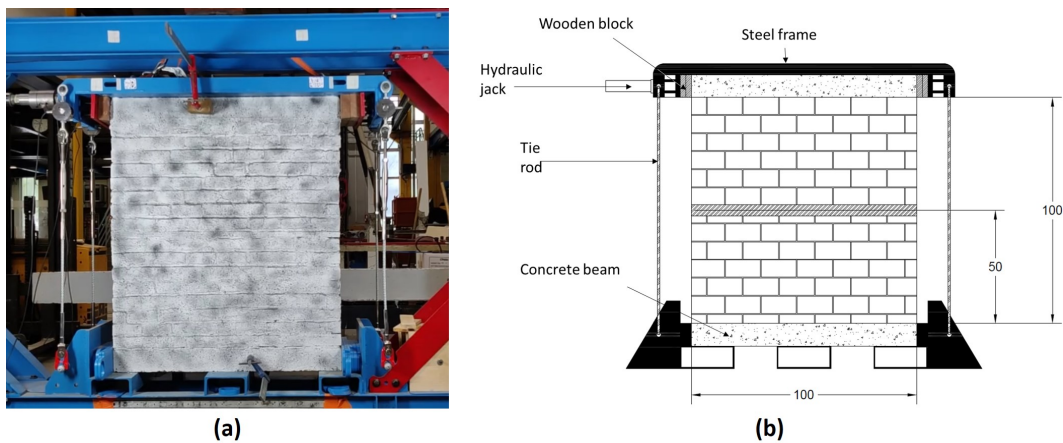


Figure 8.11: (a) Apparatus for the quasi-static test of Yadav and (b) diagram thereof for the identification of elements

The experimental device is shown in Figure 8.11. The wall is placed between two concrete beams. The upper beam is used for applying the horizontal displacement and well distribute

the vertical reaction due to the steel beam, and the lower beam serves as the foundation. The wall is considered to be perfectly embedded in the two beams. Four tie rods (two are visible in Figure 8.11) are used to apply a vertical stress of about 11.4 kPa. For modeling purposes, it is assumed that the vertical load applied by the tie rods is uniformly distributed across the wall. The tie rods are also used to keep the wall horizontal during the test and prevent it from rocking. Therefore, it is considered as a double restrained wall and the displacement acting on the top of the wall is the displacement of the hydraulic cylinder. This method to limit the rocking of the wall leads to an additional confinement of the masonry when the horizontal displacement is applied. Thus, the vertical load applied on the masonry when the maximal strength is reached is twice higher than 11.4 kPa.

The cyclic horizontal displacement loading is shown in Figure 8.12. The same loading protocol is used for both walls. However, the wall without bands does not experience the entirety of the signal because it breaks beforehand.

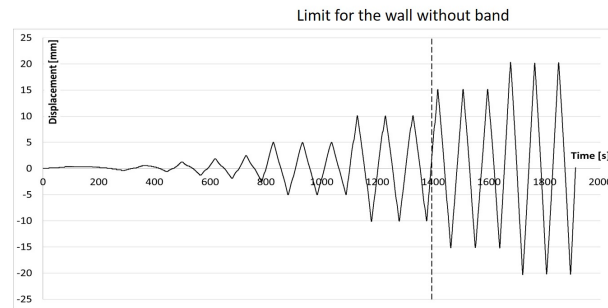


Figure 8.12: Cyclic horizontal displacement loading used by Yadav [7]

The bricks and mortar used for these tests are the same as those used for the shaking table tests presented in the next chapter. The properties of the masonry are determined by fitting the results of the DFM with the results of the experimental tests. These properties are compared with the data from the literature to see if they are meaningful or not. Only the parameters of hysteresis are not fitted as they are determined using the formulas proposed in Chapter 4.

Table 8.6: Properties of the adobe walls for the quasi-static tests

Dimension	Value	Dimension	Value
Height [h_m]	1 m	Width [l_m]	1 m
Thickness [t_m]	0.175 m	Density of masonry [ρ_m]	2000
Height of the band [h_{int}]	2 cm	Height of the bricks [h_b]	5 cm
Width of the bricks [l_b]	12.5 cm	Thickness of the bricks [t_b]	17.5 cm
Thickness of mortar [h_j]	1 cm	Initial vertical stress [σ_v]	11.4 kPa
Maximal vertical stress [σ_v]	22 kPa		

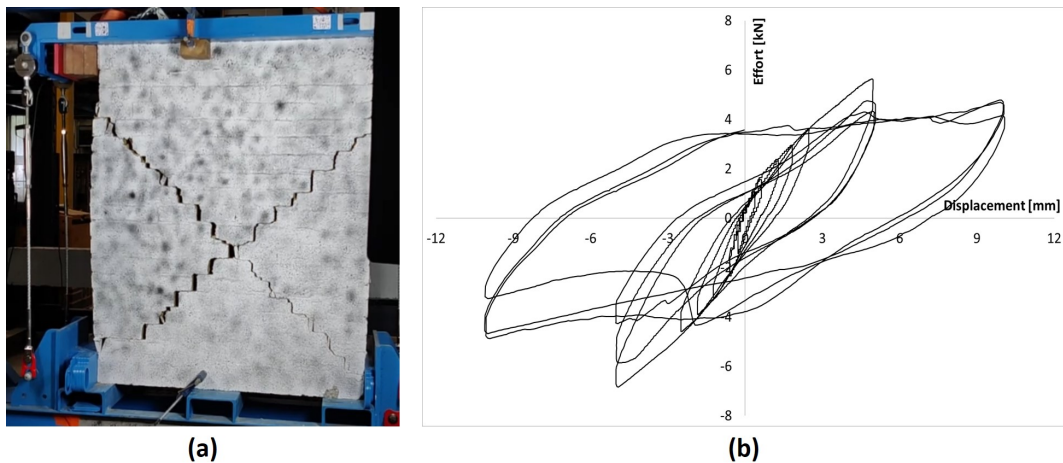


Figure 8.13: Experimental results for the wall without bands: (a) mode of failure of the URM wall and (b) experimental force-displacement response [7]

8.3.1 Wall without bands

The experimental curve and the state of the wall at the end of the test are shown in Figure 8.13. The wall has a diagonal failure during the experiment. This mode of failure has to be the same for the DFM. The properties of the adobe are determined to make it possible. Unlike the previously studied walls, the hysteresis loop changes shape after failure. This is a consequence of the failure occurring. During the last displacement cycles, the wall is divided into four parts. As a result, the parts sometimes slid only along the cracks (visible in the plateau for positive displacements after failure). This change in the shape of the loop implies that the parameter β does not have the same value before and after failure. This phenomenon cannot be captured by the model. Therefore, the hysteresis loops of the last cycles are not considered to assess the accuracy of the DFM.

The identified mechanical properties are listed in Table 8.7. The material properties for the determination of shear strength are in the same range as those measured by Reyes et al. [120] for their adobe wall. The cohesion and coefficient of friction are given in Table 8.7, but it is not possible to obtain a real value because there is not shear/sliding failure. The value of the coefficient of friction is a commonly used value for adobe constructions [124, 125, 126]. For the cohesion, the same ratio cohesion/tensile strength as for Reyes et al. [120] is chosen.

The curves obtained with the DFM are shown in Figure 8.14. A trilinear envelope is used for the diagonal elements. Figure 8.14.(a) shows the curve for small displacements to better see how the experimental curve is approximated before the maximum strength is reached. The experimental curve is not symmetrical. The material properties were determined to approximate both loading directions. It can be seen in Figure 8.14.(a) that the proposed definitions of the hysteresis loop parameters lead to a good approximation of the unloading/reloading behavior of the adobe. For the last cycles, the DFM captures the cyclic damage and plasticity well with the parameters α and δ .

Table 8.7: Material properties of adobe for Yadav's experiment

Stiffness of the DFM	
Young's modulus [E_m]	61.3 MPa
Shear modulus [G_m]	25.5 MPa
Shear strength of the DFM	
Tensile strength [f_t]	22.5 kPa
Cohesion [c]	37.5 kPa
Friction coefficient [μ] ¹	0.6
Trilinear behavior of the DFM	
Appearance of cracks F_{cr}/F_u	0.5
Displacement when the maximal strength is reached d_u/d_{cr}	6.
Parameters of the hysteresis	
Cyclic damage [α]	0.9
Force for change of stiffness [β]	0.2
Plasticity [δ]	-0.4

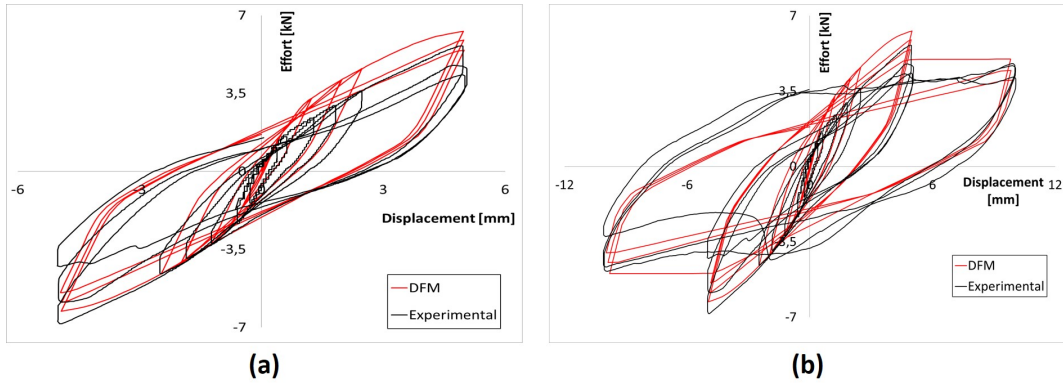


Figure 8.14: Curve obtained with the DFM and experimental curve for the URM wall: (a) Curve for small displacements and (b) complete curve. The red curve is the curve computed with the DFM and the black like is the experimental curve.

8.3.2 Sensitivity analysis for masonry properties

A sensitivity analysis is proposed to show the influence of the masonry properties on the wall behavior. The influence of the Young modulus E_m , the tensile strength f_t , the cohesion c and the coefficient of friction μ is studied. For the influence of the Young modulus E_m , the shear modulus G_m also varies, but the ratio E_m/G_m is always the same. All properties except the one that varies have the value given in Table 8.7. The parameters vary by $\pm 20\%$, a value that can correspond to the coefficient of variation for experimental determination of the material properties [7].

For sake of clarity, push-over curves are used to analyze the influence of some parameters.

These curves are shown in Figure 8.15. It can be seen that the elastic properties of the masonry have a great influence on the initial behavior of the wall. They also have a small influence on the strength of the wall. Figures 8.15 (b-c) show that the values of the tensile strength and the cohesion play a role in the strength of the wall. The curves of $1.1f_t$ and $1.2f_t$ are superimposed. This means that the tensile strength does not lead to failure in these cases. Similarly, the curves of $0.8c$ and $0.9c$ do not overlap with the other curves. This means that the wall exhibits shear/sliding failure in these cases. Therefore, in the context of this experiment, a small variation in the values of the tensile strength or the cohesion may lead to a different mode of failure of the wall. Interestingly, the coefficient of friction is not of great importance for this test. Even a low value for this coefficient does not lead to a change in the mode of failure, since the original value of the cohesion is already high enough (see Figures 8.15.(d)).

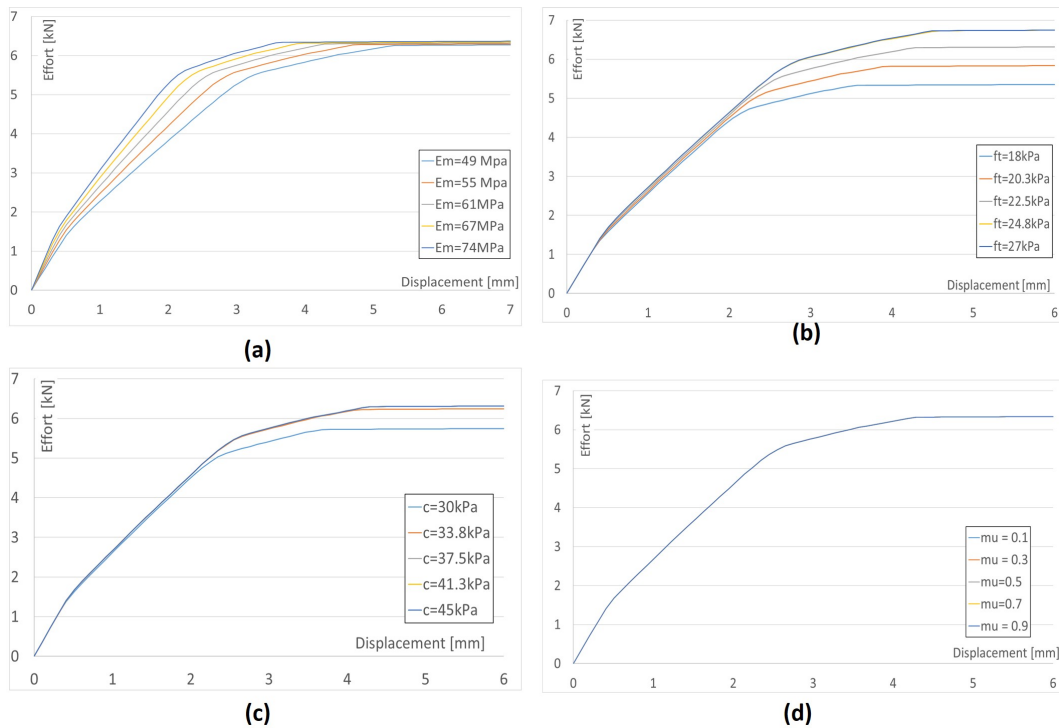


Figure 8.15: Sensitivity analysis for masonry properties: (a) the Young modulus E_m ; (b) the tensile strength f_t ; and the cohesion c and (d) the coefficient of friction μ .

8.3.3 Wall with timber band

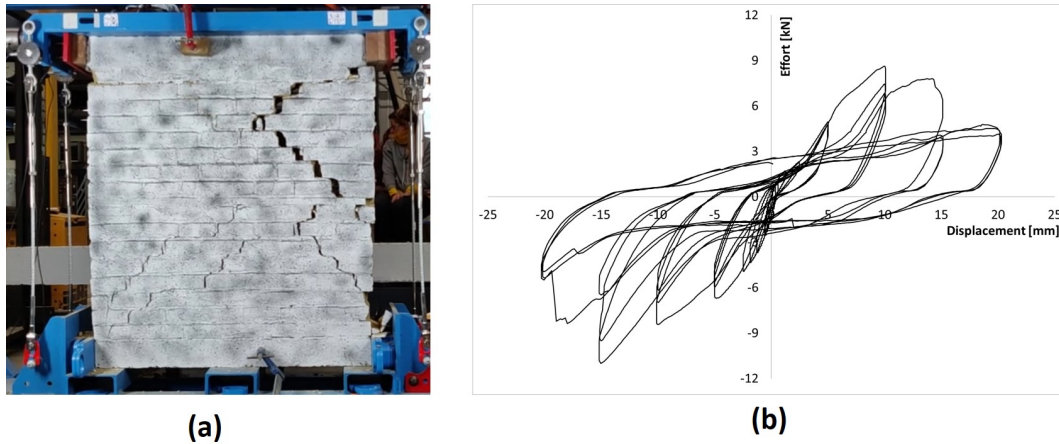


Figure 8.16: Experimental results for the wall with timber bands: (a) failure of the RM wall and (b) force-displacement response [7]

Figure 8.16 shows the failure of the wall with a wooden band and the measured force-displacement behaviour. The pattern of cracking differs from that of the wall without bands. Above the band, diagonal failure occurred on the right side, but not on the left side. Below the band, crack propagation is more diffuse with diagonal cracks with a limited opening. The interface between the masonry and the band is not broken, so there was no sliding between the two elements. This is due to the crack pattern in the upper part of the wall. Once the crack reaches the band, it would propagate along the band with respect to the loading direction. During the experimental test, it occurs when the wall is pushed and leads to the splitting of the masonry portion. When the wall is pulled, the free part of the wall (right side) is no longer in contact with the loaded part. Therefore, the damaged joint is no longer under shear load and crack propagation along the band cannot occur.

The experimental curve is not symmetrical and shows quite different behavior in the two different loading directions. The wall is initially loaded in the negative direction. Therefore, the interface response is adjusted to fit this part of the curve. Comparing Figure 8.16 and Figure 8.13, it can be seen that the wall with wood band has a higher maximum strength than the wall without band. This difference in strength cannot be reproduced by the model. The DFM elements experience the same loading as in the previous experiment. Therefore, the maximum strength for the numerical model is unchanged. There may be two causes in this experiment for the difference in maximum strength: (i) variability in the mechanical properties of the material or related to the experimental manipulation; (ii) the wall without band was too damaged by the cyclic loading before the actual maximum strength was reached, and therefore a lower strength is measured. Indeed, the envelope curve for a cyclic test is not the push-over curve. The presence of the band may limit the crack propagation through the wall and lead to a less damaged masonry wall. Thus, the wall with the band have a higher strength. Another possible reason is related to the definition of the parameter b used in the definition of the strength for the diagonal failure. The definition for pier elements is used for the DFM. Yet, the masonry parts of the wall may be assimilated to spandrels. In this case, the parameter b is defined as the ratio l_m/h_m with the same

limit values as shown in Equation (4.9). This would considerably increase the strength of the wall when modeled with the DFM. Yet, this hypothesis is not consistent with the experimental results of Aranguren et al. [45] (see Section 2.5.1).

The method and the assumptions used for the determination of the curve are:

- The properties of the masonry are unchanged. The differences between the two experimental curves are due to the properties of the band.
- Since there is not any sliding at the masonry/band interface, the coupling parameter φ_{int} between the DFM and the interface element cannot be determined.
- The properties of the interface are chosen so that there is not any sliding.

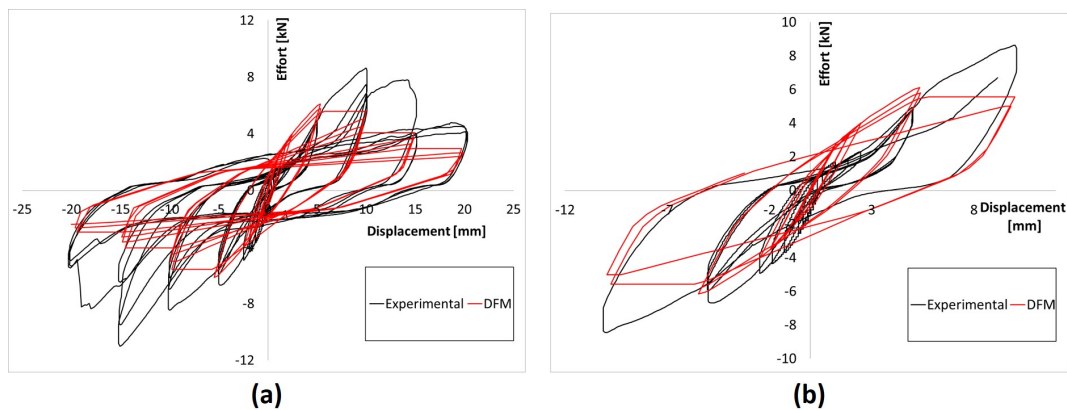


Figure 8.17: Cyclic behavior of the wall with wood band: (a) shear force-displacement for small displacements and (b) zoom on the curve for small displacements

Figure 8.17 shows the experimental curve and the curve obtained with the model. The hysteresis loops are not well approximated for small displacements. Their shape is different for both experiments, even if the parameters α , β and δ keep the same value. For cycles with higher amplitudes, the hysteresis loop is better approximated. As already mentioned, the maximum strength of the model is the same as in the previous test. It leads to an important difference between the envelope curves of the experimental test and the numerical model.

The properties of the interface are shown in Table 8.8. The coefficient of friction is taken equal to $\mu = 0.5$ as done by Illampas et al.[127]. In their study, Illampas et al.[127] took this value and performed a sensitivity analysis by varying the friction coefficient from 0.5 to 1.5. They concluded that a value higher than 0.65 for wood/adobe interface gives none realistic results. The energy release rate and tensile strength are taken from Tarque et al. [124], who used these values for the interface of the simplified micro-model for modeling an adobe wall. The elastic properties of the interface are set similar to those of the masonry since Aranguren et al. [45] determined a similar stiffness for their URM and RM walls (see Section 2.5.1). that the initial stiffness of the numerical model matches the stiffness of the wall. The value of φ_{int} is suggested as the minimum value that does not cause the interface element to yield. The cohesion of the

interface is kept as the cohesion of the adobe wall. The tensile strength is determined by taking the relationship between the tensile strength and the cohesion taken from Wilding et al. [128]:

$$f_t = \frac{c}{2\mu} \quad (8.1)$$

Table 8.8: Mechanical properties of the interface for Yadav's experiment

Elastic properties of the interface	
Normal stiffness [k_n]	61.3 MPa/m
Tangential stiffness [k_t]	25.5 MPa/m
Strength of the interface	
Cohesion [c]	37.5 kPa
Friction coefficient [μ]	0.5
Tensile strength [f_{ty}]	37.5 kPa
Fracture energy [G_t]	0.0008 N/mm
Coupling with the DFM	
φ_{int}	4

8.3.4 Sensitivity analysis interface

A sensitivity analysis is proposed to show the influence of the properties of the band on the behavior of the wall. The influence of the interface stiffness (k_n and k_t), the Poisson's ratio of the mortar ν_{int} , the cohesion c and the coupling parameter φ_{int} are studied. The sensitivity to coefficient of friction is not studied because the initial value of the cohesion is enough to ensure the failure of the masonry before the failure of the interface. Therefore, it is more appropriate to hold the cohesion constant and study both the friction coefficient and the coupling parameter φ_{int} .

The wall with the wood band is considered as the initial configuration. In each analysis, only the considered parameter varies and all others have the value given in Table 8.8. Push-over curves are used for the stiffness, Poisson's ratio and cohesion to better illustrate the differences. Figure 8.18 shows the results for the sensitivity analysis. For the effect of the interface stiffness, only the value of the normal stiffness k_n is shown in Figure 8.18, but the ratio between the normal stiffness k_n and the tangential stiffness k_t is kept the same. Therefore, both the normal stiffness and the tangential stiffness change. It can be seen in Figure 8.18.(a) that they have a great influence on the final result. This influence of the band was noticed in the experimental campaign of Spence and Coburn [46] seen in Section 2.5.

The Poisson's ratio defines the relationship between the normal stiffness k_n and the tangential stiffness k_t . It does not have a great influence on the behavior of the wall (see in Figure 8.18.(b)), since the value of the tangential stiffness does not vary significantly.

The cohesion defines the maximum strength of the interface. The damage occurs first in the element with lower strength between the masonry and the interface. Thus, depending on the

value of the cohesion, the damage occurs at the interface or in the masonry (difference between $c = 11.4\text{kPa}$ and higher values in Figure 8.18.(c)).

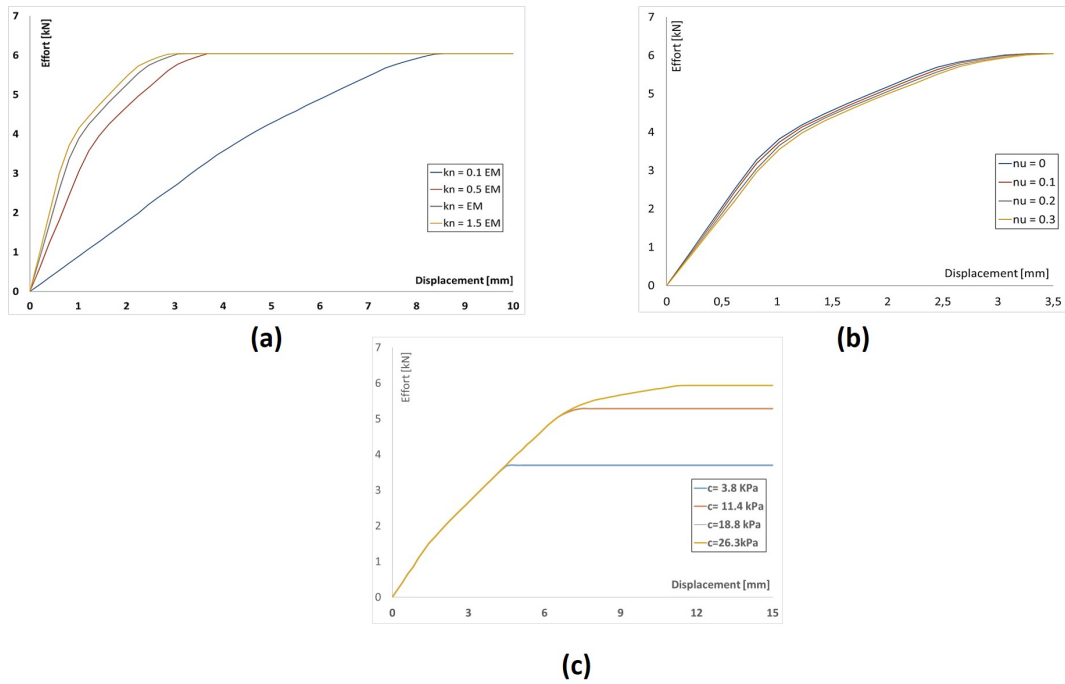


Figure 8.18: Sensitivity analysis of interface properties: (a) the stiffness of the interface ; (b) the Poisson's ratio of the mortar and (c) the coefficient of the interface

It was not possible to see the coupling between the DFM and the interface with the study of the wall, as no sliding occurred at the masonry/band interface. A sensitivity analysis is performed on the parameter φ_{int} to show how it affects the results and whether or not it is an effective means of modeling crack propagation from the masonry to the interface. To better see the damage to the interface with the force-displacement curves, the parameter α , which defines the cyclic damage in the DFM, is set to 1.

Figure 8.19 shows the cyclic behavior of the adobe wall with wood band for different values of φ_{int} . In the upper left corner of each curve, the envelope curve of the diagonal elements shows where the value of the parameter φ_{int} is compared to the displacement at the maximal strength F_u . Figures 8.19.(a-b) are cases where the interface is rapidly damaged and is the main source of energy dissipation. In Figure 8.19.(c), the interface is damaged during cycles with an amplitude of 15 mm, and in Figure 8.19.(d), the interface does not appear to be damaged. Comparing the hysteresis loop for the last cycles in Figure 8.19.(c) and Figure 8.19.(d), we can see that the dissipated energy is more important in the case of Figure 8.19.(c). It can be well seen that the energy is dissipated both in the masonry and at the masonry/band interface.

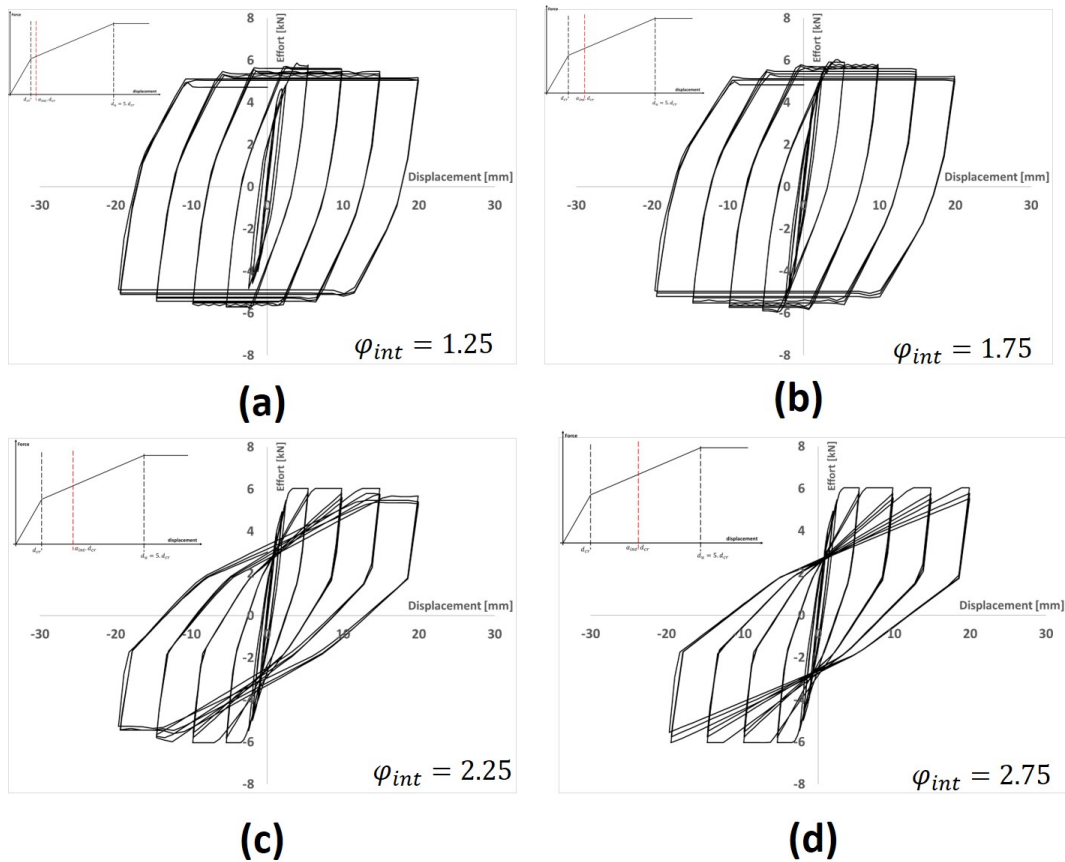


Figure 8.19: Sensitivity of the coupling between the DFM and the interface

8.3.5 Conclusion

The DFM was used in this final section to model quasi-static tests on two walls, one without bands and one with timber bands. Unlike the previous analysis, the properties of the masonry were determined by fitting the experimental curves with the DFM modeling. These properties will be used as reference data for the modeling of the shaking table tests. However, some remarks have to be made:

1. The band did not fail for this test. Therefore, it was not possible to determine its real properties but values from the literature were giving adequate results.
2. The wall with bands had a higher strength. There could be different reasons for the difference with the URM wall:
 - the variability in the mechanical properties of the material or related to the experimental manipulation

- the wall without band was too damaged by the cyclic loading before the actual maximum strength was reached
- the masonry portions in presence of bands have to be considered as spandrels.

The modeling of the interface was also tested and the influence of its properties was highlighted. Its stiffness, friction coefficient and cohesion can have an important influence on the global behavior of the wall.

The parameter φ_{int} can well represent the crack propagation from the masonry to the interface. It was not used to study the wall with bands because the interface did not break, but may be useful for other modeling.

8.4 Conclusion

In this chapter, the capabilities of the DFM and the interface model to model masonry structures with bands have been demonstrated. The following conclusions can be drawn for the DFM and the interface model:

- The DFM reproduces the cyclic behavior of URM piers with a good accuracy as well as the envelope curves of the experimental tests. It successfully captures the diagonal shear failure and the rocking failure.
- The definition of hysteresis with only three parameters is good enough to obtain sufficient accuracy of the cyclic behavior of masonry. The proposed formulas with the three parameters give a good prediction of the cyclic behavior of the tested walls.
- The DFM can reproduce the cyclic behavior of a wide wall with opening. Yet, the accuracy is less good than for URM piers. It may be related to the definition of the hysteresis parameters or the presence of the openings.
- The interface model can reproduce the change in stiffness of the wall and model the sliding at the band/masonry interface. The coupling between the DFM and the interface model can reproduce the damage of the interface due to crack propagation from the DFM.
- The DFM may need a different definition of the maximal strength in presence of bands. To know this, additional studies have to be done to compare the behavior of URM and RM walls. Experiments by Yadav [7] and Aranguren et al. [45] do not lead to the same conclusions.

The capacity of the DFM for modeling walls with different configurations has been demonstrated. Therefore, it is possible to use it for dynamic analysis of masonry structures.

Chapter 9

Dynamic analysis

In the previous chapters, it has been shown that the DFM can be used for modal analysis of masonry structures and can predict the cyclic behavior of walls with satisfactory accuracy. In this chapter, the DFM and the interface model are used for the dynamic analysis of three structures: one without band, one with RC bands and one with wooden bands. These structures are representative of the designs in the Nepalese catalog [43]. They were fabricated at a reduced scale and tested on a shake table at Institut Technologique FCBA (Technical Institute Forest Cellulose Wood -Construction and Furnitures) in late November 2020.

The first section of the chapter describes the shaking table used for the seismic test, the three samples, and the measurements taken during the tests. Then, the sections 9.2.1 through 9.3 focus on the numerical analysis of the three sample houses. The final section of the chapter draws conclusions about the three studies. For the modeling of the dynamics tests, the damping ratio is taken as null. It is considered that all the dissipated energy is encompassed by the diagonal elements of the DFM and the interfaces. Additional energy dissipation causes (viscosity) are considered negligible compared to the effects of the cracks.

All numerical analyzes in this chapter were performed using a computer with an Intel(R) Core(TM) i5-8250U @ 1.6-1.8 GHz processor and 16.0 Gb of RAM. Appendix B shows images of the samples at each stage of the campaign to illustrate the evolution of the damage.

9.1 The experimental campaign

9.1.1 The shaking table

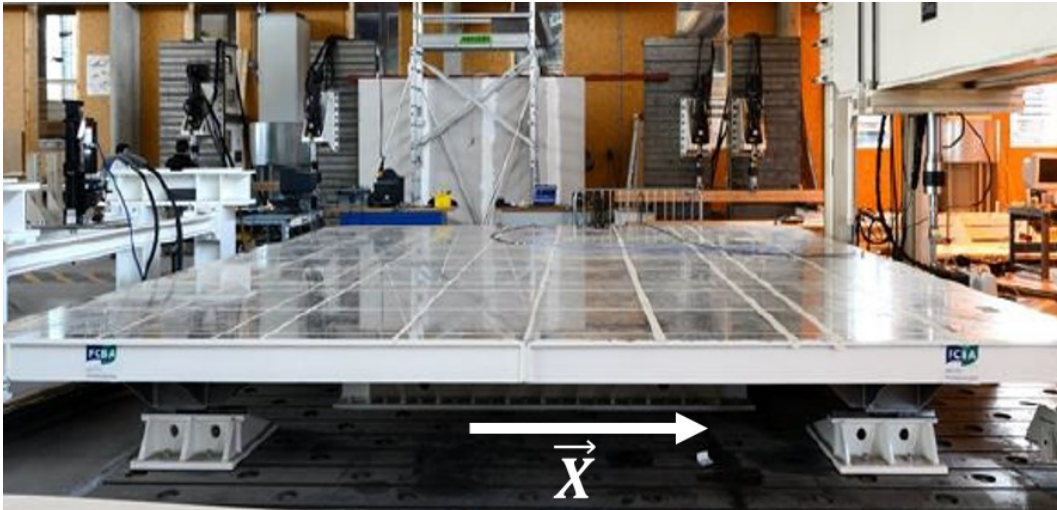


Figure 9.1: The shaking table of Institut Technologique FCBA

The shaking table of Institut Technologique FCBA is the single-axis shaking table shown in Figure 9.1. The X-axis in the figure is the loading axis. It can accommodate specimens with a size of 6 m x 6 m, making it one of the largest shaking tables in France. The maximum permissible dead weight of the shaking table is 5.5 tons.

In the context of this experimental campaign, the characteristics of the shaking table are:

- Maximum acceleration: $3g = 29.43 \text{ m.s}^{-2}$
- Maximum velocity: 0.7 m.s^{-1}
- Maximum displacement: 0.1 m in both direction
- Range of the excited frequencies: 0-30 Hz

The shaking table is moved by a servo-hydraulic jack having a maximal force of 250 kN with the help of roller bearing guides.

9.1.2 The sample houses

The three houses are shown in Figure 9.2. The houses have the same dimensions, and the bands are in the same place, to draw some conclusions about the difference between wooden bands and RC bands. The design is inspired by the designs in the Ministry of Urban Development of Nepal catalog [43]. The most noticeable change in the design is the position of the doorway on the wall inside the house. In the design catalog, the opening is not centered in the wall, while in the tested house, it was decided to place it in the center of the wall so as not to create torsion when the house is loaded along the X-axis. Every specimen has wooden frames at the openings.

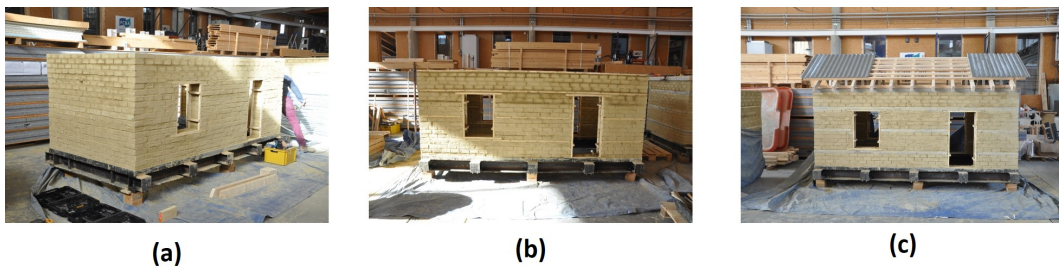


Figure 9.2: The three houses for the shaking table tests: (a) house without band; (b) house with wood bands; (c) house with RC bands

Table 9.1: Cauchy similitude law

Quantity	Symbol	Similitude
Length	L	$L_p = \lambda L_M$
Modulus of elasticity	e	$E_p = e E_M$
Density	ρ	$\rho_p = \rho \rho_M$
Area	A	$A_p = \lambda^2 A_M$
Volume	V	$V_p = \lambda^3 V_M$
Mass	m	$m_p = \rho \lambda^3 m_M$
Velocity	v	$v_p = e^{1/2} \rho^{-1/2} v_M$
Acceleration	a	$a_p = e \lambda^{-1} \rho^{-1} a_M$
Force	F	$F_p = e \lambda^2 F_M$
Stress	σ	$\sigma_p = e \sigma_M$
Time	t	$t_p = e^{-1/2} \lambda \rho^{1/2} t_M$

These houses were scaled 1:2 due to the size and maximum weight allowed on the shaking table. Cauchy's similitude law was used to create the samples. In Table 9.1, the relationship between the properties of the model M and the properties of the prototype P is shown. In the context of this experimental campaign, $\lambda = 0.5$, $e=1$ and $\rho=1$. The dimensions of the samples are shown in Figure 9.3. In this figure, the cardinal points are shown to identify the different walls. The wall on the left side of the figure is the South wall, the IP walls are the East and West walls, the "door wall 2" is the middle wall, and the last wall is the North wall.

The samples could not be tested in the same time. To shorten the duration of the experimental campaign, they were built in the same time away from the shaking table. The houses were built on a steel structure for the transfer to the shaking table (black metal parts in Figure 9.2). The wooden blocks in Figure 9.2 allow the steel structures to be lifted to attach wheels. These wheels are used to transport the samples to the shaking table. The disadvantage of this method is that the transfer of the house to the shaking table may cause unexpected vibrations. A wooden platform and car hydraulic jacks were used to lift the house to the height of the shaking table (see Fig. 9.4). This step was not possible with an overhead crane because the specimens were too heavy. The wooden blocks in Figure 9.4 serve to stabilize the house during lifting. Once the specimen is on the shaking table, the steel assembly is fastened to the shaking table with a total of 16 bolts.

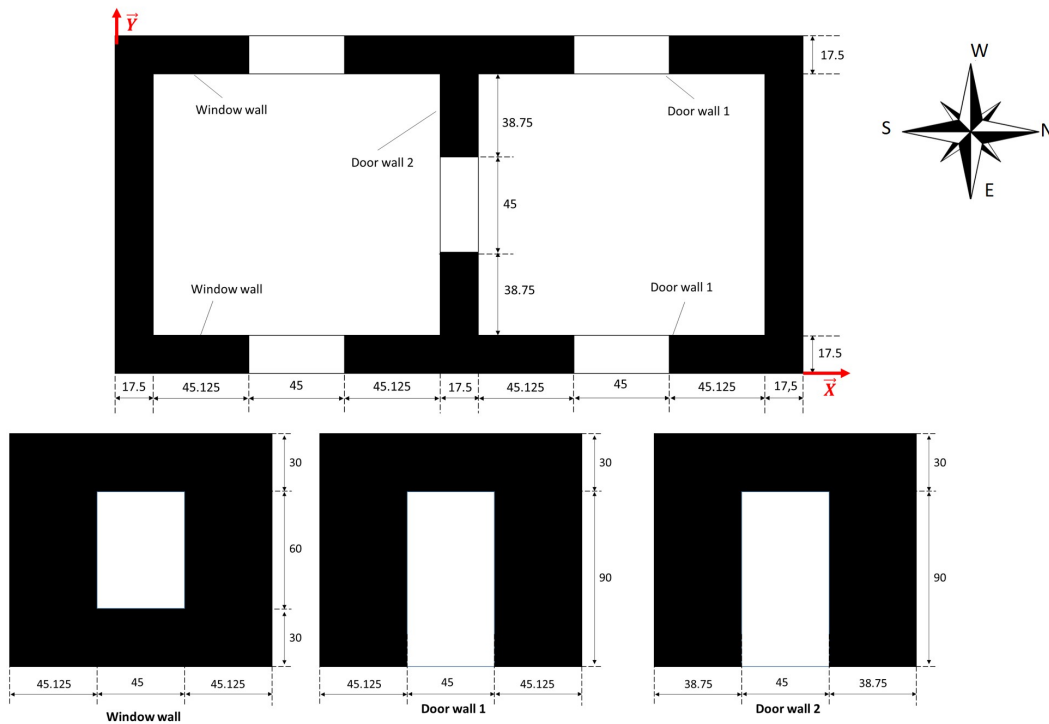


Figure 9.3: Schemes of the reduced scale houses



Figure 9.4: Installation of the samples on the shaking table: (a) the wood platform ; (b) specimen with RC bands during the transfer to the shaking table

The houses were built with the extruded adobe bricks used for the quasi-static tests presented in the previous chapter. However, this experimental campaign began three weeks after the houses were built (21 days), while the quasi-static tests were conducted more than 90 days later. In addition, the environmental conditions for this experimental test were different from those for the

quasi-static test. To ensure good storage conditions for the wood elements, the relative humidity is maintained at 60% in the FCBA room, while it was not controlled in the 3SR laboratory. Therefore, the mechanical properties of the walls determined in the previous chapter cannot be used because the curing conditions and curing time of the mortar are different.

9.1.3 The seismic signals

The experimental campaign consisted of five seismic loads of increasing amplitude. The seismic signal used for the experimental campaign is a modification of the natural acceleration signal of the Miyagi earthquake [Japan, 2003] measured at the K-Net station. This signal was adapted to be representative of a remote subduction earthquake in Guadeloupe using the method proposed by Youngs et al. [129]. It corresponds to a reference return period of 475 years for a type B soil according to Eurocode 8 [78]. For a period of 50 years, this gives an exceedance probability of the reference peak ground acceleration of 10 %. This is the "no collapse" condition in Eurocode 8 [78].

The 5 seismic signals used in the tests are Guadeloupe 50%, Guadeloupe 100%, Guadeloupe 150%, Guadeloupe 200%, and Guadeloupe 300%. The reference signal is the Guadeloupe 100%. The designation Guadeloupe 50 % means that the amplitude of the acceleration signal is half the amplitude of the reference signal. The evolution of the ground displacement, ground velocity, and ground acceleration of the Guadeloupe 100% signal is shown in Figure 9.5. These signals have already been modified with the Cauchy similitude law. The maximum values for each Guadeloupe seismic signal used for the experimental campaign are given in Table 9.6. In this table, the values are those of the launched signal with the shaking table. The signal is computed for acceleration control knowing the properties of the house before each test. However, the strength of the house decreases during the tests and it leads to an error between the computed signal and the applied signal. That is why the values of the acceleration in Table 9.6 are not multiplied by the expected factor (1.6 aside from 2 between Guadeloupe 50% and Guadeloupe 100% for example).

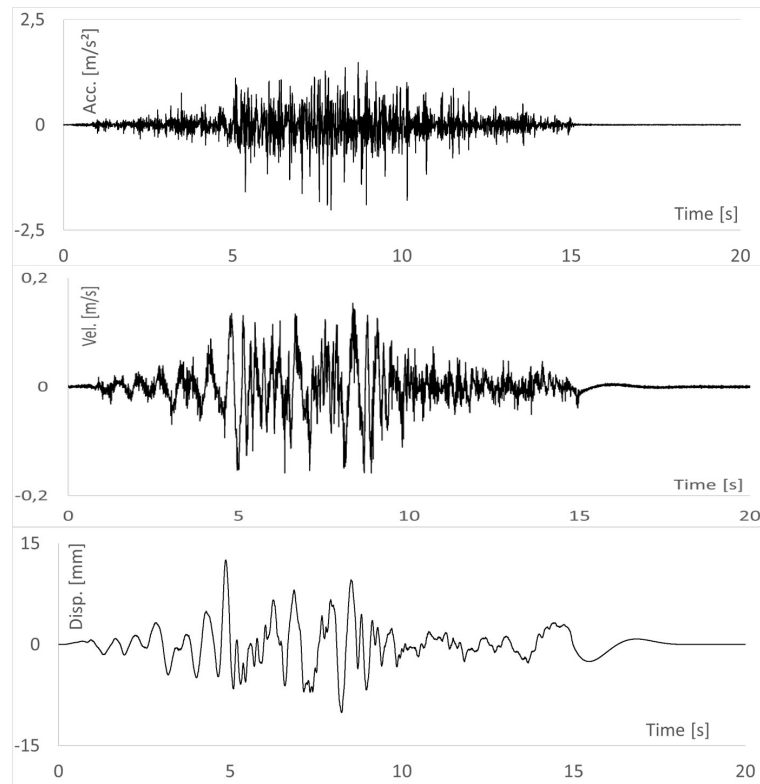


Figure 9.5: Ground displacement, ground velocity and ground acceleration of the Guadeloupe seismic signal

Table 9.2: Maximum values of the Guadeloupe signal

Signal	Displacement [mm]	Velocity [m.s ⁻¹]	Acceleration [g]
Guadeloupe 50 %	6.82	0.10	0.7
Guadeloupe 100 %	11.83	0.16	1.12
Guadeloupe 150 %	16.58	0.21	1.48
Guadeloupe 200 %	22.42	0.28	1.81
Guadeloupe 300 %	35.86	0.44	2.75

9.1.4 The measurements

During the tests, displacements were measured with cable sensors at seven points on the north wall of the house. Their location is shown in Figure 9.3. These measurements were validated with the Digital Image Correlation and stereovision [7]. The measurements from sensors 6 and 7 are used as a reference for the numerical model results to validate the displacement of the IP excited walls. The OOP displacement of point 2 is also used to see how well the numerical model can predict it.



Figure 9.6: Positions of the cable sensors on the North wall of the reduced scale houses

9.2 Dynamic analyses

9.2.1 Study of the house without bands

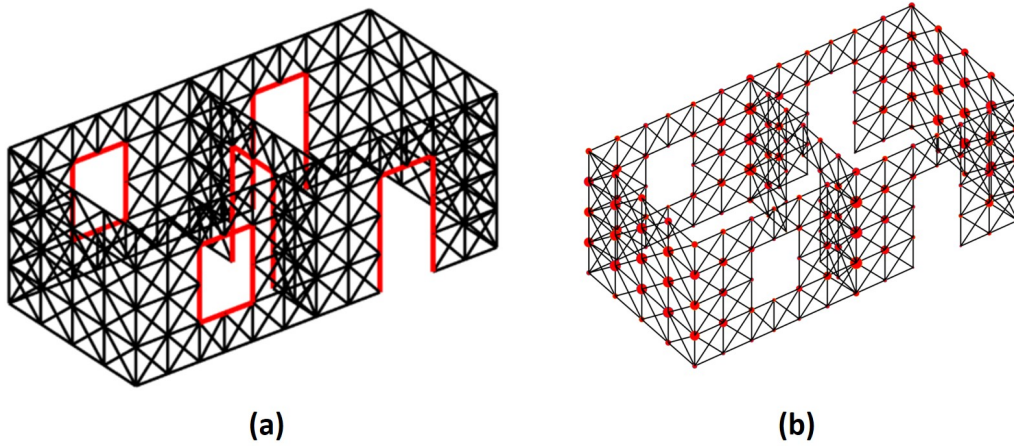


Figure 9.7: Modeling of the house without bands: (a) mesh for the dynamic analysis and (b) mass distribution

9.2.1.1 Modeling with the determined material properties

The material properties identified in the previous chapter are used to model the URM specimen. These properties are reminded in Table 9.3. The parameters of the hysteresis loops are not given in this table since their value changes from an element to another.

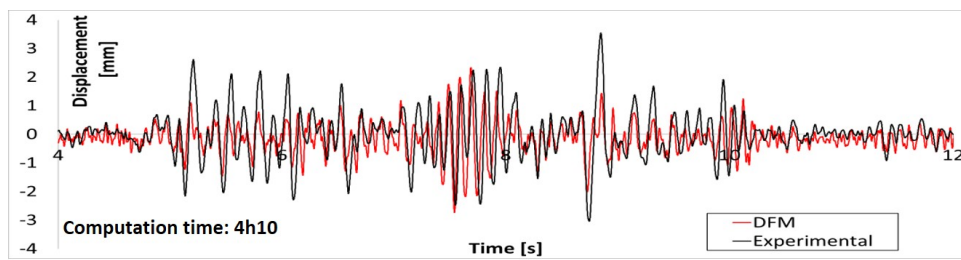
Table 9.3: Material properties of adobe determined in Section 8.3

Stiffness of the DFM	
Young's modulus [E_m]	61.3 MPa
Shear modulus [G_m]	25.5 MPa
Shear strength of the DFM	
Tensile strength [f_t]	22.5 kPa
Cohesion [c]	37.5 kPa
Friction coefficient [μ] ¹	0.6
Trilinear behavior of the DFM	
Appearance of cracks F_{cr}/F_u	0.5
Displacement when the maximal strength is reached d_u/d_{cr}	6.
Elastic properties of frames at the openings	
Young modulus [E_f] ^(c)	9 GPa
Poisson's ratio lintels [ν_f] ^(c)	0.2
Section lintels [A_f] ^(b)	5x5 cm ²
Density lintels [ρ_f] ^(c)	700 kg.m ⁻³

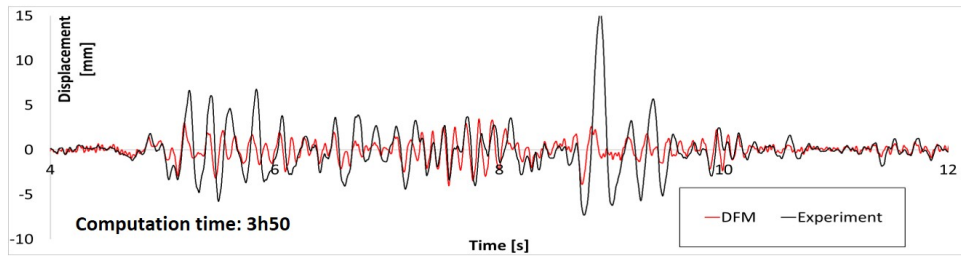
The modeling of the house with the DFM is shown in Figure 9.7. This mesh corresponds to the Matlab_1 mesh seen in Chapter 7. It consists of 126 meso-elements with a total of 840 degrees of freedom. The red elements in this figure are the beam elements that model the frames at the openings. The real displacement of the shaking table is imposed at the base of the house. To reduce the computation time, only the first 15 seconds of the signals are used, since after this time the excitations are small.

Figure 9.8 shows the evolution of the displacement at points 6 and 7 measured experimentally and determined with the DFM. The calculation time for each experiment is given with the corresponding displacement-time curve. The DFM can determine the dynamic behavior of the specimen with a very interesting calculation time. The calculation time for the first experiment is more important than for the second experiment because it includes preparatory steps to determine the actual vertical stress applied to each DFM element and to apply the static load.

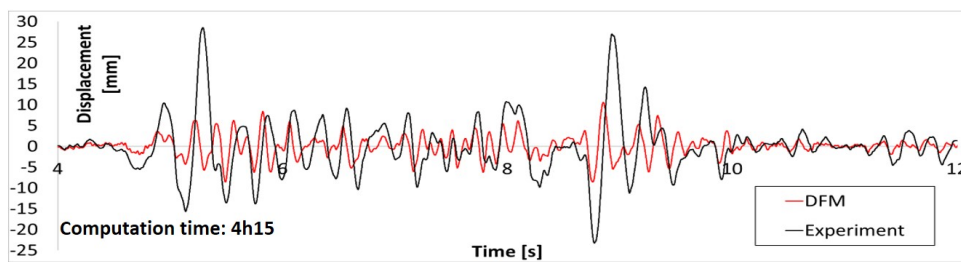
In Figure 9.8 it can be seen that the DFM greatly underestimates the displacements of the East and West walls for each test. A zoom is performed on the interval [4s.; 12s.], since in this interval the displacements are the largest. Looking at the first seconds of the first test, one can see that the initial stiffness of the numerical model is too high compared to the stiffness of the tested specimen since at each peak, the model underestimates the IP deformation of the walls. However, between the 7th second and the 9th second, the numerical model exhibits similar displacement to the experimental one. However, the model significantly underestimates the displacement when the highest displacement is reached experimentally at approximately 9s. This implies an underestimation of the damage in the walls that will affect the following test. This phenomenon is observed for each test.



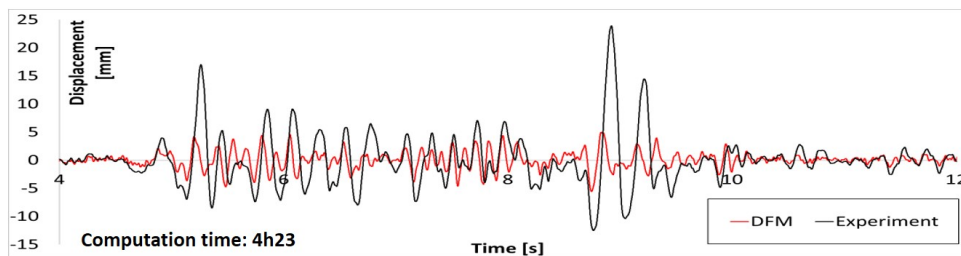
(a)



(b)



(c)



(d)

Figure 9.8: Experimental and numerical displacements histories of the house without bands with properties of adobe determined in Section 8.3: (a) Guadeloupe 50%; (b) Guadeloupe 100%; (c) Guadeloupe 150%; (d) Guadeloupe 200%

Table 9.4 shows the peak values of the displacements of the curves in Figure 9.8 for both directions. The error in determining the peak values is calculated by using the experimental value as a reference. As expected, the error of the numerical model in determining the displacements is considerable (70 % on average). The difference is smaller for the first experiment because the excitations are smaller. The error in determining the displacement is not the same in both directions. It is higher in the positive direction for every test. Interestingly, the error increases dramatically between the first and second test but changes little for the other tests.

Table 9.4 shows the OOP displacement measured at point 2 (see Figure 9.6). This value is determined by considering the differential displacement between this point and the points 6 and 7. Therefore, the error in determining the IP displacement of the walls does not affect the results for the OOP displacement. As with the IP displacement, the numerical model underestimates the OOP displacement for achtest. For the first tests this can be explained by the excessive stiffness of the model found in the analysis of the IP displacement curves. The error increases because the model maintains an elastic behavior while the tested sample is actually damaged.

Table 9.4: Maximum displacements measured experimentally and determined with the DFM with the properties of adobe determined in Section 8.3 for the house without bands

Signal		$d_{IP,DFM}$ [mm]	$d_{IP,exp}$ [mm]	err_{IP}	$d_{OOP,DFM}$ [mm]	$d_{OOP,exp}$ [mm]	err_{OOP}
Guadeloupe 50 %	+	2.34	3.54	34%	3.37	7.77	56.6%
	-	-2.73	-3.04	10.1%	-3.26	-7.31	55.4%
Guadeloupe 100 %	+	3.47	15.62	77.8%	4.28	6.12	30.2%
	-	-4.02	-7.31	45%	-4.07	-3.21	27%
Guadeloupe 150 %	+	4.95	23.90	79.3%	4	13.8	71%
	-	-5.57	-12.51	55.5%	-4.04	-9.9	59.2%
Guadeloupe 200 %	+	10.55	28.52	64%	3.71	28.3	87%
	-	-8.6	-23.23	63%	-4.27	-28.8	85%

9.2.1.2 Modification of the material properties

The excessive stiffness of the numerical model can be explained by the differences in the curing conditions between the seismic and the quasi-static tests. Two factors are considered for the reduction of the mechanical properties compared to those of the previous section: the curing time and the environmental conditions.

- Time of curing
Zonno et al. [130] studied the evolution of the modal frequencies of three adobe walls made with mud mortar as a function of curing time. The curing was performed with a relative

humidity of approximately 80%. Assuming that the frequency for first-order modes is determined by Equation 9.1, the measurements showed a change in stiffness between day 28 and day 90 of about 20%.

$$f = \frac{1}{2\pi} \sqrt{K/M} \quad (9.1)$$

Giamundo et al. [131] measured a difference of 13% of the strength of their adobe bricks and mortar between 21 days and 28 days of curing. This coefficient will be used to adjust between the values of the properties of the masonry between the first tested specimen (the RC bands house) and the two other specimens.

- Environment conditions

The curing conditions affects the properties of the materials. No studies on the effects of the curing with dry air comparatively with normal conditions have been found for adobe. For concrete, Liu et al. [132] showed that the use of dry air (50% RH) for the curing lead to a compression strength reduction of 88% at 28 days comparatively with a normal curing. The same difference of strength was observed at 21 days of curing. Because of the lack of information for adobe, the hypothesis is made that the same difference of strength affects adobe constructions despite the differences between the two materials.

The coefficient of reduction of the material properties were indicated either for the elastic properties (Zonno et al. [130], or for the strength of the material (Giamundo et al. [131], Liu et al. [132]) because it is the only data that can be identified from these articles. For the following dynamic studies, the hypothesis is made that the coefficient affecting the elastic properties affect the strength as well, and vice versa.

9.2.1.3 Modeling with the modified material properties

The specimen without bands was tested after 28 days of curing. The properties of the masonry are assumed to be reduced by 20% due to the curing time and by 10% due to the different curing conditions. Overall, the coefficient of reduction of material properties is 72%.

The mechanical properties for the numerical analysis are shown in Table 9.5. All the parameters that are not shown in this table keep the same value shown in Table 9.3.

Table 9.5: Modified properties for the adobe

Stiffness of the DFM	
Young's modulus [E_m]	44 MPa
Shear modulus [G_m]	22.2 MPa
Shear strength of the DFM	
Tensile strength [f_t]	18.4 kPa
Cohesion [c]	27 kPa

9.2.1.4 Numerical modeling with adjusted properties

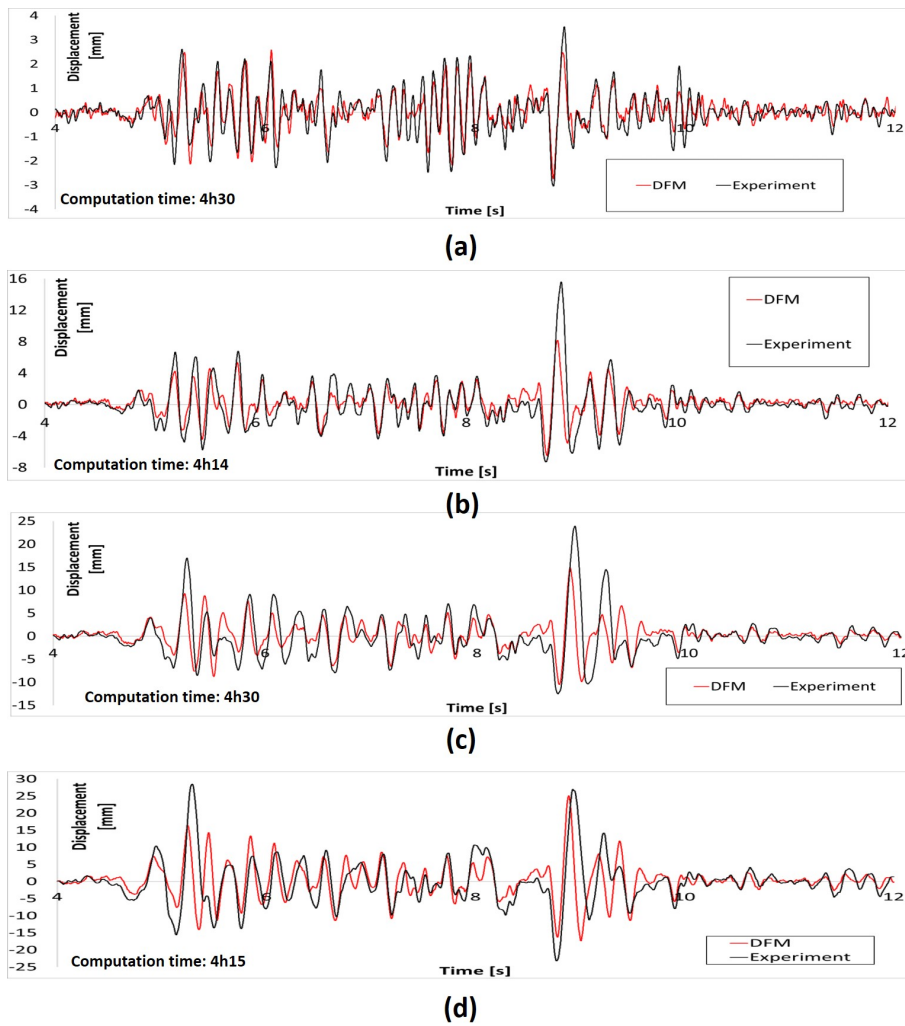


Figure 9.9: Experimental and numerical displacements histories of the house without bands: (a) Guadeloupe 50%; (b) Guadeloupe 100%; (c) Guadeloupe 150%; (d) Guadeloupe 200%

Table 9.6 shows the maximum displacements obtained by the DFM with the modified material properties and those measured experimentally during the shake table tests. The DFM performs better with the new values for the properties of adobe. The displacement of the IP walls in the negative direction is well approximated by the numerical model. In this direction, the maximum error is 25% for the last test and about 10% for the reference signal. However, in the positive direction, the error is considerable and can reach almost 50%. The difference between the model and the experimental results is still the inability of the model to reproduce the peak displacement at 9s.

For the OOP displacement, the model also performs better, with an error of less than 20% for the reference signal. For higher intensity signals, the presence of cracks at the junction of the walls and damage to the walls cause the models to be unable to accurately determine the OOP displacement.

Table 9.6: Comparison of displacements determined with the DFM and measured experimentally for the house without bands

Signal		$d_{IP,DFM}$ [mm]	$d_{IP,exp}$ [mm]	err_{IP}	$d_{OOP,DFM}$ [mm]	$d_{OOP,exp}$ [mm]	err_{OOP}
Guadeloupe 50 %	+	2.59	3.54	26.9%	3.74	7.77	51.9%
	-	-2.74	-3.04	9.99%	-3.46	-7.31	52.7%
Guadeloupe 100 %	+	8.18	15.62	47.6%	5.02	6.12	18%
	-	-6.48	-7.31	11.3%	-3.83	-3.21	19%
Guadeloupe 150 %	+	14.9	23.90	37.5%	4.7	13.8	65.9%
	-	-10.5	-12.51	16.1%	-3.51	-9.9	64.5%
Guadeloupe 200 %	+	25.1	28.52	12.2%	5.35	28.25	81%
	-	-17.4	-23.23	25.1%	-7.8	-28.8	73%

One reason for the differences between the model results and the experimentally measured displacements is the presence of large cracks before the first test (see Figure 9.10 and Appendix B). The walls not shown in Figure 9.10 did not exhibit large cracks. The cracks were due to shrinkage of the masonry. At the openings, the frames did not allow for deformation, so the constraints of displacement caused stresses in the masonry that resulted in cracks. The cracks were filled with mortar just prior to testing, but this did not result in the masonry retaining its normal mechanical properties. These cracks are related to the boundary conditions of the masonry and their influence was not considered in the reduction of the properties of the masonry due to the curing conditions.

Another explanation for the difference may be that the effects of curing were underestimated because there is a limited number of studies on this subject, or the lack of accuracy because of the mesh size (14% error for the first mode in the load direction, as shown in Chapter 7).

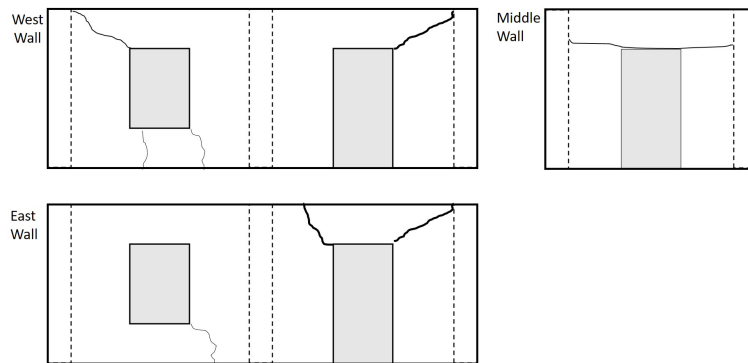


Figure 9.10: Crack pattern before the tests of the house without bands

9.2.2 Study of the house with wood bands

9.2.2.1 Material properties

In the previous section, it was noted that the material properties determined with the quasi-static test could not be used and had to be adapted to be more appropriate for the context of the shaking table tests. The house with wooden bands was tested 25 days after its construction. Considering a linear evolution of the mechanical properties with the curing time in the fourth week of curing, the masonry is considered to have 92.5% of its mechanical properties used for the model of the house without bands [131]. The adobe and interface properties for this model are shown in Table 9.7. The properties of the interface are modified by the same coefficient as the properties of the adobe house, except for the coefficient of friction that is considered to remain unchanged. The properties not listed in Table 9.7 have the values given in Table 9.3.

Table 9.7: Mechanical properties of the wood bands specimen

Stiffness of the DFM	
Young's modulus [E_m]	40.8 MPa
Shear modulus [G_m]	17 MPa
Density adobe [ρ_m]	2000 kg.m ⁻³
Mass of the roof [m_r]	185 kg
Shear strength of the DFM	
Tensile strength [f_t]	17 kPa
Cohesion [c]	25 kPa
Friction coefficient [μ]	0.6
Elastic properties of the interface	
Normal stiffness [k_n]	40.8 MPa/m
Tangential stiffness [k_t]	17 MPa/m
Strength of the interface	
Cohesion [c]	50 kPa
Friction coefficient [μ]	0.5
Tensile strength [f_{ty}]	50 kPa
Fracture energy [G_t]	0.0008 N/mm

9.2.2.2 Numerical modeling of the house with wood bands

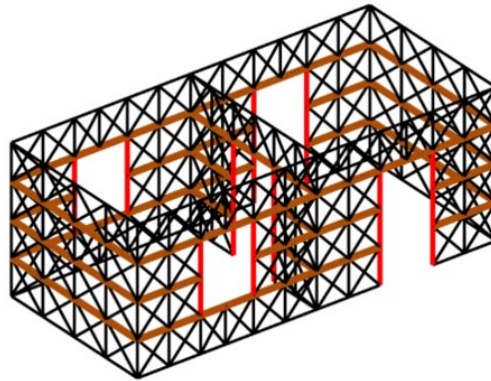
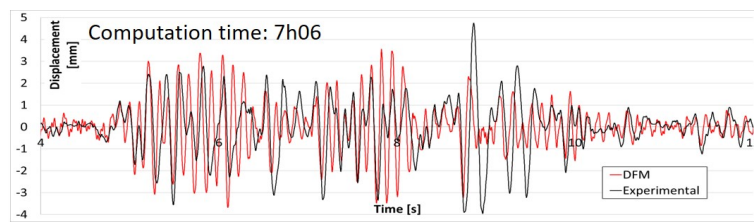
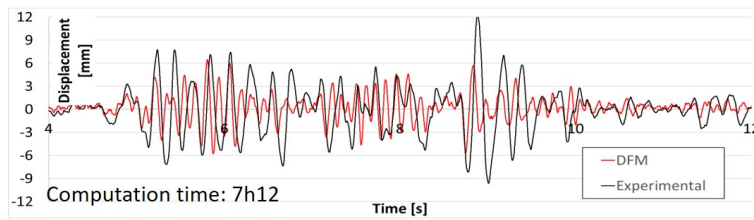


Figure 9.11: Mesh of the numerical modeling of houses with bands

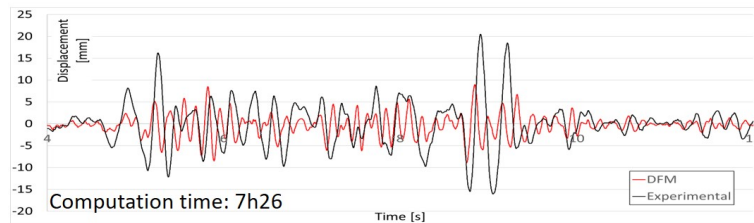
The modeling of the wood bands house is shown in Figure 9.11. Due to the separation of the meso-elements by interface elements (shown in brown in Figure 9.11), there are 999 degrees of freedom. The computation time for every test is shown in Figure 9.12. This time is about 60% higher than for the house without bands. This is due to a higher number of DDL and the presence of interface elements, which are numerically very expensive.



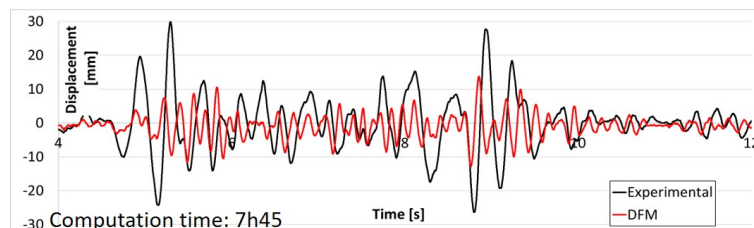
(a)



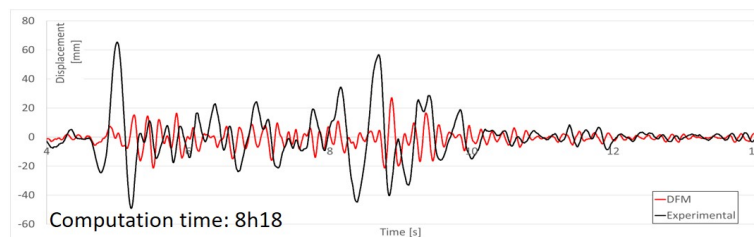
(b)



(c)



(d)



(e)

Figure 9.12: Experimental and numerical displacements histories of the house with wood bands: (a) Guadeloupe 50%; (b) Guadeloupe 100%; (c) Guadeloupe 150%; (d) Guadeloupe 200%; (e) Guadeloupe 300%

The experimentally measured displacements for the East and West walls and the values obtained with the numerical model are shown in Figure 9.12. As with the specimen without a band, the numerical model tends to oscillate more than the real specimen during the first few seconds of seismic excitation. However, the peak values of the experimental test and the numerical model are of the same order of magnitude. The main difference between the numerical model and the experimental test occurs about 9 seconds after the seismic excitation starts. The numerical model underestimates the displacement and leads to an underestimation of the damage induced by the seismic excitation as in the sample without bands. Similarly to the previous study, this has implications for the following tests. At the beginning of the Guadeloupe 100% test, the numerical model is shown to have a higher stiffness than the tested samples, as it underestimates the displacements for the first peaks. As in the first test, the maximum measured displacement at about 9 seconds is underestimated by the DFM. This difference between the experimental measurements and the displacements calculated by the numerical model increases after each test.

Table 9.8: Comparison of displacements determined with the DFM and measured experimentally for the house with wood bands

Signal		$d_{IP,DFM}$ [mm]	$d_{IP,exp}$ [mm]	err_{IP}	$d_{OOP,DFM}$ [mm]	$d_{OOP,exp}$ [mm]	err_{OOP}
Guadeloupe 50 %	+	3.55	4.75	25.2%	0.96	1.26	24%
	-	-3.68	-3.95	7%	-1.07	-1.06	0.7%
Guadeloupe 100 %	+	6.47	12.3	47.3%	0.88	2.35	62.5%
	-	-5.8	-9.6	40%	-1.04	-2.75	62%
Guadeloupe 150 %	+	9	20.5	56.2%	0.97	3.7	73.6%
	-	-8.9	-16.1	44.4%	-1.26	-4.32	71%
Guadeloupe 200 %	+	13.7	30	54.2%	1.83	3.84	52%
	-	-12.8	-26.4	51.4%	-1.31	-3.63	64%
Guadeloupe 300 %	+	27	65.3	59%	3.11	5.1	39%
	-	-21.4	-49.1	56.5%	-2.3	-7.8	71%

The maximum values in the positive and negative directions for the dynamic tests are shown in Table 9.8. It can be seen that the differences between the numerical model and the experimental tests are slightly larger for the wood band sample than for the house without bands. For the first modeled sample, the error after the fourth test was less than 50% for the displacements of the IP-loaded walls, while for the sample with wooden bands it was more than 56% after the

third test. Interestingly, the OOP displacement calculated with the DFM at point 2 does not change for the first three tests despite the increasing amplitude of the triggered signals. Thus, if the model approximates the maximum OOP shifts well for the first test, it underestimates them for the other tests.

The differences between the numerical model and the experimental tests can be explained by: (i) the presence of cracks at the top part of the East and West walls at the start of the tests; (ii) the lack of knowledge for the properties of the interface elements of the numerical model; (iii) a simplification of the kinematics at the level of the band that does not allow bending.

9.3 Study of the house with RC bands

9.3.1 Input data

This specimen was tested 21 days after its manufacture. Therefore, the mechanical properties of the masonry are 13% lower than those of the URM house [131]. Since information on the interfaces between concrete and masonry could not be found in the literature, the interface properties were determined assuming that the RC bands have higher strength than wooden bands thanks to a better bond between masonry and bands, as shown in the tests of Spence et al.[133] presented in Chapter 2.

The properties of the materials used for modelling the specimen are listed in Table 9.9. The coefficient of friction masonry/concrete is from King and Pandey [134]. It is not a coefficient of friction for the adobe/concrete interface, but it is the only data found in the literature on coefficients of friction of concrete with masonry . The properties of the interface are modified by the same coefficient as the adobe properties, except for the coefficient of friction, which is considered unchanged. The properties not listed in Table 9.9 have the values given in Table 9.3.

Table 9.9: Material properties for the RC bands specimen

Stiffness of the DFM	
Young's modulus [E_m]	37.5 MPa
Shear modulus [G_m]	15.6 MPa
Density adobe [ρ_m]	2000 kg.m ⁻³
Mass of the roof [m_r]	185 kg
Shear strength of the DFM	
Tensile strength [f_t]	13.8 kPa
Cohesion [c]	23 kPa
Friction coefficient [μ]	0.6
Elastic properties of the interface	
Normal stiffness [k_n]	45 MPa/m
Tangential stiffness [k_t]	18.7 MPa/m
Strength of the interface	
Cohesion [c]	43 kPa
Friction coefficient [μ]	0.6
Tensile strength [f_{ty}]	35.8 kPa
Fracture energy [G_t]	0.0008 N/mm

9.3.2 Numerical modeling

The average of the displacements measured at points 6 and 7 is shown in Figure 9.13, and the maximum displacements for both tests are given in Table 9.10. The zoom for these curves is different to show the residual displacement at points 6 and 7 at the end of the tests. It can be seen that there is a small residual shift at the end of the Guadeloupe 200% for the experimental test. This shows that there is a failure of one band or more and that there is friction. It affects the displacements for the Guadeloupe 300% tests where the displacement peaks are wider and the maximum displacement is not reached in the positive direction anymore. The numerical model has no residual displacement. That is why the difference in shape between the experimental test and the numerical model is considerable.

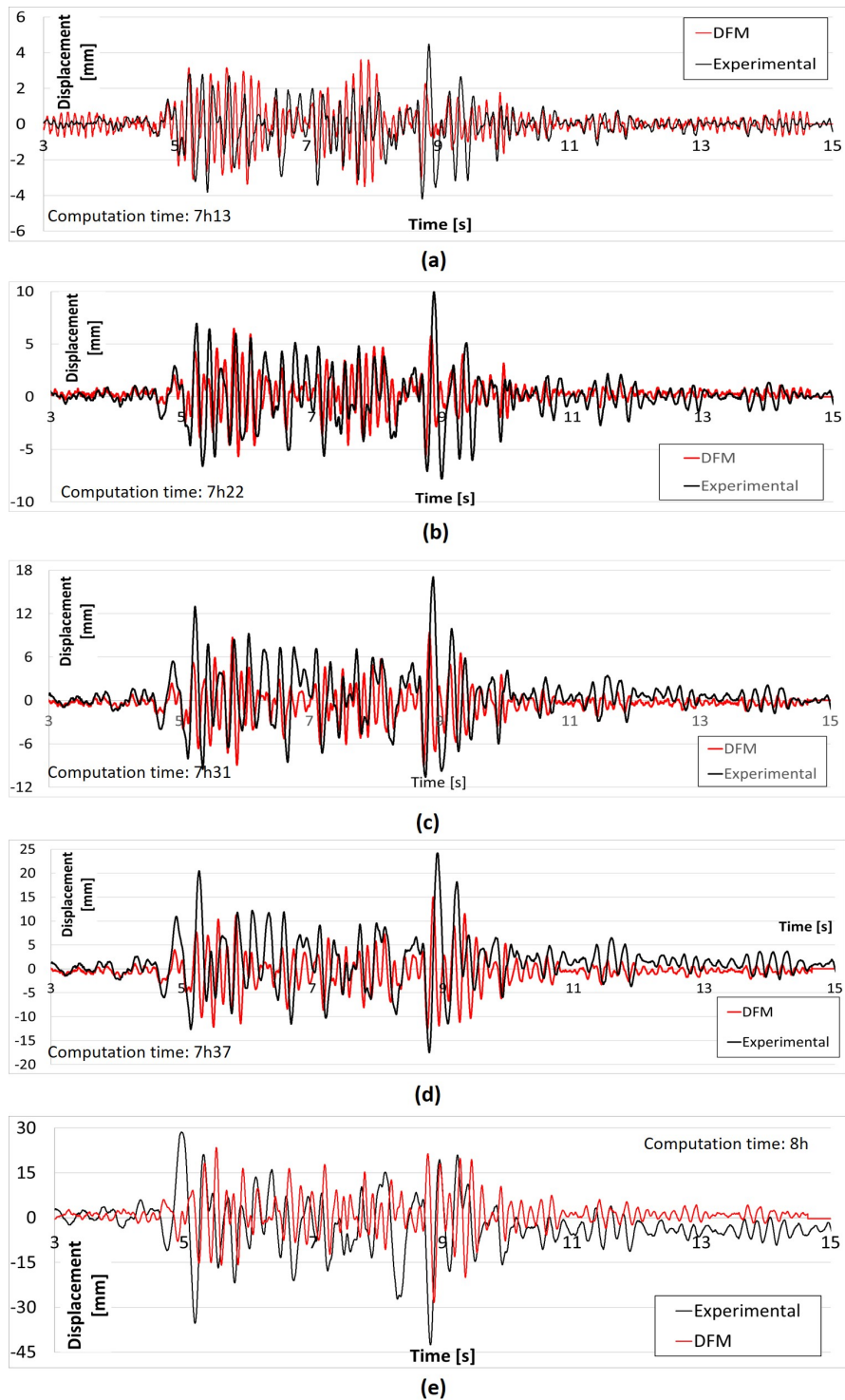


Figure 9.13: Experimental and numerical displacements histories of the house with RC bands: (a) Guadeloupe 50%; (b) Guadeloupe 100%; (c) Guadeloupe 150%; (d) Guadeloupe 200%; (e) Guadeloupe 300%

For the first tests, the observations made for the previous specimen also apply to this specimen. There are, however, some marked differences:

- the displacements of the IP loaded walls are better determined with the DFM for this specimen compared to the wood bands house.
- the error for the OOP displacements is quite high for this test. This is because the experimentally OOP displacement is close to zero for every test. Therefore, even if the model calculates a small deformation, it is easily higher than the experimental one. Then, the computed error is very important.

The computation time is of the same order of magnitude of that of the modeling of the house with wood bands.

Table 9.10: Comparison of displacements determined with the DFM and measured experimentally for the house with RC bands

Signal			$d_{IP,DFM}$ [mm]	$d_{IP,exp}$ [mm]	err_{IP}	$d_{OOP,DFM}$ [mm]	$d_{OOP,exp}$ [mm]	err_{OOP}
Guadeloupe 50 %	+		3.6	4.5	19.1%	0.96	0.22	346%
	-		-3.5	-4.2	16.3%	-0.96	-0.17	481%
Guadeloupe 100 %	+		6.5	10	35%	1.03	0.14	619%
	-		-5.7	-7.8	26.7%	-1.01	-0.23	347%
Guadeloupe 150 %	+		9.4	17.1	44.8%	1.25	0.41	204%
	-		-9	-10.6	15.1%	-1.5	-0.18	753%
Guadeloupe 200 %	+		15	24.2	38%	2.4	0.4	487%
	-		-12.6	-17.5	27.8%	-1.67	-0.33	407%
Guadeloupe 300 %	+		28.5	28.6	0.6%	5.08	0.13	3674%
	-		-23.5	-42.6	45%	-3.5	-0.9	285%

9.4 Analysis of the effects of bands

9.4.1 Deformation during seismic excitation

The deformed shapes of the specimens at the peak displacements for each test in the negative and positive directions are used to identify the changes in the behaviour of the house due to the presence of bands. Figure 9.14 shows the deformations for the specimen without bands and Figure 9.16 shows the deformed shapes for the specimen with wooden bands. The colormap shows the amplitude of the displacement in the X-direction.

The deformed shape for the first test in the positive direction is different from that for the following tests because the peak displacement is not reached at the same time step (see Fig. 9.9). For all other tests, the deformed shapes are similar. Figure 9.15 shows the top view of the deformed shapes of the house without bands to better see the OOP deformation of the IP-loaded walls. In the positive direction, the deformation resembles the first OOP mode of the small walls identified in the previous chapter. In the negative direction, the deformation of the wall is related to the IP bending mode of the long walls.

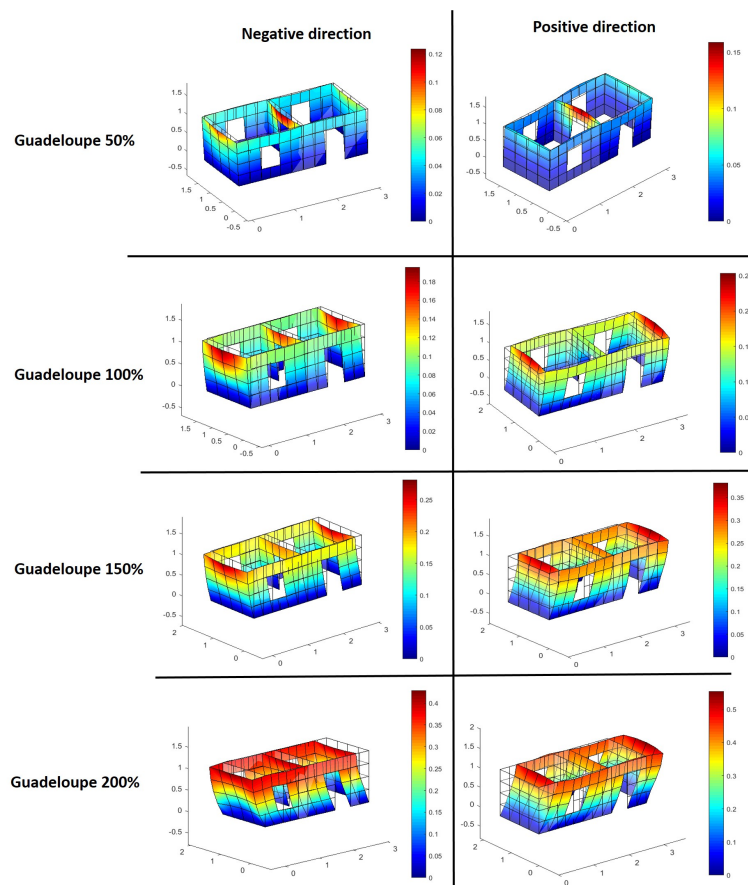


Figure 9.14: Deformed shapes of the house without bands according to the numerical model when the maximum displacements are reached in the negative and positive directions for both seismic tests increased by a factor of 20

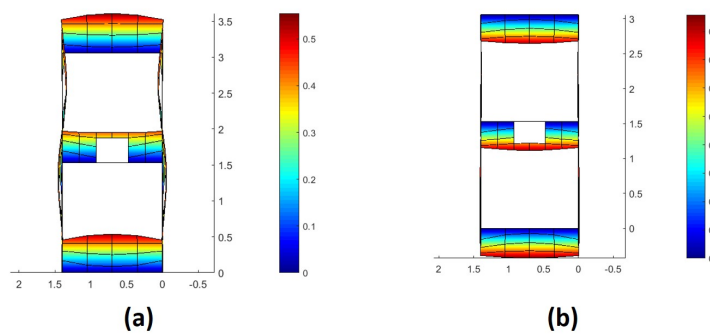


Figure 9.15: Top view of the deformed shapes of the house without bands according to the numerical model: (a) positive direction; (b) negative direction

In the case of the house with wooden bands, the presence of the bands is clearly visible with the colormap. Even the first test shows a difference in displacement between the upper and lower ends of the bands, indicating that there is already sliding. However, this sliding is not irreversible, as the house returns to its deformed shape at the end of the tests, as shown in Figure 9.17, except for the last test.

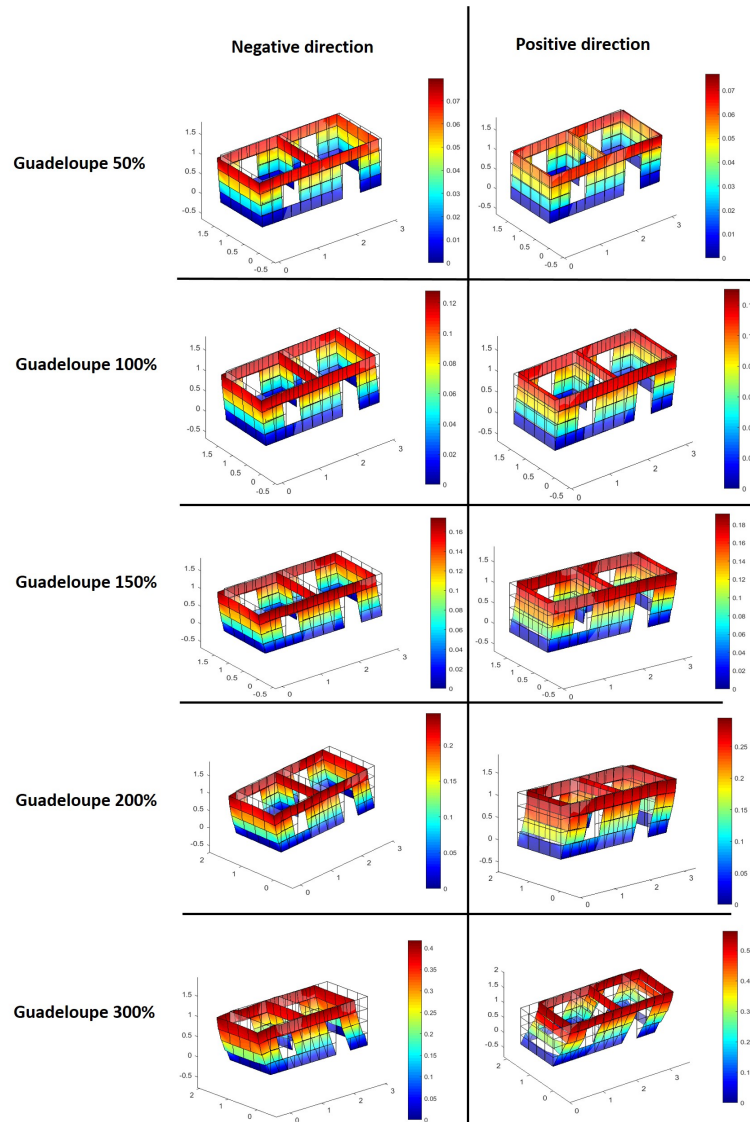


Figure 9.16: Deformation of the house with wood bands according to the numerical model when the maximum displacements are reached in the negative and positive directions for both seismic tests magnified by a factor of 20

Figure 9.17 shows the deformed shape of the specimens at the end of each test, magnified

50 times so that the deformations can be easily seen. It can be seen that the house without bands has plastic deformation after the last two tests, while this is not the case for the specimens with bands. This shows another advantage of the bands: to limit the irreversible damages of the house. In addition, the two specimens with bands do not behave the same. In the case of the house with wooden bands, sliding occurred at the level of the lower band during the last test while nothing happened for the RC bands house. This shows that different interface properties at the bands play a role in the overall behavior of the structure.

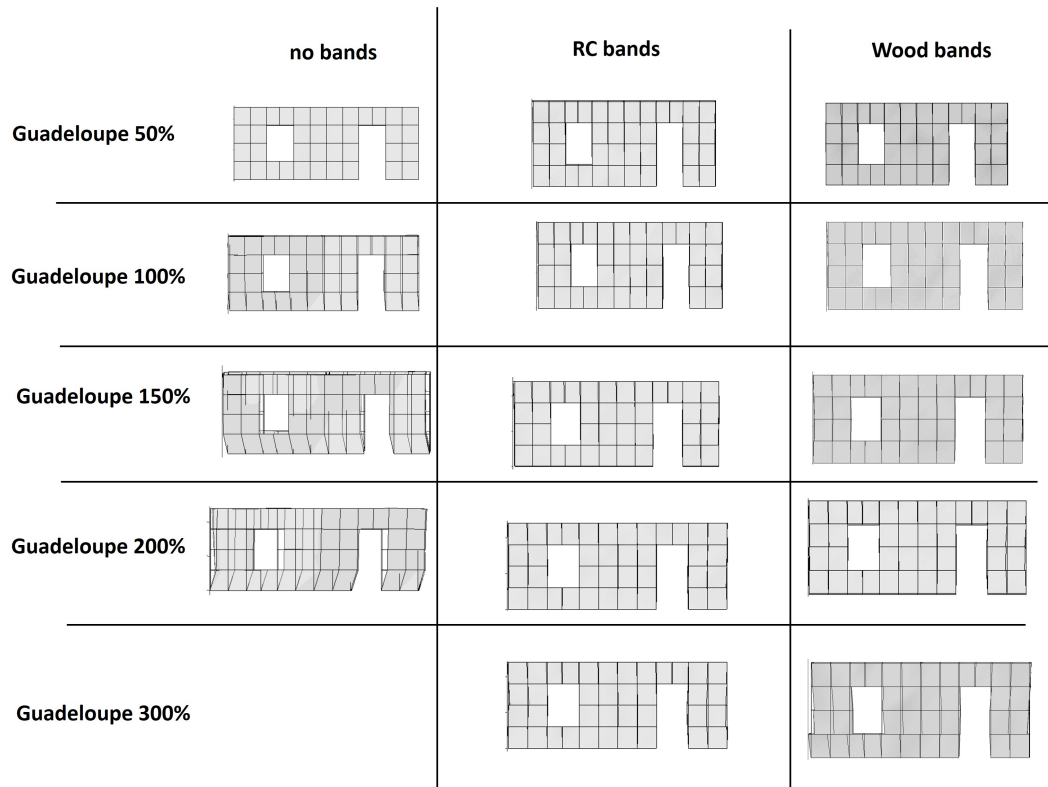


Figure 9.17: Deformed shapes of the houses at the end every test magnified by a factor of 20

9.4.2 Damage after the seismic tests

The second criterion for analyzing the impact of the bands is the damage to the masonry after each seismic load. The maximum allowable drift of the masonry is used to determine a damage parameter D_{test} . This maximum drift depends on several parameters, such as the boundary conditions, the type of loading (static or dynamic), and the loading history [135]. In addition, the maximum allowable drift depends on the height of the wall. According to Wilding and Beyer [128], it is higher for walls with a height of less than 1.2 m than for walls with a normal height. Therefore, there are no defined values for the maximum allowable drift for the tested specimens.

For the determination of the damage parameter D_{test} , the value $\delta_{max} = 0.015h_m$ is used in order to have a good representation of the evolution of the damage after each test. This value is used only to see well the evolution of the damage and does not rely on any definition from the literature. For each diagonal element, the damage parameters are defined as follows:

$$D_{test} = \frac{d_{max} - d_{cr}}{\delta_{max} - d_{cr}} \quad (9.2)$$

In this equation, the displacement d_{max} is the maximum achieved elongation of the considered diagonal element and d_{cr} is the displacement defining the occurrence of the cracks of the diagonal elements as defined in Section 8.2.2. Figure 9.18 shows the damage after each seismic test owing to the numerical model. It can be seen that the damage at the bottom of the walls is higher in all samples. Moreover, despite having the weakest properties, the samples with bands have less damage than the house without bands. This shows that the bands improve the strength of the structure under seismic loading.

After the last test, the model with RC bands is more damaged than the model with wooden bands. This is to be expected, as the material properties of adobe in this test are lower than those in the wooden band house test.

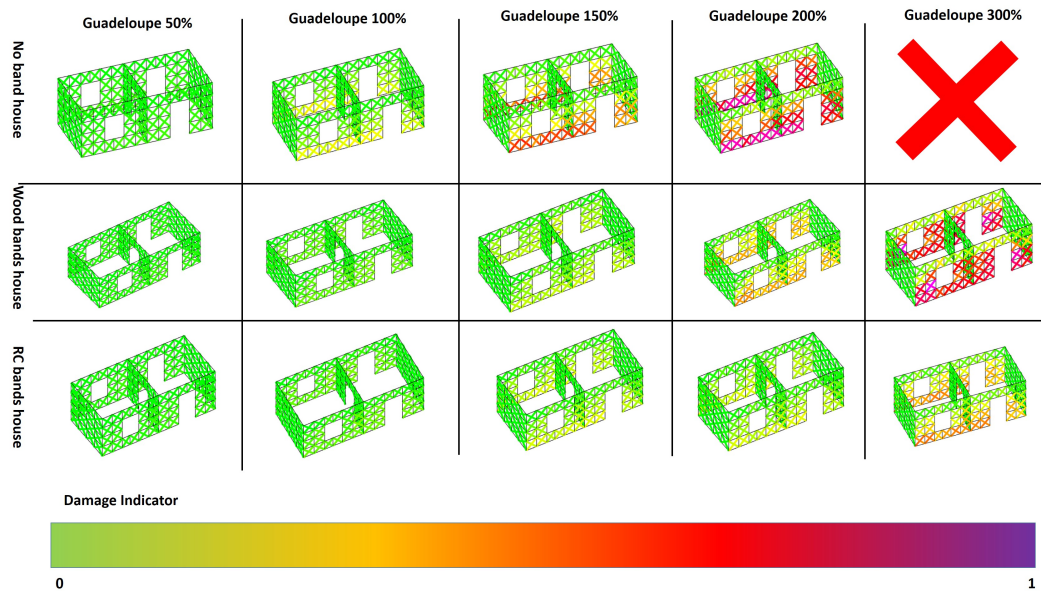


Figure 9.18: Evolution of the damage owing to the numerical model

Figure 9.19 shows the crack patterns in the tested houses at the end of the experimental campaigns. In all houses, there are vertical cracks at the junctions of perpendicular walls. This phenomenon cannot be reproduced with the DFM. In the house without bands, the cracks in the upper part of the walls were already present before the tests. Therefore, it is not a problem that this damage cannot be reproduced with the model. The cracks caused by stress concentration at the corners of the openings also cannot be reproduced by the model. In the house with wooden bands, the upper part of the wall was also cracked before the tests. For all specimens, the numerical model shows higher damage in the lower part of the walls. However, Figure 9.19 shows no major cracks in the houses with bands in this area. The differences between the tested specimens and the numerical model can be explained by: (i) the localization of the damage in the large vertical cracks at the wall junctions, which the model cannot capture, and (ii) the fact that the damage shown by the model can account for large cracks but also diffuse damage.

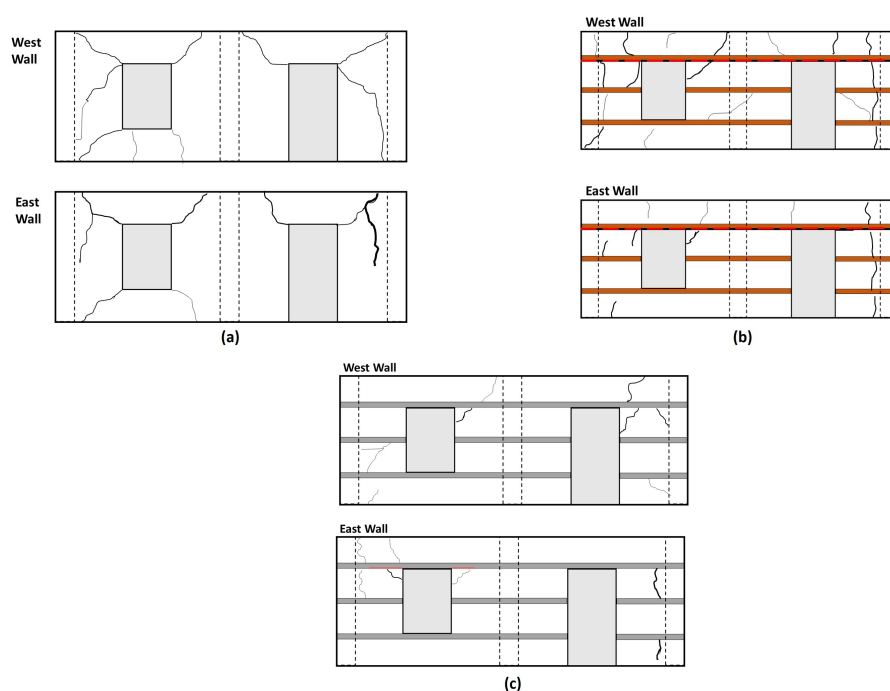


Figure 9.19: Damage in the specimens at the end of the experimental campaign: (a) house without bands; (b) house with wood bands; (c) house with RC bands. The red dashed line shows that that the interface failed.

9.5 Conclusion

In this chapter, dynamic analyses of three different houses were performed. These houses were reduced scale houses inspired by the designs proposed in the Nepalese building catalog [43]. They were tested individually with the shaking table at Institut Technologique FCBA. Six signals of increasing amplitude were used: Guadeloupe 50%, Guadeloupe 100%, Guadeloupe 150%,

Guadeloupe 200%, and Guadeloupe 300%. In all tests, displacements were measured at specific locations on the North wall of the houses (see Figure 9.6).

The three houses were modeled using the DFM. The properties of the materials used for the tested specimens were determined in the previous chapter. However, due to the differences in the curing conditions, these properties do not match those of the materials used for the shake table test. Despite the lack of studies on the influence of curing time and curing method, reduction coefficients were determined for the different specimens. The displacements measured at the corners of the wall were used to verify the performances of the DFM. These displacements correspond to the displacements of the IP-excited walls (East and West walls). Thanks to the limited number of degrees of freedom, the computation time with a normal computer is about 4h30 for a test of the house without bands and 7h30 for a test of the houses with bands. The peak values of the OOP displacements of the North wall were compared with the experimentally measured values.

With the different analyzes, the following conclusions were drawn after numerical modeling of each sample:

- The numerical model predicts the displacements of the East and West walls (IP loaded walls) with satisfactory accuracy for the house without bands. However, it significantly underestimates the OOP deformations of the North wall. This was expected since the numerical model has an elastic behavior in the OOP direction while, in reality, the wall is damaged. Therefore, this leads to an overestimation of the stiffness after a series of seismic loads. This may result in the need to develop a specific criterion to capture the collapse of the wall.
- For all samples, the model fails to capture the peak displacements of each test. This implies an underestimation of the damage, which affects subsequent tests.
- For samples with bands, there is a major difference between the results of the models and those of the experimental tests: the DFM oscillates more after the first displacement peaks (5-7 s.), which leads to an overestimation of the displacements during this period. In the numerical model, the maximum displacement in the positive direction is measured at this time. Therefore, there is a non-negligible difference between the results of the model and the experimental measurements in this direction.
- The numerical model predicts the behavior of the house with wood bands with acceptable accuracy, for both IP and OOP behavior. The error in the OOP direction is high (70%) because it remains almost the same with the numerical model after each test despite the increasing amplitude of the seismic loads. In reality, the OOP displacement is proportional to the amplitude of the signal.
- The numerical model predicts the behavior of the house with RC bands better than that of the wood bands specimen. In the negative direction, the model approximates the maximum displacement well. The OOP displacement is well predicted by the numerical model despite an important computed error. This error is actually high because the reference value is very low.
- The bands strongly limit the OOP deformations. This phenomenon has already been described in the previous chapters and is reproduced by the numerical model.

In addition to the displacements measured at points 6 and 7, the deformed shapes of the houses were analyzed using DFM. It could be seen that the displacement field was different in the presence of bands. The displacement of the parts separated by the bands is clearly different. It can also be seen that the OOP bending of the walls is greatly reduced.

The analysis of the damage evolution has shown that the bands allow to reduce the damage in the masonry during a seismic loading. However, the damage pattern between the numerical model and the experimental test is different. This could be explained by (i) the localization of the damage in the large vertical cracks at the wall junctions, which the model cannot capture, and (ii) the fact that the damage shown by the model can capture large cracks but also diffuse damage. However, more detailed investigations need to be carried out to determine if there are not other reasons that can explain the differences in the crack patterns, such as material properties.

Conclusion

Summary of the manuscript

Masonry buildings make up a large proportion of existing structures. In developed countries, these are mainly historic buildings, while in developing countries they are still commonly used for new buildings, especially in rural areas. Masonry buildings have low tensile strength, so they can fail quickly during earthquakes. To improve their strength under seismic loading, local people have developed architectural methods. One of them is the use of horizontal bands, also called seismic bands. This earthquake resistant strategy is mainly used in Mediterranean and Himalayan countries. It is suggested in several building codes [14, 15] for masonry structures in earthquake prone areas. However, the number of bands, their location, and the material they are made of differ from one code to another. In addition, none of the codes consider the degree of seismic hazard in the design of the structures.

In order to better understand the validity of this type of structures in relation to the latest seismic codes, a numerical model is proposed in this thesis to predict their behavior. Its development is described in three parts: (i) the literature review; (ii) the development of the numerical model; (iii) the validation of the numerical model.

The literature review

Chapter 1 imparts knowledge of masonry construction in general. The various elements that make up masonry (units and joints) were defined, as was the classification of joints (head joints, bed-joints and cross-joints). Then four classes of constructions were identified: URM constructions, RM constructions, CM constructions and FIM constructions. A good identification of the type of masonry construction is essential for a good modeling of the structure. The behavior of a structure during an earthquake is characterized by the cyclic behavior of IP-loaded walls and the bending deformation of OOP-loaded walls. Therefore, numerical models must be able to reproduce both for 3D analysis. The cyclic behavior of masonry under shear loading is defined by the mode of failure and a hysteretic behavior. There are four types of failure: (i) crushing-toe failure; (ii) diagonal/shear failure; (iii) the rocking/bending failure, which is related to the flexural behavior of the wall; (iv) shear/sliding failure.

Chapter 2 focuses on masonry structures with horizontal bands. These bands can be made of a variety of materials: wood, RC, bamboo, or brick. Wood was the first material used as an insert in masonry. Therefore, it is important to determine which types of structures fall within the scope of this thesis and which do not. Only URM structures and RM structures fall within the scope of this thesis. Thus, it is necessary to distinguish between structures with timber frames and masonry infill (FIM structures) and masonry structures with timber bands (RM structures). After identifying the type of structures, the typologies in the different building codes were presented. It was found that there is no uniform way to construct masonry buildings with bands and that the number of bands varies from country to country. It was also possible to identify the different elements in these structures: (i) masonry blocks separated by horizontal bands and openings; (ii) the bands; (iii) frames and other reinforcements. A meso-scale was defined as the scale of the masonry blocks. To find out how to model these different elements, experimental tests on masonry specimens with horizontal bands were then analyzed. It was found that the masonry is modeled at the meso-scale, the bands are modeled with interface elements and additional elements such as frames at the openings and the reinforcements are modeled with elastic beams.

The masonry is the most difficult element to model. Chapter 3 focused on studying the bibliography and identifying the most relevant numerical models for masonry in this thesis. Three categories of numerical models for masonry can be distinguished: (i) micro-models, (ii) meso-models and (iii) macro-models. To achieve reasonable computation time, only meso-models and macro-models can be considered. Since the structures considered in this work may be URM structures or RM structures, some existing models can be used. The most interesting model is the RMEM proposed by Calió et al. [2] in 2005 and improved since then. This model was originally developed for discrete element oriented software, but more recently a FE has been proposed. It is defined by a rigid frame with a diagonal spring in itself. The frame is connected to the adjacent elements by two different types of springs: (i) normal springs for tension/compression; (ii) transversal springs for IP and OOP sliding. The shear behavior is modeled with diagonal elements. Since each element is associated with a specific solicitation, the definition of their properties is straightforward. The main limitation of the model is the need for a fine mesh to correctly capture the bending behavior of the wall. To avoid this limitation, a new meso-model was developed for the masonry.

The numerical model

The new meso-model, called DFM, is presented for 2D analysis in Chapter 4. This meso-model is inspired by the RMEM and is proposed for FE oriented software. It consists of a frame with diagonal struts within itself. However, unlike the RMEM, the frame of the DFM is deformable under tension/compression. This allows to get rid of the normal springs on the sides of the frame. Since the model was specifically proposed to analyze the behavior of masonry structures with bands under seismic loading, only the diagonal elements show inelastic behavior. This behavior is defined by a bi-linear envelope curve and a hysteretic cyclic behavior. The model is defined to capture diagonal/shear failure, shear/sliding failure and rocking failure. All element properties are defined knowing the mechanical properties of the masonry at the meso-scale and the geometry of the element.

The modeling of the bands and reinforcement is presented in Chapter 5. The bands are modeled by zero-thickness interface elements. Their constitutive law is a simplification of the law used for simplified micro-models. It has a brittle tensile behavior and retains an elastic behavior under compression. Under shear it behaves inelastically, with the yield force defined by the Mohr-Coulomb criterion. The cohesion of the interface is affected by the damage due to tensile loading and the shear damage in the DFM. Therefore, the model can capture the sliding at the masonry/band interface due to crack propagation. All reinforcements of the structures are modeled by elastic beams. The only special feature relates to the modeling of lintels.

Chapter 6 extends the definition of the DFM to 3D analysis. To capture the OOP bending behavior of masonry, the frame is formed by beam elements. In order not to change the definition of the meso-model for 2D analysis, the rotation around the OOP axis is not considered. Since the OOP behavior of masonry does not play a major role in the energy dissipation during an earthquake, the DFM has an elastic behavior in this direction. The objective is only to capture the OOP bending deformation and to compare it with a maximum allowable value. In addition to the definition of the DFM for 3D analysis, the definition of the mass matrix for the whole model is presented in Chapter 6 to allow dynamic analysis.

The numerical analysis

In Chapter 7, several modal analyzes performed with the DFM are presented. These studies are used to validate the elastic properties of the meso-model and the definition of the mass matrix. The smallest structure analyzed is a square wall and the largest is a 5-wall structure. In order to determine how well the meso-model performs, the results were compared with those of a 2D FE model and a 3D FE model. From these studies, it appears that the DFM can approximate the modes well, except for the vertical modes where it underestimates the modal mass. Since the model is used for seismic analysis, this is not a problem. The computation time of the DFM is very satisfactory for each analysis.

Chapter 8 presented the numerical analysis of three experimental campaigns. The first is that of Anthoine et al. [5]. It consists of cyclic shear tests on two URM piers with different slenderness. The DFM was able to predict the results of the two tests with good accuracy. The second modeled experiment was that of Reyes et al. [6, 120]. It consists of cyclic experiments on an adobe wall. Unlike the walls of the experiments of Anthoine et al. [5], the walls of this second experiment have two openings and lintels. The model was able to predict the envelope curve of the experimental test with good accuracy, but overestimated the size of the hysteresis loops. The third experiment was that of Yadav [7]. It consists of two quasi-static tests on square adobe walls. One of them is without bands and the second has a wooden band in the middle of the height. Unlike the previous tests, the aim was not to predict the cyclic behavior of the walls, but to determine the properties of the DFM for the dynamic analysis of the last chapter. Since only one experiment was performed on a wall with a horizontal band, a sensitivity analysis of the properties of the interface elements was performed to determine their influence on the behavior of the wall.

Chapter 9 presented the dynamic analysis of three houses: (i) a URM house; (ii) a house with wooden bands; (iii) a house with RC bands. These three specimens were tested on the shaking

table of Institut Technologique FCBA. Due to time constraints, the houses were tested only three to four weeks after their construction. Therefore, the mechanical properties of the masonry and interfaces had to be adjusted to account for this. The results showed that the numerical model was able to predict the displacement of the IP loaded walls with a good accuracy for the three specimens. However, the model underestimated the OOP deformation of the wall when there are not any bands. The main reason for this overestimation is the inability of the model to capture the damage to the connection between perpendicular walls that affects the boundary conditions of the walls and the elastic behavior of the masonry under this type of loading. The bands alter the displacement field and reduce the damage of the house as well.

Future research

The study presented in this manuscript focuses on the development of a numerical tool for the analysis of the dynamic behavior of masonry structures with horizontal bands. The following ideas are proposed to improve this model or for its use:

- **To investigate the strength of walls with bands:** In this thesis, two quasi-static tests on walls have been presented (those of Aranguren et al. [45] and Yadav [7]). The conclusion regarding the effect of bands on the shear strength of the wall is different in both cases. A deeper investigation would allow to draw a conclusion on this aspect and to adjust, if necessary, the definition of the maximum strength of the DFM. It would allow to have values for the properties of the interface wood/masonry or concrete/masonry, coupling coefficient φ_{int} included, as well.
- **To model additional cyclic tests:** In this thesis, only three cyclic shear tests were modeled using the DFM. For masonry piers, the DFM was able to predict the cyclic behavior. However, for the widest wall, it overestimated the hysteresis loops. The additional modeling would allow to check the proposed values of the parameters defining the hysteresis loops and to change their definition if necessary.
- **To have a criterion for the maximal displacement in the OOP and IP directions:** The DFM does not capture the OOP displacement well for constructions without bands. In theory, this model is used to model masonry constructions with bands however it should be able to model walls without bands as well. The elastic behavior for OOP excitation leads to an underestimation of the displacements. Therefore, when the wall collapses in reality, the model does not exhibit the same deformation. In order for the model to capture the failure, either the DFM must exhibit inelastic behavior in the OOP direction, which leads to an increase in computation time and the need of a modeling strategy, or a specific criterion must be defined. For IP loading, a maximal displacement has to be defined as well in order to determine when the construction is considered too damaged.
- **To consider a second story:** Some designs in the Nepalese catalogs [43, 44] are two-story constructions. The study in this thesis focused on the dynamic analysis of one-story designs and some additional tools would be necessary (modeling of the floor, connection between the two floors).

- **To account for the seismic hazard level:** In the building codes of India, Pakistan and Nepal, the proposed designs for masonry structures are identical irrespective of the seismic hazard level. The numerical model can be used to test different typologies and determine whether the use of a limited number of bands placed at specific locations is sufficient for areas with low seismic hazard. Moreover, the use of bands does not bring sufficient strength to the constructions for areas with high seismic hazard owing to these building codes. In the end, it can give construction workers simple rules for construction. These kinds of rules already exist in building codes and catalogs. However, the model could provide rules that correlate with the number of bands in the house in relation to the seismic hazard level.

Bibliography

- [1] G. Amato, M. Fossetti, L. Cavaleri, M. Papia, An updated model of equivalent diagonal strut for infill panels (2008) 119–128.
- [2] I. Caliò, M. Marletta, B. Pantò, A simplified model for the evaluation of the seismic behaviour of masonry buildings, in: Proceedings of the 10th international conference on civil, structural and environmental engineering computing. Stirlingshire, UK: Civil-Comp Press, Paper, Vol. 195, 2005.
- [3] V. Turnšek, F. Čačovič, Some experimental results on the strength of brick masonry walls, in: Proc. of the 2nd International Brick Masonry Conference, 1971, pp. 149–156.
- [4] T. Panagiotakos, M. Fardis, Seismic response of infilled RC frames structures, in: 11th world conference on earthquake engineering, no. 225, 1996.
- [5] A. Anthoine, G. Magonette, G. Magenes, Shear-compression testing and analysis of brick masonry walls, in: Proceedings of the 10th European conference on earthquake engineering, Vol. 3, 1994, pp. 1657–1662.
- [6] J. C. Reyes, L. E. Yamin, W. M. Hassan, J. D. Sandoval, C. D. Gonzalez, F. A. Galvis, Shear behavior of adobe and rammed earth walls of heritage structures, *Engineering Structures* 174 (2018) 526–537.
- [7] S. Yadav, Horizontal seismic band in masonry structure: seismic vulnerability analysis using experiments, Ph.D. thesis, Université Grenoble Alpes (2021).
- [8] W. Mann, et al., Failure of shear-stressed masonry: an enlarged theory, tests and application to shear walls (1982).
- [9] V. Turnšek, P. Sheppard, The shear and flexural resistance of masonry walls, 1980.
- [10] S. Lagomarsino, A. Penna, A. Galasco, S. Cattari, TREMURI program: an equivalent frame model for the nonlinear seismic analysis of masonry buildings, *Engineering Structures* 56 (2013) 1787–1799.
- [11] A. Fallahi, Lessons learned from the housing reconstruction following the bam earthquake in iran, *Australian Journal of Emergency Management*, The 22 (1) (2007) 26–35.
- [12] S. Lagomarsino, Damage assessment of churches after LAquila earthquake (2009), *Bulletin of Earthquake Engineering* 10 (1) (2012) 73–92.

-
- [13] J. Ortega, G. Vasconcelos, H. Rodrigues, M. Correia, P. B. Lourenço, Traditional earthquake resistant techniques for vernacular architecture and local seismic cultures: A literature review, *Journal of Cultural Heritage* 27 (2017) 181–196.
- [14] N. . 2015, Guidelines on loading bearing masonry (2015).
- [15] B. of Indian Standards, Improving Earthquake Resistance of Low Strength Masonry Buildings: Guidelines, The Bureau, 1993.
- [16] A. S. Arya, T. Boen, Y. Ishiyama, Guidelines for earthquake resistant non-engineered construction, UNESCO, 2014.
- [17] D. Gautam, J. Prajapati, K. V. Paterno, K. K. Bhetwal, P. Neupane, Disaster resilient vernacular housing technology in nepal, *Geoenvironmental Disasters* 3 (1) (2016) 1–14.
- [18] M. Schildkamp, Y. Araki, School buildings in rubble stone masonry with cement mortar in seismic areas: literature review of seismic codes, technical norms and practical manuals, *Frontiers in Built Environment* 5 (2019) 13.
- [19] N. . 1994, Mandatory rules of thumb for loadbearing masonry (2007).
- [20] N. . 2015, Guidelines for earthquake resistant building construction: low strength masonry (2015).
- [21] Building Code of Pakistan - Seismic Provisions (2007).
- [22] S. Grange, Atl4s, a tool and language for simplified structural solution strategy, Tech. rep., GEOMAS INSA-Lyon (2016).
- [23] P. Verpeaux, A. Millard, A. Hoffmann, L. Ebersolt, Castem 2000: a modern approach of computerized structural analysis, Tech. rep., CEA Centre d'Etudes Nucleaires de Saclay (1988).
- [24] A. Zucchini, P. Lourenço, A micro-mechanical model for the homogenisation of masonry, *International journal of Solids and Structures* 39 (12) (2002) 3233–3255.
- [25] S. Casolo, Modelling in-plane micro-structure of masonry walls by rigid elements, *International Journal of Solids and Structures* 41 (13) (2004) 3625–3641.
- [26] A. Zucchini, P. B. Lourenço, Mechanics of masonry in compression: Results from a homogenisation approach, *Computers & structures* 85 (3-4) (2007) 193–204.
- [27] A. Zucchini, P. B. Lourenço, A coupled homogenisation–damage model for masonry cracking, *Computers & structures* 82 (11-12) (2004) 917–929.
- [28] F. Vieux-Champagne, S. Grange, Y. Sieffert, L. Daudeville, Multi-scale analysis of timber framed structures filled with earth and stones, in: *COMPLAS XII: proceedings of the XII International Conference on Computational Plasticity: fundamentals and applications*, CIMNE, 2013, pp. 431–440.
- [29] M. M. Eladly, Numerical study on masonry-infilled steel frames under vertical and cyclic horizontal loads, *Journal of Constructional Steel Research* 138 (2017) 308 – 323. doi:<https://doi.org/10.1016/j.jcsr.2017.07.016>. URL <http://www.sciencedirect.com/science/article/pii/S0143974X17303826>

-
- [30] A. Mohyeddin, H. M. Goldsworthy, E. F. Gad, FE modelling of RC frames with masonry infill panels under in-plane and out-of-plane loading, *Engineering Structures* 51 (2013) 73–87.
- [31] C. M. Network, *Seismic design guide for low-rise confined masonry buildings*, Earthquake Engineering Research Institute (EERI): Oakland, CA, USA (2011).
- [32] B. Pantò, E. Raka, F. Cannizzaro, G. Camata, S. Caddemi, E. Spacone, I. Calì, Numerical macro-modeling of unreinforced masonry structures: a critical appraisal, in: *Proceedings of the Fifteenth International Conference on Civil, Structural and Environmental Engineering Computing*, 2015.
- [33] D. Combesure, *Modélisation du comportement sous chargement sismique des structures de bâtiment comportant des murs de remplissage en maçonnerie*, Ph.D. thesis, Châtenay-Malabry, Ecole centrale de Paris (1996).
- [34] P. G. Asteris, S. Antoniou, D. S. Sophianopoulos, C. Z. Chrysostomou, Mathematical macromodeling of infilled frames: state of the art, *Journal of Structural Engineering* 137 (12) (2011) 1508–1517.
- [35] R. Hughes, Cator and cribbage construction of northern pakistan, in: *Proceedings of Earthquake-Safe: Lessons To Be Learned From Traditional Construction—International Conference on the Seismic Performance of Traditional Buildings*, 2000, pp. 16–18.
- [36] A. Caimi, *Cultures constructives vernaculaires et résilience: entre savoir, pratique et technique: appréhender le vernaculaire en tant que génie du lieu et génie parasinistre*, Ph.D. thesis, Grenoble (2014).
- [37] R. Hughes, *Vernacular architecture and construction techniques in the karakoram*, *Karakoram: Hidden Treasures in the Northern Areas of Pakistan* (2005) 99–132.
- [38] T. Schacher, *Bhatar construction, Timber reinforced masonry*, Guidebook prepared by Awiss Agency for Development and Cooperation SDC and French Red Cross FRC, in collaboration with Belgian Red Cross Architectural and Development, UN Habitat, NESPAK (2007).
- [39] M. Kázmér, *Living with earthquakes along the silk road*, in: *Socio-Environmental Dynamics along the Historical Silk Road*, Springer, Cham, 2019, pp. 153–176.
- [40] A. Abdessemed Foufa, D. Benouar, *Rediscovery and revival of traditional earthquake-resistant techniques in Algeria: The Casbah of Algiers (Algeria)*, in: *Disaster Reduction Hyperbase*.
- [41] M. Hofmann, *Le facteur séisme dans l’architecture vernaculaire*, Tech. rep., EPFL (2015).
- [42] A. Abdessemed-Foufa, *Historic earthquake-resistant constructive techniques reinforced by wooden logs in algeria*, in: *Historical Earthquake-Resistant Timber Framing in the Mediterranean Area*, Springer, 2016, pp. 33–45.
- [43] Department of Urban Development and Building Construction, *Design catalogue for reconstruction of earthquake resistant houses*, Ministry of Urban Development (October 2015).
- [44] Department of Urban Development and Building Construction, *Design catalogue for reconstruction of earthquake resistant houses Volume II*, Ministry of Urban Development (March 2017).

- [45] J. Aranguren, F. Vieux-Champagne, M. Duriez, J.-E. Aubert, Experimental analysis of timber inclusions effect on paraseismic behavior of earth masonry walls, *Engineering Structures* 212 (2020) 110429.
- [46] R. Spence, A. Coburn, Strengthening buildings of stone masonry to resist earthquakes, in: *Masonry Construction*, Springer, 1992, pp. 213–221.
- [47] Q. Ali, A. N. Khan, M. Ashraf, A. Ahmed, B. Alam, N. Ahmad, M. Javed, S. Rahman, M. Fahim, M. Umar, Seismic performance of stone masonry buildings used in the Himalayan Belt, *Earthquake Spectra* 29 (4) (2013) 1159–1181.
- [48] A. A. Costa, A. Arède, A. Costa, J. Guedes, B. Silva, Experimental testing, numerical modelling and seismic strengthening of traditional stone masonry: comprehensive study of a real azorian pier, *Bulletin of Earthquake Engineering* 10 (1) (2012) 135–159.
- [49] L. Gambarotta, S. Lagomarsino, Damage models for the seismic response of brick masonry shear walls. Part II: the continuum model and its applications, *Earthquake engineering & structural dynamics* 26 (4) (1997) 441–462.
- [50] K. F. Abdulla, L. S. Cunningham, M. Gillie, Simulating masonry wall behaviour using a simplified micro-model approach, *Engineering Structures* 151 (2017) 349–365.
- [51] A. Mohebkah, A. Tasnimi, H. Moghadam, Nonlinear analysis of masonry-infilled steel frames with openings using discrete element method, *Journal of constructional steel research* 64 (12) (2008) 1463–1472.
- [52] A. M. D’Altri, F. Messali, J. Rots, G. Castellazzi, S. de Miranda, A damaging block-based model for the analysis of the cyclic behaviour of full-scale masonry structures, *Engineering Fracture Mechanics* 209 (2019) 423–448.
- [53] A. Bacigalupo, L. Gambarotta, Computational two-scale homogenization of periodic masonry: characteristic lengths and dispersive waves, *Computer Methods in Applied Mechanics and Engineering* 213 (2012) 16–28.
- [54] S. Casolo, F. Pena, Rigid element model for in-plane dynamics of masonry walls considering hysteretic behaviour and damage, *Earthquake engineering & structural dynamics* 36 (8) (2007) 1029–1048.
- [55] S. Casolo, Rigid element model for non-linear analysis of masonry façades subjected to out-of-plane loading, *Communications in numerical methods in engineering* 15 (7) (1999) 457–468.
- [56] S. Casolo, F. Pena, Modelling micro-structure aspects of masonry walls by a simplified approach, *WIT Transactions on The Built Environment* 66 (2003).
- [57] E. Bertolesi, G. Milani, S. Casolo, Non-linear dynamic analyses of 3D masonry structures by means of a homogenized rigid body and spring model (hrbsm), in: *AIP Conference Proceedings*, Vol. 1790, AIP Publishing, 2016, p. 130007.
- [58] G. Pande, J. Liang, J. Middleton, Equivalent elastic moduli for brick masonry, *Computers and Geotechnics* 8 (3) (1989) 243–265.
- [59] E. Papa, About damage mechanics with particular reference to masonry, *Dissertation*, Politecnico di Milano (1990).

-
- [60] P. B. Lourenço, Computational strategies for masonry structures (1996).
- [61] D. Addessi, E. Sacco, A multi-scale enriched model for the analysis of masonry panels, *International Journal of Solids and Structures* 49 (6) (2012) 865–880.
- [62] S. Forest, K. Sab, Cosserat overall modeling of heterogeneous materials, *Mechanics Research Communications* 25 (4) (1998) 449–454.
- [63] D. Addessi, E. Sacco, A. Paolone, Cosserat model for periodic masonry deduced by non-linear homogenization, *European Journal of Mechanics-A/Solids* 29 (4) (2010) 724–737.
- [64] M. L. De Bellis, D. Addessi, A cosserat based multi-scale model for masonry structures, *International Journal for Multiscale Computational Engineering* 9 (5) (2011) 543.
- [65] A. Bacigalupo, L. Gambarotta, Second-order computational homogenization of heterogeneous materials with periodic microstructure, *ZAMM-Journal of Applied Mathematics and Mechanics/Zeitschrift für Angewandte Mathematik und Mechanik* 90 (10-11) (2010) 796–811.
- [66] A. Bacigalupo, L. Gambarotta, Non-local computational homogenization of periodic masonry, *International Journal for Multiscale Computational Engineering* 9 (5) (2011).
- [67] M. Mistler, A. Anthoine, C. Butenweg, In-plane and out-of-plane homogenisation of masonry, *Computers & Structures* 85 (17-18) (2007) 1321–1330.
- [68] B. Mercatoris, T. Massart, A coupled two-scale computational scheme for the failure of periodic quasi-brittle thin planar shells and its application to masonry, *International journal for numerical methods in engineering* 85 (9) (2011) 1177–1206.
- [69] G. Uva, G. Salerno, Towards a multiscale analysis of periodic masonry brickwork: A FEM algorithm with damage and friction, *International journal of solids and structures* 43 (13) (2006) 3739–3769.
- [70] A. Rossi, P. Morandi, R. R. Milanesi, G. Magenes, In-plane seismic performance of RC structures with an innovative masonry infill with sliding joints through non-linear analyses, in: *COMPADYN 2017, 6th ECCOMAS Thematic Conference on Computational Methods in Structural Dynamics and Earthquake Engineering, GRC, 2017*.
- [71] H. Xu, C. Gentilini, Z. Yu, H. Wu, S. Zhao, A unified model for the seismic analysis of brick masonry structures, *Construction and Building Materials* 184 (2018) 733–751.
- [72] S. Polyakov, On the interaction between masonry filler walls and enclosing frame when loaded in the plane of the wall, *Translations in Earthquake Engineering, Earthquake engineering Research Institute, Oakland, California* (1960) 36–42.
- [73] A. Fiore, A. Netti, P. Monaco, The influence of masonry infill on the seismic behaviour of RC frame buildings, *Engineering structures* 44 (2012) 133–145.
- [74] F. J. Crisafulli, A. J. Carr, Proposed macro-model for the analysis of infilled frame structures, *Bulletin of the New Zealand Society for Earthquake Engineering* 40 (2) (2007) 69–77.
- [75] C. Symakezis, V. Vratsanou, Influence of infill walls to RC frames response, in: *Proceedings of the eighth European conference on earthquake engineering, Lisbon, no. vol 3, 1986*.

-
- [76] F. J. Crisafulli, A. J. Carr, R. Park, Analytical modelling of infilled frame structures-a general review, *Bulletin-New Zealand Society for Earthquake Engineering* 33 (1) (2000) 30–47.
- [77] E. Quagliarini, G. Maracchini, F. Clementi, Uses and limits of the Equivalent Frame Model on existing unreinforced masonry buildings for assessing their seismic risk: A review, *Journal of Building Engineering* 10 (2017) 166–182.
- [78] P. Code, Eurocode 8: Design of structures for earthquake resistance-part 1: general rules, seismic actions and rules for buildings, Brussels: European Committee for Standardization (2005).
- [79] P. FEMA, Fema 356 (2000).
- [80] G. Magenes, A. Della Fontana, Simplified non-linear seismic analysis of masonry buildings, *Proceedings of the British Masonry Society* 8 (1998) 190–195.
- [81] G. Magenes, A method for pushover analysis in seismic assessment of masonry buildings, in: *Proceedings of the 12th world conference on earthquake engineering*, Vol. 42, 2000.
- [82] L. Pasticier, C. Amadio, M. Fragiaco, Non-linear seismic analysis and vulnerability evaluation of a masonry building by means of the SAP2000 V. 10 code, *Earthquake Engineering & Structural Dynamics* 37 (3) (2008) 467–485.
- [83] T. Salonikios, C. Karakostas, V. Lekidis, A. Anthoine, Comparative inelastic pushover analysis of masonry frames, *Engineering Structures* 25 (12) (2003) 1515–1523.
- [84] L. Gambarotta, S. Lagomarsino, Sulla risposta dinamica di pareti in muratura, *Atti del Convegno Nazionale "La Meccanica delle Murature tra Teoria e Progetto"*, Messina (1996) 18–20.
- [85] L. Gambarotta, S. Lagomarsino, Computational models for the seismic response of damaging structures, on *Seismic Evaluation and Retrofit* (1997) 45.
- [86] A. Brencich, L. Gambarotta, S. Lagomarsino, A macroelement approach to the three-dimensional seismic analysis of masonry buildings, in: *11th European Conference on Earthquake Engineering*, 1998, pp. 6–11.
- [87] P. D'Asdia, A. Viskovic, Analyses of a masonry wall subjected to horizontal actions on its plane, employing a non-linear procedure using changing shape finite elements, *WIT Transactions on Modelling and Simulation* 12 (1995).
- [88] A. A. Mobarake, M. Khanmohammadi, S. Mirghaderi, A new discrete macro-element in an analytical platform for seismic assessment of unreinforced masonry buildings, *Engineering Structures* 152 (2017) 381–396.
- [89] B. Pantò, I. Caliò, P. B. Lourenço, A 3D discrete macro-element for modelling the out-of-plane behaviour of infilled frame structures, *Engineering Structures* 175 (2018) 371–385.
- [90] T. Takeda, M. A. Sozen, N. N. Nielsen, Reinforced concrete response to simulated earthquakes, *Journal of the Structural Division* 96 (12) (1970) 2557–2573.
- [91] C. Chácaras, F. Cannizzaro, B. Pantò, I. Caliò, P. B. Lourenço, Assessment of the dynamic response of unreinforced masonry structures using a macroelement modeling approach, *Earthquake Engineering & Structural Dynamics* 47 (12) (2018) 2426–2446.

-
- [92] I. Caliò, M. Marletta, B. Pantò, A new discrete element model for the evaluation of the seismic behaviour of unreinforced masonry buildings, *Engineering Structures* 40 (2012) 327–338.
- [93] S. Caddemi, I. Caliò, F. Cannizzaro, B. Pantò, New Frontiers on Seismic Modeling of Masonry Structures, *Frontiers in Built Environment* 3 (2017) 39.
- [94] B. Pantò, L. Silva, G. Vasconcelos, P. Lourenço, Macro-modelling approach for assessment of out-of-plane behavior of brick masonry infill walls, *Engineering Structures* 181 (2019) 529–549.
- [95] C. Chácara Espinoza, P. Lourenco, B. Pantó, F. Cannizzaro, I. Calió, Macro-element mass matrix for the dynamic assessment of unreinforced masonry structures, 2017.
- [96] B. Pantò, P. P. Rossi, A new macromodel for the assessment of the seismic response of infilled RC frames, *Earthquake Engineering & Structural Dynamics* (2019).
- [97] S. Mazzoni, F. McKenna, M. H. Scott, G. L. Fenves, et al., *OpenSees command language manual*, Pacific Earthquake Engineering Research (PEER) Center 264 (2006).
- [98] D. Benedetti, M. Tomazevic, Seismic assessment of masonry constructions, *Ingegneria Sismica* 1 (0) (1984) 9–16.
- [99] S. Petrovčič, V. Kilar, Seismic failure mode interaction for the equivalent frame modeling of unreinforced masonry structures, *Engineering structures* 54 (2013) 9–22.
- [100] L. Cavaleri, F. Di Trapani, Cyclic response of masonry infilled RC frames: Experimental results and simplified modeling, *Soil Dynamics and Earthquake Engineering* 65 (2014) 224–242.
- [101] F. J. Crisafulli, Seismic behaviour of reinforced concrete structures with masonry infills (1997).
- [102] T. Tassios, Masonry infill and R/C walls under cyclic actions, in: *CIB Symposium on Wall Structure, Invited State-of-the Art Report*, Warsaw, 1984.
- [103] O. Dowell, F. Seible, E. L. Wilson, Pivot hysteresis model for reinforced concrete members, *ACI Structural Journal* 95 (1998) 607–617.
- [104] J. Humbert, Caractérisation du comportement des structures bois à assemblages métalliques sous sollicitations sismiques, Ph.D. thesis, Thèse de doctorat de l'Université Joseph Fourier (2010).
- [105] R. E. Goodman, R. L. Taylor, T. L. Brekke, A model for the mechanics of jointed rock, *Journal of the soil mechanics and foundations division* 94 (3) (1968) 637–659.
- [106] G. Beer, An isoparametric joint/interface element for finite element analysis, *International journal for numerical methods in engineering* 21 (4) (1985) 585–600.
- [107] C. Desai, M. Zaman, J. Lightner, H. Siriwardane, Thin-layer element for interfaces and joints, *International Journal for Numerical and Analytical Methods in Geomechanics* 8 (1) (1984) 19–43.
- [108] R. Van der Pluijm, Shear behaviour of bed joints (1993).

-
- [109] B. Pantò, F. Cannizzaro, I. Calì, P. B. Lourenço, Numerical and experimental validation of a 3D macro-model for the in-plane and out-of-plane behavior of unreinforced masonry walls, *International Journal of Architectural Heritage* 11 (7) (2017) 946–964.
- [110] S. Casolo, Modelling the out-of-plane seismic behaviour of masonry walls by rigid elements, *Earthquake engineering & structural dynamics* 29 (12) (2000) 1797–1813.
- [111] P. Asteris, L. Cavaleri, F. Di Trapani, A. Tsaris, Numerical modelling of out-of-plane response of infilled frames: State of the art and future challenges for the equivalent strut macromodels, *Engineering Structures* 132 (2017) 110–122.
- [112] F. Di Trapani, P. Shing, L. Cavaleri, Macroelement model for in-plane and out-of-plane responses of masonry infills in frame structures, *Journal of Structural Engineering* 144 (2) (2018) 04017198.
- [113] F. Mazza, In-plane–out-of-plane non-linear model of masonry infills in the seismic analysis of rc-framed buildings, *Earthquake Engineering & Structural Dynamics* 48 (4) (2019) 432–453.
- [114] F. Di Trapani, P. Shing, L. Cavaleri, Macroelement model for in-plane and out-of-plane responses of masonry infills in frame structures, *Journal of Structural Engineering* 144 (2) (2017) 04017198.
- [115] P. G. Asteris, I. P. Giannopoulos, C. Z. Chrysostomou, Modeling of infilled frames with openings, *The Open Construction and Building Technology Journal* 6 (1) (2012) 81–91.
- [116] S. Degli Abbati, S. Lagomarsino, Out-of-plane static and dynamic response of masonry panels, *Engineering Structures* 150 (2017) 803–820.
- [117] K. Doherty, M. C. Griffith, N. Lam, J. Wilson, Displacement-based seismic analysis for out-of-plane bending of unreinforced masonry walls, *Earthquake engineering & structural dynamics* 31 (4) (2002) 833–850.
- [118] M. Godio, K. Beyer, Evaluation of force-based and displacement-based out-of-plane seismic assessment methods for unreinforced masonry walls through refined model simulations, *Earthquake Engineering & Structural Dynamics* 48 (4) (2019) 454–475.
- [119] J. Ahrens, B. Geveci, C. Law, Paraview: An end-user tool for large data visualization, *The visualization handbook* 717 (8) (2005).
- [120] J. C. Reyes, J. P. Smith-Pardo, L. E. Yamin, F. A. Galvis, J. D. Sandoval, C. D. Gonzalez, J. F. Correal, In-plane seismic behavior of full-scale earthen walls with openings retrofitted with timber elements and vertical tensors, *Bulletin of Earthquake Engineering* 17 (7) (2019) 4193–4215.
- [121] G. Magenes, G. M. Calvi, In-plane seismic response of brick masonry walls, *Earthquake engineering & structural dynamics* 26 (11) (1997) 1091–1112.
- [122] F. E. M. A. (FEMA), Interim testing protocols for determining the seismic performance characteristics of structural and nonstructural components, report no. fema-461 (2007).
- [123] J. D. Sandoval Triana, et al., Estudio experimental y modelación del comportamiento de estructuras en adobe, Master’s thesis, Uniandes.

-
- [124] N. Tarque, G. Camata, E. Espacone, H. Varum, M. Blondet, Numerical modelling of in-plane behaviour of adobe walls, in: *Sísmica 2010, 8th Congresso de Sismología e Engenharia Sísmica*, 2010.
- [125] S. H. Rafsanjani, A. Bakhshi, M. A. Ghannad, M. Yekrangnia, F. Soumi, Predictive tri-linear benchmark curve for in-plane behavior of adobe walls, *International Journal of Architectural Heritage* 9 (8) (2015) 986–1004.
- [126] Z. Cao, H. Watanabe, Earthquake response prediction and retrofitting techniques of adobe structures, in: *Proceedings of the 13th World Conference on Earthquake Engineering*, 2004.
- [127] R. Illampas, D. C. Charmpis, I. Ioannou, Laboratory testing and finite element simulation of the structural response of an adobe masonry building under horizontal loading, *Engineering Structures* 80 (2014) 362–376.
- [128] B. V. Wilding, K. Beyer, Analytical and empirical models for predicting the drift capacity of modern unreinforced masonry walls, *Earthquake Engineering & Structural Dynamics* 47 (10) (2018) 2012–2031.
- [129] R. Youngs, S.-J. Chiou, W. Silva, J. Humphrey, Strong ground motion attenuation relationships for subduction zone earthquakes, *Seismological Research Letters* 68 (1) (1997) 58–73.
- [130] G. Zonno, R. Aguilar, R. Boroschek, P. B. Lourenço, Experimental analysis of the thermo-hygrometric effects on the dynamic behavior of adobe systems, *Construction and Building Materials* 208 (2019) 158–174.
- [131] V. Giamundo, G. P. Lignola, A. Prota, G. Manfredi, Nonlinear analyses of adobe masonry walls reinforced with fiberglass mesh, *Polymers* 6 (2) (2014) 464–478.
- [132] B. Liu, J. Jiang, S. Shen, F. Zhou, J. Shi, Z. He, Effects of curing methods of concrete after steam curing on mechanical strength and permeability, *Construction and Building Materials* 256 (2020) 119441.
- [133] R. Spence, R. Hughes, D. Nash, A. Coburn, Damage assessment and ground motion in the Italian earthquake of 23.11. 1980, in: *Proceedings of 7th European conference on earthquake engineering*, Athens, 1982.
- [134] G. King, P. Pandey, The analysis of infilled frames using finite elements., *Proceedings of the Institution of Civil Engineers* 65 (4) (1978) 749–760.
- [135] S. Petry, K. Beyer, Influence of boundary conditions and size effect on the drift capacity of urm walls, *Engineering structures* 65 (2014) 76–88.
- [136] M. Crisfield, An arc-length method including line searches and accelerations, *International journal for numerical methods in engineering* 19 (9) (1983) 1269–1289.
- [137] S. L. Chan, Geometric and material non-linear analysis of beam-columns and frames using the minimum residual displacement method, *International Journal for Numerical Methods in Engineering* 26 (12) (1988) 2657–2669.
- [138] B. W. Forde, S. F. Stiemer, Improved arc length orthogonality methods for nonlinear finite element analysis, *Computers & structures* 27 (5) (1987) 625–630.

- [139] J. Humbert, C. Boudaud, J. Baroth, S. Hameury, L. Daudeville, Joints and wood shear walls modelling i: Constitutive law, experimental tests and fe model under quasi-static loading, *Engineering Structures* 65 (2014) 52–61.

Appendix A

Diagonal strut explanations

The first design of the DFM had horizontal struts to reproduce the shear behavior of the masonry, like the model proposed by Xu et al. [71]. The design of the meso-element is shown in Figure A.1 for 2D modeling. As in the current design, the DFM was defined by four nodes. For a more elegant representation of the element, only one horizontal strut for shear is shown in Figure A.1 instead of two. The element inside the frame in Figure A.1 connects nodes 1 and 3.

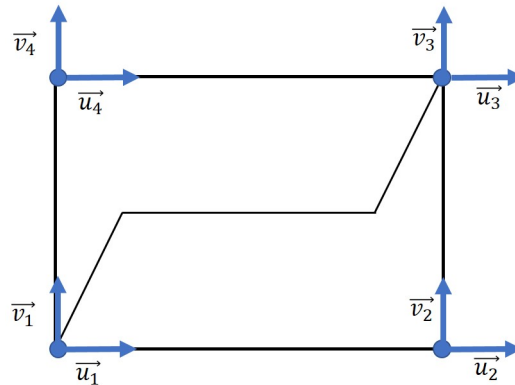


Figure A.1: The first design for the DFM

The advantage in this representation over the final design of the DFM is obvious: there is no coupling between the vertical and horizontal elements. Therefore, the definition of the stiffness of the elements is simple and has no constraints on the shape of the element. Nevertheless, this definition implies the impossibility to reproduce rocking. In fact, the horizontal direction and the vertical direction are completely independent. To illustrate this, let us consider the example in Figure A.2. (a). A displacement d along the horizontal axis is imposed on the node 3 of a meso-element in equilibrium. This displacement implies a stretching of the horizontal strut 4-3 and the horizontal strut 1-3. The node 2 is not connected to the node 3 by an element that can perform a horizontal deflection. Therefore, there is no direct effect on this node. Depending on the boundary conditions, this imposed displacement will produce a displacement d_4 at node 4

and a displacement d_1 at node 1. Since the solicited elements are horizontal struts, it stands to reason that the displacements d_4 and d_1 are also horizontal. This is the situation shown in Figure A.2.(b). These displacements d_4 and d_1 generate a horizontal displacement d_2 at node 2 for similar reasons as described above, until a new equilibrium is established. Finally, the horizontal displacement d does not generate a vertical displacement.

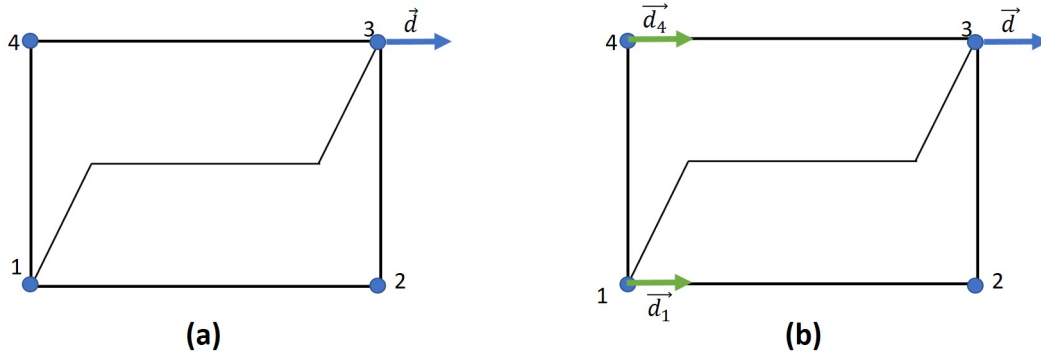


Figure A.2: Kinematics of the DFM with horizontal diagonal strut:(a) Case of a displacement applied at the node 3 ; (b) Direct kinematic consequence of the displacement d

To have a vertical displacement as a result of horizontal loading, there are two solutions. The first is to have elements that are coupled both vertically and horizontally, like the diagonal struts. The second solution is to use beam elements. This second choice would lead to a more difficult definition of the properties of the meso-element. For this reason, diagonal struts were chosen for the DFM.

Appendix B

Creation of the problem

This appendix is intended to describe some of the specifics of creating the model and determining the characteristics of the elements.

B.1 Inelastic behavior of diagonal struts

The diagonal struts of the DFM have a maximal strength that depends on the vertical stress applied on the meso-element. This vertical stress is not an input of the model. It is determined with a pre-study once the model is created and the load is defined. The procedure is illustrated in Figure B.1. The term vertical load in this figure includes all vertical loads acting on the structure as well as the weight of the structure. With such a method, the stress for all elements can be locally defined and the diagonal struts can be correctly defined. The time step in which the complete vertical load is applied is denoted by t_v .

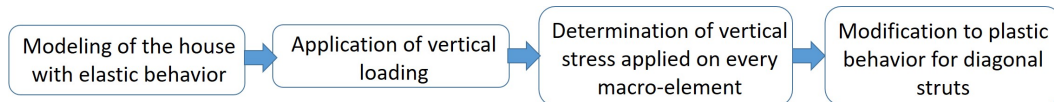


Figure B.1: Procedure to define the plastic behavior of the diagonal struts

During the computational work, the vertical load is first applied. From the first time step to the time step t_v , the diagonal struts are deformed by this vertical load. Thus, it is possible that in a certain configuration the diagonal elements reach their ultimate strength F_u . This is an undesirable phenomenon. To avoid the problem, the diagonal struts keep an elastic behavior from the first time step to the time step t_v . At the end of the time step t_v , the deformation d_{t_v} of each diagonal element is recorded. After the time step t_v , the diagonal elements have their inelastic behavior and their deformation d_{t_v} is set as offset so that the initial state of their constitutive law is the state after the vertical load is applied.

B.2 Rocking failure

As explained in the chapter on the definition of the DFM for in-plane analysis, the rocking failure is not considered in the definition of the maximal strength of the model. However, it is possible to capture it. For the modeling of a masonry wall, a first step is to examine the wall with the boundary conditions and loads shown in Figure B.2. These boundary conditions may be different from the real boundary conditions of the experimental test, it does not matter, the study in Figure B.2 is always the same. The maximum force F_{push} resulting from the push-over test is compared with the ultimate force of the diagonal brace F_u . If $F_u > F_{push}$, the ultimate force of all diagonal struts is multiplied by the ratio F_{push}/F_u . The results shown in Chapter 8 were obtained using this method.

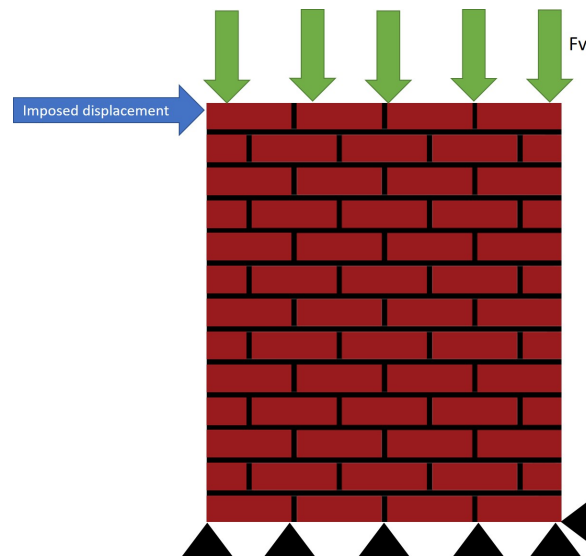


Figure B.2: Procedure to determine the rocking failure

Appendix C

ATL4S

A Tool and Language for Simplified Structural Solution Strategy

ATL4S is a FE toolbox developed in Matlab. The creation of this toolbox is the result of the desire to have a basis for numerical modeling and dynamic analysis of structures in Matlab. There are already many FE software with numerous constitutive laws and elements that are updated every year to provide more capabilities, improve computational efficiency, and make the software more user-friendly. However, when one wants to add new constitutive laws, this task is often difficult for several reasons: (i) a new language needs to be learned, (ii) the source code needs to be changed, (iii) the debug mode is not efficient enough, which further complicates the implementation of new constitutive laws.

Matlab provides an easy way to add new constitutive laws and check their working with an efficient debug mode. The use of Matlab also allows the use of a unique software for numerical modeling and analysis of the results. Moreover, Matlab is very simple compared to other languages.

C.1 Numerical dynamic analysis with ATLAS

At each time step, Newton's second law of motion for a system with multiple degrees of freedom (Equation (C.1)) is solved. In this equation, \underline{U} is the displacement vector, $\underline{\dot{U}}$ is the velocity vector, $\underline{\ddot{U}}$ is the acceleration vector, and \underline{P} is the external forces vector. The other terms are the mass matrix \underline{M} , the damping matrix \underline{C} and the stiffness matrix \underline{K} .

$$\underline{M}.\underline{\ddot{U}} + \underline{C}.\underline{\dot{U}} + \underline{K}.\underline{U} = \underline{P} \quad (\text{C.1})$$

This equation can be solved by various methods. The most common is the Newton Raphson's method with Newmark integration scheme. It is the method used in this thesis. This method uses two parameters β and γ , so that:

$$u_{n+1} = u_n + \Delta t \dot{u}_n + (0.5 - \beta) \Delta t^2 \ddot{u}_n + \beta \Delta t^2 \ddot{u}_{n+1} \quad (\text{C.2})$$

$$\dot{u}_{n+1} = \dot{u}_n + (1 - \gamma) \Delta t \ddot{u}_n + \gamma \Delta t \ddot{u}_{n+1} \quad (\text{C.3})$$

For the analyzes, the case $\beta=0.25$ and $\gamma=0.5$ is chosen. This is an unconditionally stable case.

In some specific cases like snap-backs, the Newton Raphson's method does not converge. This problem can be overcome with ATLAS with the use of other numerical techniques such as:

- Arc-length method (Crisfield's version [136])
- Minimum increment of displacement method (proposed by Chan [137])
- Update normal plane (method proposed by Forde and Stiemer [138])

C.2 Modal analysis

Let us consider the mass matrix \underline{M} and the stiffness matrix \underline{K} . The natural angular frequencies ω of the structure are determined by solving the equation:

$$\det(\underline{K} - \omega^2 \underline{M}) = 0 \quad (\text{C.4})$$

The modal frequency f_i is defined as:

$$\omega_i = 2\pi f_i \quad (\text{C.5})$$

The eigenvector Φ_i associated to the angular frequency ω_i verifies the equation:

$$(\underline{K} - \omega_i^2 \underline{M})\Phi_i = 0 \quad (\text{C.6})$$

The eigenvectors and angular frequencies for the modal analyzes in Chapter 7 are determined using the function *eig* in Matlab.

The generalized modal mass m_i of the mode i is defined as:

$${}^t\Phi_i \underline{M} \Phi_i = m_i \quad (\text{C.7})$$

The modal mass \tilde{m}_i is related to the generalized modal mass m_i by the following equation:

$$\tilde{m}_i = \frac{\left({}^t\Phi_i \underline{M} \underline{\Delta}\right)^2}{m_i} \quad (\text{C.8})$$

The vector $\underline{\Delta}$ is defined by the direction of loading. Its term Δ_j is equal to 1 if j is a translation in the loading direction. Otherwise, it is zero. In a 3D modal analysis, as in Chapter 7, all terms of the vector $\underline{\Delta}$ are equal to 1.

C.3 Constitutive laws for the elements

C.3.1 Already implemented laws

- 2D beam element with Bernoulli's theory
- 3D beam element with Bernoulli's theory
- 3D beam element with Timoshenko's theory
- Fiber elements with Timoshenko's theory
- Humbert's constitutive law for timber connections [139]
- Discrete Elements interface
- Perfect elastoplastic law
- TRI3 elements for linear and non-linear analysis
- QUA4 elements for linear and non-linear analysis

C.3.2 Added laws

- Pivot model (see Chapter 4)
- Constitutive law of the diagonal element of the DFM (see Chapter 4)
- Interface element used in the thesis for 2D and 3D analysis (see Chapter 5)
- Beam elements of the DFM
- Creation of the mesh with DFM
- Determination of the modal mass

Appendix D

Evolution of damage during the experimental tests

D.1 House without bands

D.1.1 Beginning of the tests

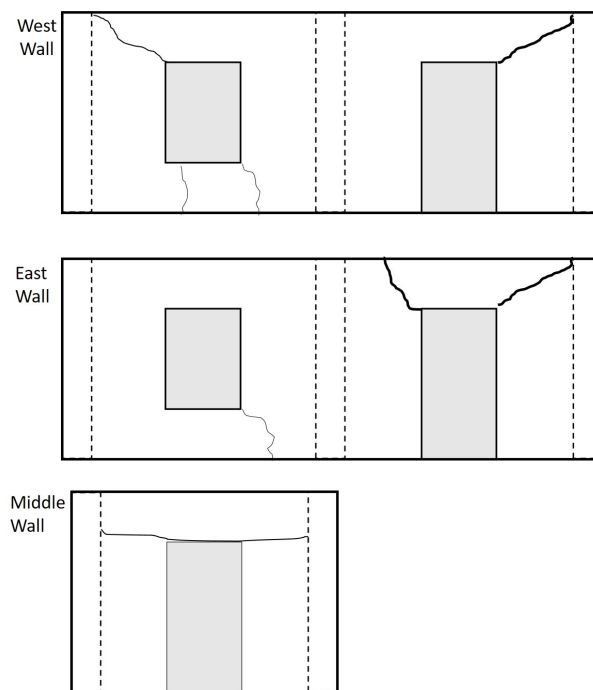


Figure D.1: Drawing of crack pattern of the house without band at the beginning of the tests



(b)



(d)



(a)



(c)

Figure D.2: Cracks in the house without bands at the beginning of the tests: (a-b) West wall; (c) East wall; (d) Middle wall

D.1.2 After the Guadeloupe 100%

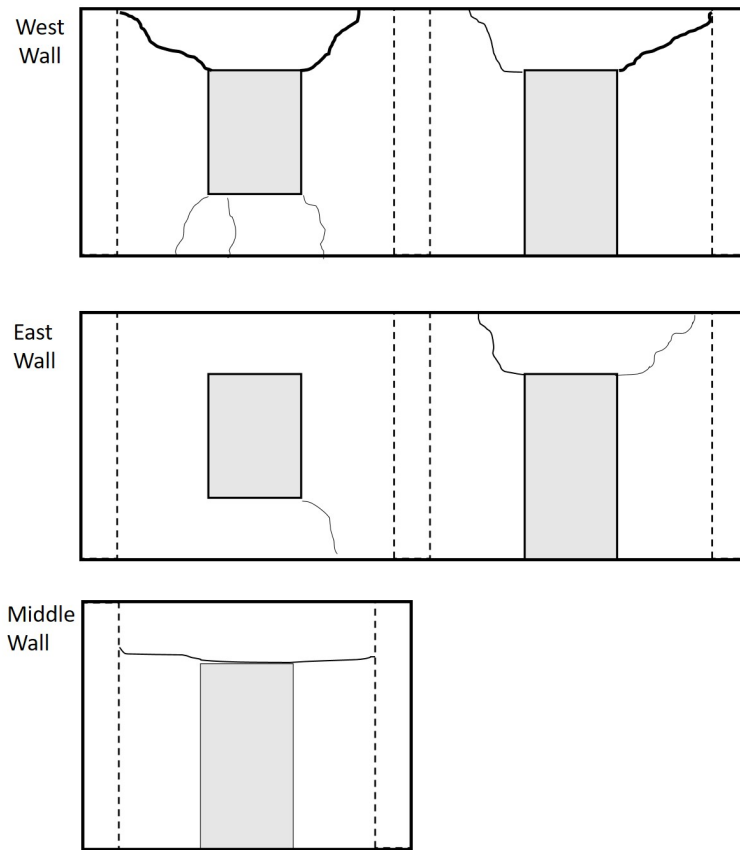


Figure D.3: Drawing of crack pattern of the house without band after the Guadeloupe 100%

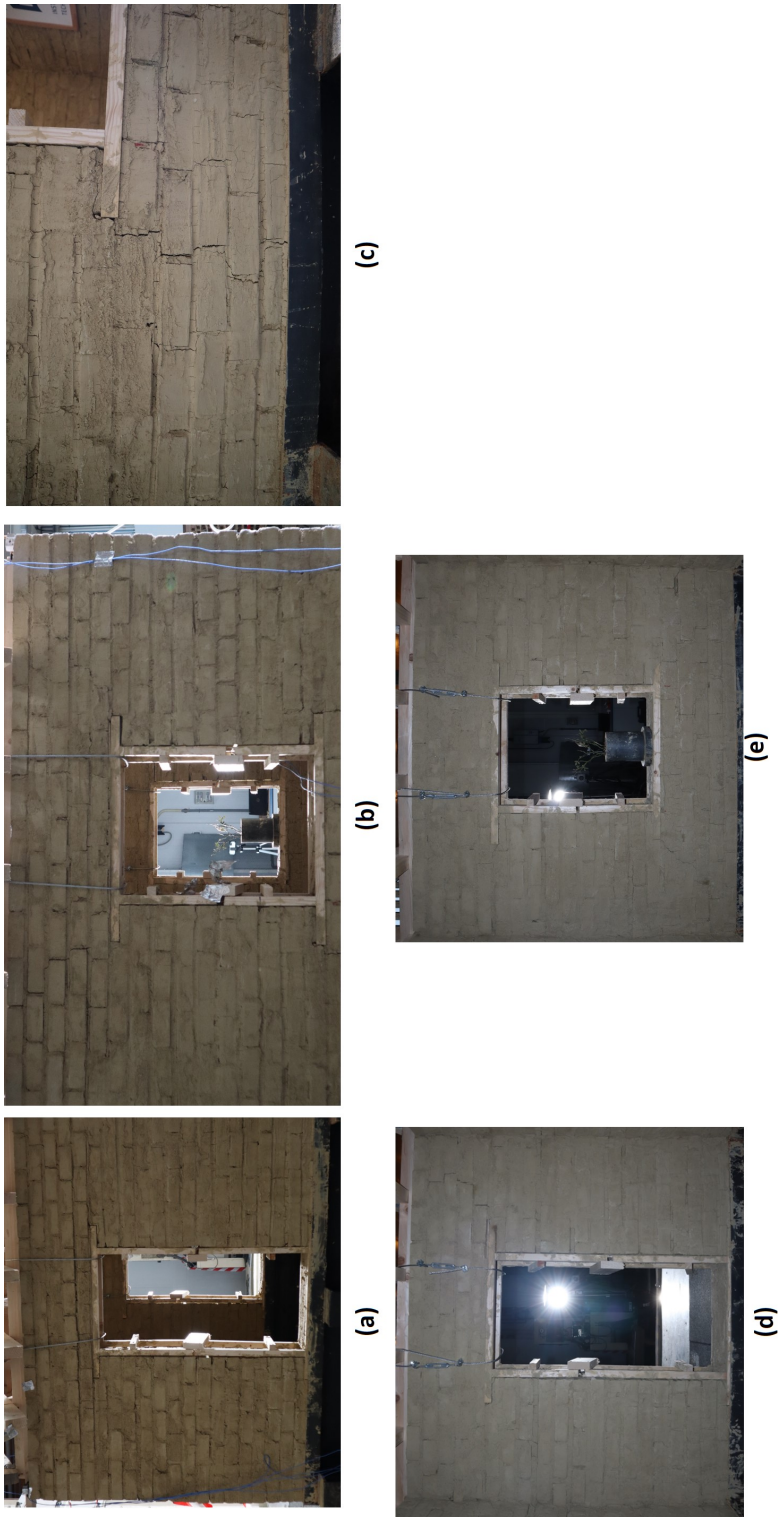


Figure D.4: Cracks in the house without band after the Guadeloupe 100%: (a-c) West wall; (d-e) East wall

D.1.3 After the Guadeloupe 150%

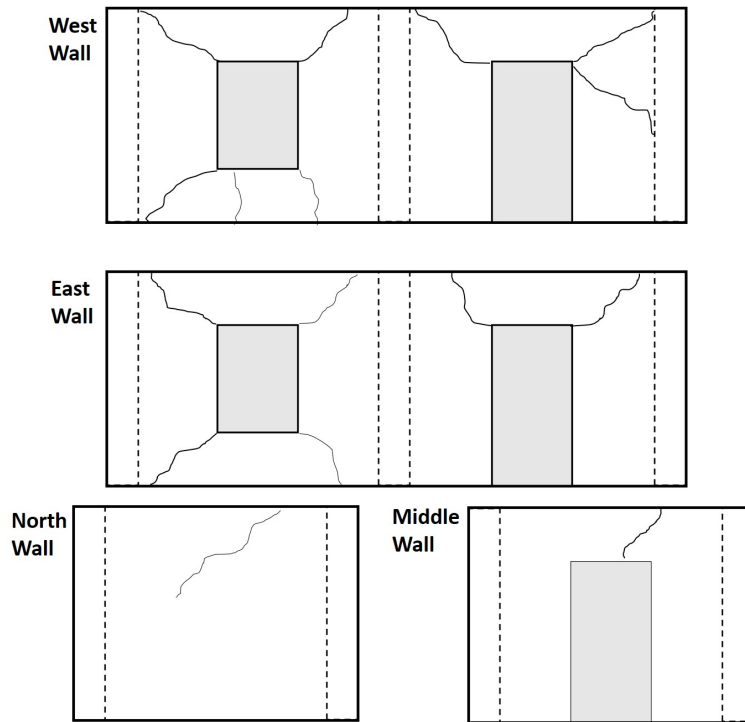


Figure D.5: Drawing of crack pattern of the house without band after the Guadeloupe 150%

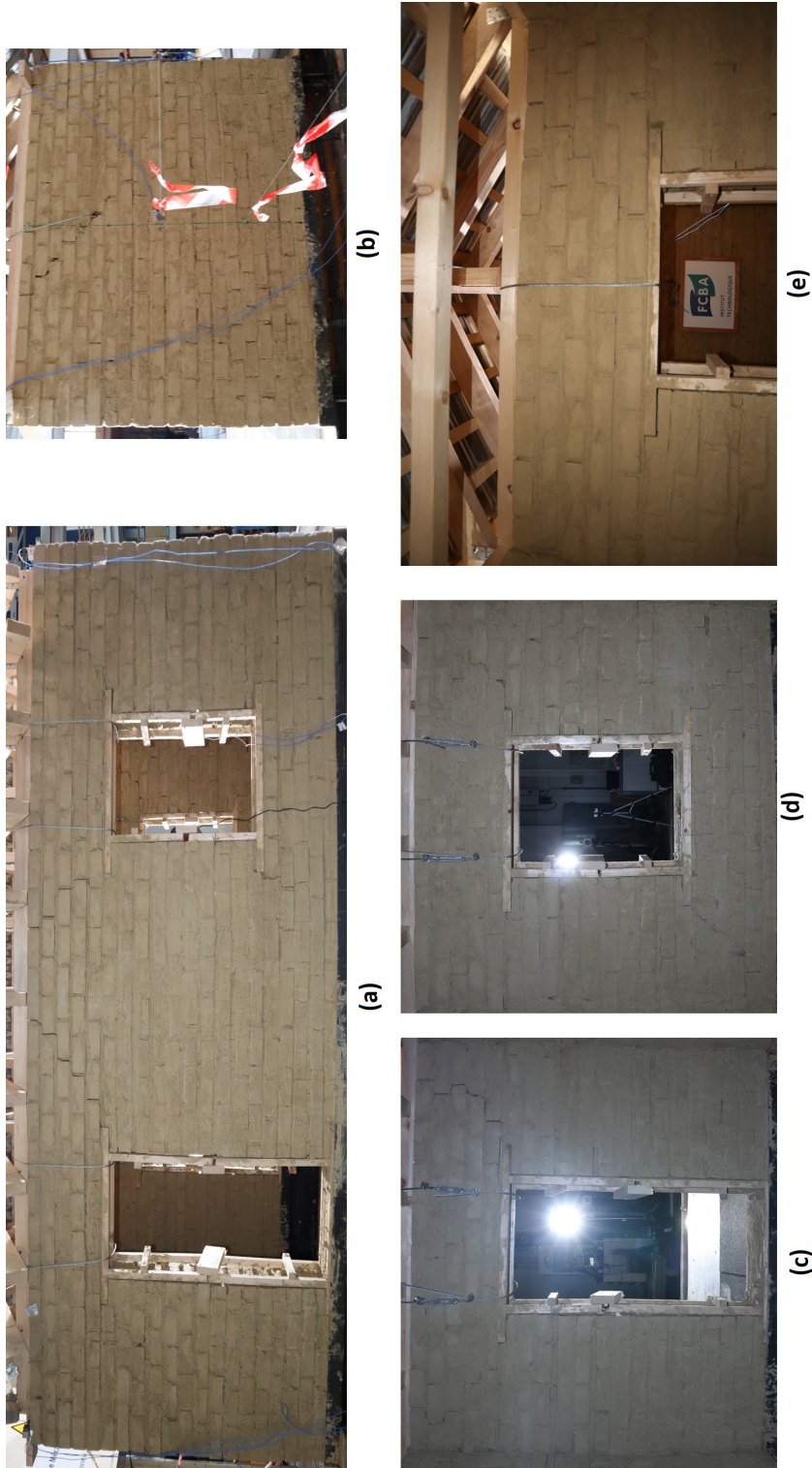


Figure D.6: Cracks in the house without band after the Guadeloupe 150%: (a) West wall; (b) North Wall; (c-d) East wall; (e) Middle Wall

D.1.4 After the Guadeloupe 200%

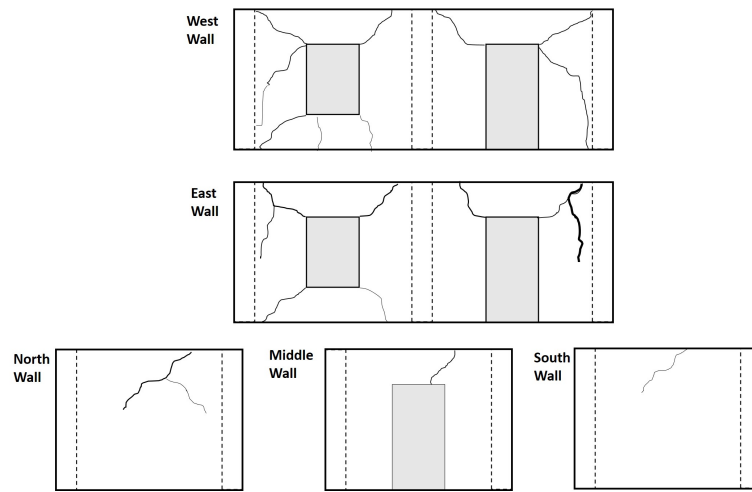


Figure D.7: Drawing of crack pattern of the house without band after the Guadeloupe 200%

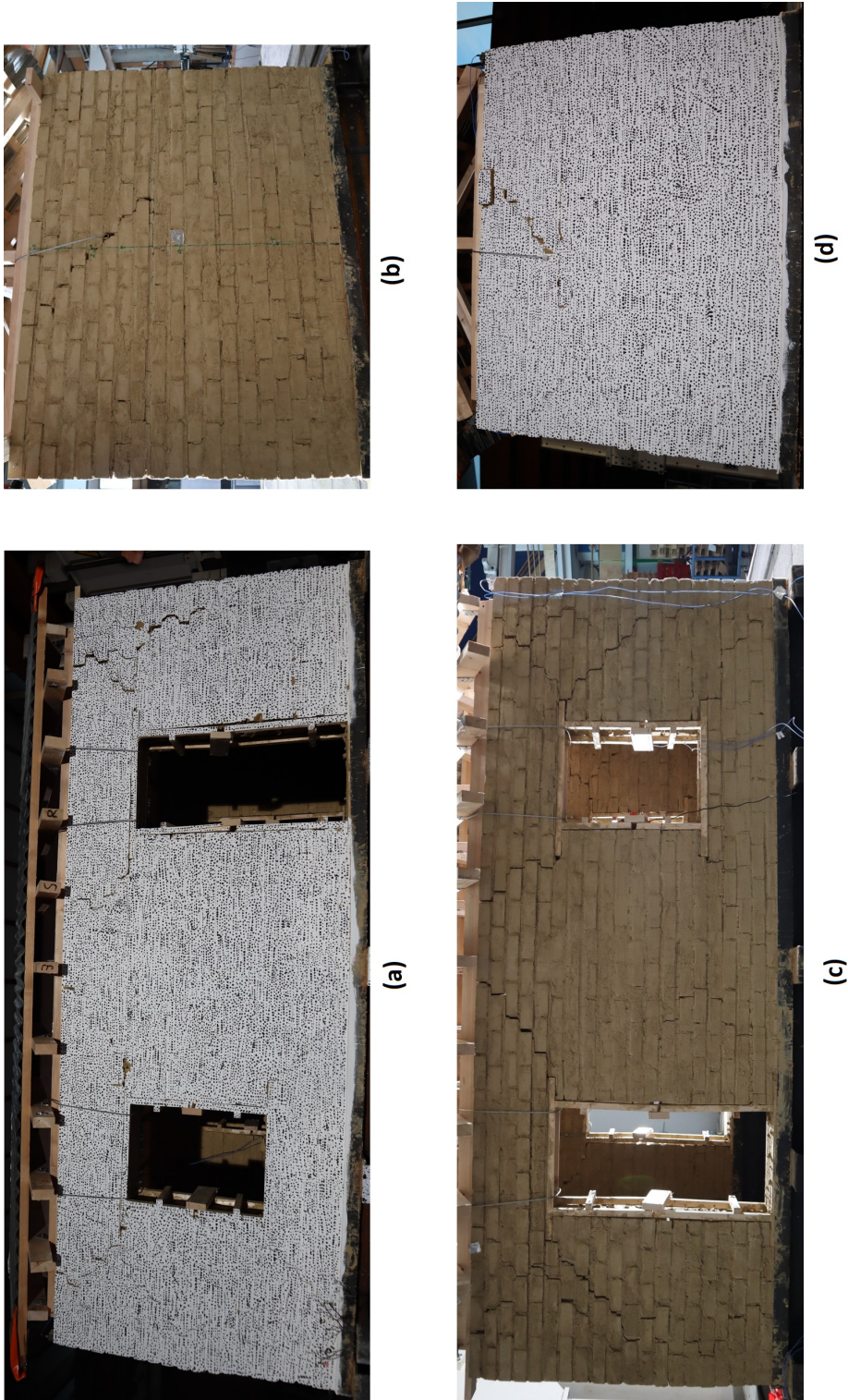


Figure D.8: Cracks in the house without band after the Guadeloupe 200%: (a) East wall; (b) South Wall; (c) West wall; (d) North Wall

D.1.5 After the Guadeloupe 300%



Figure D.9: House without band after the Guadeloupe 300%

D.2 House with timber bands

D.2.1 Beginning of the tests

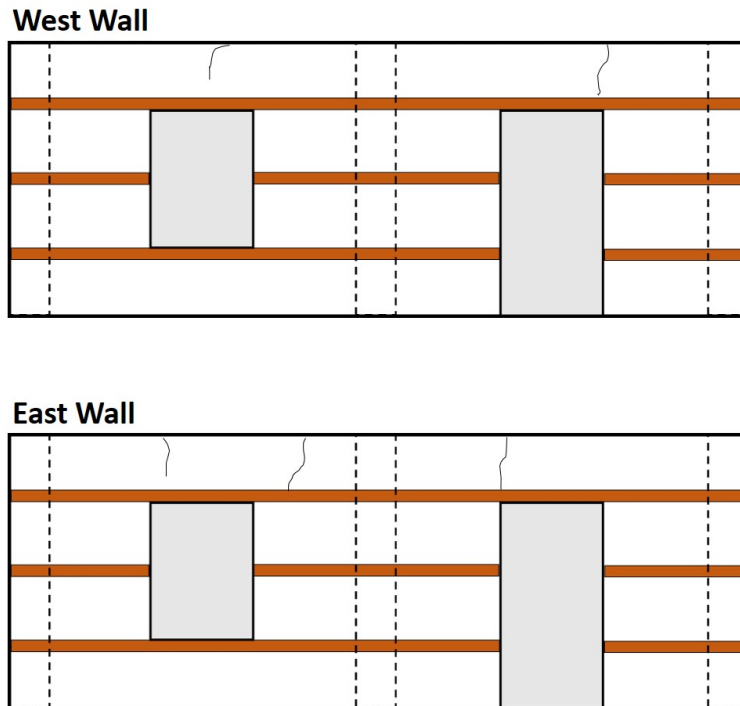


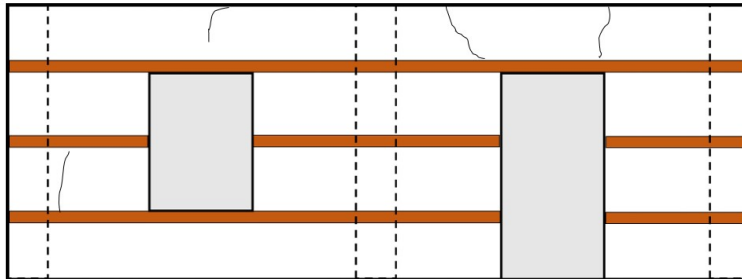
Figure D.10: Drawing of crack pattern of the house with wood bands at the beginning of the tests



Figure D.11: Cracks in the house with wood bands at the beginning of the tests: (a-b) West wall; (c-d) East wall

D.2.2 After the Guadeloupe 100%

West Wall



East Wall

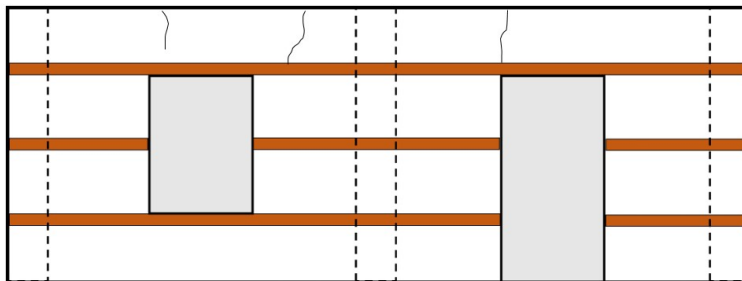


Figure D.12: Drawing of crack pattern of the house with wood bands after the 100% Guadeloupe test



(a)



(b)

Figure D.13: Cracks in the house with wood bands after the 100% Guadeloupe test: (a-b) West wall

D.2.3 After the Guadeloupe 150%

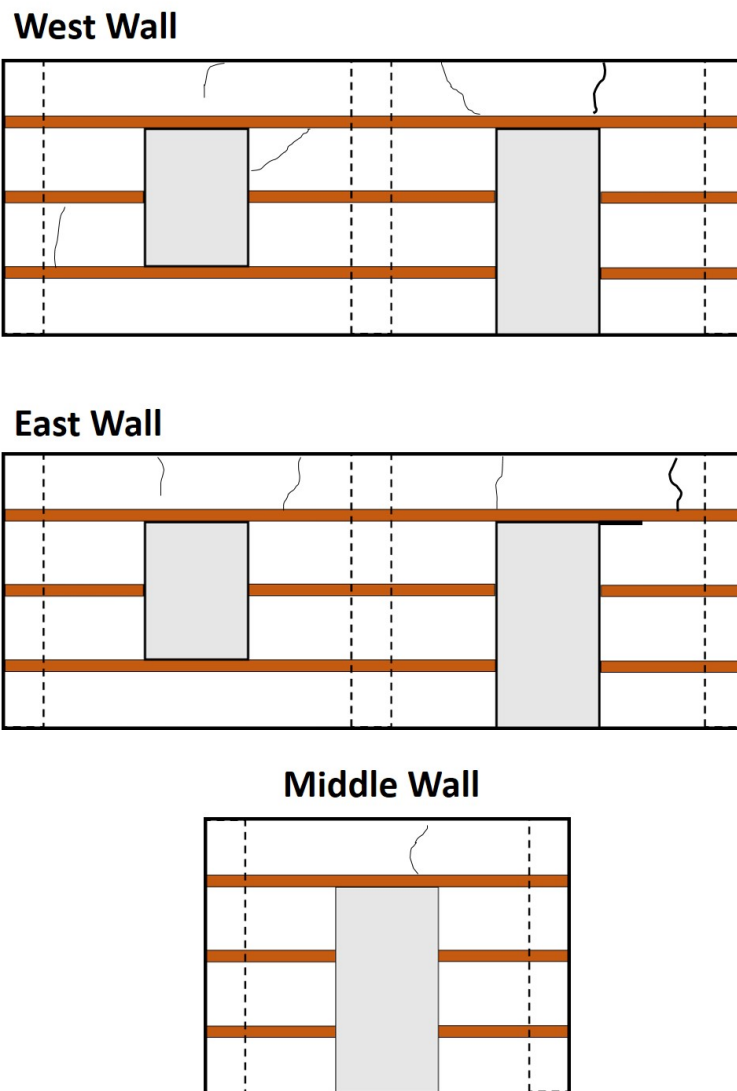


Figure D.14: Drawing of crack pattern of the house with wood bands after the 150% Guadeloupe test

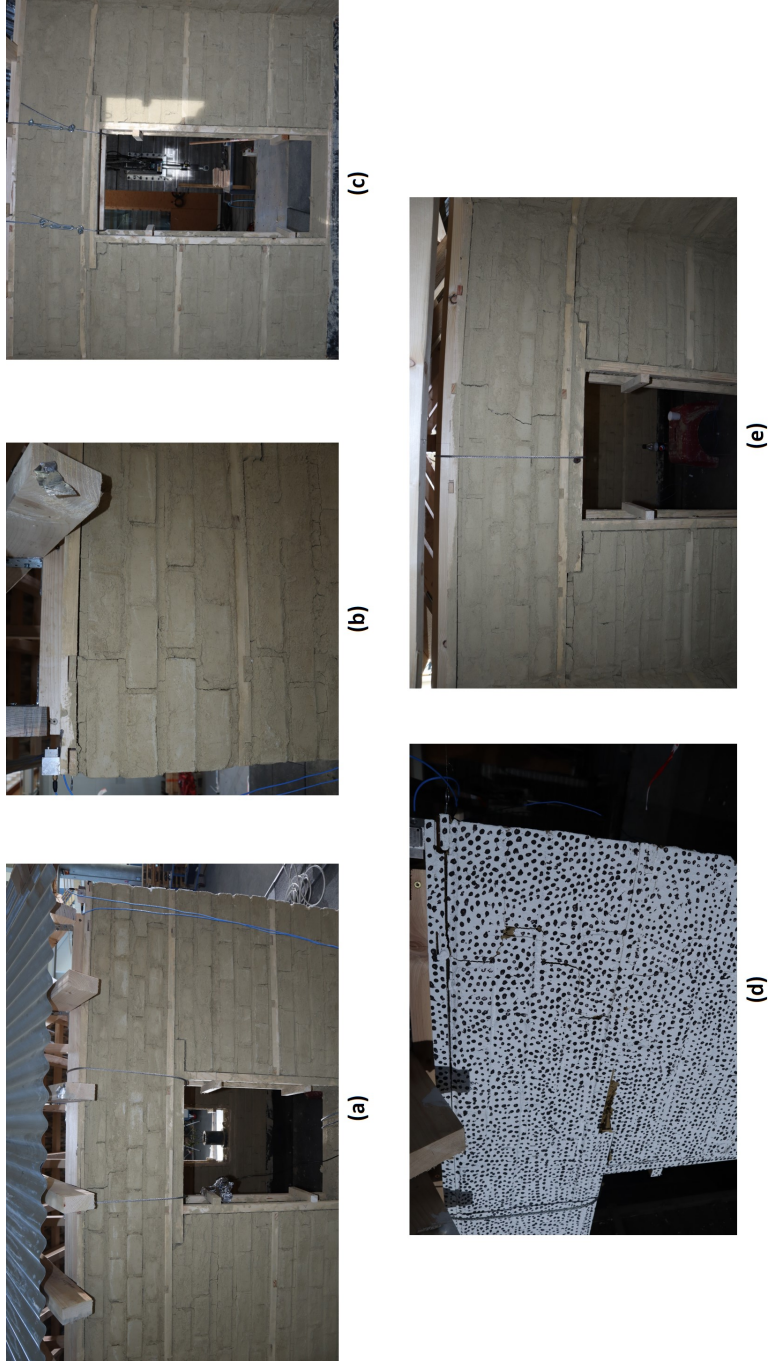


Figure D.15: Cracks in the house with wood bands after the 150% Guadeloupe test: (a-c) West wall; (d) East Wall; (e) Middle Wall

D.2.4 After the Guadeloupe 200%

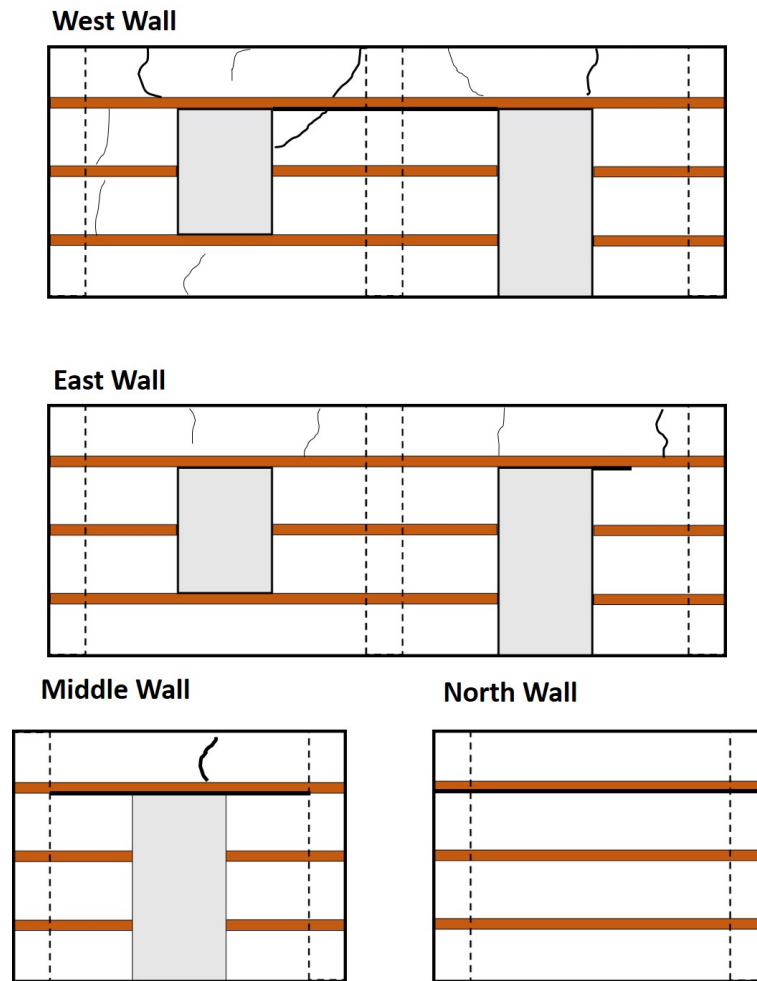


Figure D.16: Drawing of crack pattern of the house with wood bands after the 200% Guadeloupe test

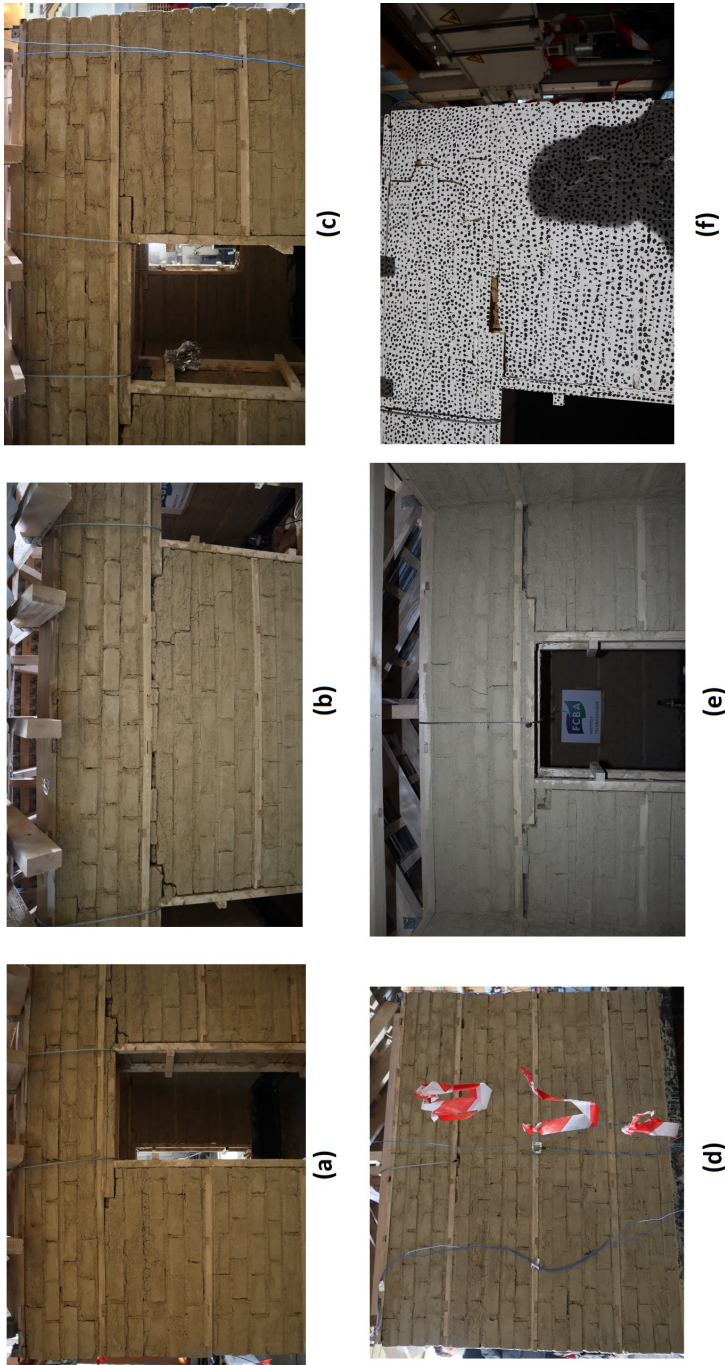


Figure D.17: Cracks in the house with wood bands after the 200% Guadeloupe test: (a-c) West wall; (d) North Wall; (e) Middle Wall; (f) East Wall

D.2.5 After the Guadeloupe 300%

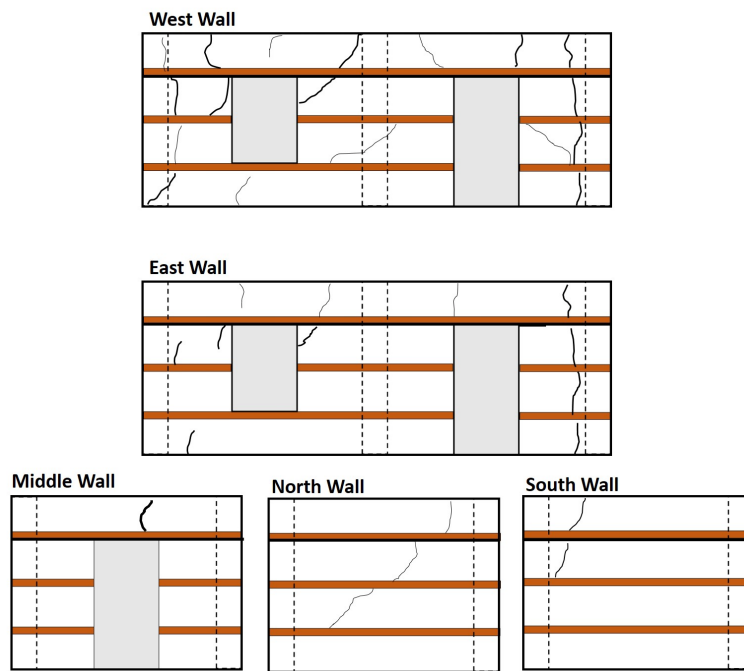


Figure D.18: Drawing of crack pattern of the house with wood bands after the 300% Guadeloupe test



Figure D.19: Cracks in the house with wood bands after the 300% Guadeloupe test: (a-c) West wall; (d) North Wall; (e-f) East Wall; (g) South Wall

D.3 House with RC bands

D.3.1 Beginning of the tests

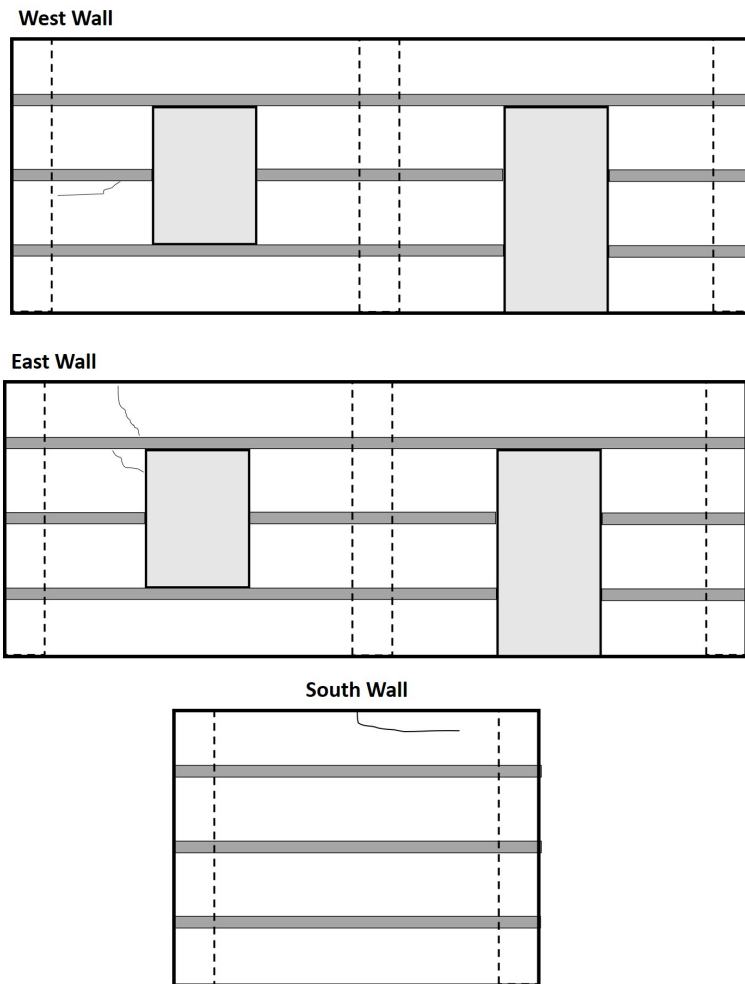


Figure D.20: Drawing of crack pattern of the house with RC bands at the beginning of the tests



(a)



(b)

Figure D.21: Cracks in the house with RC bands at the beginning of the tests: (a) East wall; (b) West wall

D.3.2 After the Guadeloupe 100%

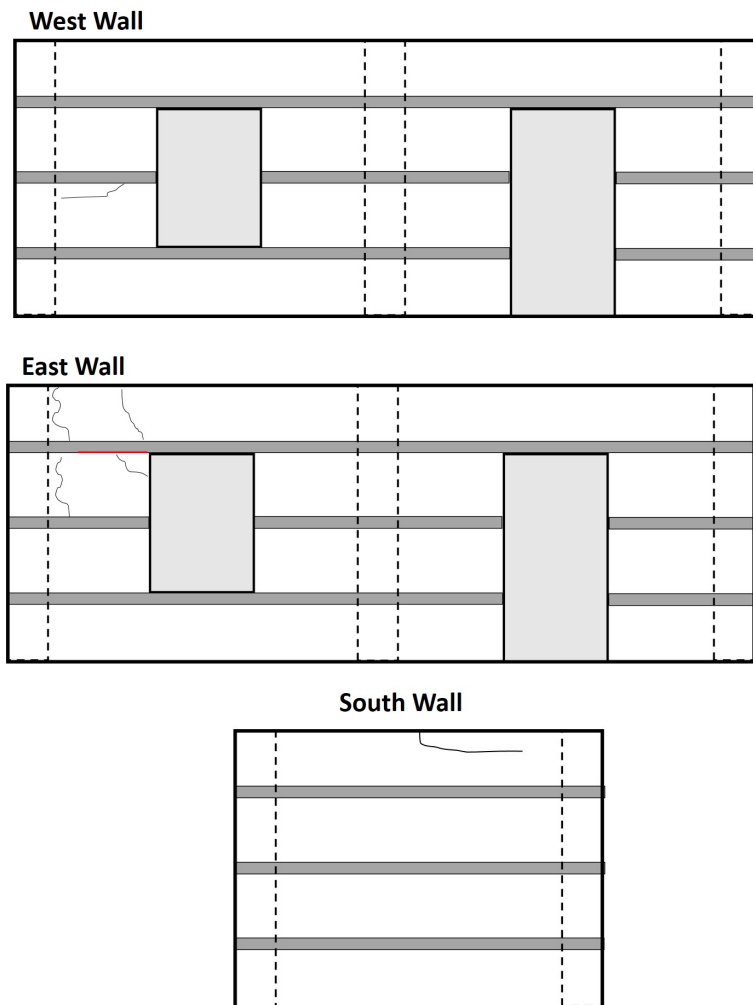


Figure D.22: Drawing of crack pattern of the house with RC bands after the 100% Guadeloupe test



(b)



(a)

Figure D.23: Cracks in the house with RC bands after the 100% Guadeloupe test: (a) West wall; (b) South Wall

D.3.3 After the Guadeloupe 150%

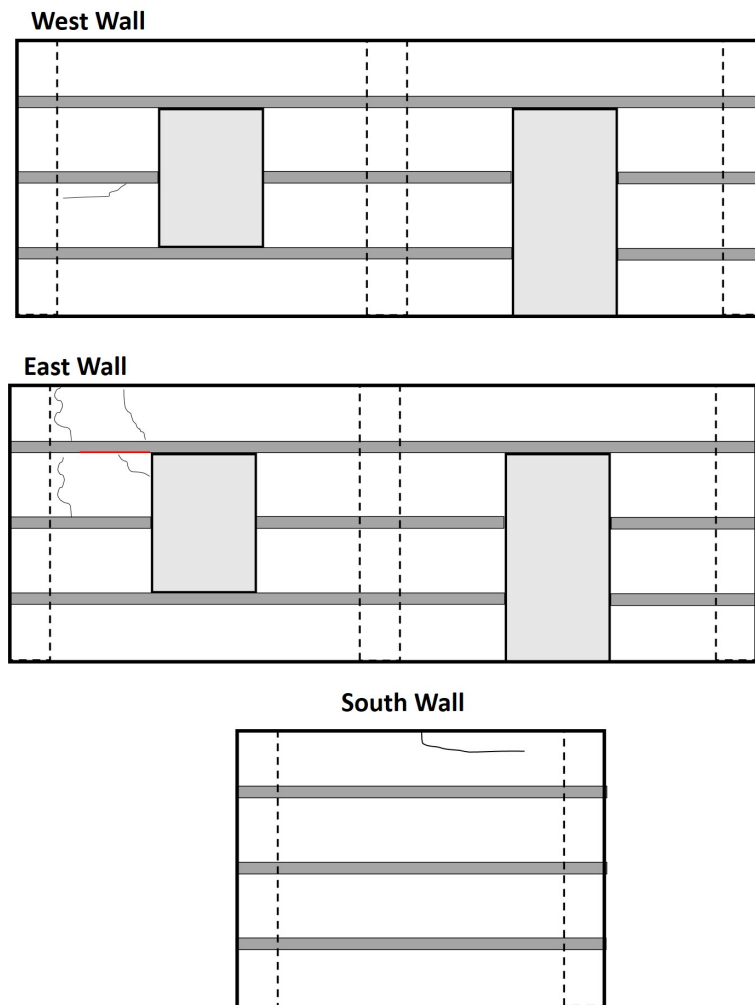


Figure D.24: Drawing of crack pattern of the house with RC bands after the 150% Guadeloupe test



(b)



(a)

Figure D.25: Cracks in the house with RC bands after the 150% Guadeloupe test: (a-b) East wall

D.3.4 After the Guadeloupe 200%

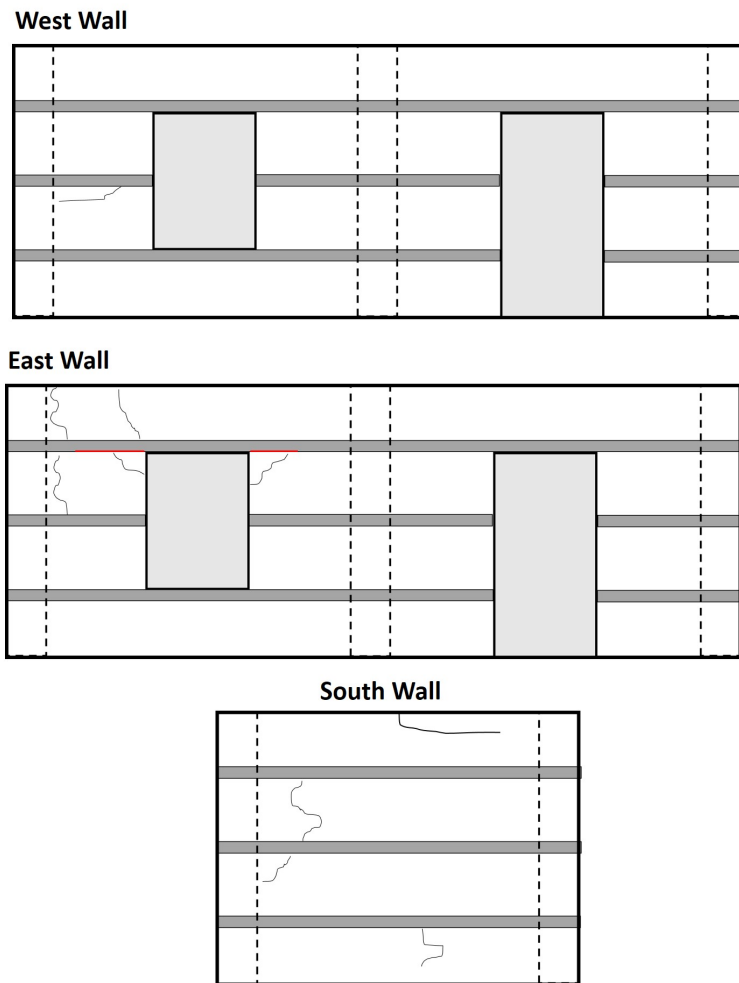
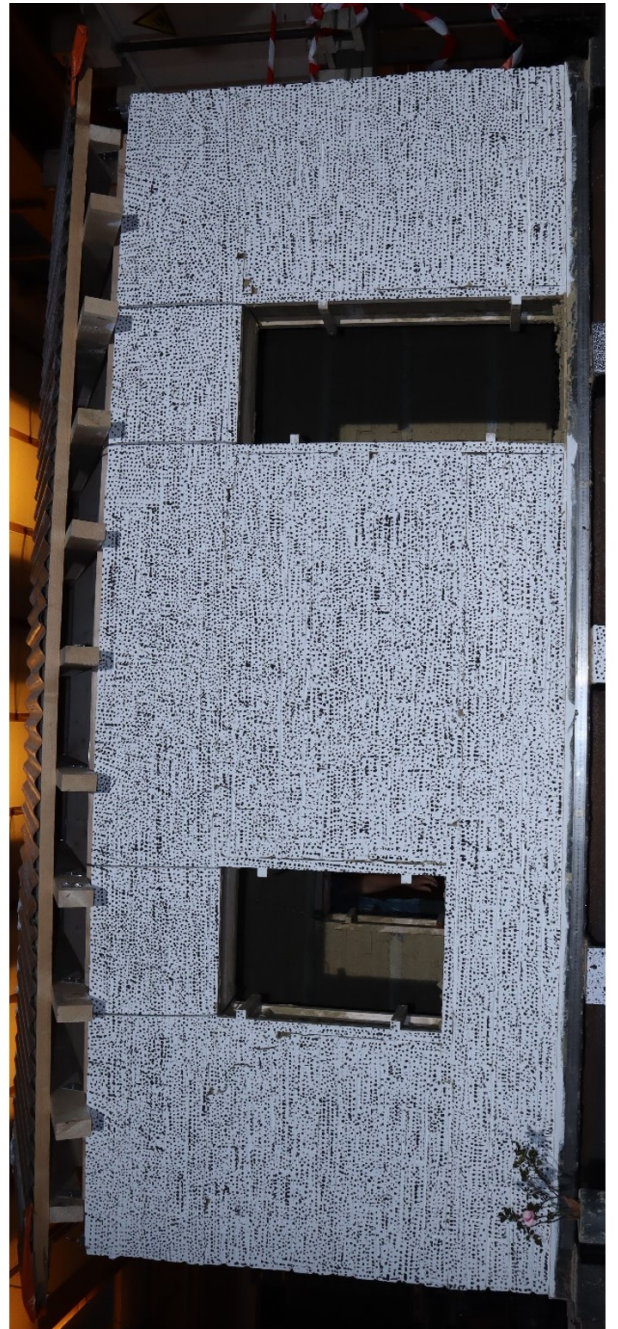


Figure D.26: Drawing of crack pattern of the house with RC bands after the 200% Guadeloupe test



(a)



(b)

D.3.5 After the Guadeloupe 300%

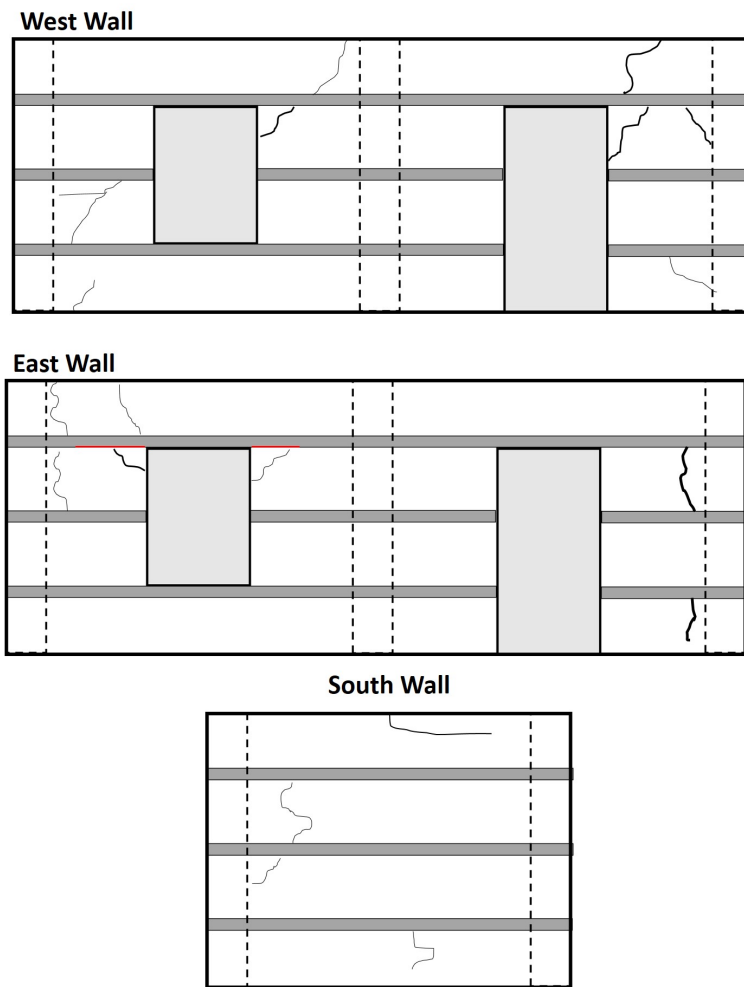


Figure D.28: Drawing of crack pattern of the house with RC bands after the 300% Guadeloupe test

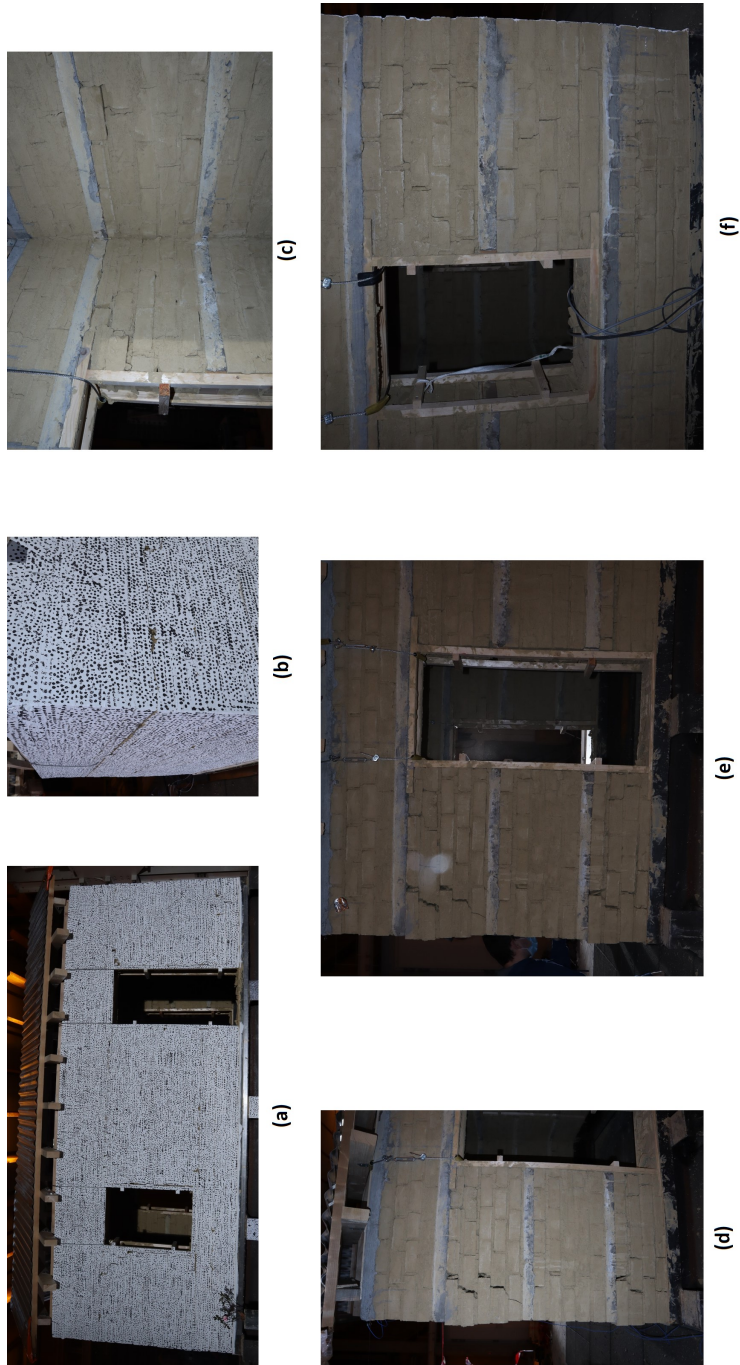


Figure D.29: Cracks in the house with RC bands after the 300% Guadeloupe test: (a-b) East wall; (c) South Wall; (d-f) West Wall